

**Doctoral Dissertation**

**博士論文**

**Integrated Design of Mechanical and Control System  
of High-Precision Dual Stage  
with Catapult Structure and Wireless Power Transfer**

(カタパルト構造及びワイヤレス給電を用いた  
超精密 2 段ステージの機構と制御の統合設計)

by

37-167081 **Yuma Yazaki**

Dissertation Submitted to

**Department of Electrical Engineering and Information Systems**

for the Degree of

**Doctor of Philosophy**

at

**The University of Tokyo**

**November. 2018**

Supervisor:

**Professor Hiroshi Fujimoto**

# 要約

半導体・液晶製造装置は半導体や液晶ディスプレイを製造するための装置であり、製品の高性能化、低価格化の要求に伴い、装置の大型化、高速高精度化が求められている。それらの装置に用いられる精密位置決めステージの位置決め誤差を低下させる要因は複数存在するが、本論文ではそのうち機械共振及びケーブル外乱に着目し、新たな機構の精密位置決めステージを提案することによりそれらの問題を解決する。

まず第2章では機械共振を改善する新たな構造の精密位置決めステージを紹介する。従来の精密位置決めステージでは2段アクチュエータ構造を用いることにより微動部の軽量化を目指していたが、粗微動間の接触を許さないため粗動部と微動部を同じ加速度で加減速させる必要があり、微動部にも大出力大重量のアクチュエータが必要であった。そのため微動部の軽量化にも限界があり、微動部の制御帯域の向上にも限界を迎えつつあった。そこで本研究室は粗微動間連結分離機構を有する新たな構造の精密位置決めステージ（カタパルトステージ）を作成した。カタパルトステージは粗微動間の接触を許容する精密位置決めステージであり、加減速時において粗動部が微動部を押すことにより加速度を与えるため、微動部自身は加減速を行なう必要がなく、定速時の制御を行なうだけの推力があれば十分である。従って微動部のアクチュエータを軽量化できるため微動部の制御帯域の向上が見込める。

次に第3章においてカタパルトステージの特徴を考慮した基本となる制御系設計を行なった。これは粗微動間の接触を許容するという従来の精密位置決めステージとは全く異なる特徴を考慮した、カタパルトステージ独自の制御系である。しかし基本制御系では定速領域に入ってから微動部の制御が始まるため、定速領域突入時の位置誤差が避けられない。実際の製造装置は定速領域において誤差がある閾値よりも小さくなってから初めて製品を製造し始めるため、定速領域突入時において微動部の誤差が零であることが望ましい。

そこで第4章において微動部の加速時における終端状態制御を用いた軌道生成法を提案し、定速領域突入時において軌道追従制御を零にできることを示した。更に微動部の推力制約を考慮するために制約付き終端状態制御を用いたモード切替条件を導出し、加速時の軌道生成を行なうことにより、微動部の推力制約を考慮したフィードフォワード（FF）制御系を設計した。

第5章では制約を考慮したフィードバック（FB）制御に関する提案を行なう。一般に精密位置決めにおける軌道追従制御ではFF制御とFB制御を組み合わせた2自由度制御系が広く用いられている。加減速時には目標軌道に対する軌道追従特性を向上させるためにFF制御が重視され、定速時においては外乱抑圧性能を向上させるためにFB制御が重要である。通常、FB制

御器を設計する際には事前に想定される外乱のスペクトルを解析し、その外乱に対する抑圧性能を最適化した制御器を設計する場合が多い。この場合制御器は想定外乱に対しては良好な外乱抑圧性能を示すものの、想定されていない突発外乱に対してはアクチュエータの飽和などにより外乱抑圧性能が悪化する場合がある。そのため、想定外乱に対しては良好な外乱抑圧性能を示しつつ、想定されていない突発外乱に対しても拘束条件の存在を陽に考慮しつつ対応できる制御法が求められる。

そこで第5章においてリファレンスガバナの考え方をを用いたオンライン計算に基づく外乱抑圧制御法を提案する。リファレンスガバナとは外部からの参照信号を整形する機構を制御系に追加する手法であり、参照入力を適切に整形することにより定められた制約を達成する。従来のリファレンスガバナに関する研究はおもに定値参照入力に対する追従性能について議論を行っており、外乱抑圧性能に対する議論は行なわれていない。第5章ではリファレンスガバナの考え方をを用いて参照入力を適切に整形することにより、定められた制約の範囲内で外乱抑圧性能を高めることを可能にする。

更に精密位置決めステージのもう一つの誤差要因であるケーブル外乱について述べる。精密位置決めステージでは強電・弱電の電力ケーブル、エアガイドの空気配管、空冷/水冷の配管、通信線など多くのケーブルがステージに繋がっており、現在ではこれらに起因するケーブル外乱が主要な外乱要因となっている。ケーブル外乱は装置の姿勢によって変化する再現性のない外乱であるため、除去することが難しいとされており、多くの先行研究において実験結果の誤差はケーブル外乱だと説明されている。

そこで本研究ではケーブル外乱を解決するために無線電力伝送技術を精密位置決めステージに適用する。無線給電によりアクチュエータやセンサに電力を送ることで、センサやアクチュエータにつながれていた配線を除去し、ケーブル外乱を抜本的に解決する。第6章においては実際に作成した無線電力伝送を用いた精密位置決めステージを2つ紹介する。まず一つ目は磁界共振結合により無線電力伝送し、軽量の Moving coil 型の3相リニアモータにより駆動される1軸精密ステージ (Wireless High Precision Stage : WHPS1) である。WHPS1は1軸の精密位置決めステージであり、無線電力伝送を精密位置決めステージに適用する際に必要な技術や条件を検証するために作成した。しかし実際の精密位置決めステージは少なくともX, Y方向の2つの自由度を持つことが多いため、もう一つのステージとしてX, Yの2つの自由度を持つ無線電力伝送を用いた精密位置決めステージ (WHPS2) を作成した。WHPS2は2段階に渡って無線給電を行なうという特徴があり、その特徴を考慮した設計が重要である。更に目標軌道やモータドライバの定格などから電力や効率などの要求仕様が事前に与えられるため、それらの要求仕様を考慮したコイル設計が必要である。

そこで第7章では85kHz帯無線電力伝送システムのための要求仕様を考慮したコイル設計法を提案する。無線電力伝送に関する多くの研究ではコイル設計は経験的にしか行なわれておらず、理論的なコイル設計法に関する研究は少ない。本研究では効率、伝送電力、送受電側電圧など様々な要求仕様を考慮したコイル設計法について述べる。そのためにまずコイル設計のために解くべき最適化問題を定式化し、コイルの相互インダクタンス及び交流抵抗の計算法につ

いて述べる。最後に最適化問題を解くことにより所望の条件を満たすコイルを設計できることを示す。

第8章では WHPS1 を実際に動作させ、ケーブル外乱が軌道追従に与える影響を検討する。本システムはコンデンサが送電側、受電側ともに直列に接続された S-S 方式の回路を用いているが、一般に S-S 方式の回路にモータのような定電力負荷を接続するとシステムが不安定になることが知られている。そのため WHPS1 では受電側においてヒステリシスコンパレータを用いた2モード制御を行なうことにより DC リンク電圧の安定化を行なっている。そしてケーブルキャリアの有無による軌道追従誤差を解析し、無線電力伝送を用いることによりケーブル外乱が抜本的解決に解決され、軌道追従制御が大幅に改善することを実験により示す。

第9章では WHPS2 の制御法について述べる。WHPS2 は無線電力伝送を2段階に渡っておこなうという特徴があり、その特徴を考慮した設計が重要である。また精密位置決めステージにおいては温度の上昇を避けるために無線電力伝送の効率を高めることが重要である。そこでステージの目標軌道から必要電力の目標軌道を導出し、必要電力を目標軌道に追従させることでシステムの更なる効率化を目指した。そして実際に WHPS2 を動作させることにより無線電力伝送を用いた多軸精密位置決めステージというコンセプトが実現できることを実験により示し、その有効性を検証した。

以上より、新たな構造の精密位置決めステージにより、精密位置決めステージの性能を劣化させる2大要因である機械共振とケーブル外乱を解決した。第2～5章の研究によりカタパルトステージを実際の目標軌道で駆動させることが可能になり、カタパルトステージを実用化するための基礎となる手法が確立された。またそれだけでなく、上記の研究で得られた知見は制約を有する制御対象に広く適用可能である。現実の制御対象にはアクチュエータの飽和や位置、速度に関する制約など様々な制約が存在する。一連の研究においてフィードフォワード制御及びフィードバック制御の両方において制約を考慮した制御系設計を提案しており、制約を考慮する制御系の新たな枠組みを構築したと言える。そして本研究では理論の提案とシミュレーションによる検証だけでなく実際の実験装置での検証もおこなっているため、現実の機械にも適用可能なことが実証されている。陽に制約を考慮できるということは、機械設計の保守性を制御によって低減できるということであるため、本稿で提案した手法によって精密位置決めステージだけでなく、その他の産業機械の性能向上や低価格化も達成されることが期待される。

第6～9章の研究では WHPS を実用化するための諸技術について検討を行ない、WHPS のシステム設計法を体系化した。これにより無線電力伝送を用いた多軸精密位置決めステージが実現できることを示し、その有効性を実験により示した。また本研究で提案した無線電力伝送用コイル設計法は要求仕様を有する一般のシステムにも適用可能である。本設計法を用いることにより無線電力伝送におけるコイル設計が簡略化され、無線電力伝送技術が更に広まっていくことが期待される。

最終的にはこれらの2つのステージを統合することにより、精密位置決めステージの性能を劣化させる要因を全て除去した究極の精密位置決めステージが完成することを願う。

# Outline

<b>1 Introduction</b>	<b>1</b>
1.1 High-precision stage . . . . .	1
1.2 High-precision stage in FPD manufacturing equipment . . . . .	1
1.2.1 Importance of FPD manufacturing equipment in modern society . . . . .	1
1.2.2 Structure of FPD equipment . . . . .	2
1.3 Causes of tracking error in the high-precision stage. . . . .	2
1.3.1 Tracking error compensation by controls . . . . .	2
1.3.2 Tracking error compensation by mechanical improvement . . . . .	4
1.4 Purpose of this thesis . . . . .	5
1.5 Structure of this thesis . . . . .	6
<b>PartI Catapult stage</b>	<b>9</b>
<b>2 Structure of catapult stage</b>	<b>10</b>
2.1 Classification of dual actuator . . . . .	10
2.1.1 Type 1: Dual-actuator in which the coarse and fine parts are mechanically connected . . . . .	10
2.1.2 Type 2: Dual-actuators in which the coarse and fine parts are not mechanically connected, and do not contact each other . . . . .	11
2.1.3 Type 3: Dual-actuator in which the coarse and fine parts are not mechanically connected, and are allowed to contact each other . . . . .	12
2.2 Concept and mechanical structure of catapult stage . . . . .	13
2.2.1 Mechanical structure of the catapult stage . . . . .	13
2.2.2 Movement of the catapult stage . . . . .	13
2.2.3 Model of the catapult stage . . . . .	14
2.2.4 Discussion of mechanical structure of catapult stage . . . . .	15
<b>3 Basic control system of catapult stage</b>	<b>17</b>
3.1 Control system for fine stage . . . . .	17

3.2	Control system of coarse stage . . . . .	19
3.3	Verification by simulation of basic control system . . . . .	19
3.4	Verification by experiment of basic control system . . . . .	20
<b>4</b>	<b>Zero settling time control based on final-state control considering with constraints</b>	<b>23</b>
4.1	New concept of the motion of catapult stage . . . . .	23
4.2	Zero settling time control in acceleration region . . . . .	24
4.2.1	Final State Control [1] [2] . . . . .	24
4.2.2	Application of FSC to Catapult Stage . . . . .	25
4.2.3	Verification by simulation of zero settling time control in acceleration region .	26
4.2.4	Verification by experiment of zero settling time control in acceleration region	26
4.2.5	Conclusion of zero settling time control . . . . .	27
4.3	Mode switching control using FSC with constrains . . . . .	30
4.3.1	Applications of mode switching control . . . . .	30
4.3.2	Condition of initial stage of FSC with thrust limitation . . . . .	31
4.3.3	Analysis on existence condition of initial state variable . . . . .	33
4.3.4	Conclusion of initial state condition in FSC with thrust limitation . . . . .	34
4.4	Real time determination of initial state variable condition using ellipsoid . . . . .	39
4.4.1	Applying the condition of initial state variable to catapult stage . . . . .	39
4.4.2	Approximation of initial state variable condition by ellipsoid . . . . .	39
4.4.3	Drawing ellipsoid approximation for initial state variable condition . . . . .	40
4.4.4	Implementation by parameterization of parameters constituting an ellipsoid .	42
4.4.5	Experimental verification of real time condition determination method using ellipsoid approximation . . . . .	42
4.4.6	Experiment1 . . . . .	43
4.4.7	Experiment2 . . . . .	44
4.5	Comparison with another control scheme with constraints . . . . .	44
4.6	Conclusion of zero settling time control based on FSC considering with constraints . .	45
<b>5</b>	<b>Sudden disturbance suppression control considering with constraints based on reference governor</b>	<b>48</b>
5.1	Importance of disturbance suppression . . . . .	48
5.2	Sudden disturbance suppression control using model predictive control without con- straints . . . . .	50
5.2.1	Impulse disturbance response . . . . .	50
5.2.2	Reference modification based on MPC without constraints . . . . .	51
5.2.3	Verification of sudden disturbance suppression performance by simulation . .	53

5.3	Sudden disturbance suppression control using reference governor . . . . .	54
5.3.1	Maximal output Admissible Set . . . . .	54
5.3.2	Design of RG . . . . .	56
5.3.3	Verification of impulse disturbance suppression control based on RG by simulation . . . . .	57
5.4	Verification of impulse disturbance suppression control by experiment . . . . .	58
5.4.1	Experimental condition . . . . .	58
5.4.2	Experimental results . . . . .	59
5.5	Comparison with reference modification method based on RG and the other control methods . . . . .	62
5.5.1	Reference modification method based on RG vs MPC with constraints . . . . .	62
5.5.2	Reference modification method based on MPC without constraints vs disturbance observer . . . . .	65
5.6	Conclusion of sudden disturbance suppression control considering with constraints . . . . .	66

## **PartII Wireless High-Precision Stage 67**

### **6 High-precision stage using wireless power transfer 68**

6.1	Background of Wireless High-Precision Stage (WHPS) . . . . .	68
6.2	Single-axis high precision stage using a moving coil wireless linear motor (WHPS1) . . . . .	69
6.2.1	Mechanical structure for WHPS1 . . . . .	69
6.2.2	Circuit structure for WHPS1 . . . . .	69
6.3	Wireless multi-axis high precision stage (WHPS2) . . . . .	71
6.3.1	Mechanical structure of the WHPS2 . . . . .	71
6.3.2	Circuit structure for WHPS2 . . . . .	71

### **7 Coil design method for wireless power transfer considering required specifications 77**

7.1	Importance of coil design for wireless power transfer . . . . .	77
7.2	Wireless power transfer using magnetic resonance coupling . . . . .	78
7.2.1	Power Transmission Characteristics in Wireless Power Transmission System with Magnetic Field Resonant Coupling Method . . . . .	78
7.2.2	Formulation of coil design problem . . . . .	79
7.3	Modeling of mutual inductance . . . . .	80
7.3.1	Mutual inductance between opposing rectangular coils . . . . .	80
7.3.2	The method of image and change of self inductance by mirror image . . . . .	81
7.3.3	Assumption of virtual mirror plane . . . . .	83
7.3.4	Mutual inductance when the ferrite exists above and below . . . . .	83

7.3.5	Consideration about distance from coil to image . . . . .	85
7.3.6	Comparison with electromagnetic field analysis . . . . .	85
7.4	Modeling of resistance . . . . .	87
7.4.1	Factor of AC resistance . . . . .	87
7.4.2	AC resistance of solid wire [3] . . . . .	88
7.4.3	AC resistance of litz wire [3] . . . . .	89
7.4.4	An increase of resistance when using ferrite . . . . .	90
7.4.5	Verification of solid and litz wire by simulation and experiment . . . . .	91
7.4.6	Numerical calculation method of AC resistance of Litz wire . . . . .	93
7.5	Coil design satisfying required specifications . . . . .	95
7.6	Conclusion of coil design considering required specifications . . . . .	97
<b>8</b>	<b>Drastic solution of cable disturbance by WHPS1</b>	<b>99</b>
8.1	Load voltage stabilization control on the receiving side . . . . .	99
8.2	Verification of cable disturbance rejection by experiment . . . . .	100
8.2.1	Coil design for WHPS1 . . . . .	100
8.2.2	Experiment of trajectory tracking by WHPS1 . . . . .	102
8.3	Conclusion of WHPS1 . . . . .	104
<b>9</b>	<b>Control for multi-axis high-precision stage using wireless power transfer</b>	<b>107</b>
9.1	Experimental verification of disturbance caused by cable tension in WHPS2 . . . . .	107
9.2	Transmitting power feedforward control using target trajectory in WHPS2 . . . . .	111
9.2.1	Power consumption of the primary side when using 2-mode method . . . . .	111
9.2.2	Input voltage control based on load power trajectory . . . . .	112
9.2.3	Experimental verification of input voltage control based on load power trajectory . . . . .	113
9.3	Conclusion of control system design for WHPS2 . . . . .	114
<b>10</b>	<b>Conclusion</b>	<b>116</b>
<b>11</b>	<b>Appendix</b>	<b>119</b>
11.1	Derivations of coefficient in (4-11) . . . . .	119
11.2	Derivations of coefficient in (4-16) . . . . .	120
<b>Thanks</b>		<b>122</b>
<b>Reference</b>		<b>124</b>
<b>Present</b>		<b>135</b>



# List of figures

1	LCD scanner. . . . .	3
2	Various mechanical structures in high-precision stages. . . . .	5
3	Causes of tracking error in a high precision stage . . . . .	6
4	Structure of the paper. . . . .	8
5	Classification of dual-actuators . . . . .	11
6	Structure of the catapult stage. . . . .	12
7	Structure of the catapult stage (link). . . . .	13
8	Movement of the catapult stage. . . . .	14
9	Parameter identification of the catapult stage. . . . .	15
10	Control system design of the catapult stage. . . . .	18
11	Simulation results. . . . .	21
12	Experimental results. . . . .	22
13	Conceptual diagram of thrust generation at acceleration region. . . . .	24
14	Augmented system with an integrator. . . . .	25
15	Control system of the fine stage with FSC. . . . .	26
16	Simulation results. . . . .	28
17	Experimental results. . . . .	29
18	Conceptual diagram of the set of initial state variables. . . . .	31
19	Condition of initial state variables with energy minimization. . . . .	36
20	Condition of initial state variables with jerk minimization. . . . .	37
21	Simulation results in time domain ( $N = 500$ ). . . . .	38
22	Condition of initial state variables using an approximated ellipsoid. . . . .	41
23	The change of parameters of the approximated ellipsoid. . . . .	43
24	The change of $(\mathbf{x} - \mathbf{c})^T \mathbf{P}^{-2}(\mathbf{x} - \mathbf{c})$ . . . . .	46
25	Thrust and tracking error of the fine stage in acceleration region. . . . .	47
26	Block diagram of reference governor. . . . .	49
27	Impulse input disturbance response. It becomes possible to manage the shape of response itself by modifying the original reference signal as shown in Fig. 27(b). . . . .	51

28	Simulation results of disturbance suppression control by reference command modification based on MPC. . . . .	52
29	Conceptual diagram of RG by using MAS. . . . .	55
30	Block diagram of the proposed method based on RG. . . . .	57
31	Simulation results of disturbance suppression control by reference command modification based on RG. . . . .	58
32	Experimental stage. . . . .	59
33	Experimental results of disturbance suppression control by reference command modification based on MPC. . . . .	60
34	Experimental results of disturbance suppression control by reference command modification based on RG. . . . .	61
35	Simulation results of disturbance suppression control by RG and MPC . . . . .	64
36	Simulation results of disturbance suppression control by MPC and DOB . . . . .	65
37	Conceptual diagram of the high precision stage with wireless power transfer. . . . .	70
38	Experimental high precision stage with moving coil wireless linear motor. . . . .	71
39	Electrical circuit diagram of a wired stage and the stage using WPT. . . . .	72
40	Frequency response of the system. . . . .	73
41	Experimental setup. . . . .	73
42	Schematic diagrams of WHPS2 system. . . . .	74
43	3D CAD model of WHPS2. . . . .	75
44	Electrical circuit of WHPS2. . . . .	76
45	Equivalent circuit of magnetic resonant coupling. . . . .	78
46	Rectangular coil. . . . .	81
47	Experimental results. . . . .	82
48	Image method. . . . .	83
49	Imaginary image plane. . . . .	84
50	Experimental result of the mutual inductance. Both coils have the ferrites. . . . .	84
51	Models of electromagnetic field analysis. . . . .	86
52	Cross section of a round conductor that is influenced by an external magnetic field in x-direction. The conductor is infinitely long in z-direction. . . . .	88
53	Cross-sectional area of litz-wire winding. . . . .	90
54	Equivalent circuit of the coil with ferrite. . . . .	91
55	Simulation result . . . . .	92
56	Measurement result of resistance of the solid wire. . . . .	93
57	Measurement result of resistance of the litz wire. . . . .	94
58	Modeling and resistance calculation of litz wire in [4, 5]. . . . .	95
59	Resistance of the litz wire. . . . .	96

60	Designed coil. . . . .	97
61	Operation state of 2-mode method. . . . .	100
62	Waveform of the DC link voltage. . . . .	101
63	Equivalent circuit of WPT using magnetic field resonance coupling. . . . .	101
64	The relationship between the efficiency and the equivalent load resistance. . . . .	102
65	Position dependency of the mutual inductance. . . . .	103
66	Frequency response of the system. . . . .	105
67	Experimental results. . . . .	106
68	Experimental results. . . . .	109
69	Frequency analysis of estimated disturbance. . . . .	110
70	Comparison with frequency analysis results in different speed. . . . .	110
71	Target position, velocity, acceleration, and load power trajectories. . . . .	112
72	Conceptual diagram of reference signal of transmission power. . . . .	112
73	Experimental setup of primary voltage modification . . . . .	114
74	Experimental result of the primary voltage modification. . . . .	115

# List of tables

1	Plate size of the flat panel display manufacturing system. . . . .	2
2	Measures of cable disturbance. . . . .	6
3	The catapult stage parameters . . . . .	14
4	Simulation result . . . . .	27
5	Experimental result . . . . .	27
6	Conditions of initial state variables. . . . .	34
7	Number of steps at control switching and maximum thrust. . . . .	45
8	Comparison of trajectory generation methods. . . . .	47
9	Four control methods compared in the experiment. . . . .	59
10	RG vs MPC. . . . .	63
11	RG vs MPC, Simulation results. . . . .	63
12	Prop1 vs DOB, Simulation results. . . . .	66
13	Cleanroom classification. . . . .	69
14	Mechanical parameter. . . . .	73
15	Coil (150 mm × 280 mm). . . . .	85
16	Coil (150 mm × 580 mm). . . . .	85
17	Coil (150 mm × 1040 mm). . . . .	85
18	Comparison of self inductance [ $\mu$ H]. . . . .	86
19	Coil parameters (Y axis). . . . .	98
20	Coil parameters (X axis). . . . .	98
21	Coil parameter. . . . .	102
22	Trade-off of the transmission efficiency and loss. . . . .	113
23	Experimental result. . . . .	113

# Chapter 1

## Introduction

### 1.1 High-precision stage

Semiconductor and liquid crystal display manufacturing equipment produces products by processing a silicon wafer or a glass substrate which are on the high speed and precision positioning stages [6, 7, 8, 9, 10]. In recent years, low price and miniaturization and high performance of the products are required, thus the importance of the high speed and accuracy positioning stage is more important. In this research, the stage that determines the final positioning accuracy of the semiconductor and liquid crystal display manufacturing equipment is defined as high-precision stage, especially this thesis handles liquid crystal display manufacturing equipment (FPD equipment : flat panel display equipment).

### 1.2 High-precision stage in FPD manufacturing equipment

#### 1.2.1 Importance of FPD manufacturing equipment in modern society

FPD equipment is the industrial equipment which manufactures FPD [11, 9, 10]. FPD is widely used in television, display of PCs and mobile phones, and are indispensable in modern society. In recent years, demand for large-sized panels and smartphone is increasing shown in Tab. 1 [12], and FPD is needed to be large and high definition. For example, [13] expects that shipments of smartphones reach 1.78 billion units in 2020, whereas 1.35 billion units in 2014. In addition, the 4K TV with 4 times the resolution of full high vision is expected to be rapidly spreading to 78.22 million in 2019 sold in the global market from 998,000 units in 2014 [14]. The glass substrate of  $800 \times 950$  mm is the maximum in the literature [15] of 2001, but in the latest FPD equipment  $2880 \times 3130$  mm [16] is the largest, which is approximately 11.9 times larger than the area ratio. In this way, a market demands the products larger size, higher definition and lower price, and the high-precision stage in

Tab. 1: Plate size of the flat panel display manufacturing system.

Generation	4	6	8	10	10.5
Year	2000	2003	2005	2009	2018
Plate size [mm]	700×900	1500×1850	2200×2550	2880×3130	2940×3370
Ratio	1	4.4	8.9	14.3	15.7

FPD equipment requires a larger stage and higher speed and precision control.

### 1.2.2 Structure of FPD equipment

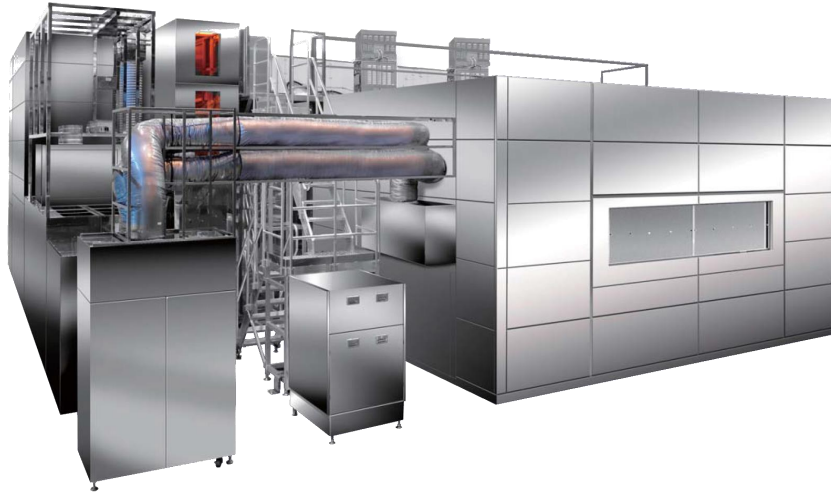
An overview of the FPD equipment and conceptual diagram of its product manufacturing part are shown in Fig. 2. The FPD equipment is very large industrial equipment whose size is about 11 m × 15 m and weight is 13 t. The product manufacturing part consists of a plate stage on which a glass substrate with a photosensitive material and a mask stage on which a mask with engraving a circuit pattern. These two stages perform scanning while synchronously tracking both stages with respect to a fixed optical system in FPD equipment [17]. The plate stage is the stage whose size is 3 m × 3 m and weight is 5 t, and repeats acceleration/deceleration with an acceleration of 0.1 G, and requires high positioning accuracy from tens to hundreds nanometer in constant velocity motion. It is called the most precise machine in human history due to the severity of these demands. Various approaches are underway in combination in the FPD equipment to improve the throughput, for example, improvement of optical system and mask [18, 17, 19, 20, 21], lighten of the stage [22, 23], anti-vibration system [24, 25], vibration suppression by using air guide [26] or magnetic force [27].

## 1.3 Causes of tracking error in the high-precision stage.

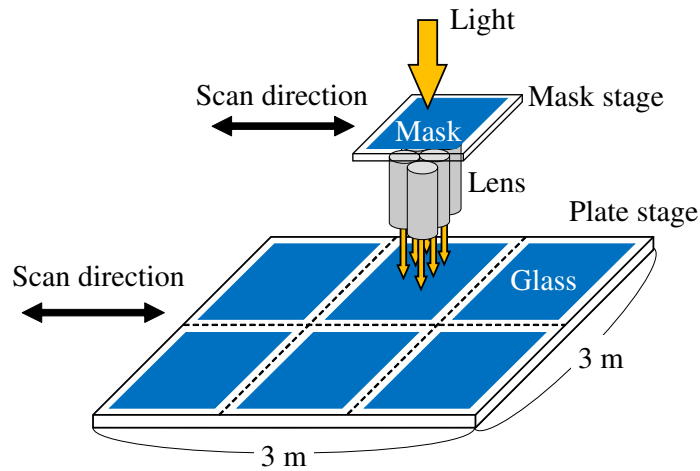
Faster and more precise positioning is required for the high-precision stage to achieve high throughput and low cost in the FPD equipment. Fig. 3 illustrates the causes of tracking errors in the high-precision stage. The causes are mainly classified into two types : control-side and mechanical-side.

### 1.3.1 Tracking error compensation by controls

To achieve precise positioning, high performance feedforward and feedback control are required. There are many studies using model-based feedforward controls, for example, Zero Phase Error Tracking Controller (ZPETC)[28], Perfect Tracking Control (PTC)[29], Final-State Control (FSC)[1][2], and MIMO feedforward controls [6, 30, 31]. The advantage of model-based control is that a control system design becomes easy because performance indexes can be given by using models. However,



(a) General view of a LCD scanner [16].



(b) Schematic of a wafer stage in the LCD scanner

Fig. 1: LCD scanner.

the disadvantages of the model-based control are that the control performance is degraded by the modeling error and a disturbance model is required to suppress the disturbance because of an internal model principle.

On the other hand in recent years, data-based control strategies have attracted attention: adaptive control [32], neural networks [33], repetitive control [34], and iterative learning control (ILC) [35], and there are many studies applying these control strategies to the high-precision stage [36, 37, 38, 26, 39]. The advantages of the data-based control are that the modeling is not required and it is possible to compensate for periodic disturbance which is difficult to handle in the model-based control because the control input is generated based on past data. However, the disadvantage of the data-based control is the control system becomes black-box because the control input is automatically updated and the control performance is low until learning the operation. Especially, ILC is usually applied to the high-precision stages because the high-precision stage often repeats the same operations and ILC is suitable with this characteristics [40, 41, 42, 43, 44, 45]. In addition, there are several novel ILC

that can handle even when the target trajectory is changed [41] and selectively suppress periodic disturbance by using sparse command signal [46].

The feedback control with high-bandwidth in the FPD equipment is difficult because the mechanical resonance frequency is very low (about 15 Hz) [9]. There are many studies to improve the control bandwidth of FB controller, for example,  $H_\infty$ -based approach [47], iterative feedback tuning [48], over-sensing and over-actuation [49], and self resonance cancellation (SRC) which suppresses mechanical resonance by using both information of motor-side and load-side [50].

The high-precision stage in FPD equipment produces the product in the constant velocity, but the tracking performance is degraded due to the interference from translational motion to pitching and rolling rotational motion [51]. In addition, [52] indicates that displacement of the sensor amplifies the pitching and FB gain cannot be increased. Thus, a decoupling control is also important. Single-input single-output control system is widely used after applying a thrust distribution matrix which reduce a cross-talk between the axes [6, 53, 54], however, there is a study considering variation of products of inertia [55]. [56, 57] discussed a optimal mechanical structure and actuation point from the point of view of minimizing the cross-talk between the axes.

### **1.3.2 Tracking error compensation by mechanical improvement**

Mechatronic causes of tracking errors are classified into the effects of mechanical resonance and disturbance.

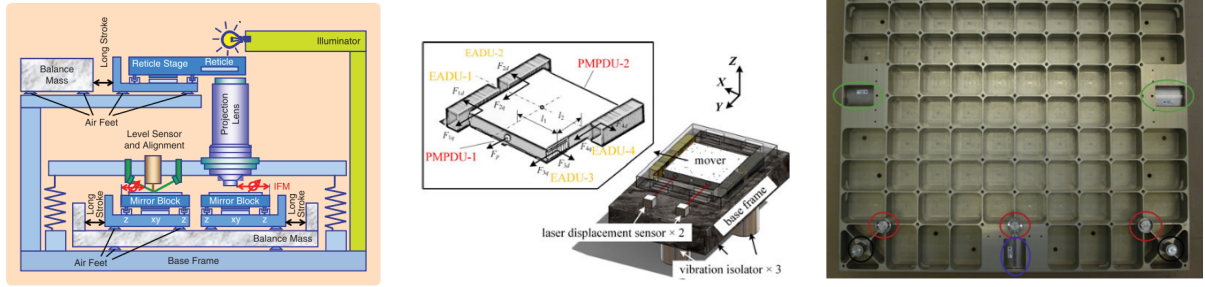
#### **Improvement of mechanical resonance**

Mechanical resonance should be sufficiently increased to achieve higher control bandwidth by improving the mechanical structure. For example, a dual actuator structure which has fine and coarse parts has been used to lighten the fine part [22, 6, 58] as shown in Fig. 2(a). In the high-precision stage, the fine stage should be controlled precisely with six degrees of freedom, thus the coarse part which limits the degrees of freedom is required. In addition, the coarse stage carries cables instead of the fine stage to reduce the effect of cable tension.

[59] proposed a high-precision stage which has two different actuators on a stage as shown in Fig. 2(b). The stage reduces energy consumption by selectively using motors at acceleration/deceleration and constant speed. This concept is similar to a stage proposed in this thesis.

[60] proposed a honeycomb structured high-precision stage with many sensors and actuators as shown in Fig. 2(c). This stage allows deformation of the stage, but compensates the influence of deformation by placing many sensors and actuators.





(a) Dual actuator structure [6]. (b) A high-precision stage which has two different actuators [59] (c) A honeycomb structured high-precision stage with many sensors and actuators [60]

Fig. 2: Various mechanical structures in high-precision stages.

## Disturbance rejection

Disturbance caused by floor vibrations and friction is almost solved by using contactless actuators (e.g. linear motors [6, 61] and voice coil motors [62]) and contactless gravity compensation (e.g. air bearings [58] and magnetic levitation [63, 64, 65]) by separating the high-precision stage from floor.

However, in reality, power cables, sensor cables, and cooling pipes are all connected. Tab. 2 shows advantage and disadvantage of types of motor. The power cable issue can be addressed by the moving magnet design, but the moving component becomes heavier, which is problematic because its control bandwidth is limited by the resonance frequency inversely proportional to the mass. In addition, using the moving magnet motor in the high-precision stage where a temperature control is severe is difficult because the moving magnet flows current in the not operated portion and the overall heat becomes large.

Alternatively, a moving coil design can lighten the moving component. However, the stiff power cables require to transmit the electrical power to the moving component, whose use should be avoided because position-dependent nonlinear disturbances caused by the stiffness and dumping of the cable aggravate the tracking performance [9, 66, 67].

## 1.4 Purpose of this thesis

The purpose of this thesis is to design two novel high-precision stage to solve these problem, especially the mechanical resonance and the cable disturbance. One is a dual actuated stage which has decoupling structure between fine and coarse parts. This stage increases the mechanical resonance by lighten the fine part. The other is a high-precision stage using wireless power transfer technology. This stage drastically rejects the cable disturbance. Unique system and control design are necessary because these are stages of new concepts that have not existed so far. This thesis will introduce the

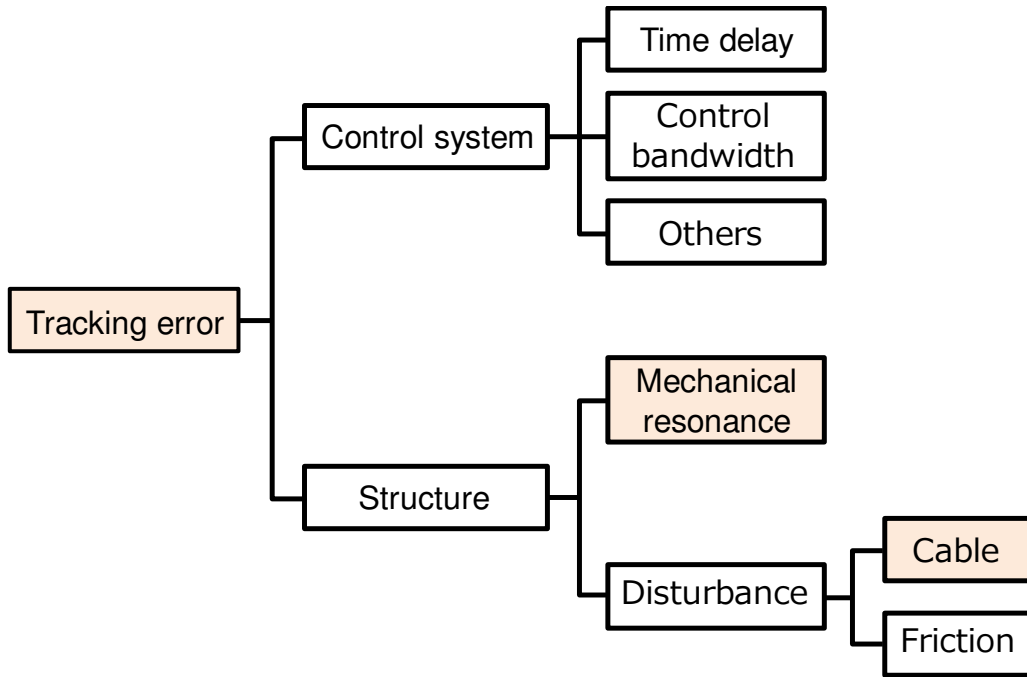


Fig. 3: Causes of tracking error in a high precision stage

Tab. 2: Measures of cable disturbance.

	Moving magnet	Moving coil
Mover	Magnet	Coil
Stator	Coil	Magnet
Mass of mover	Heavy	Light
Mechanical resonance frequency	Low	High
Required cables	Sensor	Power, Sensor
Cooling	Not required	Required
Cable disturbance	Almost zero	Exist

design for these stages.

## 1.5 Structure of this thesis

Fig. 4 shows the structure of this thesis.

In chapter 1, the background of the high-precision control is introduced and the error factors in the high-precision stage are classified. Chapter 2 introduces a novel high-precision stage called a catapult stage which has a new mechanical structure structure with the coarse and fine motion coupling and separation mechanism to improve the mechanical resonance. The catapult stage is a high-precision stage that allows contact between the coarse and fine stages, and at the time of acceleration and

deceleration, the coarse stage pushes the fine stage and gives acceleration. Thus the thrust of the fine stage becomes small because the fine stage does not need to accelerate and decelerate itself. As a result, the control performance of the fine stage is improved by reducing the weight of the actuator in the fine stage.

Next, chapter 3 proposes a basis control system design for the catapult stage which considers the characteristics of the catapult stage. However, the basic control system cannot avoid a tracking error at the beginning of the constant velocity region because the control system drives the fine stage after entering the constant velocity region. Therefore, chapter 4 proposes a feedforward control considering with constraints in the acceleration region. This chapter derives the mode switching condition using final state control with constraints and generates the trajectory at the end of acceleration region. Then, the tracking error at the beginning of the constant velocity region becomes zero considering with thrust limitations.

In addition, in chapter 5, a feedback control method considering with constraints in the constant velocity region to improve a disturbance suppression performance is proposed. This method improves the disturbance suppression performance considering with constraints by modifying the reference signal properly based on a reference governor. A basic control methods described in chapters 3, 4 and 5 establish for the practical catapult stage.

Chapter 6 introduces previous studies about the cable disturbance which is another cause of tracking error in the high-precision stage. In order to solve this problem, chapter 6 proposes novel high-precision stages using wireless power transfer (WPT) with magnetic resonance coupling. One is a single-axis wireless high-precision stage driven by WPT (Wireless High Precision Stage 1 : WHPS1), and the other is a multi-axis wireless high-precision stage (WHPS2).

A coil design method considering with required specifications such as transmission power efficiency and secondary side voltage is necessary for these stages because the required specifications are given in advance from target trajectory or the rating of the motor driver. Therefore, chapter 7 proposes a coil design method considering with required specifications for WPT at 85 kHz.

In chapter 8,9, the effect of the cable disturbance is discussed by driving WHPS1 and WHPS2. It is shown that the tracking performance is greatly improved by using WHP in the high-precision stage by analyzing the tracking error in the case of using or not using the cable carrier.

Finally, chapter 9 describes the control method of WHPS2. WHPS2 has the characteristics of performing multi-stage WHP, and control system design considering its characteristics is important. Therefore, chapter 9 derives the optimal power trajectory from the target position trajectory to achieve higher power transmission efficiency. The concept of multi-axis high-precision stage using WHP can be realized by using WHPS2, and WHPS2 drastically solves the cable disturbance which has been considered difficult to solve.

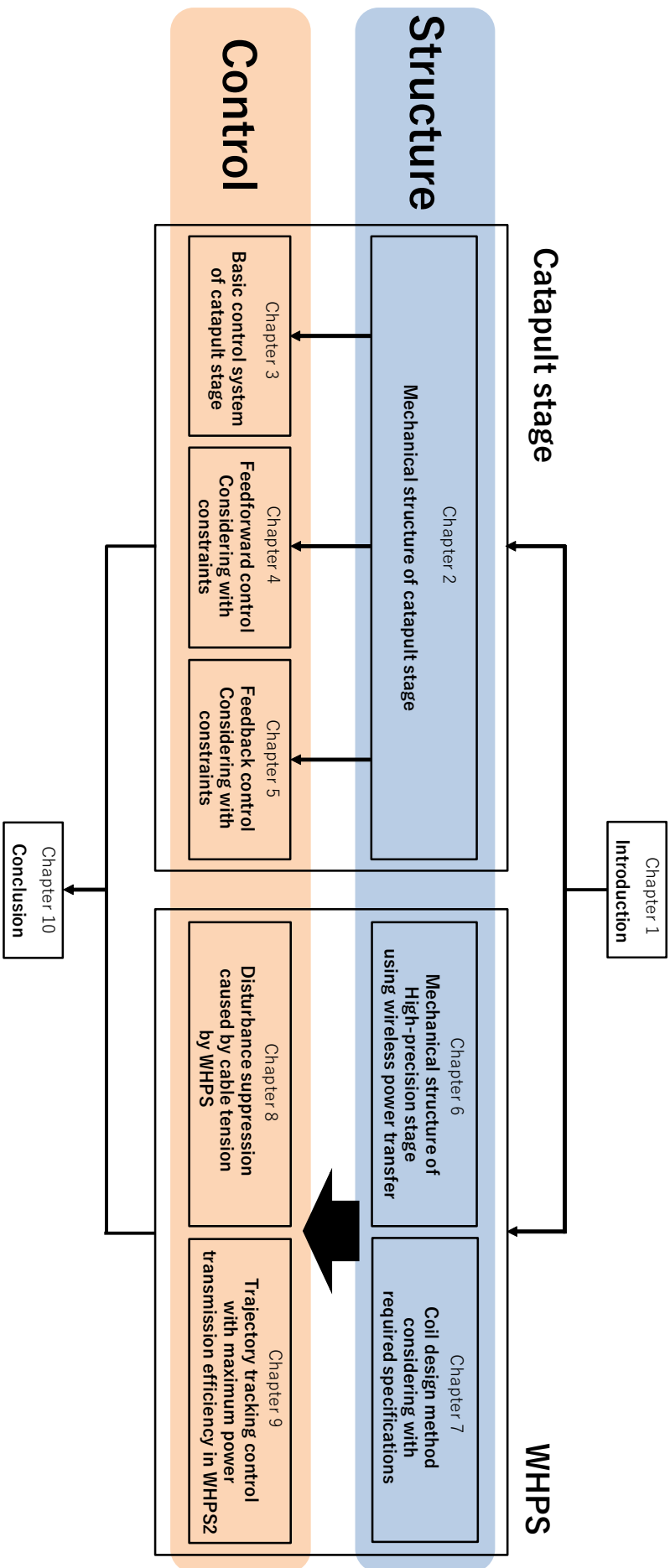


Fig. 4: Structure of the paper.

# **Part I**

## **Catapult stage**

# Chapter 2

## Structure of catapult stage

### 2.1 Classification of dual actuator

The high-precision stage demands high precision and high throughput because products made by the stage require a low price and high density. It is necessary to make the stage larger and faster for higher throughput, and to achieve further positioning accuracy by being the bandwidth of the position feedback (FB) loop higher. The FB control bandwidth is limited by the mechanical resonance frequency [49], and the frequency is represented by (2-1).

$$f = \frac{1}{2\pi} \sqrt{\frac{k}{m}} \quad (2-1)$$

Here,  $k$  is a spring constant, and  $m$  is a mass. From (2-1), the resonance frequency of the stage decreases as the size of the stage and the mass of it increase, so it is impossible to improve the bandwidth of the FB loop. In fact, the resonance frequency of the industrial high-precision stage is 15 Hz, and this limits the control performance [9]. Thus, to increase in size of the stage and to achieve high speed and high precision are conflicting demands in the high-precision stages.

Dual-actuators which have a coarse component and a fine component have been used to achieve high precision and high throughput in high-precision stages [6, 68, 65]. The coarse part is driven for long distance with large thrust and the fine part is precisely driven for short distance. This paper describes the concept of a novel high-precision stage by classifying the dual-actuators into the following three types. Fig. 5 shows a classification of the dual-actuators.

#### 2.1.1 Type 1: Dual-actuator in which the coarse and fine parts are mechanically connected

Examples of this type of dual-actuators are an optical disc [69, 70, 71], hard disk drives (HDD) [72], and the precise positioning stage without using an air guide in the fine part [73]. In this type of


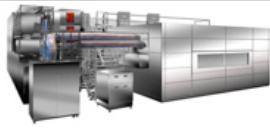
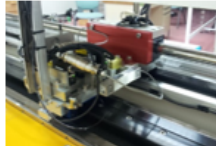
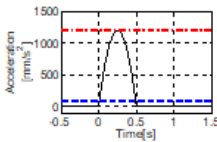
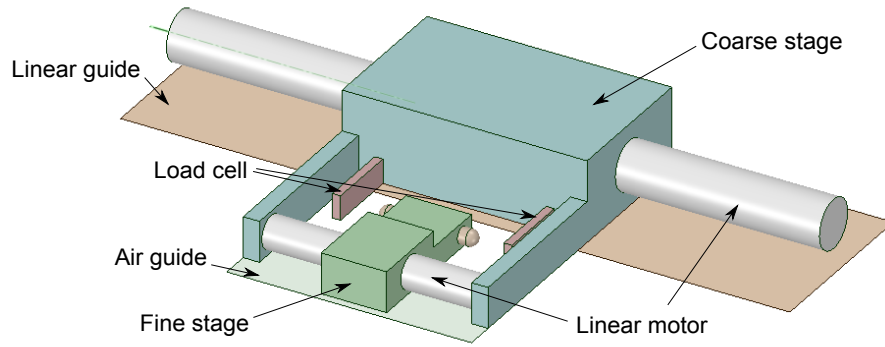
	Type 1	Type 2	Type 3
Mechanical connection	Yes	No	No
Allow contact		No	Yes
Application	 HDD	 Typical scan stage	Catapult stage 
Advantage	Light fine stage	Fine stage is isolated	Type1 + Type2
Disadvantage	Disturbance transmits to fine stage	Heavy fine stage 	Contact/Separation occurs

Fig. 5: Classification of dual-actuators

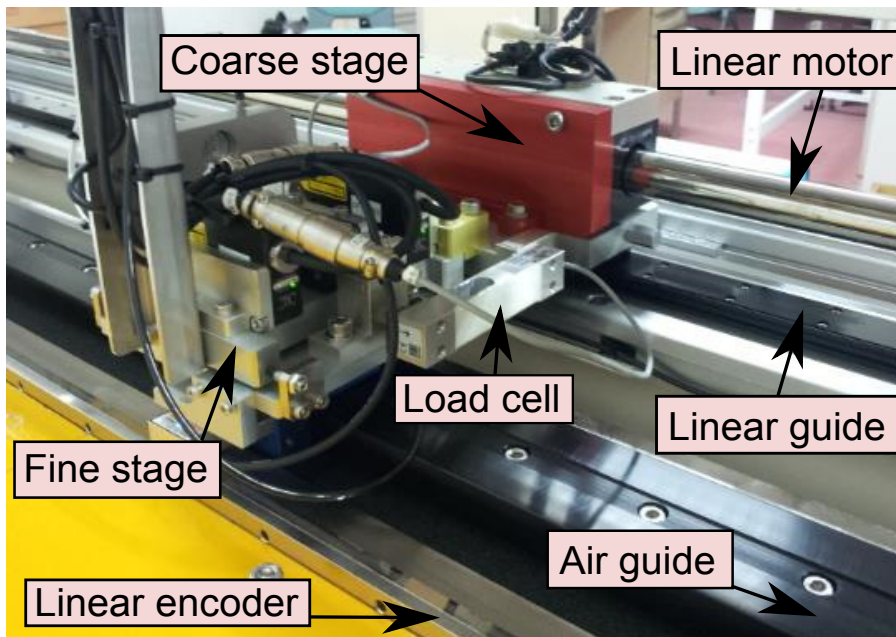
dual-actuators, the fine part can be simplified and lightened because the fine and coarse parted are mechanically connected and the coarse part can have a large motor for accelerating and decelerating the entire system. As a result, the resonance frequency of the fine part is increase and the FB bandwidth of it becomes higher. However, there is a problem that the disturbance is easily transmitted from the coarse part to the fine part because these parts are mechanically connected.

### 2.1.2 Type 2: Dual-actuators in which the coarse and fine parts are not mechanically connected, and do not contact each other

Examples of this type of dual-actuators are the high-precision stages which use the air guide or a magnetic levitation in the fine part [6, 68, 65]. This type of dual-actuator is mainly used in the equipment for producing the semiconductors and liquid crystal displays. There is an advantage that the disturbance is hard to be transmitted from the course part to the fine part because this type no mechanical connection. However, an actuator for driving the fine part becomes large because the fine and coarse parts should have same acceleration to avoid contact with each other. Therefore, it is difficult to increase the FB bandwidth of the fine part in this type of dual-actuator because the fine part need to have a large motor to accelerate itself, and it is expected that the limit of the throughput is close.



(a) Schematic of the catapult stage.



(b) Experimental stage

Fig. 6: Structure of the catapult stage.

### 2.1.3 Type 3: Dual-actuator in which the coarse and fine parts are not mechanically connected, and are allowed to contact each other

Based on the above two types of dual-actuators, we propose a novel dual-actuator called a catapult stage in this paper shown in Fig. 6, which does not mechanically connect the coarse and fine parts and allows contact between these parts [74]. Type 1 has the advantage which can simplify and lighten the fine part, and Type 2 has the advantage which does not transmit the disturbance from the course part to the fine part. The catapult stage can have the both advantages by allowing collision between the coarse and fine parts. With the new structure of the dual-actuator, it is possible to reduce the weight of the fine part while increasing the size of it, and to improve the FB bandwidth, so the catapult stage can achieve larger size, higher speed, and higher accuracy. However, a control system design considering with the unique characteristics of the catapult stage is necessary.



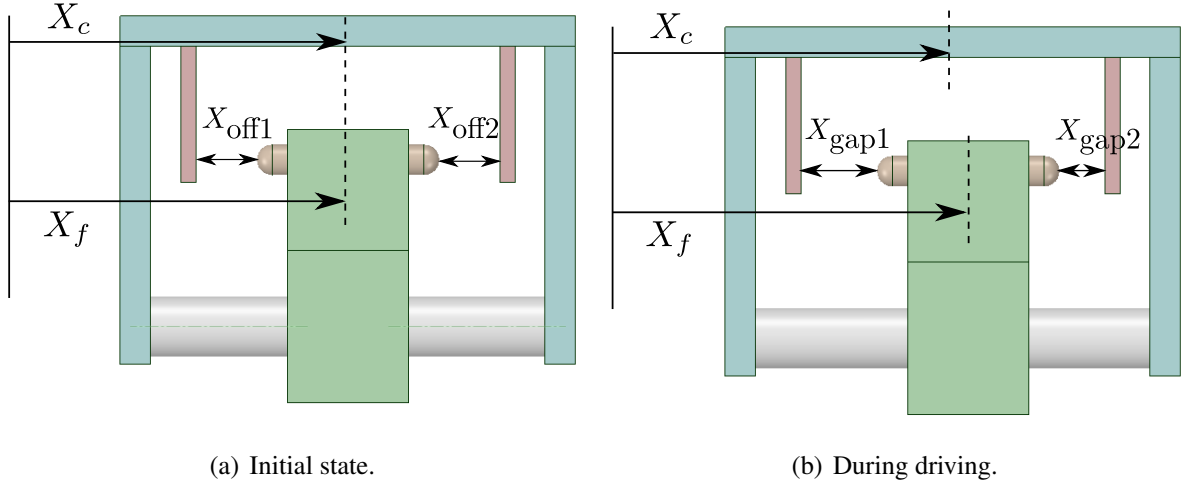


Fig. 7: Structure of the catapult stage (link).

## 2.2 Concept and mechanical structure of catapult stage

This section describes the structure, characteristics, and model of the catapult stage. The subscript “ $f$ ” means the fine stage and “ $c$ ” means the coarse stage in this paper.

### 2.2.1 Mechanical structure of the catapult stage

Fig. 6 shows the mechanical structure of the catapult stage. The coarse stage is guided by a linear guide and driven by a linear motor or a belt drive with large thrust mainly used in acceleration/deceleration. The fine stage which required high positioning accuracy is guided by an air guide and driven by a linear motor with small thrust used in the constant velocity region.

A top view of the coupling mechanism between the fine and coarse stages is shown in Fig. 7.  $X_f$ ,  $X_c$  represents the position measured by the encoder attached to the center of the fine and coarse stages, respectively.  $X_{off1}$ ,  $X_{off2}$  are the gap between the coarse and fine stages in the initial state, and  $X_{gap1}$ ,  $X_{gap2}$  represent the gap between coarse and fine stages during driving. Load cells are attached on the coarse stage and protrusions are attached on the fine stage, and the thrust of the coarse movement stage is transmitted to the fine motion stage via the load cells and the protrusions. Tab. 3 shows the parameters of the catapult stage.

### 2.2.2 Movement of the catapult stage

Fig. 8 shows the basic motion of the catapult stage. In the acceleration region, the coarse stage contacts with the fine stage and pushes the fine stage to accelerate. As a result, the motor for the fine stage can be small and light-weight because it does not have to accelerate the fine stage in this region. In the constant velocity region, the fine stage is separated from the coarse stage and each stage is controlled independently. Thus, the fine stage is controlled precisely not to be affected by

Tab. 3: The catapult stage parameters

Maximum thrust force of the fine stage	$F_{f\max}$	40.0	N
Maximum thrust force of the coarse stage	$F_{c\max}$	218	N
Mass of the fine stage	$M_f$	6.0	kg
Mass of the coarse stage	$M_c$	11	kg
Coefficient of viscosity of the coarse stage	$D_c$	101.7	$\text{N} \cdot \text{s}/\text{m}$
Left side gap	$X_{\text{off}1}$	1.0	mm
Right side gap	$X_{\text{off}2}$	1.0	mm

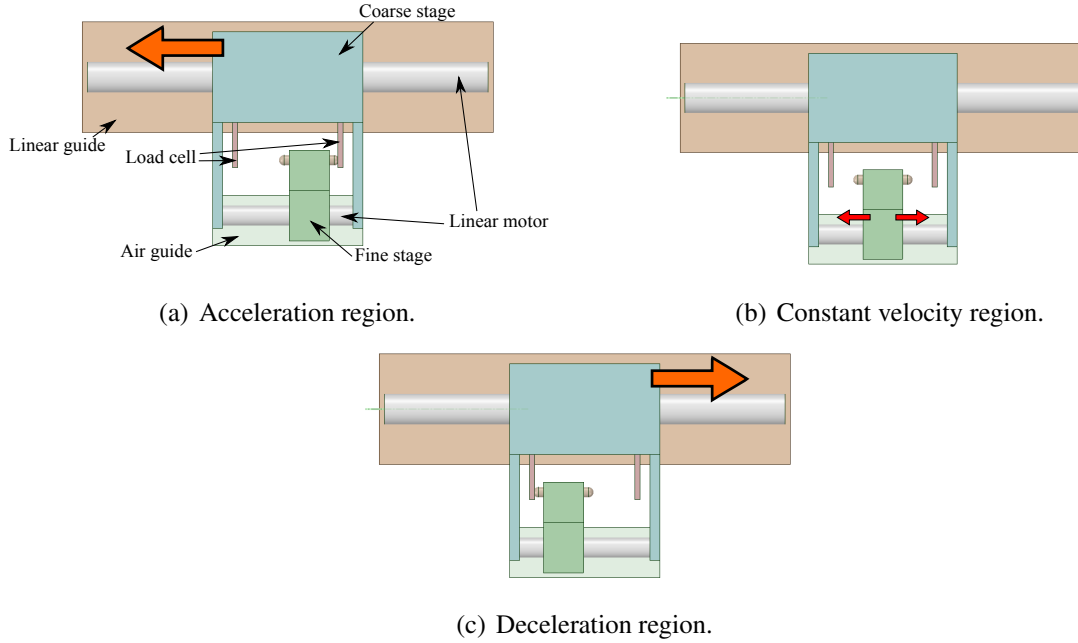


Fig. 8: Movement of the catapult stage.

the disturbance from the air guide. The positioning accuracy in this region is most important in the industrial equipment because the products are produced in this region. In the deceleration region, the coarse stage contacts with the fine stage again, and brakes and stops the fine stage by pushing it.

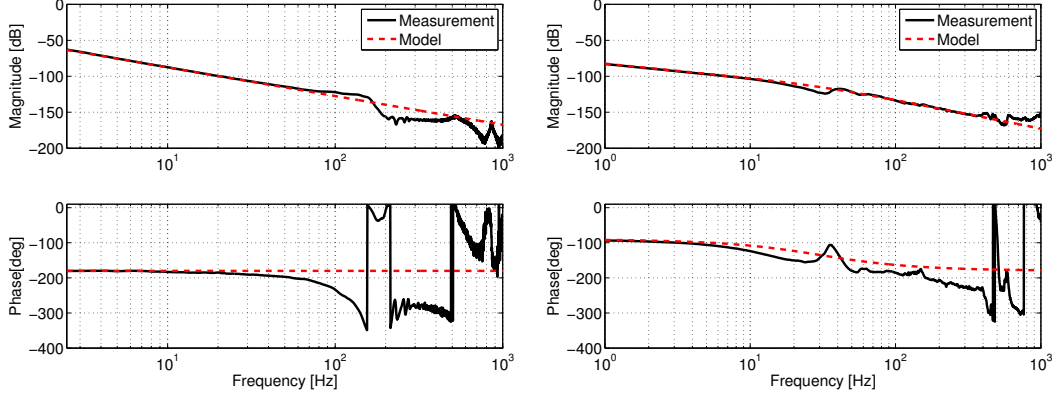
### 2.2.3 Model of the catapult stage

In this section, stage models of the catapult stage are defined. From equations of motion,

$$\begin{aligned} X_f &= P_f(s)(u_f - F_{if}), \\ X_c &= P_c(s)(u_c - F_{ic}), \end{aligned} \quad (2-2)$$

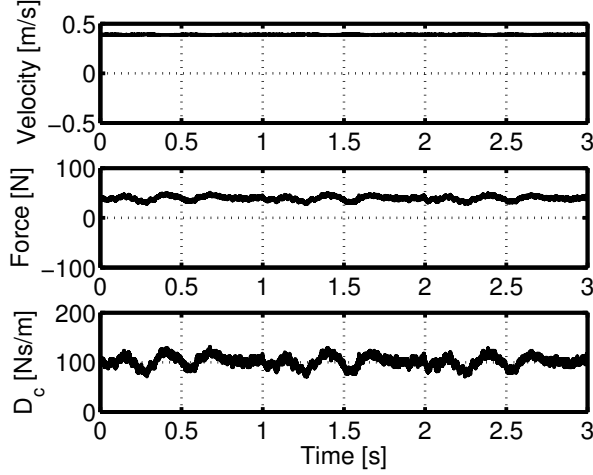
where  $u$  is the control input by the motor,  $F_i$  is the reaction force from the other stage,  $X$  is the position,  $P$  is the plants of the stage.

Since the fine and coarse stages are respectively guided by air and linear guides, viscous friction can be ignored in the fine stage, but it is not ignored in the coarse stage. In this paper, plant models



(a) Frequency response of the fine stage.

(b) Frequency response of the coarse stage.



(c) Viscosity measurement by velocity control.

Fig. 9: Parameter identification of the catapult stage.

$P_f(s)$  and  $P_c(s)$  are defined as rigid body models shown in (5-8).

$$\begin{aligned}
 P_f(s) &= \frac{1}{M_f s^2}, \\
 P_c(s) &= \frac{1}{M_c s^2 + D_c s}
 \end{aligned}
 \tag{2-3}$$

Here,  $M$  is the mass and  $D$  is the coefficient of viscosity.

Frequency responses of the fine and coarse stages are represented in Fig. 9(a), 9(b), respectively. Besides, the measurement result of viscosity coefficient by speed control is shown in Fig. 9(c). The viscosity coefficient is obtained by dividing the motor thrust by the current speed. From these results,  $M_f$ ,  $M_c$ ,  $D_c$  are identified as shown in Tab. 3.

## 2.2.4 Discussion of mechanical structure of catapult stage

The fine and coarse parts of the present catapult stage move only one direction, however, the degree of freedoms of the fine and coarse parts in the industrial high-precision stage are 6DOF and 2DOF,

respectively. It is expected that interference between the fine and coarse parts is definitely present. In particular, the control of the fine part is more difficult when the coarse part has 2DOF because the fine part has contact with two directions of X and Y. However, the methods proposed in this the thesis are useful in establishing the control system which are the basis of the catapult stage.

In addition, the fine part may behave unexpectedly due to the springiness of the contact point when the coarse and fine parts are separated, however, there is no such problem in the present catapult stage because the contact point is enough rigid. It is expected that the operation to bring the fine part into contact with one axis while contacting with another axis when the coarse part has 2DOF. In that case, the perspective of mechanical design which makes the control easy while making contact is also important.

# Chapter 3

## Basic control system of catapult stage

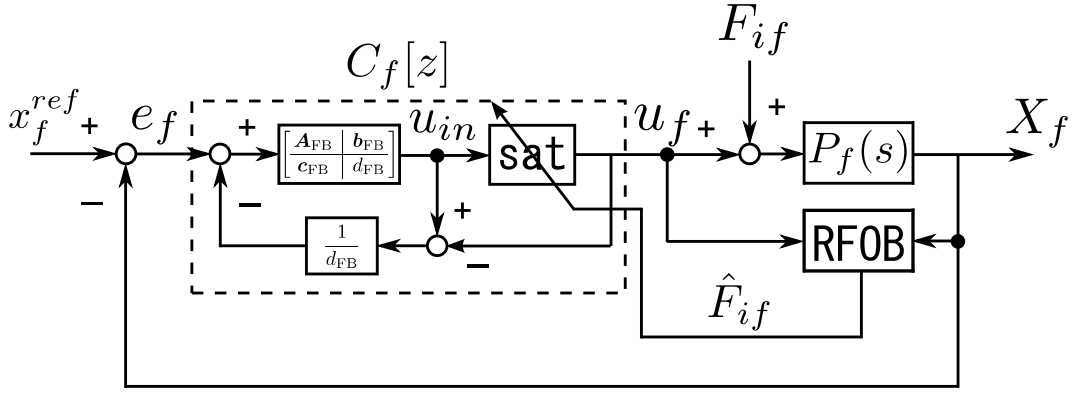
In this section, we propose a basic control system of the catapult stage. The control system of the fine stage is a control system that considers the characteristics of catapult stage which has contact between coarse and fine stages. The control system of the coarse stage is a control system which increases the positioning accuracy of the coarse stage as much as possible. As can be seen from the fact that the air guide is also used for the coarse movement stage in the conventional precision positioning stage, the precision positioning stage follows the conventional policy that the accuracy of the coarse movement stage must be high is there.

### 3.1 Control system for fine stage

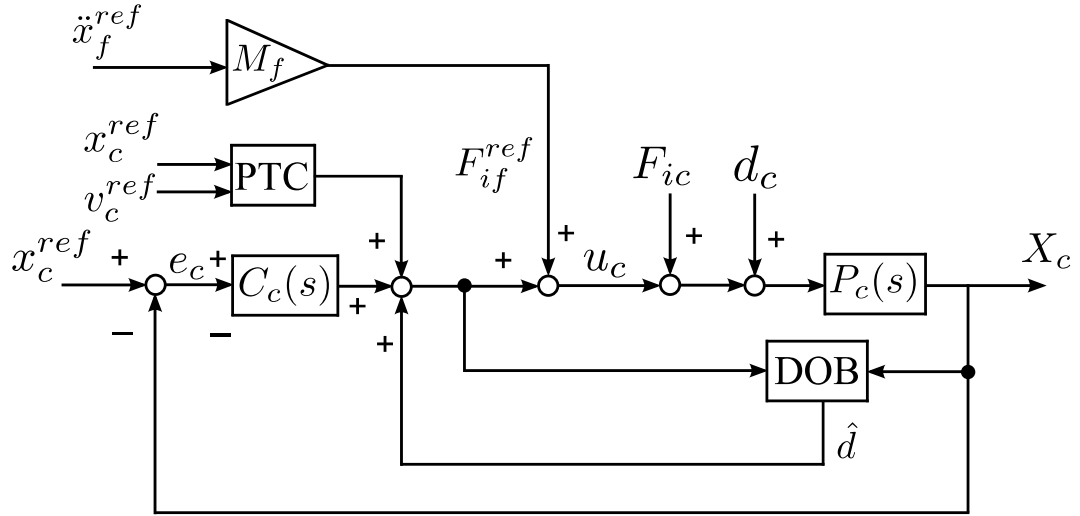
The proposed control system of the fine stage is shown in Fig. 10(a). The FB controller  $C_f(s)$  for the plant  $P_f(s)$  is designed in advance considering its robustness and stability. The fine stage needs an anti-windup control because the tracking error of the fine stage at the beginning of the constant velocity region may saturate the actuator. An anti-windup method proposed in [75] is implemented in the fine stage FB controller. Furthermore, a reaction force observer (RFOB) is designed to estimate the reaction force from the coarse stage [76]. RFOB is a disturbance observer (DOB) which regards the reaction force  $F_{if}$  as the disturbance.

The characteristics of the catapult stage is that the fine stage is not driven when accelerating or decelerating, but driven only at constant velocity, so the control switching is necessary. Therefore, we propose a control switching algorithm using saturation function and estimated reaction force  $\hat{F}_{if}$ . When contact/non-contact of the stage is determined based on the estimated reaction force  $\hat{F}_{if}$  and the threshold  $F_{if}^{thr}$ , the thrust limit value  $u_{sat}$  can be given

$$u_{sat} = \begin{cases} 0, & |\hat{F}_{if}| > F_{if}^{thr} \\ u_{lim.} & \text{otherwise} \end{cases} \quad (3-1)$$



(a) Control system of fine stage.  $x_f^{ref}$  is position reference of the fine stage. The “sat” is a saturation function.



(b) Control system of coarse stage.

Fig. 10: Control system design of the catapult stage.

The threshold  $F_{if}^{thr}$  is sufficiently larger than  $\hat{F}_{if}$  estimated when contactless to prevent malfunction. The saturation function is defined as follows.

$$u_f = \begin{cases} u_{sat}, & u_{in} > u_{sat} \\ -u_{sat}, & u_{in} < -u_{sat} \\ u_{in}, & \text{otherwise} \end{cases} \quad (3-2)$$

where  $u_{in}$  is the force reference from the controller. By this control strategy, the fine stage does not driven in the acceleration and deceleration because thrust saturation value  $u_{sat}$  is set to zero. Also, a linear control of the fine stage is performed in the constant velocity region because  $u_{sat}$  is raised to the limitation value of the actuator  $u_{lim}$ .

## 3.2 Control system of coarse stage

The proposed control system of the coarse stage is shown in Fig. 10(b).  $x^{ref}$ ,  $v^{ref}$  are position and velocity reference for the target trajectory. The FB controller  $C_c(s)$  for the plant  $P_c(s)$  is designed in advance considering its robustness and stability. The control system of the coarse stage is two degree of freedom control system which is consist of a feedforward (FF) controller based on perfect tracking control (PTC [29]) and FB controller  $C_c(s)$ . In addition a disturbance observer (DOB) is designed from (2-2) which reacts disturbance

$$d_{allc} = F_{if}^{ref} + F_{ic} + d_c, \quad (3-3)$$

where  $F_{ic}$  is the reaction force from the fine stage and  $d_c$  is the input disturbance by linear guide.  $F_{if}^{ref}$  is the required thrust of the fine stage in acceleration/deceleration, and is given by

$$F_{if}^{ref} = M_f \ddot{x}_f^{ref}. \quad (3-4)$$

Thus the coarse stage adds the fine stage the reaction force that drives the fine stage ideally if  $d_c$  and  $d_{allc}$  equal zero.

## 3.3 Verification by simulation of basic control system

This simulation shows that the basic control system realizes the desired motion of the catapult stage by simulation. The desired motion means that the fine stage is mainly driven only in the constant velocity region, but the coarse stage is always driven. The control system of the fine and coarse stages in "Proposed" method is the control system proposed in 3.1, 3.2. In "Conventional" method, the coarse stage is controlled by an acceleration FF control and Proportional-Integral-Differential (PID) control.

The target trajectory of the fine stage is shown in Fig. 16(a). The trajectory of the fine stage is 600 mm steps, maximum speed 400 mm/s, average acceleration 800 mm/s<sup>2</sup>. 0.0 s to 0.5 s is the acceleration region, 0.5 s to 1.5 s is the constant velocity region, and 1.5 s to 2.0 s is the deceleration region. The control period is 200  $\mu$ s and the PID controller is designed for each plant so that the closed-loop bandwidth of the position loop is 20 Hz. The cut-off frequency of RFOB is 40 Hz and force limitation of the fine stage  $u_{lim}$  is 20 N.

Simulation results are shown in Fig. 11. The basic control system achieves the desired motion of the catapult stage that the fine stage is driven only in the constant velocity region. It is defined that settling time is the time from the beginning of the constant velocity region to the time when the position error of the fine stage is smaller than 1  $\mu$ m. Then, the settling time of "Conventional" and "Proposed" methods are 55 ms and 55 ms, respectively. In "Proposed" Method, there was no significant difference in the settling time, although the tracking error of the coarse stage is smaller

than that of "Conventional" method. From these results, the precision of the coarse stage does not have to be high as long as it does not disturb the motion of the fine stage in the catapult stage. Thus, acceleration feedforward and PID control are enough to control the coarse stage. The control system design of the fine stage is most importance in the catapult stage because the position accuracy of the coarse stage slightly affect the position accuracy of the fine stage.

### **3.4 Verification by experiment of basic control system**

In this section, experiments show that the desired control for the catapult stage can be realized by the basic control system. From the simulation results, the importance of improving the position accuracy of the coarse movement stage is low, so the acceleration FF and PID controls are performed to the coarse stage. The target trajectory of the experiments is same to that of the simulation.

Experimental results are shown in Fig. 12. The desired motion can be achieved by estimating the reaction force between the coarse and fine stages by RFOB and switching the control law of fine stage properly. Settling time is set to 82 ms, when the settling time is the time when the position error becomes less than  $5 \mu\text{m}$ .

From the above, it was shown that the basic control system can achieve the desired motion of the catapult stage. However, it is found that the settling time of the fine stage after entering the constant velocity region is long from the experimental results. This is because that the position error at the time of entering the constant velocity region remains by a deformation of the load cell even if the coarse stage is controlled ideally according to the basic control system. In addition, the coarse stage must have tracking error at the time of entering the constant velocity region by the disturbance from linear guide. Short settling time is desirable because the settling time is directly related to improvement of the throughput. In the next chapter, this thesis will describe the control method of fine stage during acceleration to shorten settling time.



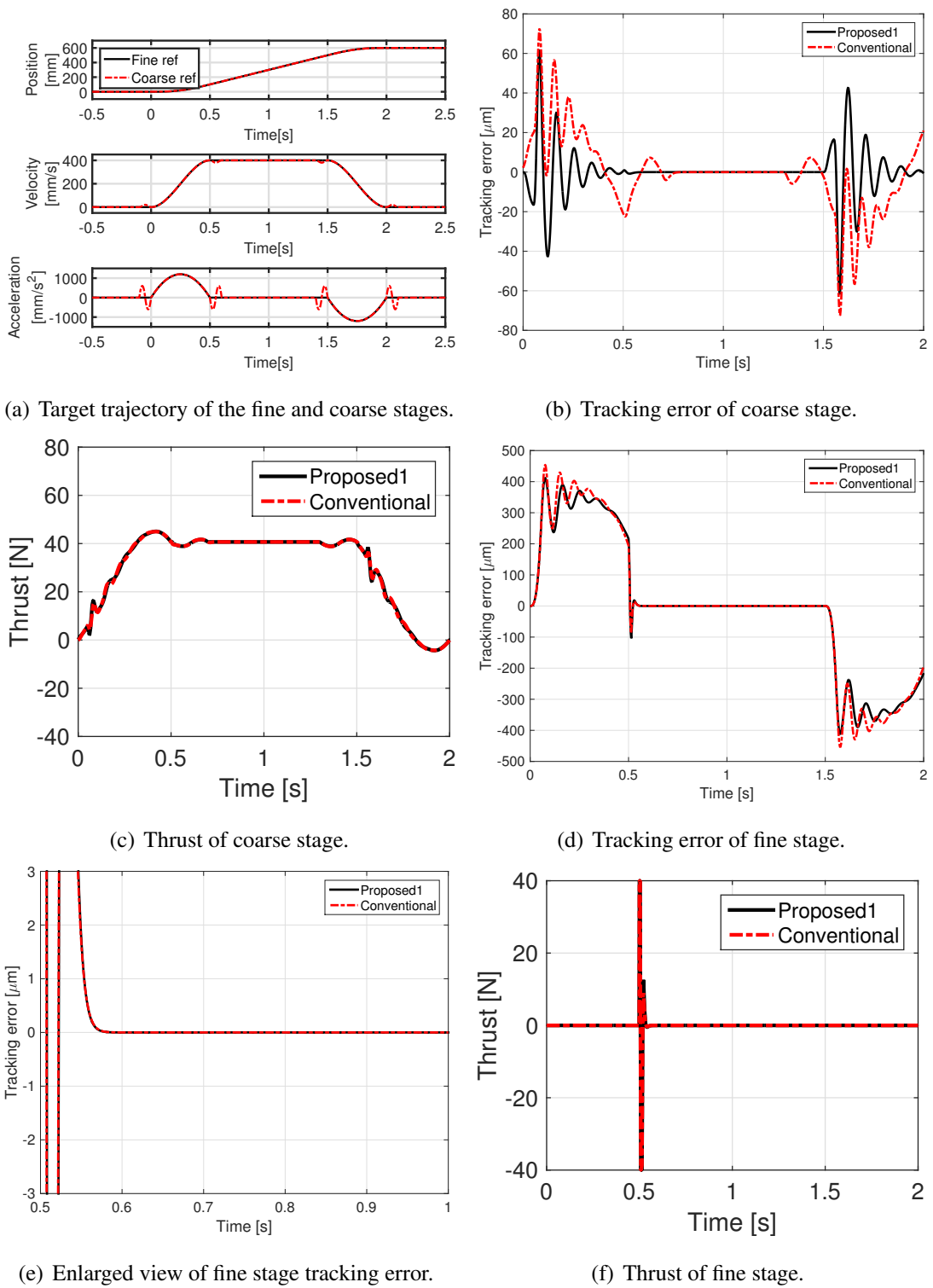
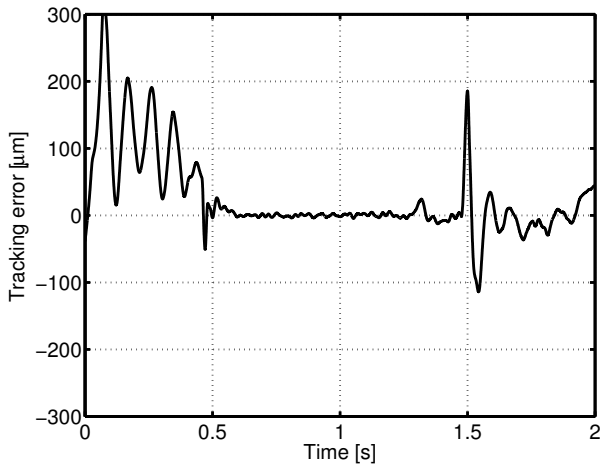
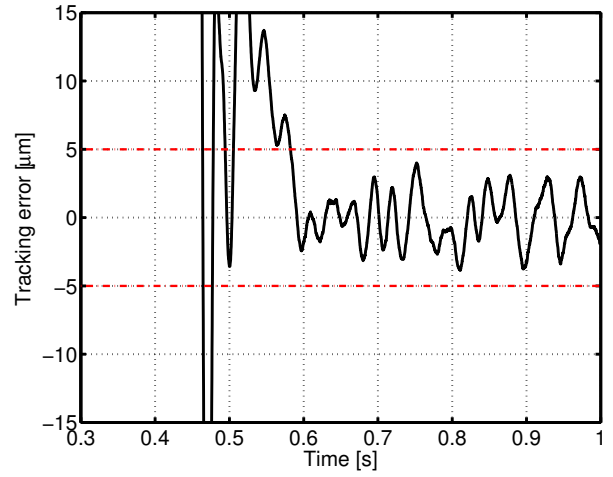


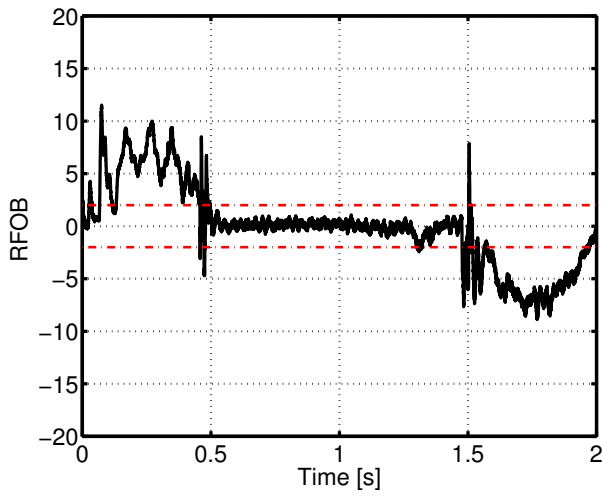
Fig. 11: Simulation results.



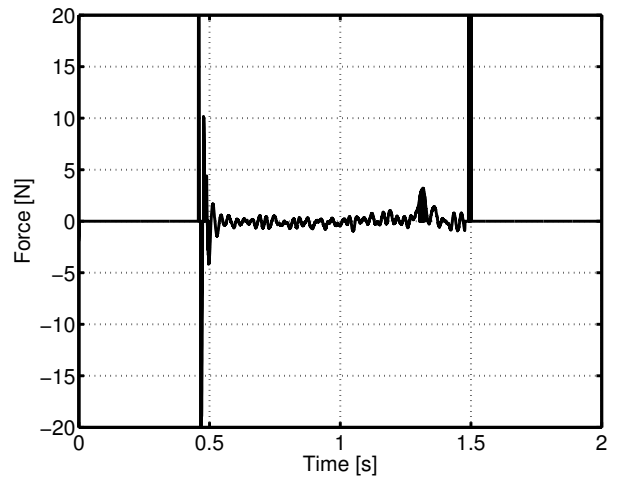
(a) Tracking error of fine stage.



(b) Enlarged view of fine stage tracking error.



(c) Value of RFOB.



(d) Thrust of fine stage.

Fig. 12: Experimental results.

# Chapter 4

## Zero settling time control based on final-state control considering with constraints

### 4.1 New concept of the motion of catapult stage

In previous chapter, we proposed the basic concept of the catapult stage. The initial concept of the catapult stage was that the fine stage was controlled only in the constant velocity region, however, it was impossible to avoid tracking error of the fine stage at the beginning of the constant velocity region due to the deformation of the load cell even if the coarse stage was controlled ideally. As a result, the settling time of the fine stage becomes large, and the motor of the fine stage are saturated.

For this reason, we propose a control method of the fine stage in the acceleration region. The settling time in the constant velocity region is reduced by activating the fine stage properly at the end of the acceleration region. Fig. 13 shows the conceptual diagram of the method. Let us consider when the fine stage is activated. If the timing is too early, the fine stage needs large thrust to accelerate itself largely. On the other hand, if the timing is too late, the fine stage also needs the large thrust to compensate the error quickly. One of the purposes of the catapult stage is to achieve a higher FB bandwidth by reducing the maximum thrust and weight of the fine stage. Thus, the fine stage should be activated at the proper timing considering with the required maximum thrust of it. From these considerations, a control method that takes the state of the fine stage to the desired state at the beginning of the constant velocity region while taking constraints into account is necessary. This paper proposes a control method based on Final-State Control (FSC [1, 2]) with thrust limitations to achieve this requirement.

4.2 shows that the settling time and the required maximum thrust of the fine stage is significantly reduced by applying FSC to the fine stage. In 4.3, a novel index for mode switching by using a set of initial state variables in a constrained FSC is derived, and it is shown that the proposed index can determine the activation timing of the fine stage quantitatively. 4.4 demonstrates the effectiveness of

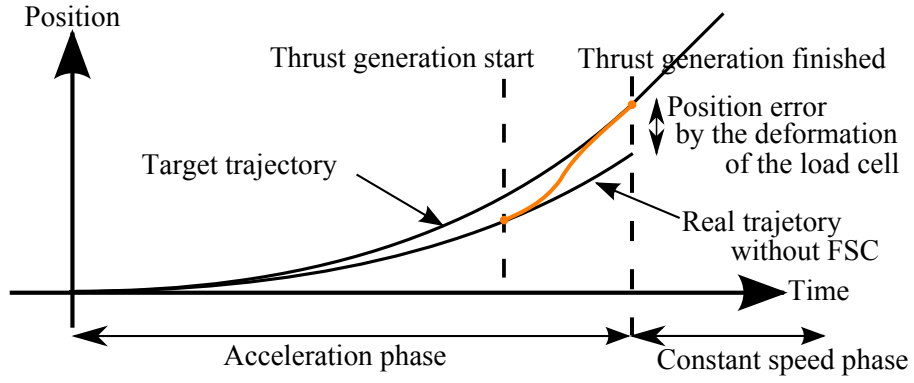


Fig. 13: Conceptual diagram of thrust generation at acceleration region.

the proposed method by implementing it to the catapult stage.

## 4.2 Zero settling time control in acceleration region

### 4.2.1 Final State Control [1] [2]

FSC is a control method which takes an initial state to a final state in finite time by applying Feedforward (FF) inputs. A state-space model of a discrete-time system is defined as follows:

$$\begin{aligned} \mathbf{x}[k+1] &= \mathbf{A}\mathbf{x}[k] + \mathbf{B}u[k], \\ y[k] &= \mathbf{C}\mathbf{x}[k]. \end{aligned} \quad (4-1)$$

Let us consider to obtain the FF input  $u[k]$  that drives an initial state  $x[0]$  to a final state  $x[N]$  by  $N$  steps control inputs. A performance index is

$$\begin{aligned} J &= \mathbf{U}^T \mathbf{Q} \mathbf{U}, \quad \mathbf{Q} > 0, \\ \mathbf{U} &= [u[0] \ u[1] \ \dots \ u[N-1]]^T, \end{aligned} \quad (4-2)$$

where  $\mathbf{Q}$  is a weighting matrix. The FF inputs minimizing (4-2) are given as follows:

$$\begin{aligned} \mathbf{U} &= \mathbf{Q}^{-1} \mathbf{\Sigma}^T (\mathbf{\Sigma} \mathbf{Q}^{-1} \mathbf{\Sigma}^T)^{-1} (\mathbf{x}[N] - \mathbf{A}^N \mathbf{x}[0]), \\ \mathbf{\Sigma} &= [\mathbf{A}^{N-1} \mathbf{B} \ \mathbf{A}^{N-2} \mathbf{B} \ \dots \ \mathbf{B}]. \end{aligned} \quad (4-3)$$

In this thisis,  $u_i$  means  $u[i]$ . The control input  $u_i$  is limited by

$$-u_{\text{lim}} \leq u_i \leq u_{\text{lim}}, \quad (4-4)$$

where  $u_{\text{lim}}$  is the limitation of the control input. Section 4.3.2, 4.3.2 describes the condition of the initial state variables considering the limitations (4-4).

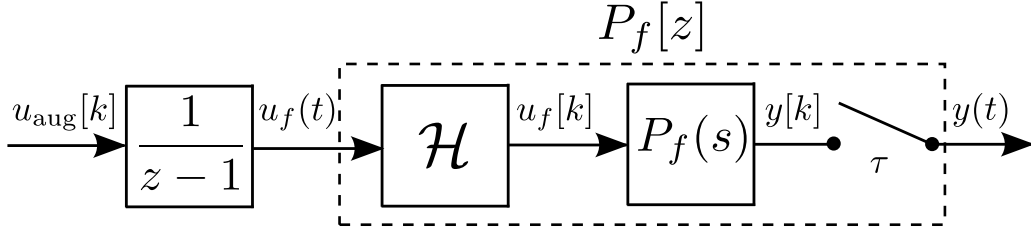


Fig. 14: Augmented system with an integrator.

## 4.2.2 Application of FSC to Catapult Stage

FSC is applied to the fine stage in the acceleration region. Let us consider when the fine stage is activated. The fine stage cannot separate from the coarse stage when inertial force from the acceleration caused by being pushed by the coarse stage is larger than the maximum thrust of the fine stage. Thus thrust should be given to the fine stage when the acceleration of the fine stage is enough small. In this section, the thrust is given when the acceleration of the fine stage reaches  $1.0 \text{ m/s}^2$  because there are no index for control switching in acceleration. The fine stage obtains the acceleration by being pushed by the coarse stage in acceleration

Next, let us consider the condition to generate FF input. Initial and final states of the position, the velocity, and the thrust are required to apply FSC to the catapult stage to consider the thrust limitation. For this reason, an augmented system with an integrator  $1/(z-1)$  is needed to add the thrust element to state variables. The state-space system of the augmented system shown in Fig. 14 is defined as follows:

$$\begin{aligned}
 \mathbf{x}_{\text{aug}}[k+1] &= \mathbf{A}_{\text{aug}}\mathbf{x}_{\text{aug}}[k] + \mathbf{B}_{\text{aug}}u_{\text{aug}}[k], \\
 y[k] &= \mathbf{C}_{\text{aug}}\mathbf{x}_{\text{aug}}[k], \\
 \mathbf{A}_{\text{aug}} &= \begin{bmatrix} 1 & \tau & \frac{\tau^2}{2M_f} \\ 0 & 1 & \frac{\tau}{M_f} \\ 0 & 0 & 1 \end{bmatrix}, \quad \mathbf{B}_{\text{aug}} = \begin{bmatrix} 0 \\ 0 \\ 1 \end{bmatrix}, \quad \mathbf{C}_{\text{aug}} = [1 \quad 0 \quad 0].
 \end{aligned} \tag{4-5}$$

Here,  $\tau$  is a control period. The FF inputs  $\mathbf{U}_{\text{aug}}$  are given by

$$\mathbf{U}_{\text{aug}} = \mathbf{Q}^{-1}\Sigma_{\text{aug}}^{\text{T}}(\Sigma_{\text{aug}}\mathbf{Q}^{-1}\Sigma_{\text{aug}}^{\text{T}})^{-1} \times (\mathbf{x}_{\text{aug}}[N] - \mathbf{A}_{\text{aug}}^N\mathbf{x}_{\text{aug}}[0]) \tag{4-6}$$

$$\Sigma_{\text{aug}} = [\mathbf{A}_{\text{aug}}^{N-1}\mathbf{B}_{\text{aug}} \quad \mathbf{A}_{\text{aug}}^{N-2}\mathbf{B}_{\text{aug}} \quad \cdots \quad \mathbf{B}_{\text{aug}}] \tag{4-7}$$

Note that  $u_{\text{aug}}[k]$  is an input whose dimension corresponds to jerk because of the augmented system shown in Fig. 14. Final states of position, velocity, and thrust of the fine stage are given in advance, however, the initial states of them are needed to be measured. The position is measured by the linear encoder, and the velocity is calculated by discretizing it. The initial thrust is calculated by multiplying the mass by the acceleration estimated by an observer. The control system of the fine stage with FSC is shown in Fig. 15.

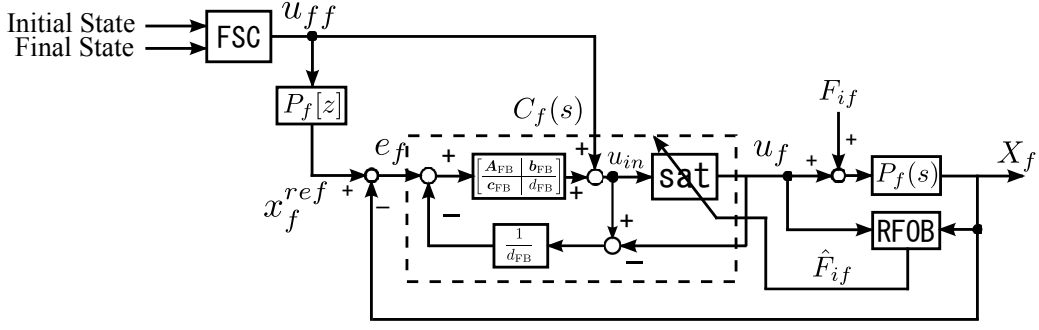


Fig. 15: Control system of the fine stage with FSC.

### 4.2.3 Verification by simulation of zero settling time control in acceleration region

This section shows that the proposed method reduces the tracking error of the fine stage at the time of entering the constant velocity region. The control system of the "Conventional" method is the method proposed in 3. The "Proposed2" applies FF control based on FSC to the fine stage in acceleration, and the acceleration FF control and PID FB control are applied to the coarse stage.

The target trajectories of the fine and coarse stages are shown in Fig. 16(a), 16(c), respectively. The trajectory of the fine stage is 600 mm steps, maximum speed 400 mm/s, average acceleration 800 mm/s<sup>2</sup>. 0.0 s to 0.5 s is the acceleration region, 0.5 s to 1.5 s is the constant velocity region, and 1.5 s to 2.0 s is the deceleration region. The target trajectory of the coarse stage is shifted from that of the fine stage by 0.8 mm. The control period is 200  $\mu$ s and the PID controller is designed for each plant so that the closed-loop bandwidth of the position loop is 20 Hz.

The simulation results are shown in Fig. 16. The proposed method generates the thrust by FSC in acceleration region from Fig. 16(b). It is defined that settling time is the time from the beginning of the constant velocity region to the time when the position error of the fine stage is smaller than 1  $\mu$ m. Then, the settling time of "Conventional" and "Proposed2" methods are 55 ms and 0.0 ms, respectively. In addition, the required thrust of "Proposed2" method can be reduced to 11 % compared with that of "Conventional" method. From this result, the thrust generation in acceleration is effective to improve the settling time and the required thrust.

### 4.2.4 Verification by experiment of zero settling time control in acceleration region

The experimental result demonstrates the effectiveness of the proposed method. The same trajectory and controller is used in the experiment as the simulation. In this experiment, FSC is applied to the fine stage when the target acceleration of the fine stage reaches 1.0 m/s<sup>2</sup>. Then the value of  $Q^{-1}\Sigma^T(\Sigma Q^{-1}\Sigma^T)^{-1}$  which is required to generate the FF input can be calculated in advance because

Tab. 4: Simulation result

	Fine	Coarse	Settling Time	Maximum Thrust
Conventional	PID	PID	55 ms	40 N
Proposed 2	PID+FSC	PID	0.00 ms	4.4 N

Tab. 5: Experimental result

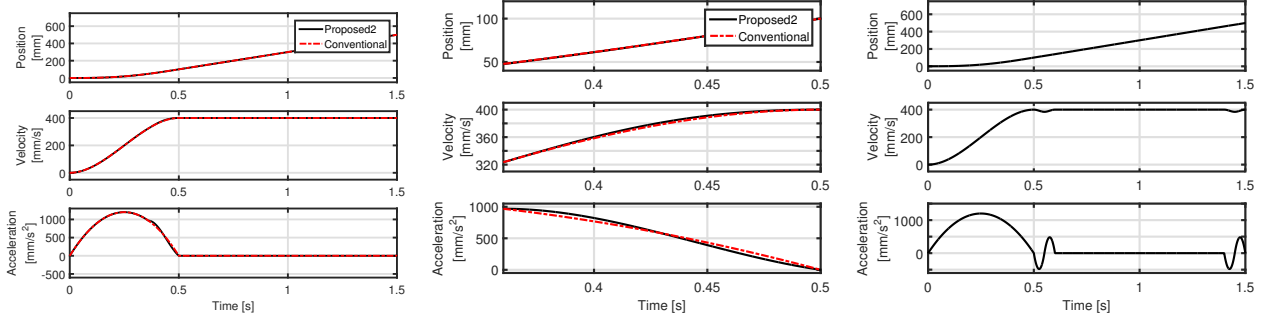
	Fine	Coarse	Settling Time	Maximum Thrust
Conventional	PID	PID	56 ms	40 N
Proposed2	PID+FSC	PID	0.00 ms	6.3 N

the number of steps  $N$  is given. It is assumed that  $Q^{-1}\Sigma^T(\Sigma Q^{-1}\Sigma^T)^{-1}$  is stored in the memory and the FF input is generated at each time by measuring the initial state variable at the predetermined number of steps  $N$ . The position is measured by a linear encoder and the velocity is obtained by difference of the position, and the thrust is estimated by multiplying the acceleration estimated by the observer by the mass of the fine stage.

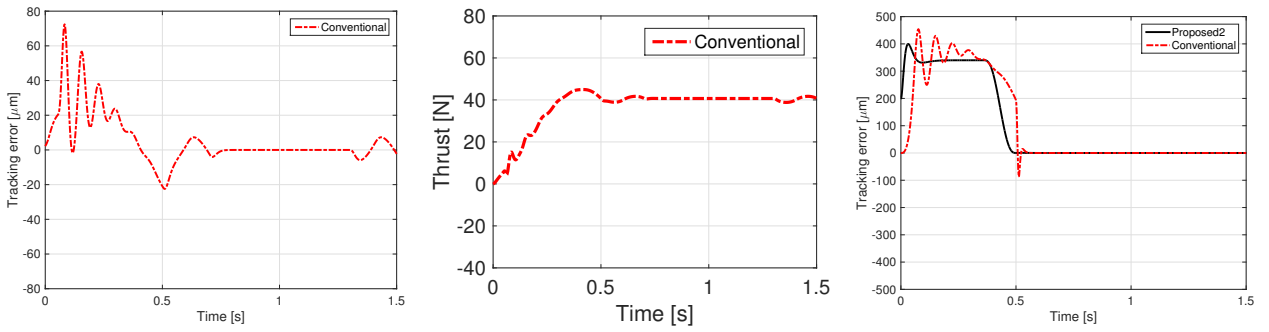
The experimental result is shown in Fig. 17. The coarse stage is greatly influenced by the disturbance from the linear guide and is inferior in accuracy from Fig. 17(d), 17(e), but the fine stage achieves the high precision positioning by using air guide. The settling time of "Conventional" and "Proposed2" methods are 55 ms and 0.0 ms, respectively, when settling time is the time when the position error becomes  $1\ \mu\text{m}$  or less. In addition, the required thrust of "Proposed2" method can be reduced to 16% compared with that of "Conventional" method.

#### 4.2.5 Conclusion of zero settling time control

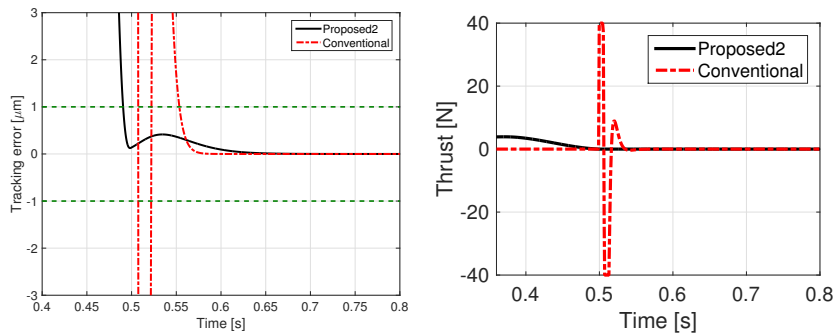
In this section, the settling time and the required maximum thrust of the fine stage are significantly improved by applying FSC to the fine stage in acceleration, however, the activation timing of the fine stage is determined trial and error because the required maximum thrust of the fine stage cannot be estimated in advance. To estimate the maximum thrust of the fine stage in advance is important because one of the purposes of the catapult stage is to achieve high control bandwidth by lightening the actuator of the fine stage. Next section discusses a method to estimate the required maximum thrust of the fine stage.



(a) Target trajectory of the fine stage. (b) Enlarged view of trajectory generation region of the fine stage. (c) Target trajectory of the coarse stage.



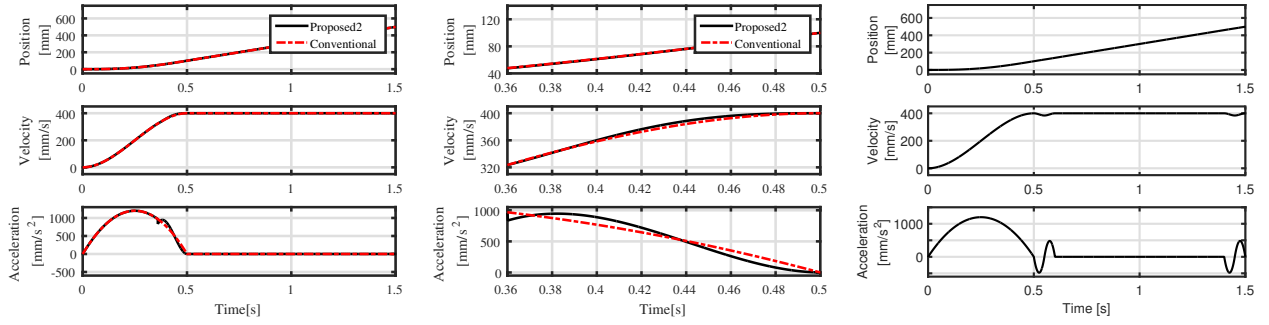
(d) Tracking error of coarse stage. (e) Thrust of coarse stage. (f) Tracking error of fine stage.



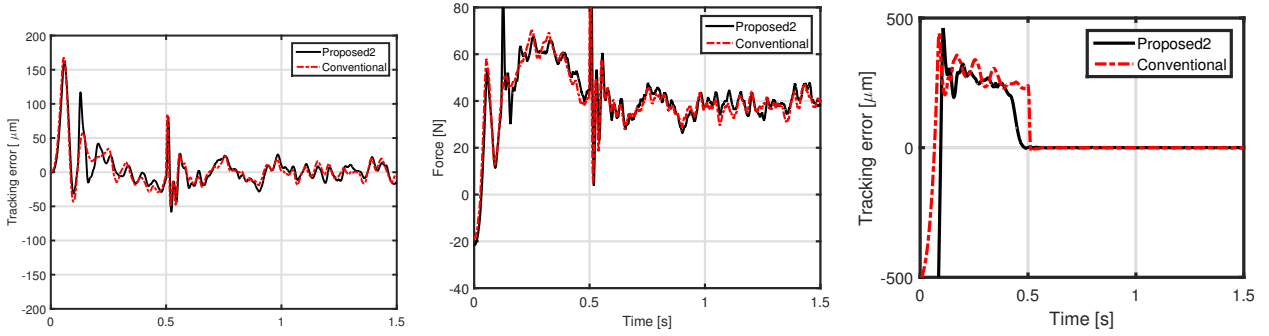
(g) Enlarged view of fine stage tracking error. (h) Thrust of fine stage.

Fig. 16: Simulation results.

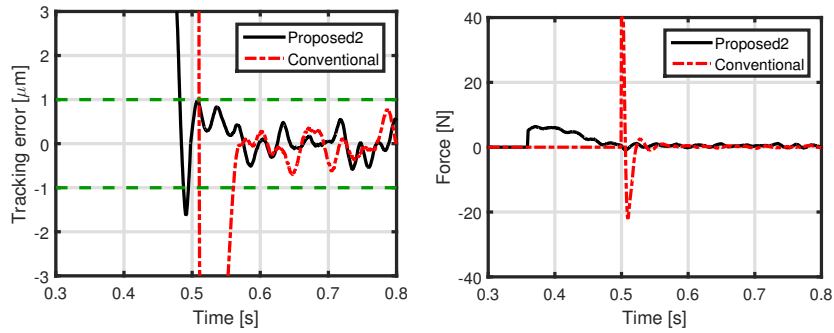




(a) Target trajectory of the fine stage. (b) Enlarged view of trajectory generation region of the fine stage. (c) Target trajectory of the coarse stage.



(d) Tracking error of coarse stage. (e) Thrust of coarse stage. (f) Tracking error of fine stage.



(g) Enlarged view of fine stage tracking error. (h) Thrust of fine stage.

Fig. 17: Experimental results.

## 4.3 Mode switching control using FSC with constrains

### 4.3.1 Applications of mode switching control

Mode Switching Control (MSC) is a control method which switches from one control mode to another according to switching conditions. MSC has been widely used in robots and hard disk drives which need to switch between several types of control while in motion. Previous studies of MSC have been mainly performed about the following two themes; (i) to set initial state variables in a controller properly at the time of switching control modes and (ii) to design a switching condition to improve the transient response. In a previous study on the former theme, Yamaguchi et al proposed an initial state value compensation which calculates the initial state of the controller by multiplying a real coefficient matrix designed in advance [77]. In another previous study on the former theme, an initial state value compensation by using feedforward (FF) input is proposed [78]. That is because setting initial state variables in a controller properly is equal to add a FF input to the output of the controller. On the other hand, in a study on the latter theme, a method to determine the optimal initial state variables from some cost functions was proposed, and its effectiveness was demonstrated by experiments [79].

However, the index to switch control modes is only based on the tracking error in most of studies on the MSC and the switching condition is decided by the experience of the designer because there are no clear criteria for switching control modes. For this reason, generally a conservative design is preferred in order not to saturate thrust of the actuator. Therefore, this section proposes a new index which enables to evaluate switching conditions quantitatively, considering actuator thrust limitation.

This criterion uses initial state variables in FSC with thrust limitations. FSC is a control method which takes an initial state to a desired final state in finite time by applying FF inputs. FSC has been widely used in the short track-seeking control of hard disk drives, etc. There are notable studies derived from FSC: Frequency-shaped FSC (FFSC) [2], which designs FF input not to excite high resonance modes; Polynomial-input-type FFSC (PFFSC) [80], which approximates the FF inputs as a polynomial; LMI PFFSC [81], which considers a limitation of the control input; Updating FSC (UFSC) [82], which can be applied to a time-varying final state. These previous researches on FSC assume that initial state variables are equal to zero. However, when FSC is applied to MSC, initial state variables are not zero because FSC in this case begins in the middle of an action.

The purpose of this section is to determine the set  $\mathcal{P}$  of initial state variables  $x[0]$  in FSC. Conceptual diagram of the set is shown in Fig. 18. The finite characteristics of the set is that initial state variables can be taken to a desired final state by using FSC while satisfying thrust limitations when the initial state variables is inside the set. Note that the thrust limitations and the final state variables  $x[N]$  have to be given in advance to generate the set  $\mathcal{P}$ . Therefore, whether initial state variables can be taken to a desired final state variables can be judged by the set  $\mathcal{P}$ , and this condition becomes one of a new index for control switching.

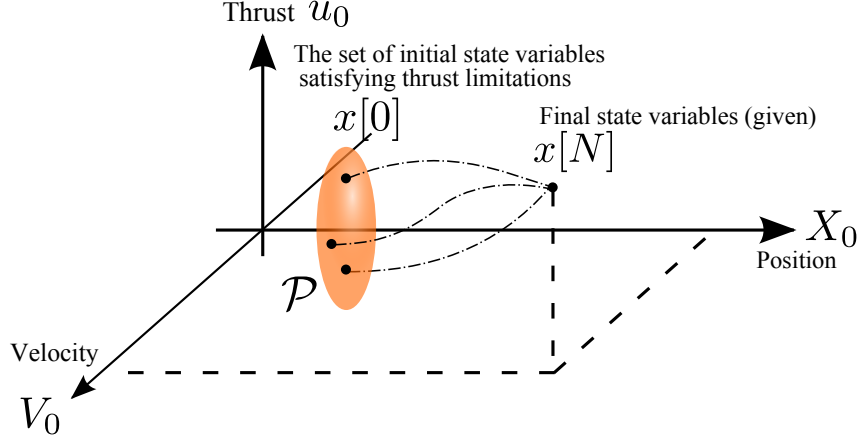


Fig. 18: Conceptual diagram of the set of initial state variables.

### 4.3.2 Condition of initial stage of FSC with thrust limitation

This section derives the conditions of the initial state variables in FSC with thrust limitations for the following two cases; (i) to minimize the energy cost and (ii) to minimize the jerk cost. In addition, the position, the velocity and the thrust are given as initial conditions in this chapter. Besides, a plant model  $P(s)$  is defined as a rigid body model and a state-space model of a discrete-time system is defined as follows:

$$\begin{aligned} \mathbf{x}[k+1] &= \mathbf{A}\mathbf{x}[k] + \mathbf{B}u[k], \\ y[k] &= \mathbf{C}\mathbf{x}[k] \end{aligned} \quad (4-8)$$

#### Condition of the initial state variables when defining the energy as a cost function

Control input minimizing energy consumption is required for applications whose control performance is degraded by the heat of the actuator. In this case, it is enough to derive feedforward input  $\mathbf{U}$ , because the dimension of  $\mathbf{U}$  is force by applying FSC to (4-1). When the initial conditions of the position, the velocity and the thrust are given, (4-3) is transformed into:

$$\mathbf{U}_{\text{tr}} = \mathbf{Q}^{-1} \Sigma_{\text{tr}}^{\text{T}} (\Sigma_{\text{tr}} \mathbf{Q}^{-1} \Sigma_{\text{tr}}^{\text{T}})^{-1} \times (\mathbf{x}[N] - \mathbf{A}^N \mathbf{x}[0] - \mathbf{A}^{N-1} \mathbf{B}u[0]), \quad (4-9)$$

$$\Sigma_{\text{tr}} = [\mathbf{A}^{N-2} \mathbf{B} \ \dots \ \mathbf{B}]. \quad (4-10)$$

By replacing each matrix with each element, (4-9) is rearranged as follows:

$$\begin{bmatrix} u_{\text{tr}1} \\ u_{\text{tr}2} \\ \vdots \\ u_{\text{tr}N-1} \end{bmatrix} = \begin{bmatrix} q_{11} & q_{12} \\ q_{21} & q_{22} \\ \vdots & \vdots \\ q_{N-11} & q_{N-12} \end{bmatrix} \left\{ \begin{bmatrix} X_F \\ V_F \end{bmatrix} - \begin{bmatrix} a_{11} & a_{12} \\ a_{21} & a_{22} \end{bmatrix} \begin{bmatrix} X_0 \\ V_0 \end{bmatrix} - \begin{bmatrix} b_1 \\ b_2 \end{bmatrix} u_0 \right\}. \quad (4-11)$$

Here,  $u_{\text{tr}i}$  ( $1 \leq i \leq N-1$ ) is an element in the  $i$ -th row of  $\mathbf{U}_{\text{tr}}$ ,  $q_{ij}$  ( $1 \leq i \leq N-1$ ,  $1 \leq j \leq 2$ ) is an element in the  $i$ -th row and the  $j$ -th column of  $\mathbf{Q}^{-1} \Sigma_{\text{tr}}^{\text{T}} (\Sigma_{\text{tr}} \mathbf{Q}^{-1} \Sigma_{\text{tr}}^{\text{T}})^{-1}$ ,  $a_{ij}$  ( $1 \leq i \leq 2$ ,  $1 \leq j \leq 2$ )

is an element in the  $i$ -th row and the  $j$ -th column of  $\mathbf{A}^N$ ,  $b_i$  ( $1 \leq i \leq 2$ ) is an element in the  $i$ -th row of  $\mathbf{A}^{N-1}\mathbf{B}$ .  $X_0$ ,  $V_0$ ,  $u_0$  are initial states of position, velocity and thrust while  $X_F$ ,  $V_F$  are final states of position and velocity, respectively.

The analysis solutions  $u_{\text{tr}i}$  must be derived to consider the thrust limitations. Hence, the analysis solutions of  $q_{ij}$  are needed and the solutions are obtained by calculating  $\mathbf{Q}^{-1}\Sigma_{\text{tr}}^T(\Sigma_{\text{tr}}\mathbf{Q}^{-1}\Sigma_{\text{tr}}^T)^{-1}$ . In this section,  $\mathbf{Q}$  is a unit matrix to minimize energy consumption. Derivations of each coefficient are shown in appendix 11.1. By combining (4-4) and (4-11), the condition of initial state variables in FSC with thrust limitations is given as follows:

$$-u_{\text{lim}} \begin{bmatrix} 1 \\ \vdots \\ 1 \end{bmatrix} \leq \begin{bmatrix} u_0 \\ \vdots \\ u_{\text{tr}N-1} \end{bmatrix} \leq u_{\text{lim}} \begin{bmatrix} 1 \\ \vdots \\ 1 \end{bmatrix}. \quad (4-12)$$

Each of the  $N$  rows in (4-12) expresses a plane, which has  $X_0$ ,  $V_0$ ,  $u_0$  as variables. The set of solutions for the condition of initial state variables in FSC with thrust limitations is limited by these  $2N$  planes in the Cartesian space  $\{X_0, V_0, u_0\}$ .

### Condition of the initial state variables when defining jerk as a cost function

A smooth control input is required not to excite the mechanical vibration modes in the case of applications where resonance frequency inhibits the improvement of its control performance, such as hard disk drives. In addition, the method proposed in this section has the advantage of being able to designate the thrust of the final state while the method proposed in section 4.3.2 cannot designate it. The method proposed in this section needs an augmented system with an integrator to evaluate the differential of the actual control input and to add the thrust element to state variables. The augmented system is shown in Fig. 14 and is defined as follows:

$$\begin{aligned} \mathbf{x}_{\text{aug}}[k+1] &= \mathbf{A}_{\text{aug}}\mathbf{x}_{\text{aug}}[k] + \mathbf{B}_{\text{aug}}u_{\text{aug}}[k], \\ y[k] &= \mathbf{C}_{\text{aug}}\mathbf{x}_{\text{aug}}[k]. \end{aligned} \quad (4-13)$$

The FF inputs  $\mathbf{U}_{\text{aug}}$  are given by

$$\mathbf{U}_{\text{aug}} = \mathbf{Q}^{-1}\Sigma_{\text{aug}}^T(\Sigma_{\text{aug}}\mathbf{Q}^{-1}\Sigma_{\text{aug}}^T)^{-1}(\mathbf{x}[N] - \mathbf{A}^N\mathbf{x}[0]), \quad (4-14)$$

$$\Sigma_{\text{aug}} = [\mathbf{A}^{N-1}\mathbf{B} \ \dots \ \mathbf{B}]. \quad (4-15)$$

Note that  $u_{\text{aug}}[k]$  is an input whose dimension corresponds to jerk because of the augmented system shown in Fig. 14. By replacing each matrix with each element, (4-14) is rearranged as follows:

$$\begin{bmatrix} u_{\text{aug}1} \\ u_{\text{aug}2} \\ \vdots \\ u_{\text{aug}N} \end{bmatrix} = \begin{bmatrix} q_{11} & q_{12} & q_{13} \\ q_{21} & q_{22} & q_{23} \\ \vdots & \vdots & \vdots \\ q_{N1} & q_{N2} & q_{N3} \end{bmatrix} \left\{ \begin{bmatrix} X_F \\ V_F \\ u_F \end{bmatrix} - \begin{bmatrix} a_{11} & a_{12} & a_{13} \\ a_{21} & a_{22} & a_{23} \\ a_{31} & a_{32} & a_{33} \end{bmatrix} \begin{bmatrix} X_0 \\ V_0 \\ u_0 \end{bmatrix} \right\}. \quad (4-16)$$

Here,  $u_{\text{aug}i}$  ( $1 \leq i \leq N$ ) is an element in the  $i$ -th row of  $\mathbf{U}$ ,  $q_{ij}$  ( $1 \leq i \leq N$ ,  $1 \leq j \leq 3$ ) is an element in the  $i$ -th row and the  $j$ -th column of  $\mathbf{Q}^{-1} \Sigma_{\text{aug}}^T (\Sigma_{\text{aug}} \mathbf{Q}^{-1} \Sigma_{\text{aug}}^T)^{-1}$ ,  $a_{ij}$  ( $1 \leq i \leq 3$ ,  $1 \leq j \leq 3$ ) is an element in the  $i$ -th row and the  $j$ -th column of  $\mathbf{A}_{\text{aug}}^N$ .  $X_0$ ,  $V_0$ ,  $u_0$  are initial states of position, velocity and thrust while  $X_F$ ,  $V_F$ ,  $u_F$  are final states of position, velocity and thrust, respectively.

The analysis solutions  $u_{\text{aug}i}$  must be derived to consider the thrust limitations. Hence, the analysis solutions of  $q_{ij}$  are needed and the solutions are obtained by calculating  $\mathbf{Q}^{-1} \Sigma_{\text{aug}}^T (\Sigma_{\text{aug}} \mathbf{Q}^{-1} \Sigma_{\text{aug}}^T)^{-1}$ . In this section,  $\mathbf{Q}$  is an unit matrix to minimize the jerk. Derivations of each coefficient are shown in appendix 11.2. Note that it is necessary to convert  $u_{\text{aug}}[k]$  to  $u_i$  because the dimension of  $u_{\text{aug}}[k]$  is not thrust but jerk. Therefore,  $u_i$  is given in (4-17) by using the initial thrust  $u_0$  and  $u_{\text{aug}i}$ .

$$u_i = \begin{cases} u_0, & i = 0 \\ \sum_{k=1}^i u_{\text{aug}k} + u_0, & i \geq 1 \end{cases} \quad (4-17)$$

By combining (4-4) and (4-17), the condition of initial state variables in FSC with thrust limitations is given as follows:

$$-u_{\text{lim}} \begin{bmatrix} 1 \\ 1 \\ \vdots \\ 1 \\ 1 \end{bmatrix} \leq \begin{bmatrix} 1 & 0 & 0 & 0 & 0 \\ 1 & 1 & 0 & 0 & 0 \\ \vdots & \ddots & \ddots & \ddots & \vdots \\ 1 & 1 & 1 & 1 & 0 \\ 1 & 1 & 1 & 1 & 1 \end{bmatrix} \begin{bmatrix} u_0 \\ u_{\text{aug}1} \\ \vdots \\ u_{\text{aug}N-1} \\ u_{\text{aug}N} \end{bmatrix} \leq u_{\text{lim}} \begin{bmatrix} 1 \\ 1 \\ \vdots \\ 1 \\ 1 \end{bmatrix}. \quad (4-18)$$

Each of the  $N + 1$  rows in (4-18) expresses a plane, which has  $X_0$ ,  $V_0$ ,  $u_0$  as variables. The set of solutions for the condition of initial state variables in FSC with thrust limitations is limited by these  $2N + 2$  planes in the Cartesian space  $\{X_0, V_0, u_0\}$ .

### 4.3.3 Analysis on existence condition of initial state variable

This section shows the condition of initial state variables itself and its effectiveness by simulation results. In this simulation, the mass of (5-8) is  $M = 6$  kg, the control period is  $200 \mu\text{s}$ , the final state is set at  $[X_N, V_N, u_N] = [0.1, 0.4, 0]$  and the limitation of the control input is  $u_{\text{lim}} = 5.0$  N.

#### Simulation 1 : Drawing the initial state variable condition $\mathcal{P}$

First simulation draws the conditions of initial state variables themselves. Plot ranges are  $X_0 \in [0, 0.1]$ ,  $V_0 \in [0, 0.4]$  and  $u_0 \in [-5, 5]$  and lattice points are provided with proper spaces. Moreover, (4-12) or (4-18) is calculated to each lattice point and it is plotted when it satisfies all of the conditions. The conditions are calculated for the case of  $N = 100, 300, 500$ .

The condition in the case of minimizing the energy cost is shown in Fig. 19. The condition in the case of minimizing the jerk cost is shown in Fig. 20. As shown in Fig. 19, 20, the conditions of

Tab. 6: Conditions of initial state variables.

Case	Type of dots	Initial states $[X_0, V_0, u_0]$
1	Red asterisk	$[0.0595, 0.37, 2.0]$
2	Yellow triangle	$[0.0620, 0.39, 2.0]$
3	Black circle	$[0.0600, 0.38, 2.0]$
4	Green square	$[0.0615, 0.38, 2.0]$

the initial state variables in each case are time-varying set, and the smaller the number of steps  $N$  becomes, the smaller the set is.

### Simulation 2 : Verification of effectiveness of proposed condition by time response

This second simulation demonstrates the effectiveness of the proposed conditions by simulation results in time domain. Four kinds of initial state variables are prepared for this simulation and the states are shown in Table I. The initial state variables are located outside the proposed set in the Cases 1 and 2 and they are located inside in the Cases 3 and 4. Therefore, it is expected that the thrust derived from FSC will violate the thrust limitations in the Cases 1 and 2. On the other hand, it is expected that the thrust derived from FSC will not violate the thrust limitations in the Cases 3 and 4.

In this simulation, the thrust derived from FSC whose evaluation function is jerk is described. The number of steps is  $N = 500$ . Fig. 21(a) shows a 2D graph of Fig. 20(e) at  $u_0 = 2.0$  N.

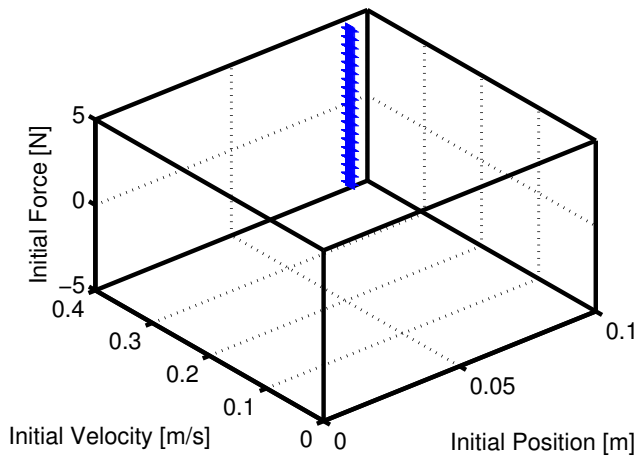
The changes of state variables and the thrust derived from FSC are shown in Fig. 21(b), (c). As shown in Fig. 21(b), initial state variables can be taken to a desired final state variables by FSC in all cases. However, as shown in Fig. 21(c), it is found that the control input derived from FSC satisfies thrust limitations only in Case 3 and 4 whose initial state variables are inside the proposed set. In this paper, note that the thrust derived from this method does not saturate in  $t \in [0, N\tau]$  because (4-12) or (4-18) is considered after obtaining an analytical solution of QP problem (4-11) or (4-16) with the assumption that the initial states are unknown variables.

### 4.3.4 Conclusion of initial state condition in FSC with thrust limitation

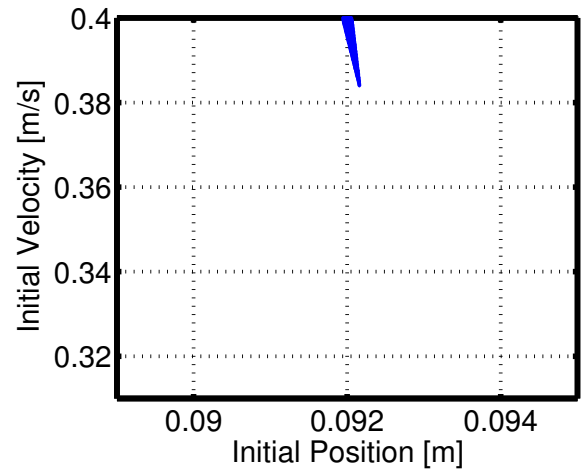
This paper proposes a new index to switch control modes which uses conditions of the initial state variables in FSC with thrust limitations. The conditions are derived in the case of defining energy or jerk as the evaluation function. The case in which jerk is defined as the evaluation function has the advantage of being able to designate the thrust of the final state. Moreover, simulation results demonstrate that the conditions are time-varying sets and that the proposed conditions can efficiently determine the time of switching control modes.

In this study, the dimension of the condition is three because the plant is defined as a rigid body model. However, the conditions can be calculated by expanding this concept even when the plant model has higher dimensions and is a more complicated expression. Thus it is expected that this condition can be applied to various industrial applications.

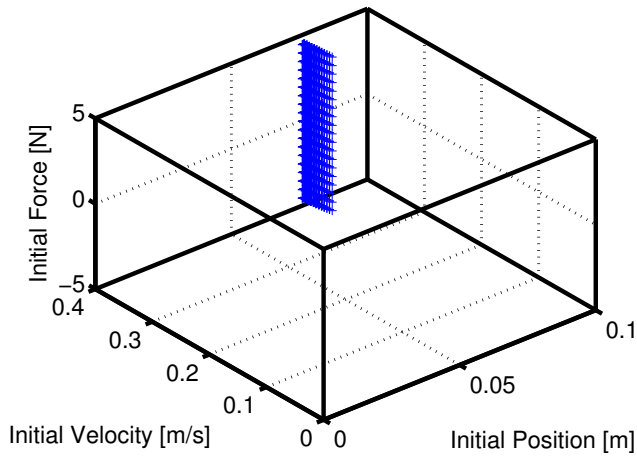
However, a real-time calculation of the proposed condition with many constraints is difficult. Thus, the next section discusses a mounting method enabling real-time calculation of the conditions.



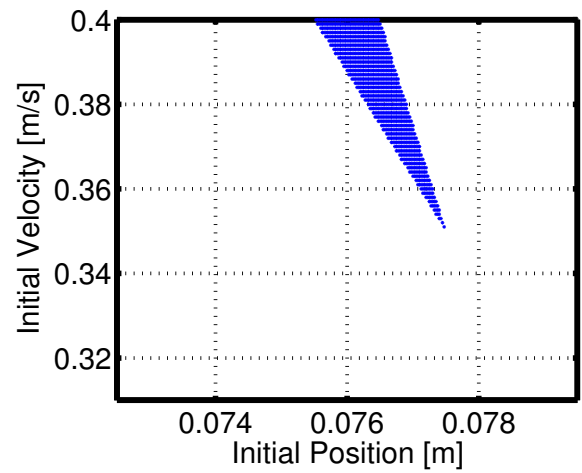
(a)  $N = 100$ .



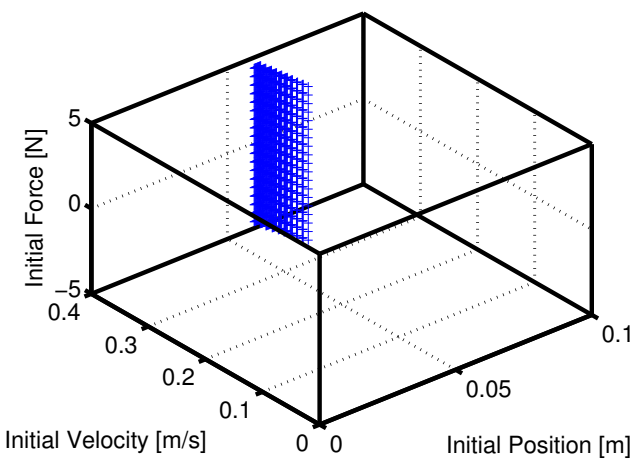
(b) 2D graph of Fig. 19(a) at  $u_0 = 0$ .



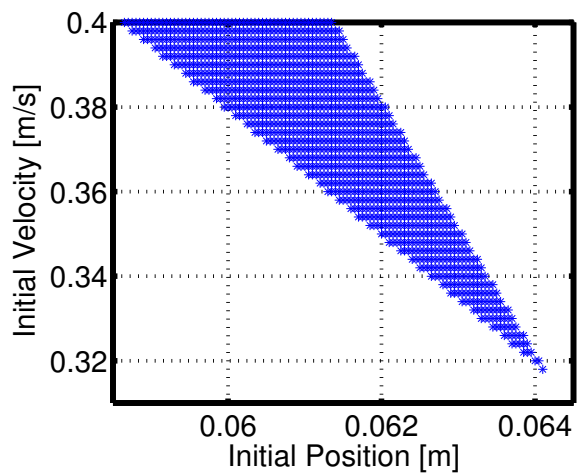
(c)  $N = 300$ .



(d) 2D graph of Fig. 19(c) at  $u_0 = 0$ .



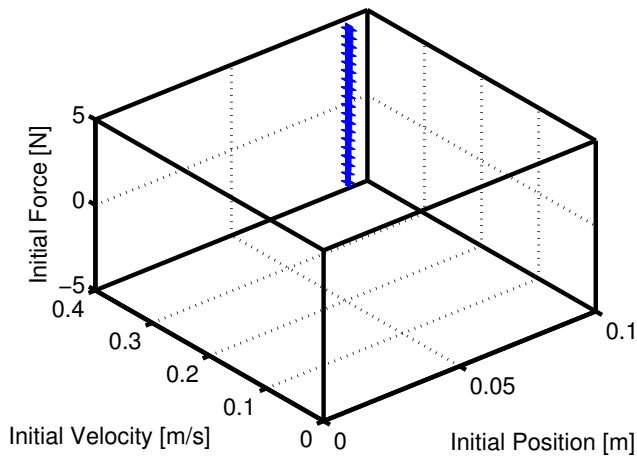
(e)  $N = 300$ .



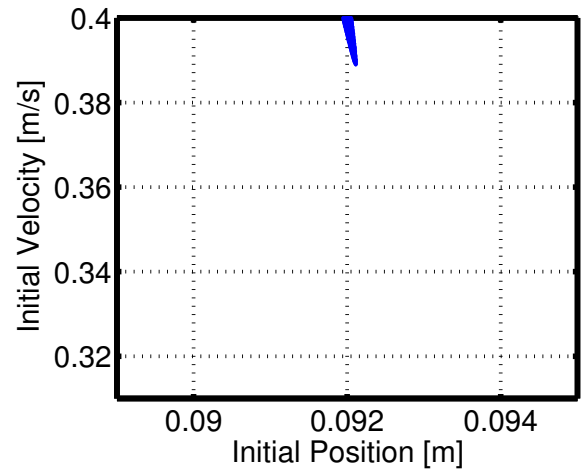
(f) 2D graph of Fig. 19(e) at  $u_0 = 0$ .

Fig. 19: Condition of initial state variables with energy minimization.

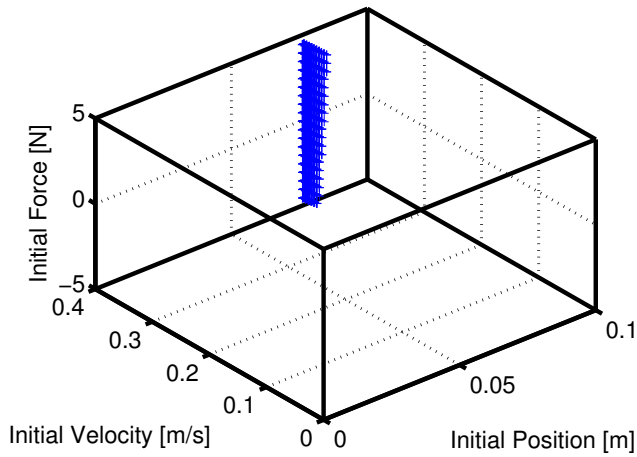




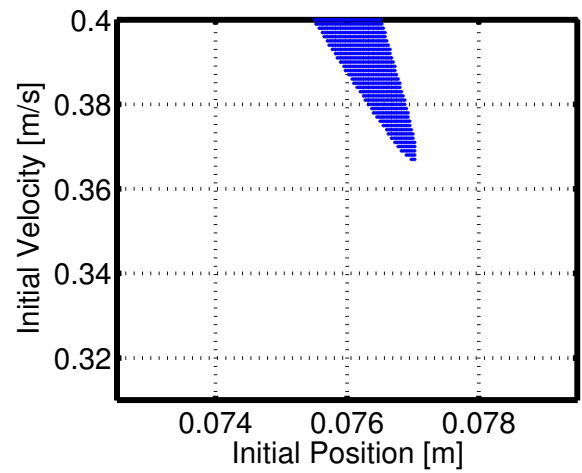
(a)  $N = 100$ .



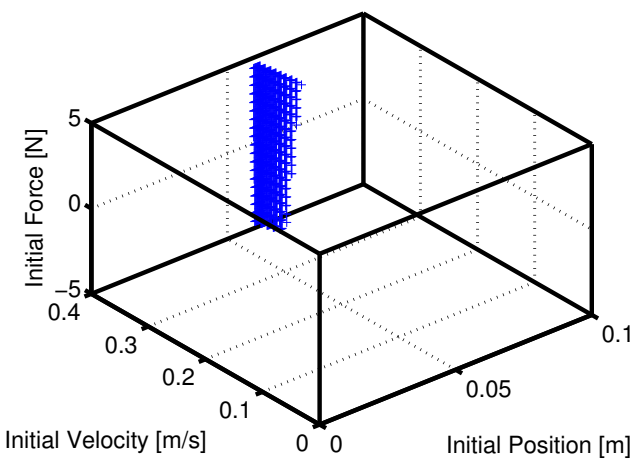
(b) 2D graph of Fig. 20(a) at  $u_0 = 0$ .



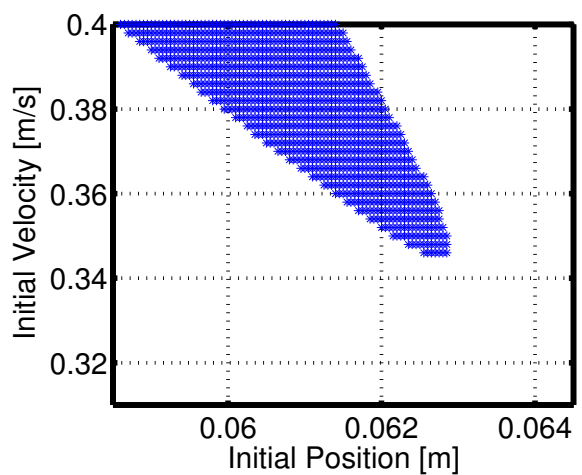
(c)  $N = 300$ .



(d) 2D graph of Fig. 20(c) at  $u_0 = 0$ .

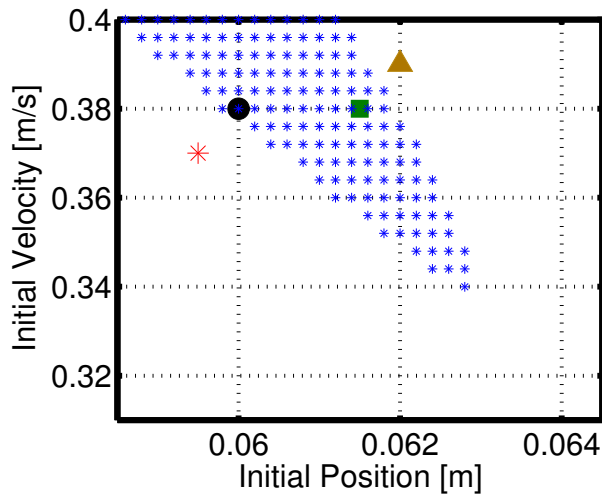


(e)  $N = 500$ .

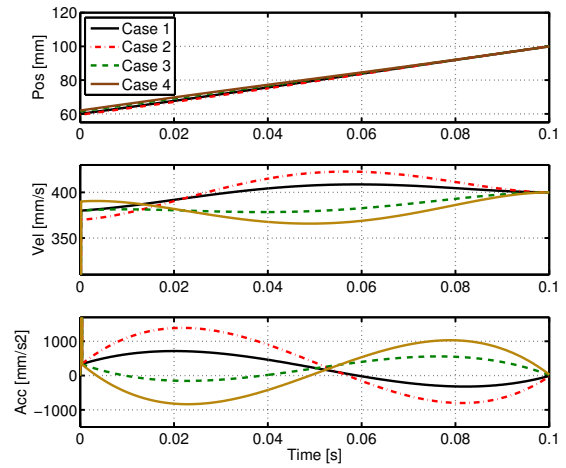


(f) 2D graph of Fig. 20(e) at  $u_0 = 0$ .

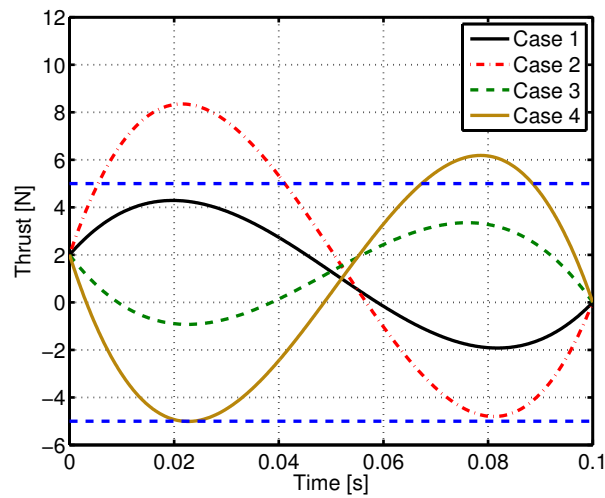
Fig. 20: Condition of initial state variables with jerk minimization.



(a) 2D graph of Fig. 20(e) at  $u_0 = 2$ .



(b) The change of position, velocity and acceleration.



(c) Thrust derived from FSC.

Fig. 21: Simulation results in time domain ( $N = 500$ ).

## 4.4 Real time determination of initial state variable condition using ellipsoid

### 4.4.1 Applying the condition of initial state variable to catapult stage

Section 4.2 shows that the settling time and the required maximum thrust of the fine stage can be improved by applying FSC to the fine stage in acceleration, however, the time when the fine stage is activated is determined by trial and error because the maximum thrust of the fine stage cannot be estimated in advance.

Therefore, section 4.3 derives the mode switching condition using the initial state variables in FSC with the thrust limitation. This condition guarantees the initial state can be taken to the desired state by FSC while satisfying thrust limitation. The time when the fine stage is activated is determined quantitatively by using the condition, however, the real-time calculation of the condition is difficult because the condition has many constraint equations. In this section, a mounting method to calculate the condition in real-time by using ellipsoids is proposed.

### 4.4.2 Approximation of initial state variable condition by ellipsoid

In this section, the condition of initial state variables is approximated by ellipsoids to reduce the calculation cost. According to (11-16),  $u_{augi}$  is given as follows:

$$u_{augi} = c_i X_0 + d_i V_0 + e_i u_{f0} + f_i,$$

$$\begin{cases} c_i = -(a_{11}q_{i1} + a_{21}q_{j2} + a_{31}q_{i3}) \\ d_i = -(a_{12}q_{i1} + a_{22}q_{i2} + a_{32}q_{i3}) \\ e_i = -(a_{13}q_{i1} + a_{23}q_{i2} + a_{33}q_{i3}) \\ f_i = -(q_{i1}X_F + q_{i2}V_F + q_{i3}u_F). \end{cases} \quad (4-19)$$

By combining (4-18) and (4-19), the constraint equations are given by

$$-\mathbf{b}' \leq \mathbf{A}' \begin{bmatrix} X_0 & V_0 & u_{f0} & 1 \end{bmatrix}^T \leq \mathbf{b}', \quad (4-20)$$

where,  $\mathbf{A}'_i$  is a vector in the  $i$ -th row of  $\mathbf{A}'$  and  $b'_i$  is a element in the  $i$ -th row of  $\mathbf{b}'$ , and  $\mathbf{A}'_i$  and  $b'_i$  are given as follows:

$$\mathbf{A}'_i = \left[ \sum_{k=1}^i c_k \quad \sum_{k=1}^i d_k \quad \sum_{k=1}^i e_k \quad \sum_{k=1}^i f_k + u_0 \right], \quad (4-21)$$

$$b'_i = u_{lim}.$$

As a result, the constraint equations are obtained as

$$\mathbf{A}\boldsymbol{\theta} \leq \mathbf{b},$$

$$\boldsymbol{\theta} = \begin{bmatrix} X_0 \\ V_0 \\ u_{f0} \end{bmatrix}, \mathbf{A} = \begin{bmatrix} \mathbf{A}' \\ -\mathbf{A}' \end{bmatrix}, \mathbf{b} = \begin{bmatrix} \mathbf{b}' - \mathbf{A}'_{i,4} \\ \mathbf{b}' - \mathbf{A}'_{i,4} \end{bmatrix}. \quad (4-22)$$

Let us consider the ellipsoid approximation of the initial state variables condition. An  $n$ th-order ellipsoid is defined in (4-23) [83, 84].

$$E(\mathbf{P}, \mathbf{c}) = \{\mathbf{x} \in R^n \mid (\mathbf{x} - \mathbf{c})^T \mathbf{P}^{-2} (\mathbf{x} - \mathbf{c}) \leq 1\} \quad (4-23)$$

$\mathbf{P} \in R^{n \times n}$  is a positive definite diagonal matrix and it decides the shape of the ellipsoid.  $\mathbf{c} \in R^{n \times 1}$  is a center of the ellipsoid. In this paper, an approximated ellipsoid is defined as a maximal ellipsoid in the condition of the initial state variables. The approximated ellipsoid is derived by solving the following optimization problem.

$$\begin{aligned} \max_{\mathbf{P}, \mathbf{c}} \quad & \{\det(\mathbf{P})\}^{\frac{1}{n}} \\ \text{s.t.} \quad & \|\mathbf{a}_i \mathbf{P}\|_2 + \mathbf{a}_i \mathbf{c} \leq b_i, \text{ for } i = 1, \dots, 2N + 2 \end{aligned} \quad (4-24)$$

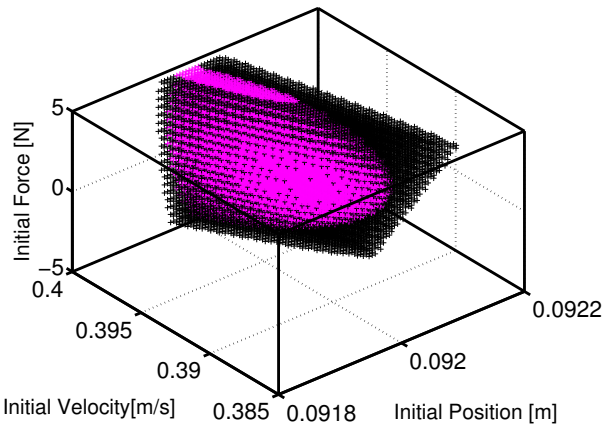
$\{\det(\mathbf{P})\}^{\frac{1}{n}}$  is an evaluation function which is proportional to a volume of the ellipsoid.  $\mathbf{a}_i$  is a vector in the  $i$ -th row of  $\mathbf{A}$ .  $b_i$  is a element in the  $i$ -th row of  $\mathbf{b}$ . The ellipsoid which is given by a quadratic form enables to express many constraint equations into one constraint equation.

### 4.4.3 Drawing ellipsoid approximation for initial state variable condition

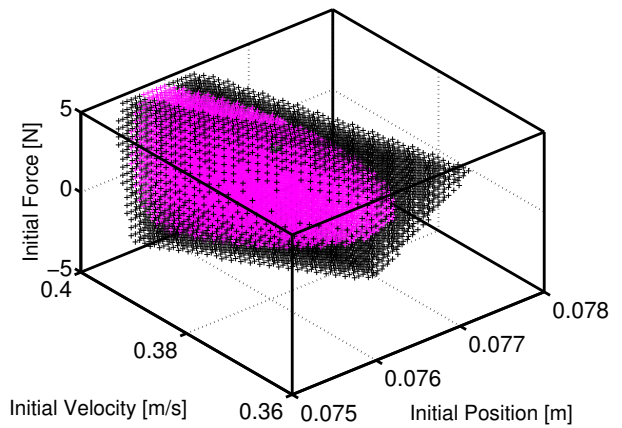
This simulation draws the approximated ellipsoids themselves. In this simulation, the mass of the fine stage is  $M_f = 6$  kg, the control period is  $200 \mu\text{s}$ , the final state is set at  $[X_F, V_F, u_{fF}]^T = [0.4, 0.1, 0]^T$  and the limitation of the control input is  $u_{\text{lim}} = 5.0$  N. The ellipsoids and original conditions are calculated for the case of  $N = 100, 300, 500$ . The order of the ellipsoid is  $n = 3$ . The optimized problem (4-24) is calculated by Primal-dual interior Point method with YALMIP [85].

The approximated ellipsoids and the original conditions are shown in Fig. 22. The black set is the original condition of the initial state variables and the red sphere is the approximated ellipsoid. Moreover, a green dot represents the state variable when the fine stage traces the target trajectory which is mentioned in section 9.1 ideally.

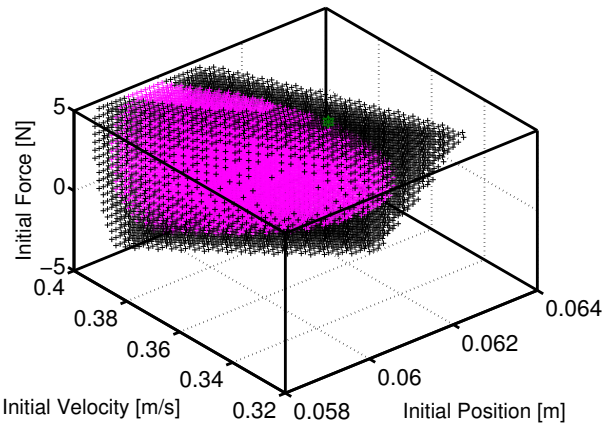
As shown in Fig. 22(a)–(c), the condition of the initial state variables is the time-varying set, and the smaller the number of steps  $N$  becomes, the smaller the set is. In addition, from these figures, the timing when the control of the fine stage is activated becomes conservative when using the approximated ellipsoid.



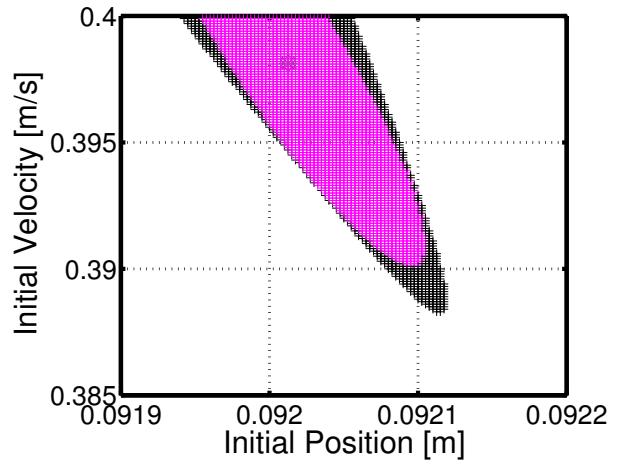
(a) Condition of initial state variables using an approximated ellipsoid ( $N = 100$ ).



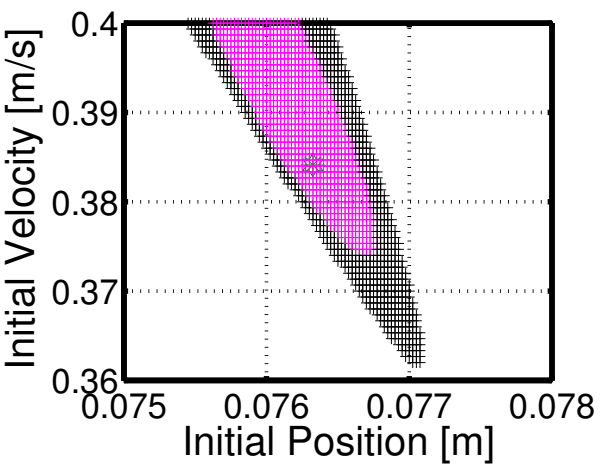
(b) Condition of initial state variables using an approximated ellipsoid ( $N = 300$ ).



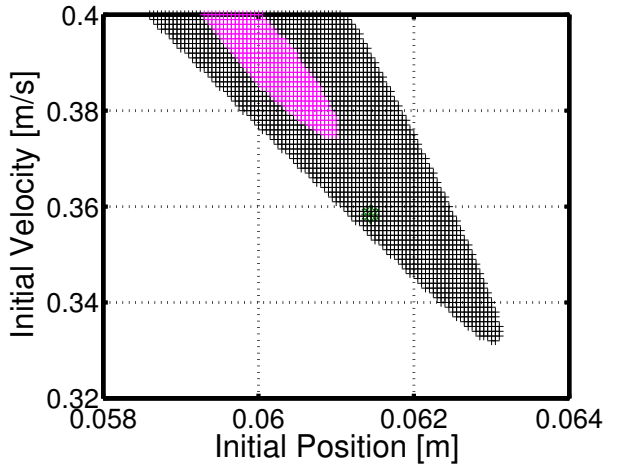
(c) Condition of initial state variables using an approximated ellipsoid ( $N = 500$ ).



(d) 2D graph of Fig. 22(a) at the ideal state of the fine stage.



(e) 2D graph of Fig. 22(b) at the ideal state of the fine stage.



(f) 2D graph of Fig. 22(c) at the ideal state of the fine stage.

Fig. 22: Condition of initial state variables using an approximated ellipsoid.

#### 4.4.4 Implementation by parameterization of parameters constituting an ellipsoid

From section 4.4.2, the number of the constraint equations is considerably reduced by approximating the condition as an ellipsoid. However, it is difficult to save parameters of the ellipsoids for all steps. This section describes a method to regard the parameters of the ellipsoids as a function. As a result, it becomes possible to calculate the conditions in real-time for all steps. The change of the ellipsoid is based on the change of  $\mathbf{P}$  and  $\mathbf{c}$ .

It is difficult to evaluate the change of  $\mathbf{P}$  because it has off-diagonal components. Thus, let us consider diagonalizing  $\mathbf{P}$  by using a rotation matrix. The rotation matrix using Euler angles is defined as

$$\mathbf{R}_{ypr}(\phi, \theta, \psi) = \begin{bmatrix} c_\theta c_\psi & c_\phi s_\theta c_\psi + s_\phi s_\psi & s_\phi s_\theta c_\psi - c_\phi s_\psi \\ -s_\theta & c_\phi c_\theta & s_\phi c_\theta \\ c_\theta s_\psi & c_\phi s_\theta s_\psi - s_\phi c_\psi & s_\phi s_\theta s_\psi + c_\phi c_\psi \end{bmatrix} \quad (4-25)$$

where  $c_\phi := \cos \phi$ ,  $s_\phi := \sin \phi$ , etc for compact notation in this section. By inserting  $\mathbf{x}^* = \mathbf{R}\mathbf{x}$  into (4-23),

$$\begin{aligned} E(\mathbf{P}, \mathbf{c}) &= (\mathbf{x} - \mathbf{c})^T \mathbf{P}^{-2} (\mathbf{x} - \mathbf{c}) \leq 1 \\ &\Leftrightarrow (\mathbf{x}^{*T} \mathbf{R} - \mathbf{c}^T) \mathbf{P}^{-2} (\mathbf{R}^{-1} \mathbf{x}^* - \mathbf{c}) \leq 1 \end{aligned} \quad (4-26)$$

As a result, it is found that the change of the ellipsoid is replaced by the change of rotation angles  $\phi$ ,  $\theta$ ,  $\psi$  and the change of diagonal components in a diagonal matrix.

Fig. 23(a), 23(b) and 23(c) show the change of center  $\mathbf{c}$ , the change of rotation angles  $\phi$ ,  $\theta$ ,  $\psi$  and the change of diagonal components in a diagonal matrix respectively. Moreover, Fig. 23(d) shows the value of the quaternions. Quaternions are substituted for Euler angles to avoid a singular point in this study. In Fig. 23(a), 23(b), 23(c) and 23(d), ‘‘data’’ means the simulation results which are got every 10 steps from  $N = 50$  to  $N = 500$  and ‘‘fitting’’ means the approximated function of ‘‘data’’ by utilizing the method of least squares. Hence, it becomes possible to generate ellipsoids in real-time for all steps because  $\mathbf{P}$  and  $\mathbf{c}$  are calculated in real-time.

#### 4.4.5 Experimental verification of real time condition determination method using ellipsoid approximation

In this section, experimental results demonstrate the effectiveness of the proposed method. In section 4.4.6, experimental results show that it become possible to judge when activating the fine stage automatically by using the approximated ellipsoid. In section 4.4.7, a comparison is made between the proposed method and a method in which the timing of control switching is fixed.

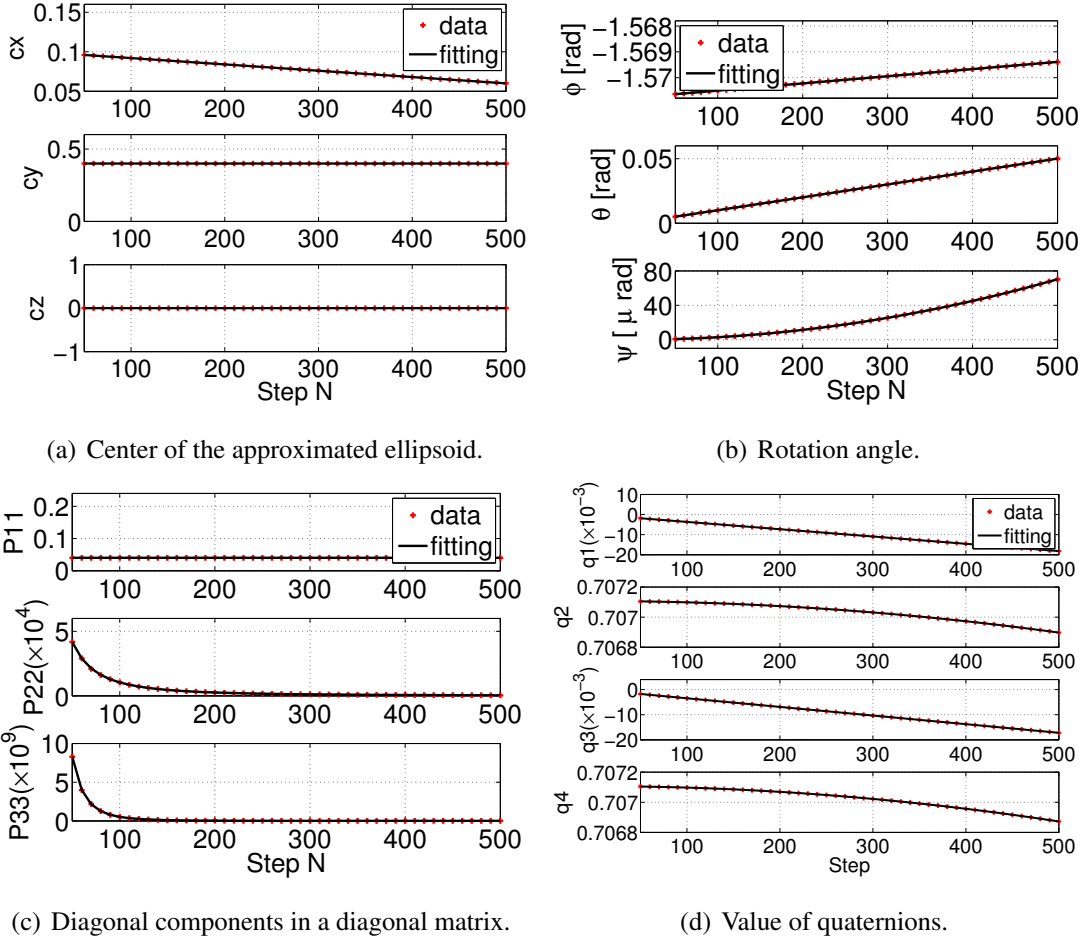


Fig. 23: The change of parameters of the approximated ellipsoid.

Fig. 24(a) shows the target position, velocity, and acceleration trajectories. The target position trajectory is based on 5th-order and 1st-order polynomials in the acceleration and deceleration regions and the constant velocity region, respectively. The distance of movement is 600 mm, the maximum velocity is 400 mm/s and the average acceleration 800 mm/s<sup>2</sup>. The trajectories during 0.0 s to 0.5 s are in the acceleration region. The trajectories during 0.5 s to 1.5 s are in the constant velocity region. The target trajectory of the coarse stage is shifted by gap lengths between the fine and coarse stages in the acceleration and deceleration regions compared with the target trajectory of the fine stage to avoid the impact force between the fine and coarse stages. The control period is 200  $\mu$ s. A PID position controller is designed for the fine and coarse stages, so that the closed-loop bandwidth of the position loop can both be 20 Hz. In this section, the movement and thrust of the coarse stage is not important because this section deals with the control method of the fine stage.

#### 4.4.6 Experiment1

In this experiment, the fine stage was controlled only in the constant velocity region to compute the change of  $(\mathbf{x} - \mathbf{c})^T \mathbf{P}^{-2} (\mathbf{x} - \mathbf{c})$  in the acceleration region. Fig. 68 shows the experimental results.

In Fig. 24(c), “flag” is elected when  $(\mathbf{x} - \mathbf{c})^T \mathbf{P}^{-2}(\mathbf{x} - \mathbf{c})$  becomes less than 1 and then it is judged that initial state variables enter the approximated ellipsoid. Moreover, it is found that there is optimal timing to activate the fine stage as shown in Fig. 24(d) This experiment shows that it become possible to evaluate quantitatively when the fine stage should be activated.

#### 4.4.7 Experiment2

The conventional method applies FSC to the fine stage when number of steps  $N$  is 300. The proposed method applies FSC to the fine stage when the initial state variables enter the approximated ellipsoid which is generated in real-time for all steps. It is defined that settling time is the time from the beginning of the constant velocity region to the time when the position error of the fine stage is smaller than  $5 \mu\text{m}$ . In this experiment, the approximated ellipsoid which generated in section 4.4.2 is used. Therefore, it is expected that the thrust in the proposed method will be less than  $u_{\text{lim}} = 5.0 \text{ N}$ .

The experiment of each method is done 6 times and Fig. 25 shows the experimental results. In addition, number of steps  $N$  at control switching and maximum thrust of the fine stage are summarized in Tab. 7. The settling time of the proposed method and that of the conventional method are almost the same. However, the proposed method does not violate the thrust limitation in any of the trials while the conventional method violates the thrust limitation in some trials. Thus, the conventional method can cause windup phenomena because of the thrust saturation and degrade the control performance. In contrast, the proposed method will not degrade the control performance because the thrust of the fine stage does not saturate.

### 4.5 Comparison with another control scheme with constraints

This chapter proposed the mode switching index based on FSC with constraints, however, there are several control method considering with constraints: model predictive control (MPC), polynomial trajectory generation, LMI-PFFSC [81], and anti-windup FB. The characteristics of FSC based approach, MPC, polynomial trajectory generation, and LMI-PFFSC are summarized in Tab. 8.

In the catapult stage, PTP control is required because the tracking error of the fine stage should be zero at the beginning of the constant velocity region. MPC and anti-windup FB are usually used to consider the constraints, but they are not suitable for the catapult stage because they are a constant value control. LMI-PFFSC is a kind of FSC, which considers a limitation of the control input. This method required long calculation time because it generates control inputs by solving an optimization problem with constraints. The catapult stage needs to judge whether the fine stage can be activated or not in 1 sample ( $=200 \mu\text{s}$ ), thus LMI-PFFSC cannot apply to the catapult stage. Finally, the polynomial trajectory generation can generate the target trajectory in real-time, however, it is un-



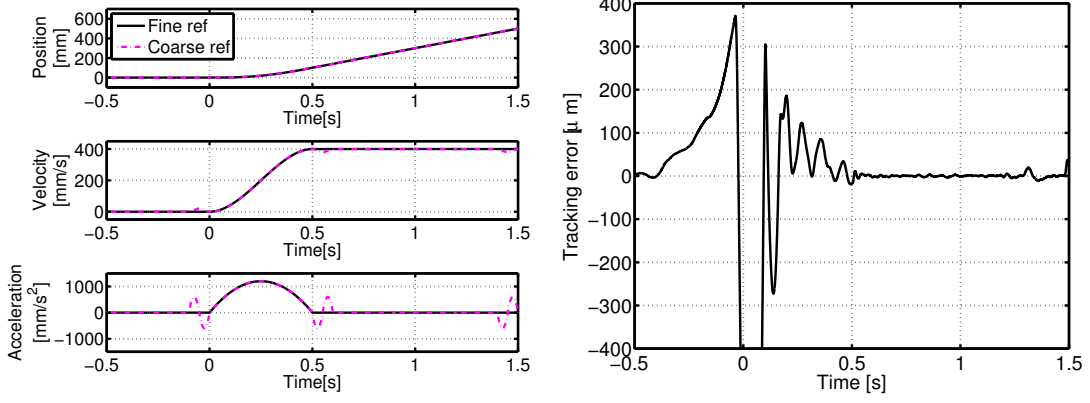
Tab. 7: Number of steps at control switching and maximum thrust.

Conventional method				
Trial	Step $N$	Maximum Thrust [N]	Thrust	Settling Time [ms]
1	300	4.12	Unsaturated	19.8
2	300	4.58	Unsaturated	17.1
3	300	5.45	Saturated	19.4
4	300	5.94	Saturated	17.6
5	300	6.38	Saturated	19.2
6	300	6.48	Saturated	17.1
Average	300	5.49		18.4
Proposed method				
Trial	Step $N$	Maximum Thrust [N]	Thrust	Settling Time [ms]
7	298	3.64	Unsaturated	16.7
8	277	4.08	Unsaturated	19.5
9	277	4.23	Unsaturated	19.9
10	392	4.27	Unsaturated	10.1
11	333	4.37	Unsaturated	18.8
12	413	4.54	Unsaturated	16.9
Average	332	4.19		17.0

known whether this method can obtain an optimal trajectory because this method does not have a cost function. Although whether the existence of saturation is good or not cannot be declared, the set of initial state variables of the proposed method is smaller than that of LMI-FSSRC because the thrust of the proposed method does not saturate, and then the judgement of the proposed method is conservative. There is a trade-off of the performance of judgement and the calculation cost. From above, the proposed method is most suitable approach for the catapult stage.

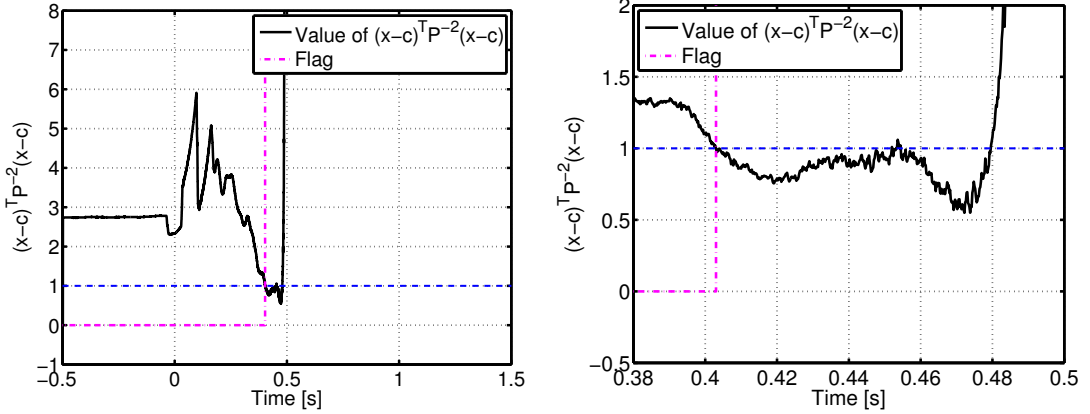
## 4.6 Conclusion of zero settling time control based on FSC considering with constraints

The basic control system proposed in 3 has problem that the tracking error of the fine stage cannot be avoided at the beginning of the constant velocity region. Thus, section 4.2 demonstrates that the settling time and the maximum thrust of the fine stage is reduced by applying FSC to the fine stage



(a) Target trajectory.

(b) Tracking errors of the fine stage.



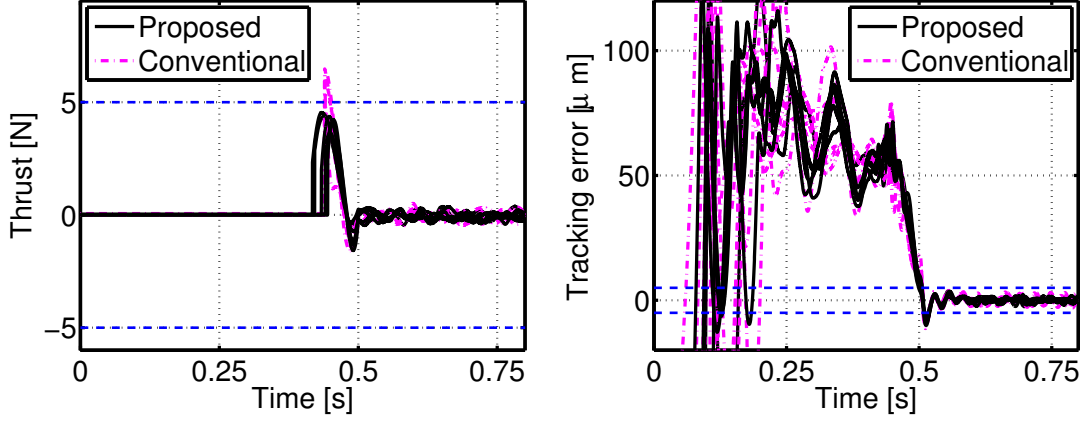
(c) Value of  $(x-c)^T P^{-2}(x-c)$ . The blue chain line means the threshold  $(x-c)^T P^{-2}(x-c) = 1$ . (d) Enlarged view of Fig. 24(c). The blue chain line means the threshold  $(x-c)^T P^{-2}(x-c) = 1$ .

Fig. 24: The change of  $(x-c)^T P^{-2}(x-c)$ .

in acceleration. However, the time when the fine stage is activated is determined by trial and error because the maximum thrust of the fine stage is not estimated in advance in 4.2.

Section 4.3 derives the mode switching condition using the initial stage variables in FSC with constraint to determine the time considering with the required maximum thrust of the fine stage, and section 4.4 proposed the mounting method by using an approximated ellipsoid to calculate the condition in real-time. Finally, experimental results show that it becomes possible to generate the ellipsoid in real-time, judge whether the current state satisfies the ellipsoid condition, and generate the control input by FSC. In addition, experimental results confirm the effectiveness of the proposed method.

From the above, it is shown that the initial state variable condition in the FSC with thrust constraint is one of the indexes of control switching and the basic theory for practicalizing the catapult stage can be constructed.



(a) Thrust of the fine stage in acceleration region. (b) Tracking error of the fine stage in acceleration region. The blue chain lines mean the threshold  $u_{lim} = \pm 5.0$  N. The blue dot lines show  $\pm 5 \mu m$ .

Fig. 25: Thrust and tracking error of the fine stage in acceleration region.

Tab. 8: Comparison of trajectory generation methods.

Control method	Defination of terminal time	Calculation cost	Cost function	Saturation
Proposed method	Possible	Low	Exist	Not exist
MPC	Impossible	High	Exist	Exist
Polynomial trajectory generation	Possible	Low	Not exist	Not exist
LMI-PFFSC	Possible	High	Exist	Exist
Anti-windup FB	Impossible	Low	Not exist	Exist

# Chapter 5

## Sudden disturbance suppression control considering with constraints based on reference governor

### 5.1 Importance of disturbance suppression

A high-precision stage is an essential piece of industrial equipment for producing semiconductors and liquid crystal displays. The stage demands high throughput and high precision because the products made by the stage should be of a low price and high space density. Several studies on the design of controllers with high feedback (FB) bandwidth are reported in the literature. For example, a dual-servo stage, which has coarse and fine components [6, 65], or the miniaturization of an actuator of the stage [86, 87]. However, the saturation of the thrust is easy to occur when the actuator is miniaturized. The dual actuator is needed to be controlled not to violate the constraints on the gap and relative speed between coarse and fine stages. Therefore, it is important to establish a control system design that positively takes account of the constraint conditions. Hence, designing a control system keeping these constraints in mind is important.

A two-degrees-of-freedom control that combines feedforward (FF) and FB control is widely used in a trajectory tracking control for a high-precision stage. The FF control is mainly used to improve the tracking performance [29] and chapter 4 proposed a control method considering thrust limitations in the FF control framework [88]. On the other hand, the disturbance suppression performance is important in the constant velocity region, and the FB controller is usually designed to optimize its performance related to suppression of disturbance that is analyzed and expected in advance [68]. In this case, the controller achieves good suppression of expected disturbances. However, the suppression performance of sudden and unexpected disturbances may degrade because of actuator saturation.

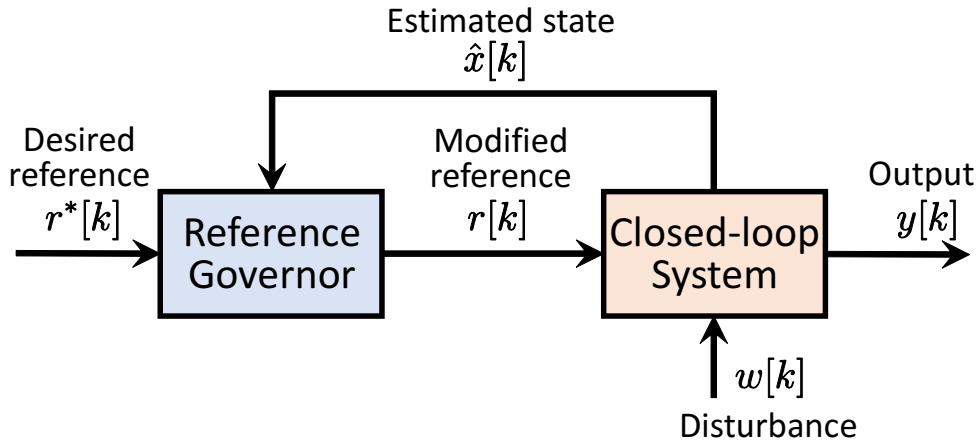


Fig. 26: Block diagram of reference governor.

Therefore, the FB controller should be able to manage not only expected disturbances but also sudden disturbances.

For this reason, this section proposes a suppression control method for sudden disturbances based on model predictive control (MPC) and RG. The block diagram of RG is shown in Fig. 26. The proposed method makes it possible to improve the disturbance suppression performance within the constraints by modifying the reference signals properly.

Several notable studies have focused on RG: Scalar Reference Governor (SRG) [89, 90], Command Governor (CG) [91, 92], Extended Command Governor (ECG) [93, 94], MPC-based RG [95]. These studies mainly discuss the tracking performance to a constant reference signal and do not discuss the disturbance suppression performance. Hatanaka and Takaba [96] proposed an RG considering with step disturbances. However, their study does not discuss disturbance suppression performance. Moreover, the method is markedly influenced by a modeling error because it calculates the modified reference signals when it is off-line.

There are many applications to which RG should be applied ( gasoline engine [97], Vehicle rollover suppression [97], output control of fuel cell for air compressor [98], posture control and trajectory design of airplanes [94, 99, 100], posture and altitude control of flying wind turbine [101], attitude control of RC helicopter [102], inverted pendulum [92], positioning control of secondary delay system[103], hard disk drives [104, 105] ), however, RG has not been experimentally verified extensively in previous studies because of its high calculation cost. The method proposed in this section can verify its effectiveness experimentally by partly using the implementation proposed in [90]. Furthermore, this thesis discusses the disturbance suppression performance of the proposed method, which has not been paid attention to in the previous studies of RG. Therefore, the proposed method gives a new perspective in this field.

The outline of this paper is as follows. Section 5.2 proposes a disturbance suppression control by shaping the reference signals based on MPC. In section 5.3, a disturbance suppression control method

by modifying the reference signals based on RG and considering the constraints is proposed. Finally, section 5.4 demonstrates the effectiveness of the proposed method through experiments. In section 5.5, the proposed method is compared with another control methods.

## 5.2 Sudden disturbance suppression control using model predictive control without constraints

In this section, the disturbance suppression control method by shaping reference signals based on MPC without constraints is introduced. Several previous studies proposed reference shaping methods using MPC, however, this is the first study in which mainly focuses on the disturbance suppression performance. This paper supposes an impulse input disturbance as the sudden disturbance.

### 5.2.1 Impulse disturbance response

In motion control, the controller often has more than one integrator to avoid steady-state errors by step-input disturbances. When an impulse input disturbance is added to such a controller, it is well known that the error  $e(t)$  satisfies the following relationship [106].

$$\int_0^{\infty} e(t)dt = 0 \quad (5-1)$$

Here,  $e(t) = r(t) - y(t)$ ,  $r(t)$  is the reference signal and  $y(t)$  is the plant output. Therefore, the impulse input disturbance response makes the integrated value of the error zero as shown in Fig. 27(a). The shape of the response waveform itself cannot be changed because the relationship shown in (5-1) is always held to the impulse input disturbance even if the FB bandwidth of the controller is improved.

Therefore, even if the original reference signals are modified, the error between the modified reference and the plant output satisfies the relationship shown in (5-1). However, the original reference signals are not related to the plant output. Hence, the response waveform can be improved by managing the reference signals properly. In other words, the proposed method is a control method that interchanges the relationship between the reference signal and the plant output in a normal control system. The conceptual diagram of the impulse input disturbance response by modifying the reference signal is shown in Fig. 27(b). This chapter discusses impulse disturbance suppression control by management of reference signals.

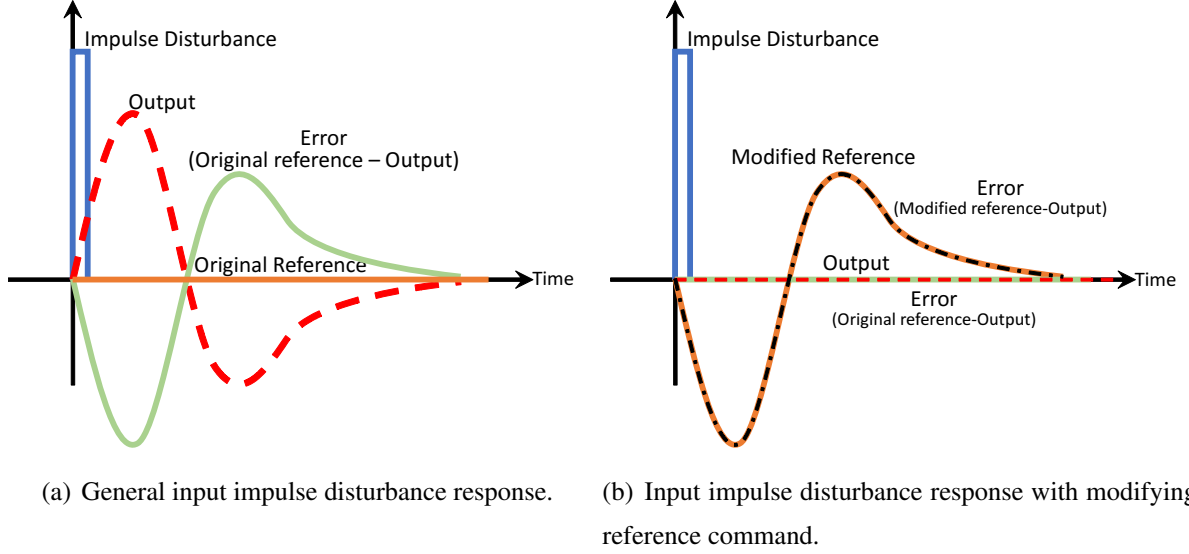


Fig. 27: Impulse input disturbance response. It becomes possible to manage the shape of response itself by modifying the original reference signal as shown in Fig. 27(b).

## 5.2.2 Reference modification based on MPC without constraints

This chapter considers a discrete-time servo system given by

$$\begin{aligned} \mathbf{x}[k+1] &= \mathbf{A}\mathbf{x}[k] + \mathbf{B}r[k], \quad \mathbf{x}[0] = \mathbf{x}_0, \\ y[k] &= \mathbf{C}\mathbf{x}[k], \end{aligned} \quad (5-2)$$

where  $\mathbf{x} \in \mathbf{R}^n$  is the closed loop state,  $y \in \mathbf{R}^1$  is the output to be controlled, and  $r \in \mathcal{R} = [r_{\min}, r_{\max}] \subseteq \mathbf{R}^1$  is the reference input of the closed system.  $\mathbf{A}$  is assumed to be a stable matrix in this paper. Then, the  $i$  ( $i \geq 1$ ) samples after the state space is estimated as follows:

$$\begin{aligned} \hat{\mathbf{x}}[k+i] &= \mathbf{A}^i \mathbf{x}[k] + \sum_{j=0}^{i-1} \mathbf{A}^{i-j-1} \mathbf{B}r[k+j] \\ \hat{y}[k+i] &= \mathbf{C}\mathbf{A}^i \mathbf{x}[k] + \mathbf{C} \sum_{j=0}^{i-1} \mathbf{A}^{i-j-1} \mathbf{B}r[k+j] \end{aligned} \quad (5-3)$$

Thus, the error between the original reference signal  $r^*$  and the plant output at  $k+i$  is estimated as

$$\begin{aligned} \hat{e}[k+i] &= r^* - \hat{y}[k+i] \\ &= r^* - \left( \mathbf{C}\mathbf{A}^i \mathbf{x}[k] + \mathbf{C} \sum_{j=0}^{i-1} \mathbf{A}^{i-j-1} \mathbf{B}r[k+j] \right). \end{aligned} \quad (5-4)$$

When the reference input  $r$  is assumed to be constant in the predictive horizon, namely  $r[k+j] = r$  ( $0 \leq j \leq i-1$ ), the error is represented as

$$\hat{e}[k+i] = r^* - \left( \mathbf{C}\mathbf{A}^i \mathbf{x}[k] + \sum_{j=0}^{i-1} \mathbf{C}\mathbf{A}^j \mathbf{B}r \right). \quad (5-5)$$

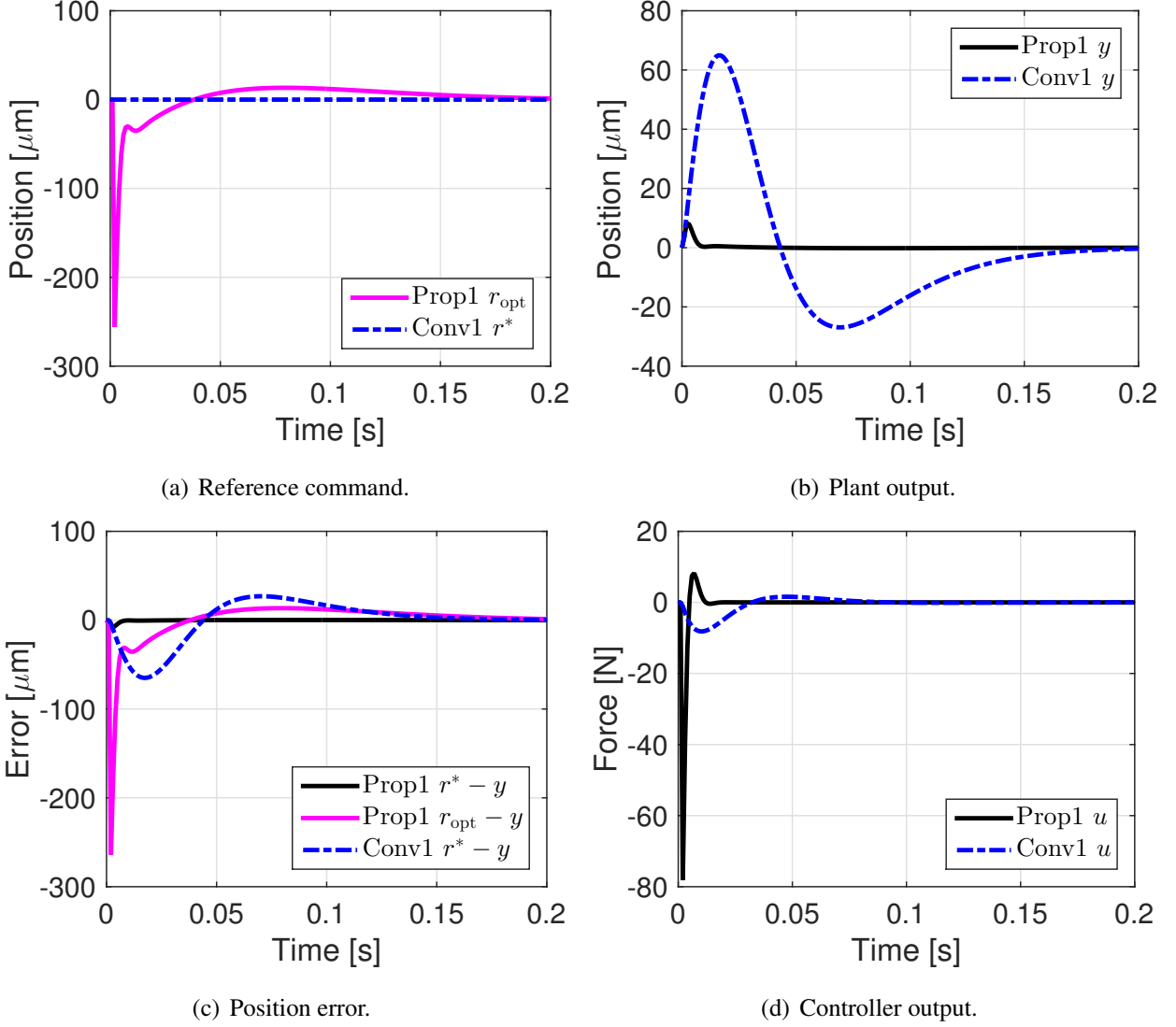


Fig. 28: Simulation results of disturbance suppression control by reference command modification based on MPC.

Here, the order of  $\hat{e}[k+i]$  is at most 1st to  $r$  because  $r^*$  is given in advance and  $x[k]$  can be measured for each sampling time. Now a performance index is set as follows:

$$J = \|\hat{\mathbf{e}}_{i-1}\|_2^P + \|\hat{e}[k+i]\|_2^Q,$$

$$\hat{\mathbf{e}}_h = \begin{bmatrix} \hat{e}[k] \\ \hat{e}[k+1] \\ \vdots \\ \hat{e}[k+h] \end{bmatrix}, h \in \mathbb{Z}_+.$$
(5-6)

$\|\hat{\mathbf{e}}_{i-1}\|_2^P$  and  $\|\hat{e}[k+i]\|_2^Q$  represent the integral square value of the error and the final state value of the error, respectively. Then, the performance index is represented as a quadratic function of  $r$ . An optimal value of the performance index  $r_{\text{opt}}$  is derived as (5-7) when the performance index is



represented in  $J = p_2(\mathbf{x}[k], r^*)r^2 + p_1(\mathbf{x}[k], r^*)r + p_0(\mathbf{x}[k], r^*)$ .

$$r_{\text{opt}} = -\frac{p_1(\mathbf{x}[k], r^*)}{2p_2(\mathbf{x}[k], r^*)} \quad (5-7)$$

It is expected that the impulse input disturbance response is improved by using  $r_{\text{opt}}$  calculated for each time as the new reference signals.

### 5.2.3 Verification of sudden disturbance suppression performance by simulation

This section demonstrates the effectiveness of the modification of reference signals based on MPC by simulation results. This simulation is conducted for the impulse disturbance suppression performance when setting the original reference signal and an initial state of the closed-loop system as  $r^* = 0$  and  $\mathbf{x}[0] = \mathbf{O}$ , respectively. The ‘‘Conventional 1’’ method does not modify the original reference signal. The ‘‘Proposed 1’’ method uses the optimal reference signal  $r_{\text{opt}}$  derived from the method proposed in section IIB as the reference signal. In addition, a plant model  $P(s)$  is defined as a rigid body model shown in (5-8) in this paper.

$$P(s) = \frac{1}{M_p s^2}, \quad M = 14.0 \text{ kg} \quad (5-8)$$

Here,  $M_p$  is a mass. The control period is  $T_s = 1.0$  ms and a PID position controller is designed for the plant so that the closed-loop bandwidth of the position loop is 10 Hz. This paper assumes that the following impulse-shaped disturbance is added.

$$w(t) = \begin{cases} 100 \text{ N}, & 0 \leq t \leq T_s \\ 0, & \text{otherwise} \end{cases} \quad (5-9)$$

In this simulation, the performance index is defined as follows:

$$J = \|\hat{\mathbf{e}}_i\|_2, \quad (5-10)$$

where, the predictive horizon is  $i = 3$ .

The simulation results are shown in Fig. 28. As shown in Fig. 28(b), ‘‘Conventional 1’’ needs a long time to converge the disturbance response because the error between the original reference signal and the plant output satisfies the relationship shown in (5-1). On the other hand, in ‘‘Proposed 1’’, the convergence of the error to the original reference signals is considerably improved by satisfying the relationship (5-1) to the error between the modified reference signals and the plant output. In this paper, the settling time is defined as the time from adding the impulse disturbance to when the position error is smaller than  $1 \mu\text{m}$ . The settling time of ‘‘Conventional 1’’ and ‘‘Proposed 1’’ are 177 ms and 7.49 ms, respectively.

The suppression performance is largely improved. However, the controller output in ‘‘Proposed 1’’ is very large as shown in Fig. 28(d). Therefore, reference signal modification with controller output constraints is required.

## 5.3 Sudden disturbance suppression control using reference governor

The method proposed in section 5.2 shows that the signal modification can reduce the effect of the impulse input disturbance. However, this method gives large controller output. A disturbance suppression method considered with controller output limitation is needed because all real actuators have output constraints. This section proposes a reference signal modification method considering constraints based on RG.

### 5.3.1 Maximal output Admissible Set

This section explains a maximal output admissible set (MAS) which is widely used in the previous studies of RG [107]. To grasp the state of the control system for the constraints, it is important to modify the reference signals properly considering the constraints. A prescribed constraint set is a set of state space that consists of all state variables satisfying the constraints. In addition, a positively invariant set is a set that always keeps a state in it for any external input if the initial state is inside the set. An output admissible set is a common set of the prescribed constraint set and the positively invariant set, and MAS is its maximal set.

The closed-loop system always satisfies the constraint conditions when the initial state variables of the system are inside MAS. MAS depends on the reference signals and the current state variables. Most previous studies of RG select the proper MAS by managing the reference signals. The conceptual diagram of RG using MAS is shown in Fig. 29.

#### Discrete-time linear system with constraints

In addition to the linear discrete-time servo system shown in (5-2), a variable to consider constraints on state and input is prepared by

$$\mathbf{z}[k] = \mathbf{L}\mathbf{x}[k] + \mathbf{D}r[k] \in \mathcal{Z}(\xi) \subseteq \mathbf{R}^p, \quad (5-11)$$

where,  $\mathbf{L} \in \mathbf{F}^{p \times n}$  and  $\mathbf{D} \in \mathbf{F}^{p \times m}$ . This paper assumes  $\mathbf{O} \in \mathcal{Z}$  and  $\mathcal{Z}$  is bounded. From these assumptions,  $\mathcal{Z}(\xi) \in \mathbf{R}^p$  is defined as a polytope given by

$$\mathcal{Z} = \{\mathbf{z} \in \mathbf{R}^p | \mathbf{M}\mathbf{z} \leq \mathbf{m}(\xi)\}. \quad (5-12)$$

In (5-12), the inequality is a component-wise inequality and  $\xi \in \Xi$  is a variable characterizing constraints that is given when the control is started.

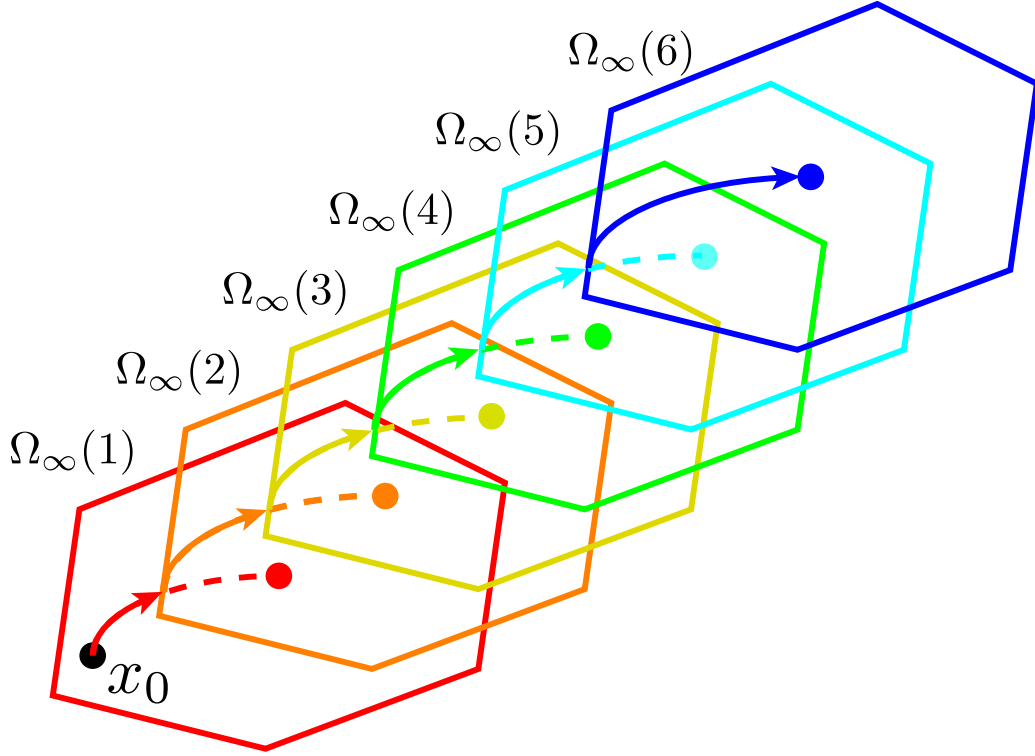


Fig. 29: Conceptual diagram of RG by using MAS.

### Definition of MAS

This section defines MAS by (5-2) and (5-11).  $\mathbf{x}[i; k, \mathbf{x}_0, \hat{r}]$  is a solution of (5-2) satisfying  $\mathbf{x}[k] = \mathbf{x}_0$ ,  $r[k+i] = \hat{r}$  for all  $i \in \mathbb{Z}_+$ , and  $\mathbf{z}[i; k, \mathbf{x}_0, \hat{r}] = \mathbf{L}\mathbf{x}[i; k, \mathbf{x}_0, \hat{r}] + \mathbf{D}\hat{r}$ . Then MAS  $\Omega_\infty$  is defined as follows [107]:

$$\Omega_\infty(\mathcal{R}, \Xi) = \{(\mathbf{x}_0, r, \xi) : \mathbf{x}_0 \in \Omega_\infty(r, \xi),$$

$$\text{for some } (r, \xi) \in \mathcal{R} \times \Xi\}, \quad (5-13)$$

$$\Omega_\infty(\hat{r}, \xi) = \{\mathbf{x}_0 : \mathbf{z}[i; k, \mathbf{x}_0, \hat{r}] \in \mathcal{Z}(\xi), \forall i \geq 0\}.$$

By the definition,  $\Omega_\infty(\hat{r}, \xi)$  is a positively invariant set. This means that if  $\mathbf{x}[k] = \mathbf{x}_0 \in \Omega_\infty(\hat{r}, \xi)$  then  $\mathbf{x}[k+i] \in \Omega_\infty(\hat{r}, \xi)$  for all  $i \in \mathcal{K}$ . Furthermore, there is an integer  $\hat{i}$  satisfying  $\Omega_\infty(\hat{r}, \xi) = \Omega_{\hat{i}}(\hat{r}, \xi)$  for each  $\hat{r} \in \mathcal{R}$  and  $\xi \in \Xi$  because  $\mathbf{A}$  is a stable matrix. This paper assumes there is an integer  $\kappa$  such that

$$\kappa = \sup_{\hat{r} \in \mathcal{R}, \xi \in \Xi} \hat{i}. \quad (5-14)$$

If  $\kappa$  can be obtained, MAS is given as follows:

$$\Omega_\infty(\hat{r}, \xi) = \Omega_\kappa(\hat{r}, \xi), \quad \forall \hat{r} \in \mathcal{R}, \forall \xi \in \Xi. \quad (5-15)$$

In this paper, such the number of steps  $\kappa$  is calculated in advance. The calculation method of  $\kappa$  is described in [108] and this paper inserts  $\mathbf{x}_{p0} = \mathbf{A}_p^{-1}\mathbf{b}_p w$  into an initial state of the plant to use the calculation method. Here,  $\mathbf{A}_p$  and  $\mathbf{b}_p$  are coefficients of a state  $\mathbf{x}_p[k]$  and an input  $u[k]$  in a discrete-time state equation of the plant  $\mathbf{x}_p[k+1] = \mathbf{A}_p\mathbf{x}_p[k] + \mathbf{b}_p u[k]$ .

## Characterization of MAS

This section characterizes MAS to calculate it in real-time [90]. From (5-3) and (5-11),  $\mathbf{z}[k+i]$  is given by

$$\begin{aligned} \mathbf{z}[k+i] &= \mathbf{L}\mathbf{A}^i\mathbf{x}[k] \\ &+ \mathbf{L}\sum_{j=0}^{i-1}\mathbf{A}^{i-j-1}\mathbf{B}r[k+j] + \mathbf{D}r[k+i]. \end{aligned} \quad (5-16)$$

Assuming  $r[k+j] = \hat{r}$  ( $0 \leq j \leq i$ ), from (5-12) and (5-16), the constraint at  $k+i$  is represented as follows:

$$\mathbf{M}\mathbf{L}\mathbf{A}^i\mathbf{x}[k] + \mathbf{M}\left(\mathbf{L}\sum_{j=0}^{i-1}\mathbf{A}^j\mathbf{B} + \mathbf{D}\right)\hat{r} \leq \mathbf{m}. \quad (5-17)$$

Let us define

$$\begin{aligned} \mathbf{h}_{l,i} &= \mathbf{M}_l\mathbf{L}\mathbf{A}^i, \quad g_{l,i} = \mathbf{M}_l\left(\mathbf{L}\sum_{j=0}^{i-1}\mathbf{A}^j\mathbf{B} + \mathbf{D}\right), \\ l \in \mathcal{L} &= \{1, 2, \dots, q\}, \quad i \in \mathcal{K} = \{0, \dots, \kappa\}. \end{aligned} \quad (5-18)$$

Then, by (5-13) and (5-18), MAS is characterized as follows:

$$\begin{aligned} \Omega_\kappa(\mathcal{R}, \Xi) &= \{(\mathbf{x}_0, \hat{r}, \xi) : \mathbf{h}_{l,i}\mathbf{x}_0 + g_{l,i}\hat{r} \leq m_l(\xi), \\ &l \in \mathcal{L}, i \in \mathcal{K}, \hat{r} \in \mathcal{R}, \xi \in \Xi\}. \end{aligned} \quad (5-19)$$

As a result, MAS can be represented by  $q \times (\kappa + 1)$  inequalities.

### 5.3.2 Design of RG

It is assumed that the state  $\mathbf{x}$  of the closed-loop system can be observed. Then,  $r[k] = \hat{r}(\alpha_k)$ , which satisfies  $\mathbf{x}[k] \in \Omega_\kappa(\hat{r}(\alpha_k), \xi)$  is calculated by

$$\hat{r}(\alpha_k) = (1 - \alpha_k)\bar{r}_{\text{opt}} + \alpha_k r_{\text{opt}}. \quad (5-20)$$

Here,  $\bar{r}_{\text{opt}} = -\beta r_{\text{opt}}$  ( $\beta > 0$ ).  $\hat{r}(\alpha_k)$  is the nearest value to the optimal solution  $r_{\text{opt}}$  satisfying the constraints when a maximal  $\alpha_k \in [0, 1]$  that satisfies  $\mathbf{x}[k] \in \Omega_\kappa(\hat{r}(\alpha_k), \xi)$  is selected. By (5-19), (5-20),  $\mathbf{x}[k] \in \Omega_\kappa(\hat{r}(\alpha_k), \xi)$  holds if

$$\begin{aligned} \alpha_k g_{l,i}(r_{\text{opt}} - \bar{r}_{\text{opt}}) &\leq m_l(\xi) - \mathbf{h}_{l,i}\mathbf{x}[k] - g_{l,i}\bar{r}_{\text{opt}}, \\ &\forall l \in \mathcal{L}, \forall i \in \mathcal{K}. \end{aligned} \quad (5-21)$$

When  $\mathbf{h}_{l,i}, g_{l,i}$  is calculated in advance,  $\alpha_k$  is given as follows:

$$\begin{aligned} \alpha_k &= \min\{1, \tilde{\alpha}_k\}, \\ \tilde{\alpha}_k &= \min_{(l,i) \in \mathcal{L} \times \mathcal{K}} \frac{m_l(\xi) - \mathbf{h}_{l,i}\mathbf{x}[k] - g_{l,i}\bar{r}_{\text{opt}}}{g_{l,i}(r_{\text{opt}} - \bar{r}_{\text{opt}})}. \end{aligned} \quad (5-22)$$

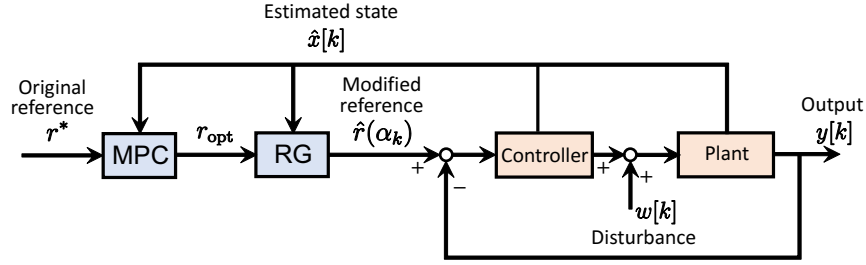


Fig. 30: Block diagram of the proposed method based on RG.

From these results, the real-time calculation of  $\alpha_k$  becomes possible.

The above method of generation of the reference signals is often used in SRG. However, most previous studies of SRG assume that the modified reference signals have a monotonic property; that is, the reference signals increased or decreased monotonically. Therefore, in the case of coinciding the initial state of the plant with the original reference and discussing only the effect of the disturbance, it is impossible to modify the reference signals in response to the disturbance.

On the other hand, the proposed method can manage the reference signals that do not have the monotonic property by applying RG after using MPC. Thus, the proposed method can modify the reference signals properly in response to the disturbance. The block diagram of the proposed method based on RG is shown in Fig. 30.

### 5.3.3 Verification of impulse disturbance suppression control based on RG by simulation

This section discusses the impulse disturbance suppression control based on RG. The simulation condition is the same as in section IIC and the limitation of the controller output is  $u_{\text{lim}} = 6.0 \text{ N}$ . “Conventional 2” does not modify the original reference signal and it applies an anti-windup compensation proposed in [75] to prevent the windup phenomenon by a controller saturation. “Proposed 2” uses the modified reference signal  $\hat{r}(\alpha_k)$  derived from the method proposed in section IIIB as the reference signal. In this paper,  $\beta = 10$ .

The simulation results are shown in Fig. 31. The settling time of “Conventional 2” and “Proposed 2” are 185 ms and 89.2 ms, respectively. As shown in Fig. 31(a), “Proposed 2” can modify the reference signals that do not have the monotone property. As a result, the disturbance suppression performance in “Proposed 2” is improved while satisfying the constraints.

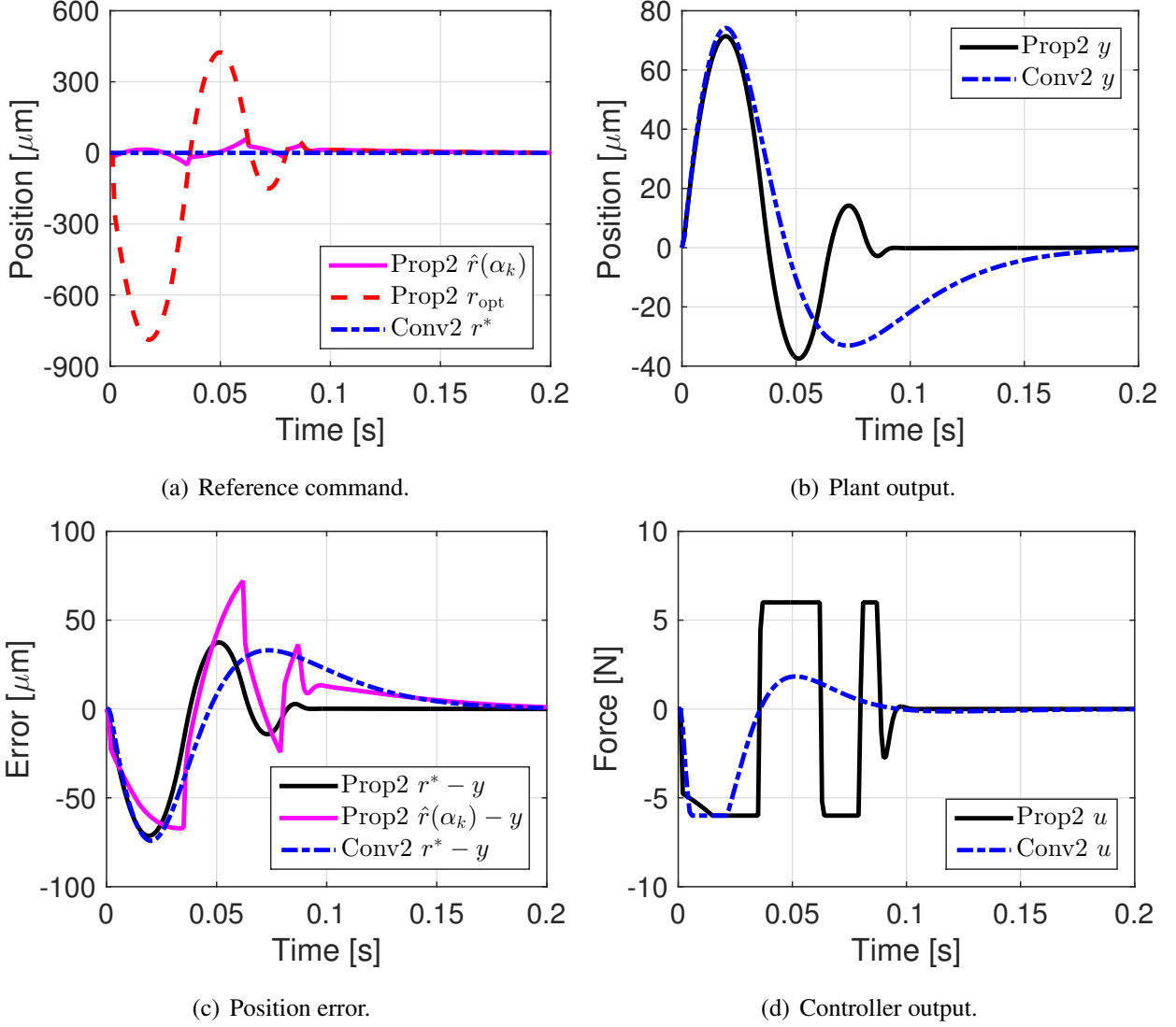


Fig. 31: Simulation results of disturbance suppression control by reference command modification based on RG.

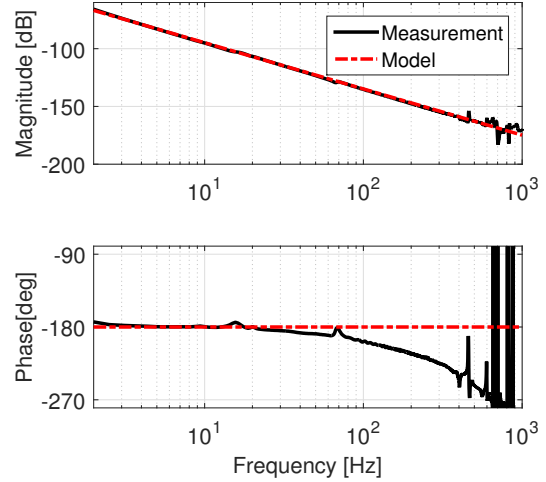
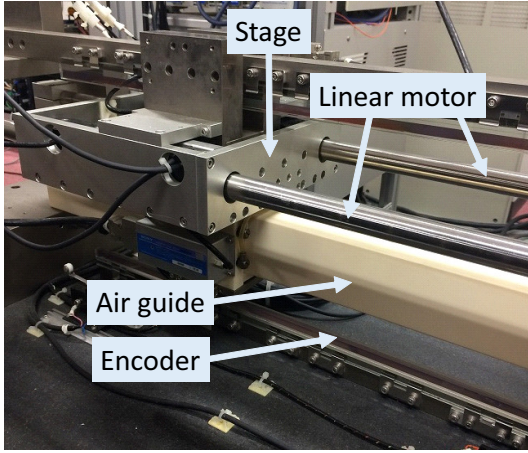
## 5.4 Verification of impulse disturbance suppression control by experiment

### 5.4.1 Experimental condition

This experiment uses a high precision stage shown in Fig. 32(a). This stage is guided by an air guide and driven by a linear motor. The position of the stage is measured by a linear encoder whose resolution is 1 nm and the velocity is the difference of the position. The frequency response of the stage is shown in Fig. 32(b). The plant model is defined as a rigid body model shown in (5-8) by fitting the frequency response data. The PID position controller is designed for the plant, so that the closed-loop bandwidth of the position loop can be 10 Hz. It is discretized by a Tustin transformation

Tab. 9: Four control methods compared in the experiment.

	Reference signal	Control method	Controller output constraints
Conventional 1	$r^*$	PID control	Not exist
Conventional 2	$r^*$	PID control with anti-windup [75]	Exist
Proposed 1	$r_{opt}$	PID control	Not exist
Proposed 2	$\hat{r}(\alpha_k)$	PID control	Exist



(a) Structure of the experimental stage.

(b) Frequency response of the experimental stage.

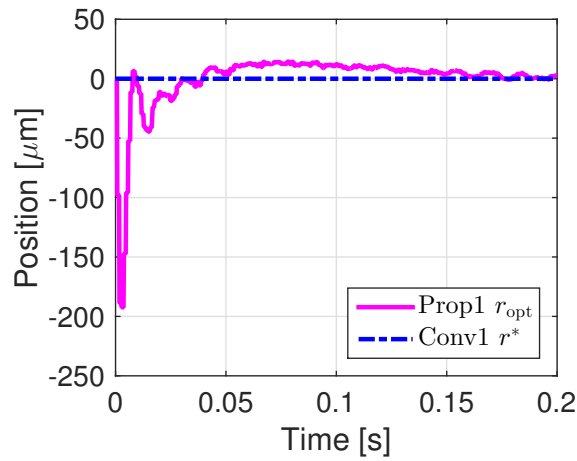
Fig. 32: Experimental stage.

with the control period of  $T_s = 1.0$  ms. The disturbance shown in (5-9) is added to the linear motor as software disturbance in the experiment.

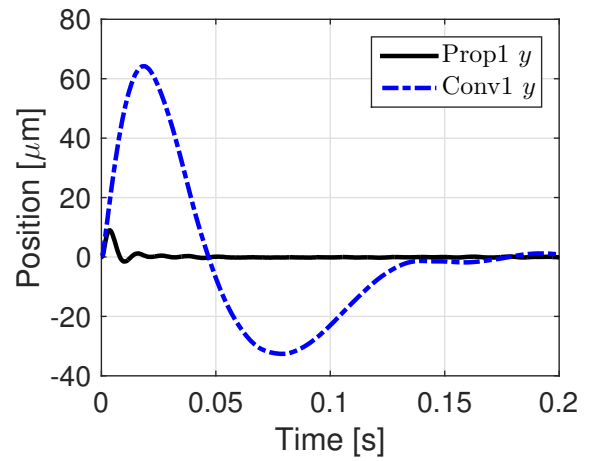
This experiment is compared with four methods as shown in Tab. 9. The limitation of the controller output is  $u_{lim} = 6.0$  N. In ‘‘Conventional 2’’, the controller output constraint  $u_{lim}$  is given on the source program. In ‘‘Proposed 2’’, however, note that the controller output constraint  $u_{lim}$  is considered only when MAS is generated and is not given on the source program.

## 5.4.2 Experimental results

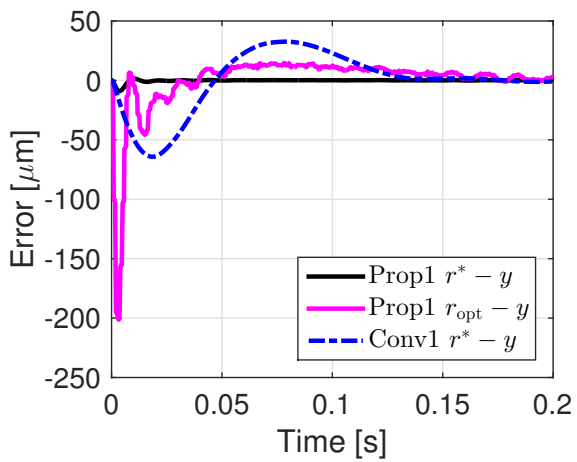
The result of comparison of ‘‘Conventional 1’’ and ‘‘Proposed 1’’ is shown in Fig. 33 and that of ‘‘Conventional 2’’ and ‘‘Proposed 2’’ is shown in Fig. 34. As shown in Fig. 33(b), the settling time of ‘‘Conventional 1’’ and ‘‘Proposed 1’’ are 198 ms and 17.1 ms, respectively. The disturbance suppression performance is also considerably improved in the experiment. Moreover, as shown in Fig. 34(b), the settling time of ‘‘Conventional 2’’ and ‘‘Proposed 2’’ are 167 ms and 112 ms, respectively. The disturbance suppression performance is improved within the constraints to modify the reference



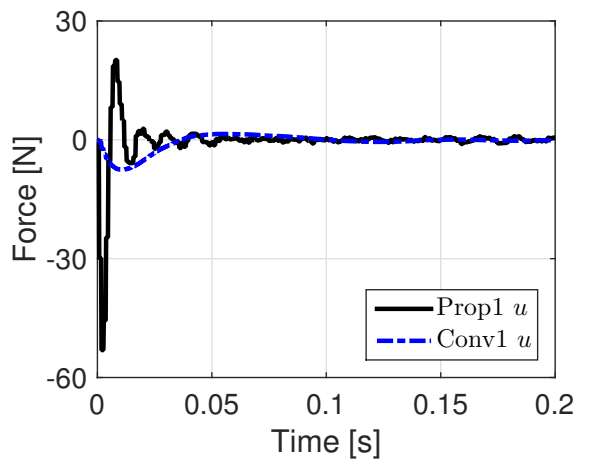
(a) Reference command.



(b) Plant output.



(c) Position error.

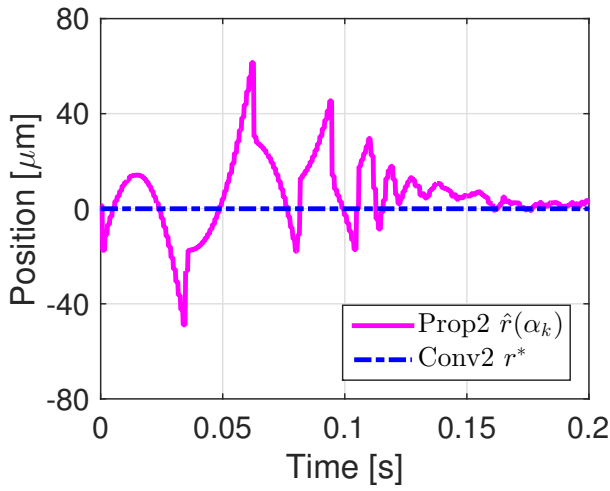


(d) Controller output.

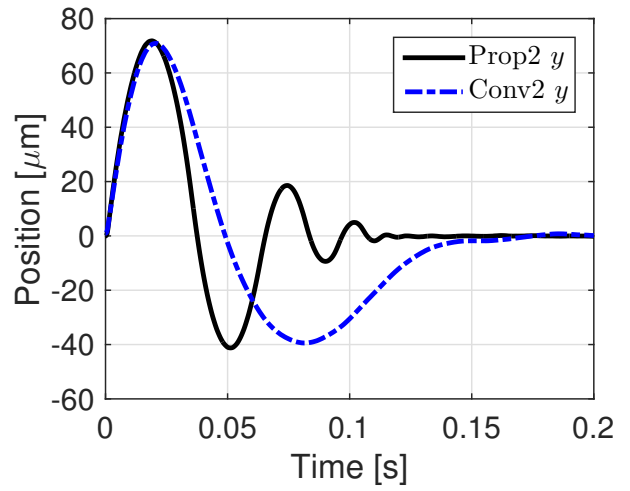
Fig. 33: Experimental results of disturbance suppression control by reference command modification based on MPC.

signal based on RG. From Fig. 34(d), it is found that RG can be calculated in real-time because the controller works within the constraint despite it being on the source program.

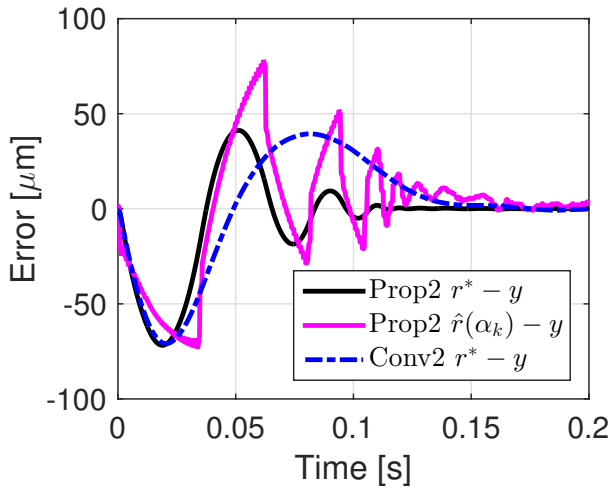




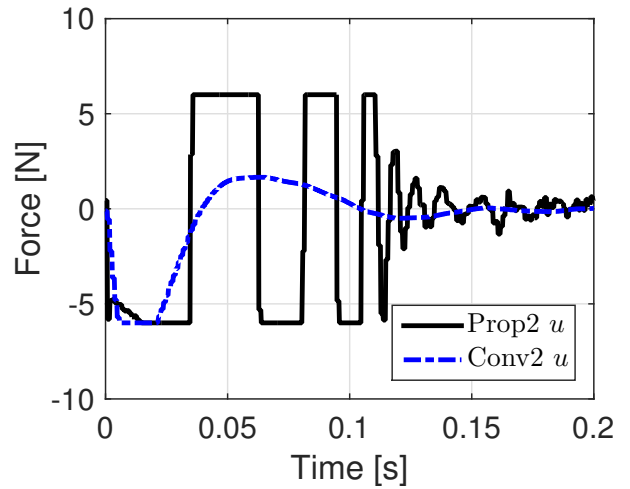
(a) Reference command.



(b) Plant output.



(c) Position error.



(d) Controller output.

Fig. 34: Experimental results of disturbance suppression control by reference command modification based on RG.

## 5.5 Comparison with reference modification method based on RG and the other control methods

The proposed method derives  $\hat{r}(\alpha_k)$  by RG to consider the constraints after calculating  $r_{\text{opt}}$  by using MPC without constraints. To modify the reference signal using constrained MPC is also conceivable for this method. Therefore, section 5.5.1 describes the performance of the reference shaping based on the constrained MPC and “Proposed 2” method.

It is also a natural idea to suppress the disturbance by using a disturbance observer when the disturbance is applied to the system. Section 5.5.2 compares the control system using the disturbance observer with “Proposed 1” method.

### 5.5.1 Reference modification method based on RG vs MPC with constraints

In this thesis, a control horizon is  $H_c$  and a prediction horizon is  $H_p$ , then  $r[i] = r$  ( $H_c \leq i \leq H_p$ ). From (5-3), (5-11), estimation values of output  $y$ , error  $e$ , and a variable to represent constraints  $z$  in the prediction horizon are summarized as follows:

$$\begin{aligned} Y &= M_{yx}x_0 + M_{yr}R, \\ E &= R^* - Y, \\ Z &= M_{zx}x_0 + M_{zr}R, \end{aligned} \tag{5-23}$$

where,  $Y$ ,  $R$ ,  $R^*$ ,  $E$ ,  $Z$  and  $M_{yx}$ ,  $M_{yr}$ ,  $M_{zx}$ ,  $M_{zr}$  are the matrix and lower triangular matrix given by

$$\begin{aligned} Y &= \begin{bmatrix} \hat{y}[0] \\ \hat{y}[1] \\ \hat{y}[2] \\ \vdots \\ \hat{y}[H_c] \\ \vdots \\ \hat{y}[H_p] \end{bmatrix}, \quad R = \begin{bmatrix} r[0] \\ r[1] \\ r[2] \\ \vdots \\ r \\ \vdots \\ r \end{bmatrix}, \quad R^* = \begin{bmatrix} r^* \\ r^* \\ r^* \\ \vdots \\ r^* \\ \vdots \\ r^* \end{bmatrix}, \quad E = \begin{bmatrix} \hat{e}[0] \\ \hat{e}[1] \\ \hat{e}[2] \\ \vdots \\ \hat{e}[H_c] \\ \vdots \\ \hat{e}[H_p] \end{bmatrix}, \quad Z = \begin{bmatrix} \hat{z}[0] \\ \hat{z}[1] \\ \hat{z}[2] \\ \vdots \\ \hat{z}[H_c] \\ \vdots \\ \hat{z}[H_p] \end{bmatrix}, \tag{5-24} \\ M_{yx} &= \begin{bmatrix} C \\ CA \\ CA^2 \\ \vdots \\ CA^{H_c} \\ \vdots \\ CA^{H_p} \end{bmatrix}, \quad M_{zx} = \begin{bmatrix} L \\ LA \\ LA^2 \\ \vdots \\ LA^{H_c} \\ \vdots \\ LA^{H_p} \end{bmatrix}, \tag{5-25} \end{aligned}$$

$$M_{yr} = \begin{bmatrix} 0 & 0 & \cdots & \cdots & \cdots & \cdots & 0 \\ \mathbf{CB} & 0 & \cdots & \cdots & \cdots & \cdots & 0 \\ \mathbf{CAB} & \mathbf{CB} & 0 & \cdots & \cdots & \cdots & 0 \\ \vdots & \vdots & \ddots & \ddots & \ddots & \ddots & \vdots \\ \mathbf{CA}^{H_c-1}\mathbf{B} & \mathbf{CA}^{H_c-2}\mathbf{B} & \cdots & \mathbf{CB} & \ddots & \ddots & \vdots \\ \vdots & \vdots & & & \ddots & \ddots & \vdots \\ \mathbf{CA}^{H_p-1}\mathbf{B} & \mathbf{CA}^{H_p-2}\mathbf{B} & \cdots & \cdots & \cdots & \mathbf{CB} & 0 \end{bmatrix}, \quad (5-26)$$

$$M_{zr} = \begin{bmatrix} \mathbf{D} & 0 & \cdots & \cdots & \cdots & \cdots & 0 \\ \mathbf{LB} & \mathbf{D} & \cdots & \cdots & \cdots & \cdots & 0 \\ \mathbf{LAB} & \mathbf{LB} & \mathbf{D} & \cdots & \cdots & \cdots & 0 \\ \vdots & \vdots & \ddots & \ddots & \ddots & \ddots & \vdots \\ \mathbf{LA}^{H_c-1}\mathbf{B} & \mathbf{LA}^{H_c-2}\mathbf{B} & \cdots & \mathbf{LB} & \ddots & \ddots & \vdots \\ \vdots & \vdots & & & \ddots & \ddots & \vdots \\ \mathbf{LA}^{H_p-1}\mathbf{B} & \mathbf{LA}^{H_p-2}\mathbf{B} & \cdots & \cdots & \cdots & \mathbf{LB} & \mathbf{D} \end{bmatrix} \quad (5-27)$$

Vector  $\mathbf{R}$  which has  $H_c + 1$  variables with  $r[0], \dots, r[H_c - 1], r$ . A cost function is defined as  $J = \mathbf{E}^T \mathbf{E}$  from (5-23), (5-12), and the reference signal  $r[0]$  is generated from  $\mathbf{R}_{\text{MPCopt}}$  which is an optimal solution calculated in every samples. This command value is expressed as  $r_{\text{MPCopt}}$  in this section. The optimization problem is solved by using a primal-dual interior point method by MATLAB ToolBox YALMIP [85]. Tab. 10 shows conditions of each method.

Simulation results are shown in Fig. 35 and Tab. 11.

Tab. 10: RG vs MPC.

	Reference signal	Predictive horizon $H_p$	Control horizon $H_c$
Proposed 2	$\hat{r}(\alpha_k)$	3	0
MPC 1	$r_{\text{MPCopt}}$	3	0
MPC 2	$r_{\text{MPCopt}}$	9	3

Tab. 11: RG vs MPC, Simulation results.

	Settling time	Calculation time
Proposed 2	89.2 ms	< 1.0 ms
MPC 1	–	320 ms
MPC 2	53.0 ms	184 ms

Comparing “Proposed 2” with “MPC 1”, only “Proposed 2” converged despite the prediction horizon and control horizons are equal. In “Proposed 2”, the horizon considering the constraint depends

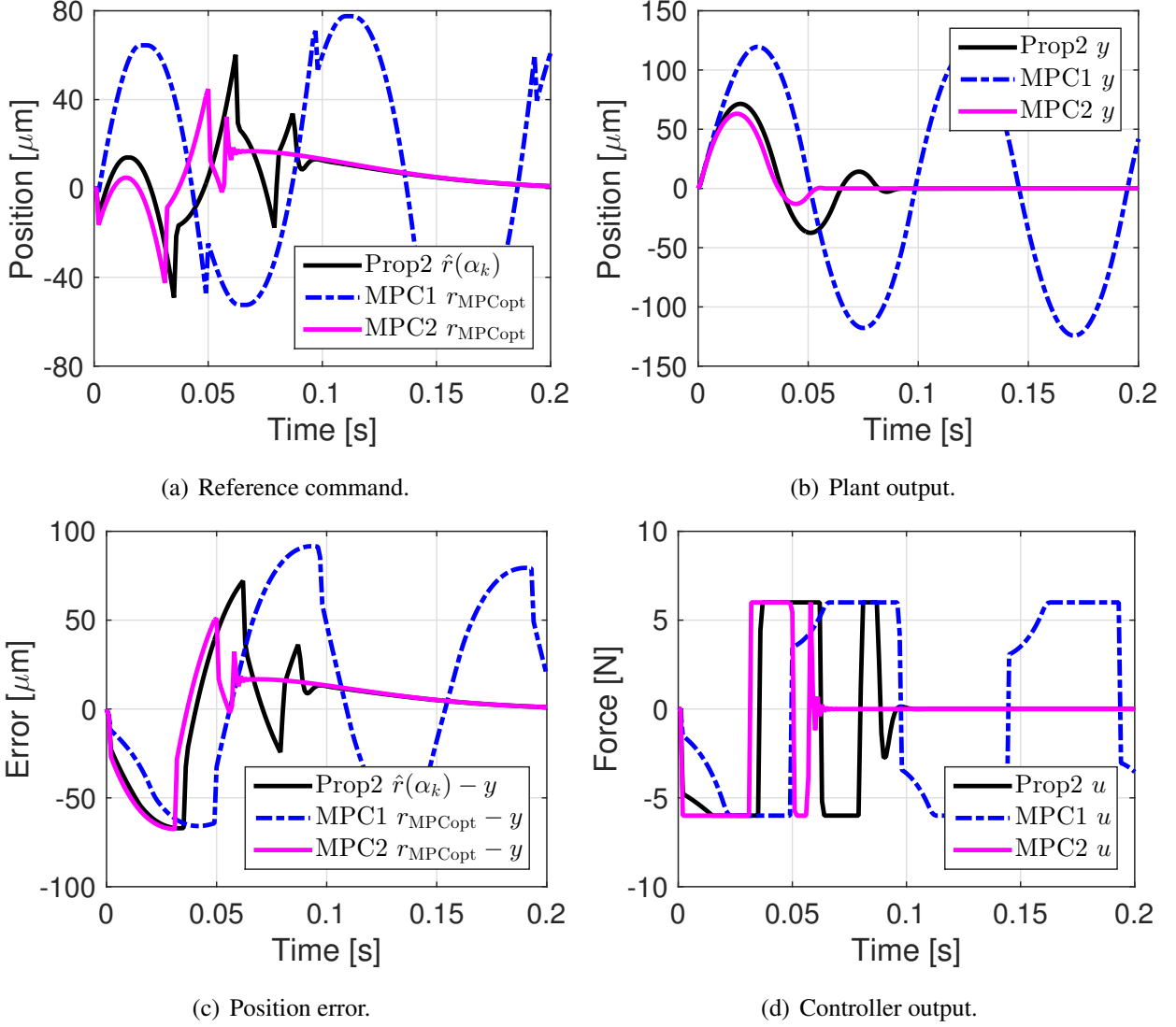


Fig. 35: Simulation results of disturbance suppression control by RG and MPC

on  $\kappa$ , not  $H_p$  because RG is applied after generating the command value by unconstrained MPC. The state of one sample ahead is enough to satisfy the constraint in this system because  $\kappa = 1$ , however, the normal MPC considers the constraint by  $H_p$ . In this case, “MPC 1” considers constraints that do not have to consider because  $H_p > \kappa$ . Thus the system diverges in “MPC 1” which derives a conservative reference signal because of the severe constraints.

However, MPC can freely determine the control horizon while RG needs to assume the command value to be constant within the prediction horizon. Therefore, it is expected that the control performance in the case of using the constrained MPC is higher than that of using RG because the degree of freedom is larger than RG in MPC. In fact, when comparing “Proposed 2” and “MPC 2”, the settling time is 89.2 ms, 53.0 ms respectively, so “MPC 2” has higher disturbance suppression performance. On the other hand, calculation cost of “MPC 2” is much higher than “Proposed 2”: calculation time of “MPC 2” is 184 ms and that of “Proposed 2” is less than 1.0 ms. Therefore, control methods should be selected according to computing resources.

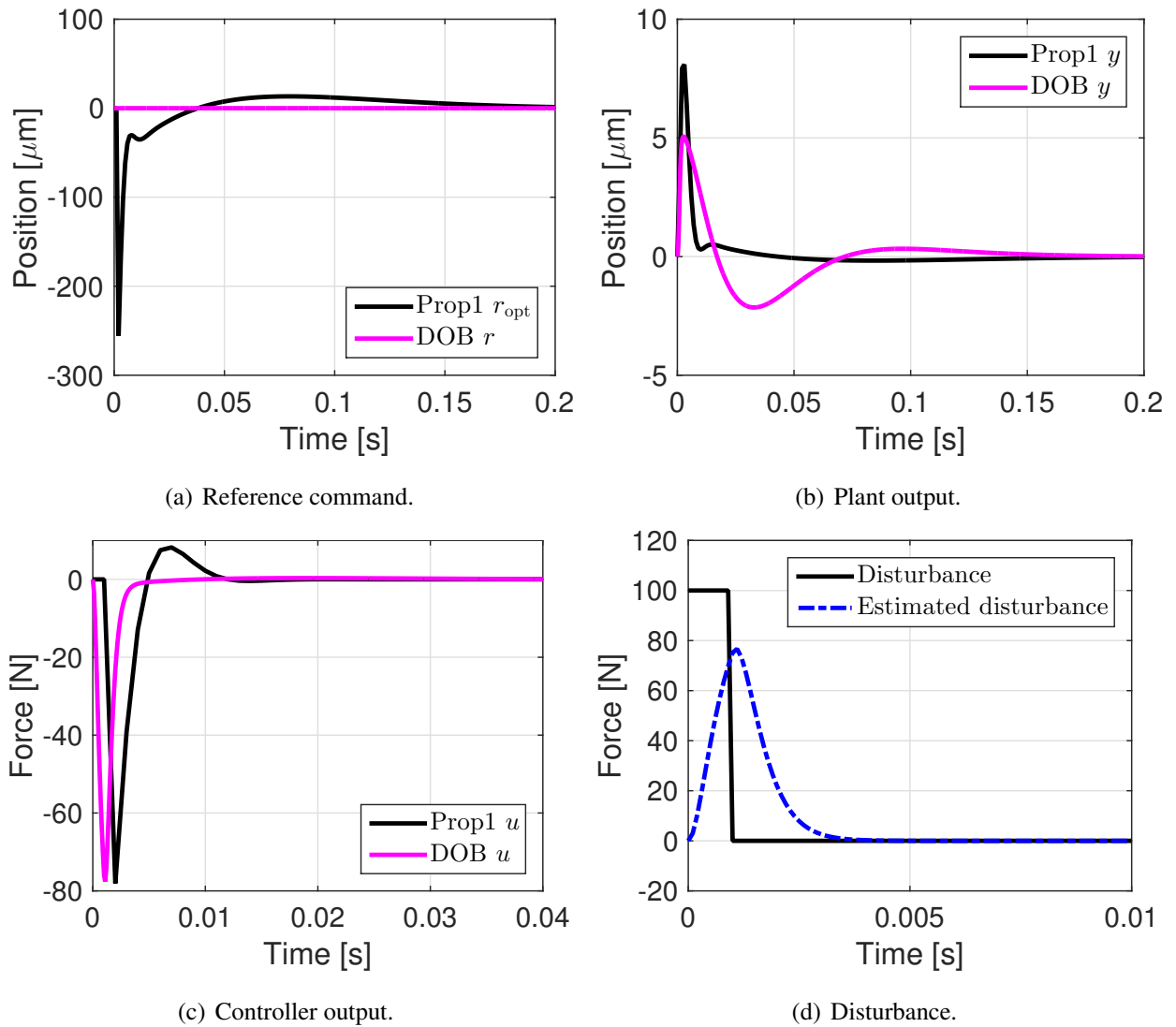


Fig. 36: Simulation results of disturbance suppression control by MPC and DOB

### 5.5.2 Reference modification method based on MPC without constraints vs disturbance observer

This section compares the disturbance suppression performance of “Proposed 1” and that of DOB. The maximum output of each controller is matched by setting a cut-off frequency of LPF in DOB at 430 Hz. The simulation results are shown in Fig. 36 and Tab. 12.

DOB is superior than “Proposed 1” in the maximum error, however, “Proposed 1” is better than DOB in the settling time. The relation between the plant output and the command value satisfies (5-1) in DOB because DOB has the property of Integral control. Thus the settling time of DOB is longer than that of “Proposed 1”. In practice, the cut-off frequency of the LPF used in DOB is lower. Then the disturbance suppression performance of DOB degrades because DOB can not estimate impulse disturbance sufficiently. Therefore, “Proposed 1” is better control method than DOB to suppress the impulse disturbance.

Tab. 12: Prop1 vs DOB, Simulation results.

	Settling time	Maximum error
Proposed 1	7.49 ms	8.1 $\mu$ S
DOB	53.1 ms	5.1 $\mu$ S

## 5.6 Conclusion of sudden disturbance suppression control considering with constraints

This chapter shows that the impulse input disturbance response is improved by modifying the reference signals properly. Next, this chapter proposes the disturbance suppression control based on RG considering the controller output constraint. Finally, the effectiveness of the proposed methods is demonstrated by experiments. This paper focuses on the disturbance suppression performance that has not been discussed in the previous studies of RG and makes it possible to modify the reference signal in response to the disturbance. Unexpected disturbances with large amplitudes can be suppressed by an extension of the proposed method. The verification of the robustness to modeling errors and of the relationship between the magnitude of disturbance and the number of steps  $\kappa$  to generate MAS will be discussed in future works.

## **PartII**

### **Wireless High-Precision Stage**

# Chapter 6

## High-precision stage using wireless power transfer

### 6.1 Background of Wireless High-Precision Stage (WHPS)

In chapter 1, this thesis classifies the causes of tracking error and mentions that the cable disturbance is the final problem to be solved in the high-precision stage. To address this issues, we designed a high-precision stage with a moving coil wireless linear motor (Wireless High Precision Stage : WHPS) [109]. Conventional high-precision stages require an electrical power supply as shown in Fig. 37(a), and so the effect of cable disturbance cannot be avoided. On the other hand, WHPS avoids the cable disturbance by sending the electrical power wirelessly to actuators and sensors. The merits of WHPS are shown as follows:

- WHPS solves the cable disturbance drastically.
- The control performance of WHPS can be improved by increasing the number of sensors because of increasing space of the stage.
- The control performance of WHPS can be improved by lightening of actuator.
- Work period is reduced because WHPS has less cables.
- Cleanrooms are classified according to the number and size of particles permitted per volume of air shown in Tab. 13. In the high-precision stage used in the semiconductor or FPD manufacturing, a cleanroom needs to satisfy "Class 10–1,000". To achieve cleanliness, contamination arising from sliding parts such as cable carriers in the coarse part is problem. WPT solves this problem to reduce the cable carriers.



Tab. 13: Cleanroom classification.

Class	Maximum particles [ $1/m^3$ ]						FED STD 209E equivalent
	$\geq 0.1 \mu m$	$\geq 0.2 \mu m$	$\geq 0.3 \mu m$	$\geq 0.5 \mu m$	$\geq 1.0 \mu m$	$\geq 5.0 \mu m$	
ISO 1	10						
ISO 2	100	24	10				
ISO 3	1,000	237	102	35			Class 1
ISO 4	10,000	2,370	1,020	352	83		Class 10
ISO 5	100,000	23,700	10,200	3,520	832		Class 100
ISO 6	1,000,000	237,000	102,000	35,200	8,320	293	Class 1,000
ISO 7				352,000	83,200	2,930	Class 10,000
ISO 8				3,520,000	832,000	29,300	Class 100,000
ISO 0				35,200,000	8,320,000	293,000	Room air

We designed and produced two WHPSs shown in following sections. One is the single-axis WHPS, and the other is the multi-axis WHPS. The mechanical structures and electrical circuits of these stages will be introduced.

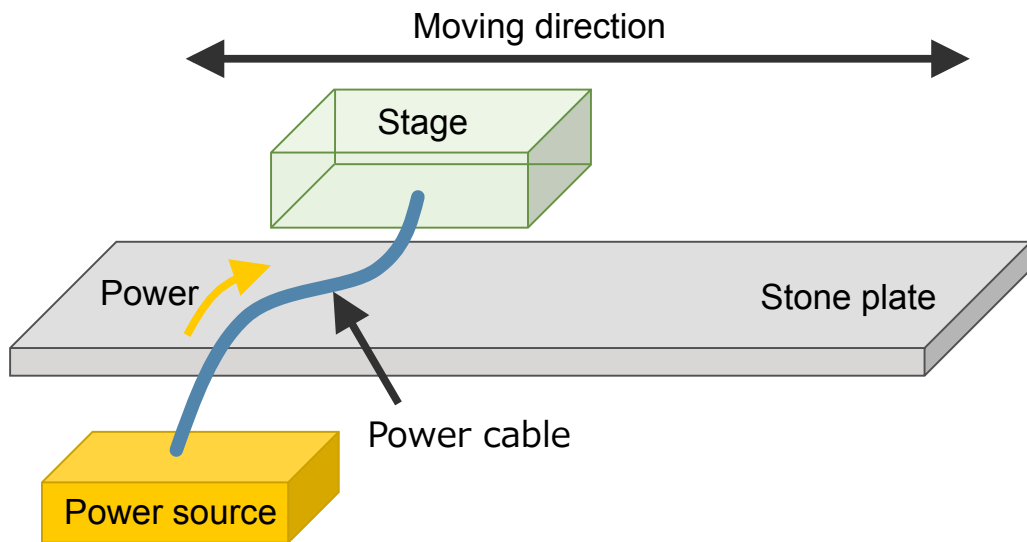
## 6.2 Single-axis high precision stage using a moving coil wireless linear motor (WHPS1)

### 6.2.1 Mechanical structure for WHPS1

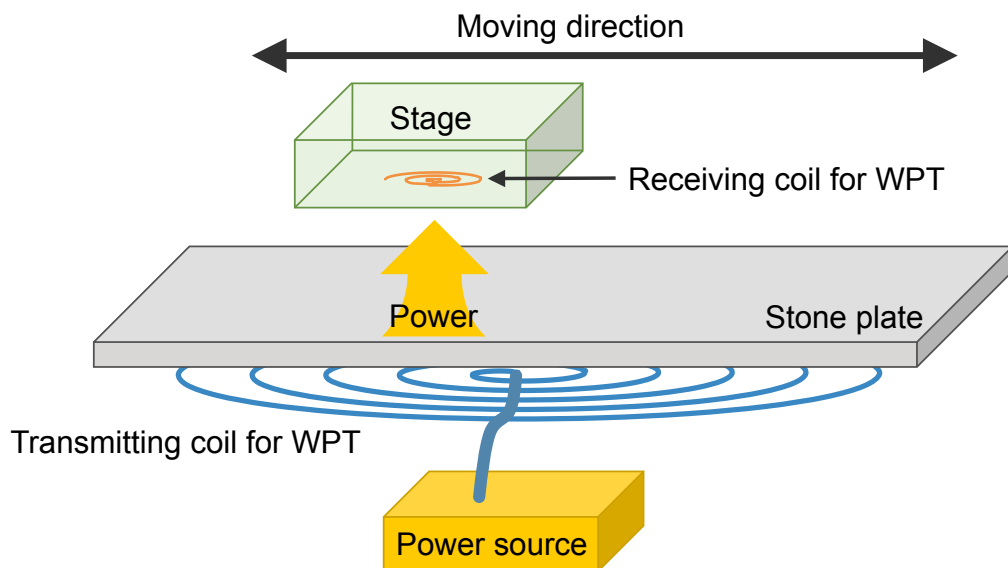
The structure of the single-axis WHPS is shown in Fig. 38. WHPS1 is guided by a busher and driven by a linear motor. The position of the stage is measured by a linear incremental encoder whose resolution is  $0.5 \mu m$  (HEIDENHAIN : LIDA27). A coil to receive power wirelessly, an electrical circuit to control transmission power and DC voltage, and a motor driver are on the stage. In addition, an influence of a cable can be measured by attaching a cable carrier to the stage. In parallel with the guide of the stage, a coil to transmit power wirelessly is arranged, and the gap between the transmission and the receiving coils can be adjusted.

### 6.2.2 Circuit structure for WHPS1

Electrical diagrams of Fig. 49 are shown in Fig. 39(a) and Fig. 39(b). In Fig. 39(a), the power is supplied from the power source via the power cable, and the linear motor receives the power through the smoothing capacitor and the motor driver. Thus, the cable disturbance cannot be avoided. In Fig. 39(b), the power is transmitted from the transmission coil to the receiving coil and is converted to DC through the rectifier circuit. After that, the linear motor receives the power through the smoothing



(a) Conventional high precision stage.



(b) High precision stage with wireless power transfer

Fig. 37: Conceptual diagram of the high precision stage with wireless power transfer.

capacitor and the motor driver. Thus, there are no cable disturbance because the power cable is not connected to the receiving side from the outside. In Fig. 39(b),  $R$  is a resistance of the coil,  $L$  is the self-inductance of the coil,  $L_m$  is a mutual inductance,  $V$  and  $I$  is a voltage and current, and  $I_{dc}$  is a current in the motor driver.

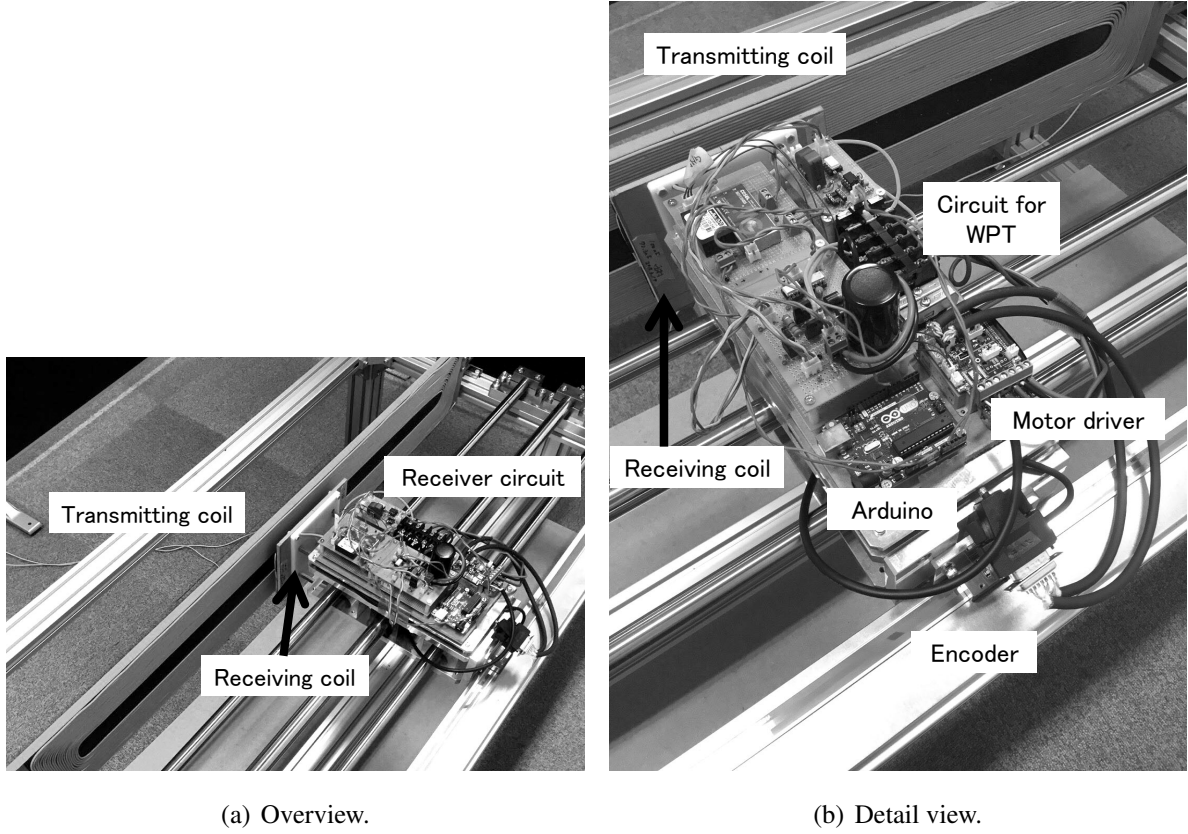


Fig. 38: Experimental high precision stage with moving coil wireless linear motor.

## 6.3 Wireless multi-axis high precision stage (WHPS2)

### 6.3.1 Mechanical structure of the WHPS2

The structure of WHPS2 is shown in Fig. 43(a). WHPS2 has two coarse stages whose axes are orthogonal to each other and one fine stage. The coarse stages are driven by linear motors and the fine stage is driven by a voice coil motor. Each stage is guided by an air guide. The position of each stage is measured by a linear encoder with 1 nm resolution.

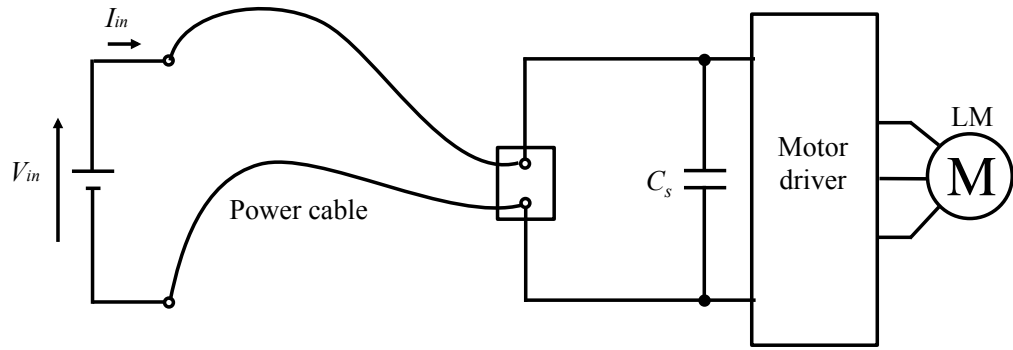
Fig. 66 shows the bode diagrams of the stages.

$$P(s) = \frac{1}{Ms^2 + Ds} \cdot \frac{s^2 + 2\xi_{ar}\omega_{ar} + \omega_{ar}^2}{s^2 + 2\xi_r\omega_r + \omega_r^2} \quad (6-1)$$

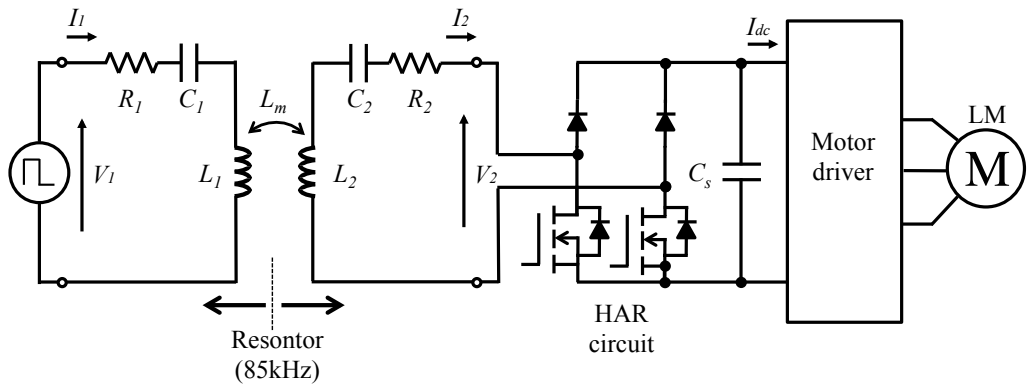
The mechanical parameters are identified shown in Tab. 14 by fitting the models to experimental data.

### 6.3.2 Circuit structure for WHPS2

The overall circuit diagram is shown in Fig. 44(a). A rectangular wave is generated from a direct current voltage source by operating the inverter at a predetermined resonance frequency. In this study, the inverter on the transmission side of each axis is designed to give a rectangular wave of 85 kHz



(a) Conventional stage using power cable.



(b) Proposed stage using WPT.

Fig. 39: Electrical circuit diagram of a wired stage and the stage using WPT.

with a duty ratio of 0.5. Generally speaking, the size of coil becomes smaller when the resonance frequency is higher, so this stage does not need to persist the frequency of 85 kHz. However, this stage uses 85 kHz because the resonance frequency should be up to 100 kHz from the point of view of SiC performance and the WPT device for EV is developing at 85 kHz. Next, WPT is performed for the Y-axis coarse stage, and the power is smoothed on the receiving side to convert it into a DC voltage  $V_{DCY}$ , which is applied to the Y-axis motor driver.  $V_{DCY}$  is used as the power transmission side voltage on the X-axis and converted to a rectangular wave by the inverter. Then, WPT is performed for the X-axis coarse and fine stages, and smoothed on the X-axis receiving side before being converted to DC voltage  $V_{DCX}$  and applied to the X-axis motor driver. In addition, FPGA is used to control voltage and power fast, and Arduino transmits important information wirelessly, for example voltage, turn on signal, and so on. The characteristics of power flow of WHPS2 is the primary voltage of X-axis is provided from secondary voltage of Y-axis. Thus, multistage wireless power transfer is required. The control strategy of WHPS2 will be discussed in chapter 9.

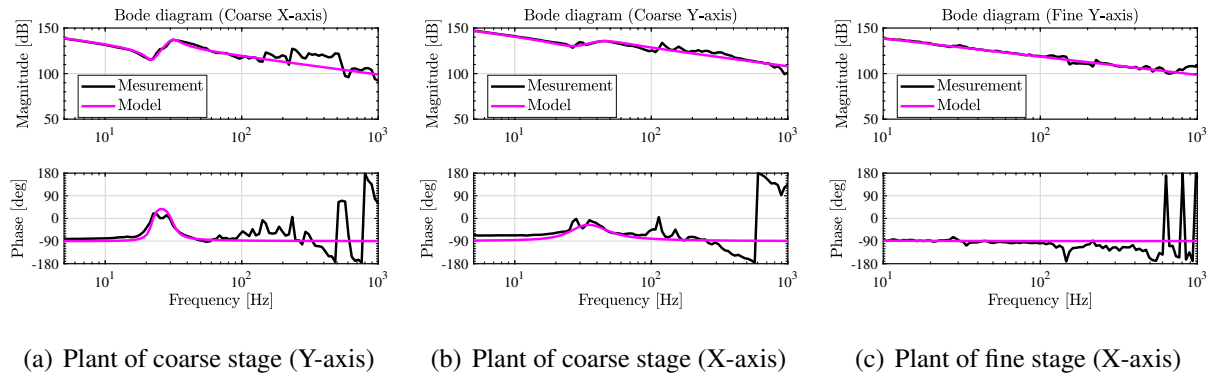


Fig. 40: Frequency response of the system.

Tab. 14: Mechanical parameter.

Name	Unit	Symbol	Coarse (X-axis)	Coarse (Y-axis)	Fine (Y-axis)
Mass	kg	$M$	40	16	3
Coefficiente of viscosity	$m^2/s$	$D$	125	125	0.0
Anti-Resonance frequency	Hz	$\omega_{ar}$	22	28	–
Damping coefficient of anti-resonance	–	$\xi_{ar}$	0.07	0.3	–
Resonance frequency	Hz	$\omega_r$	31	42	–
Damping coefficient of resonance	–	$\xi_r$	0.1	0.35	–

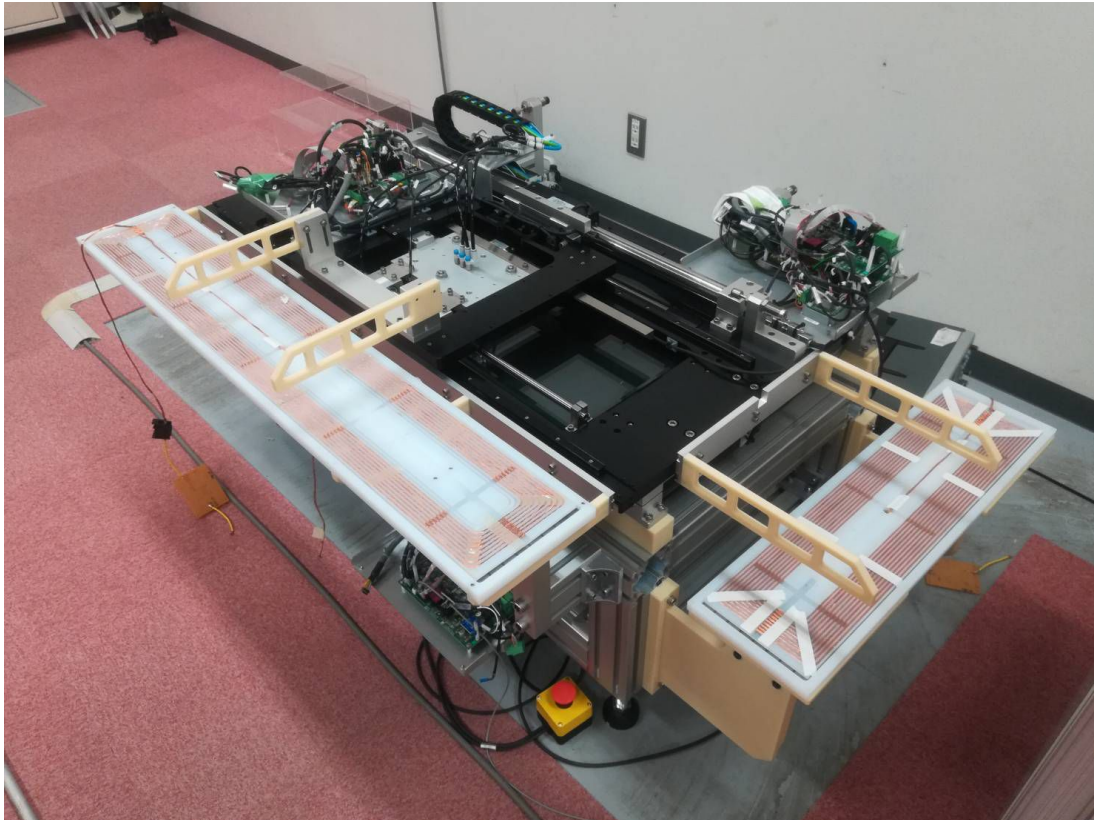
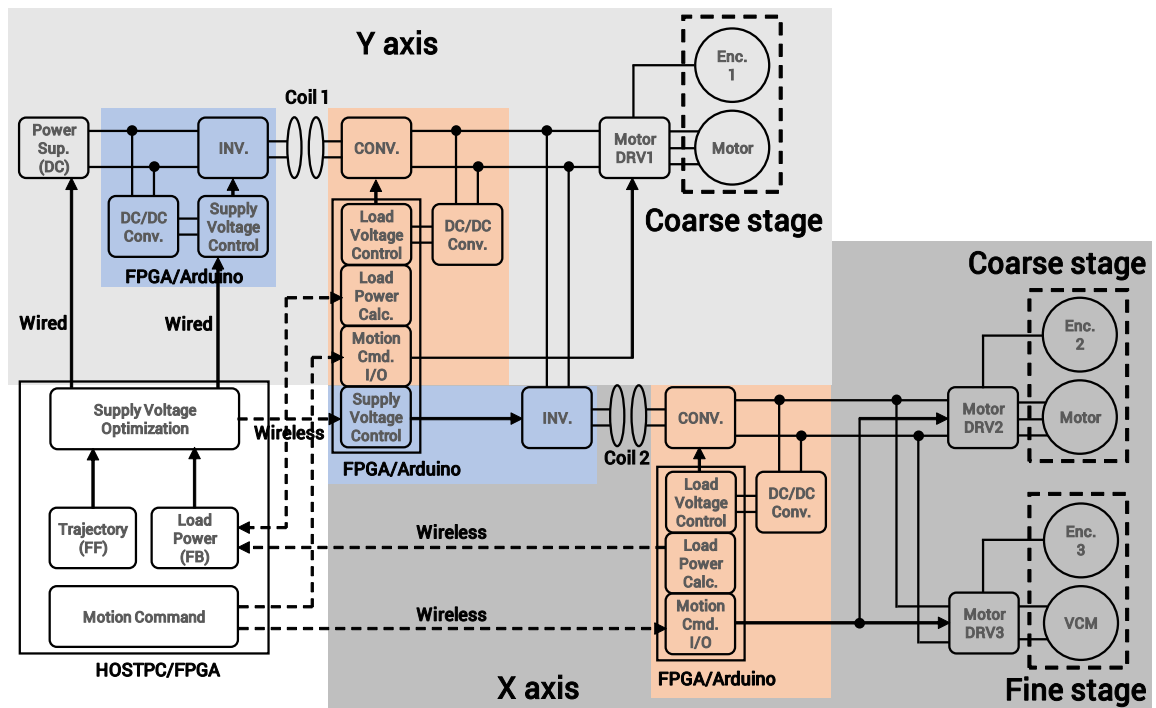
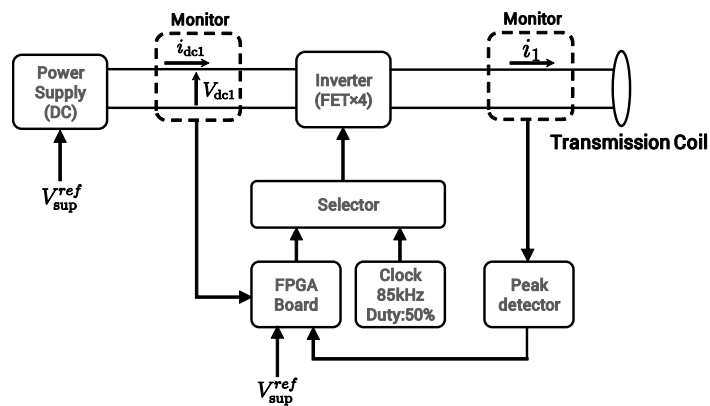


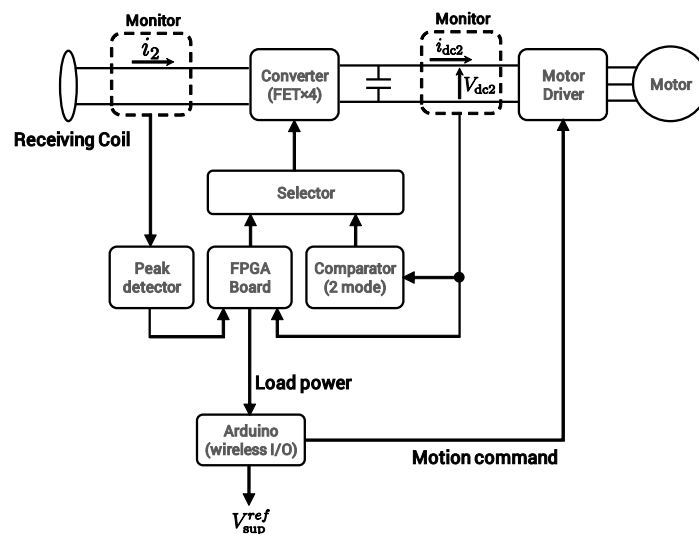
Fig. 41: Experimental setup.



(a) Whole system of WHPS2.

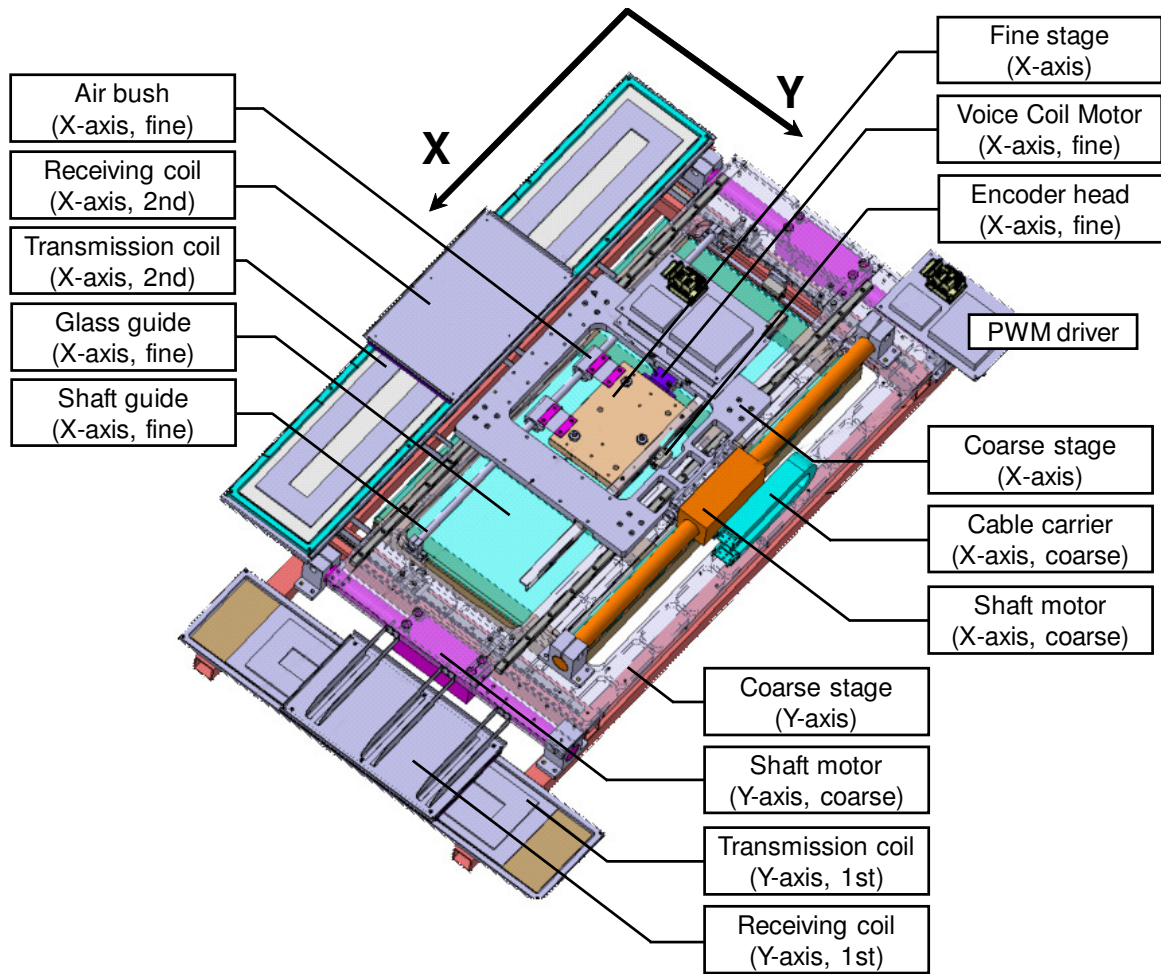


(b) Primary circuit

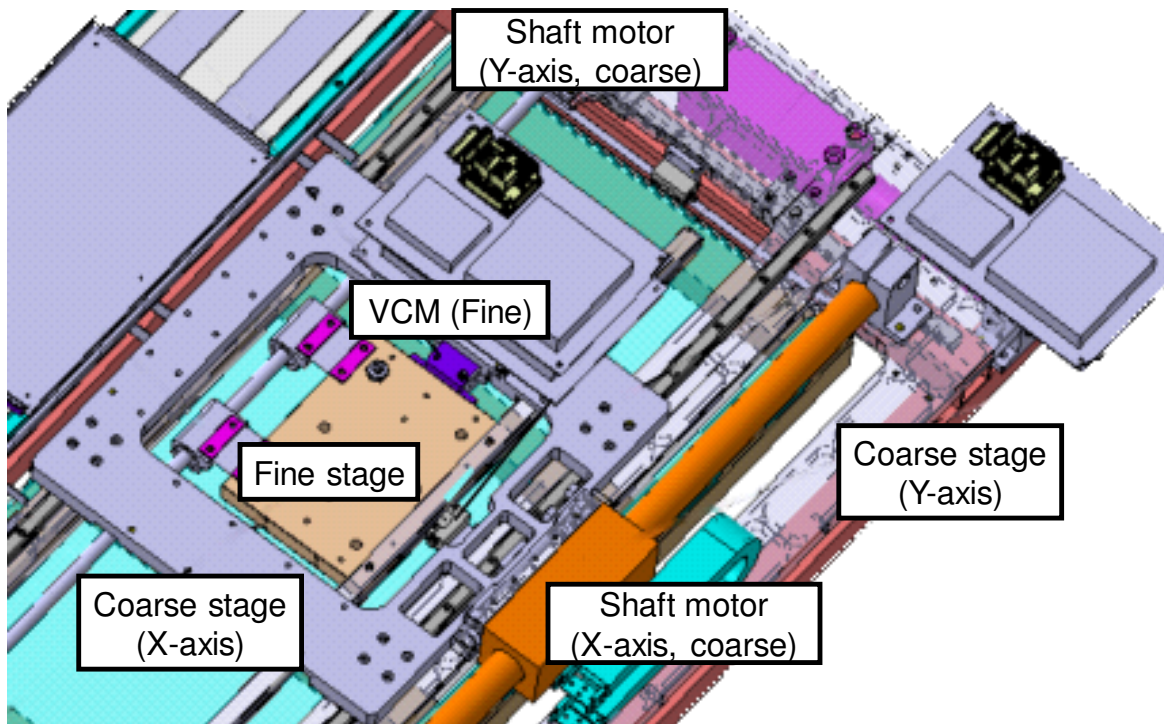


(c) Secondary circuit

Fig. 42: Schematic diagrams of WHPS2 system.

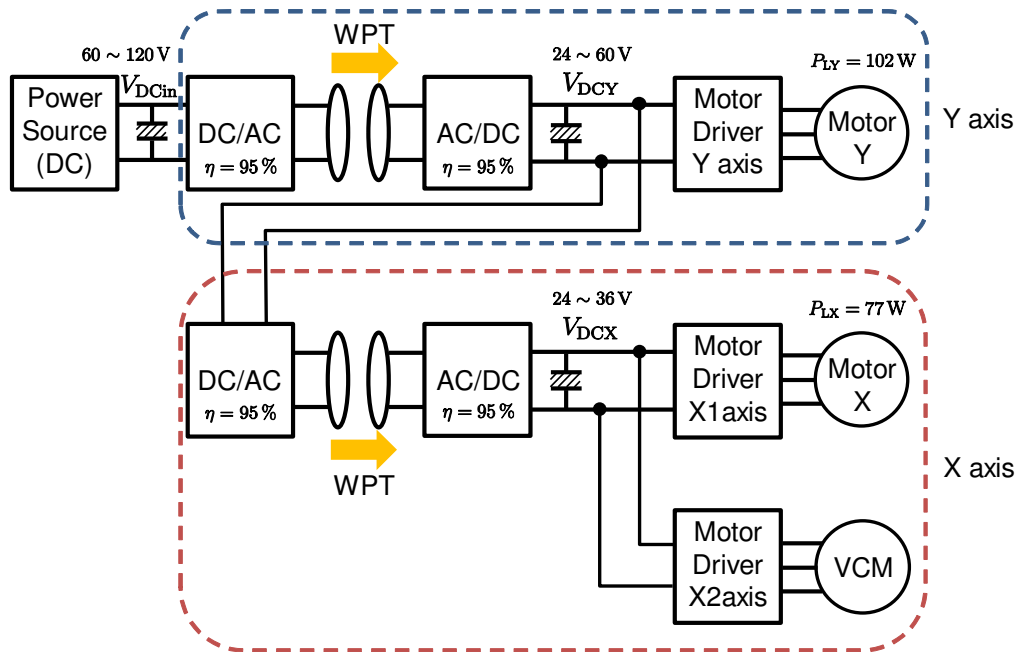


(a) Schematic diagram of WHPS2

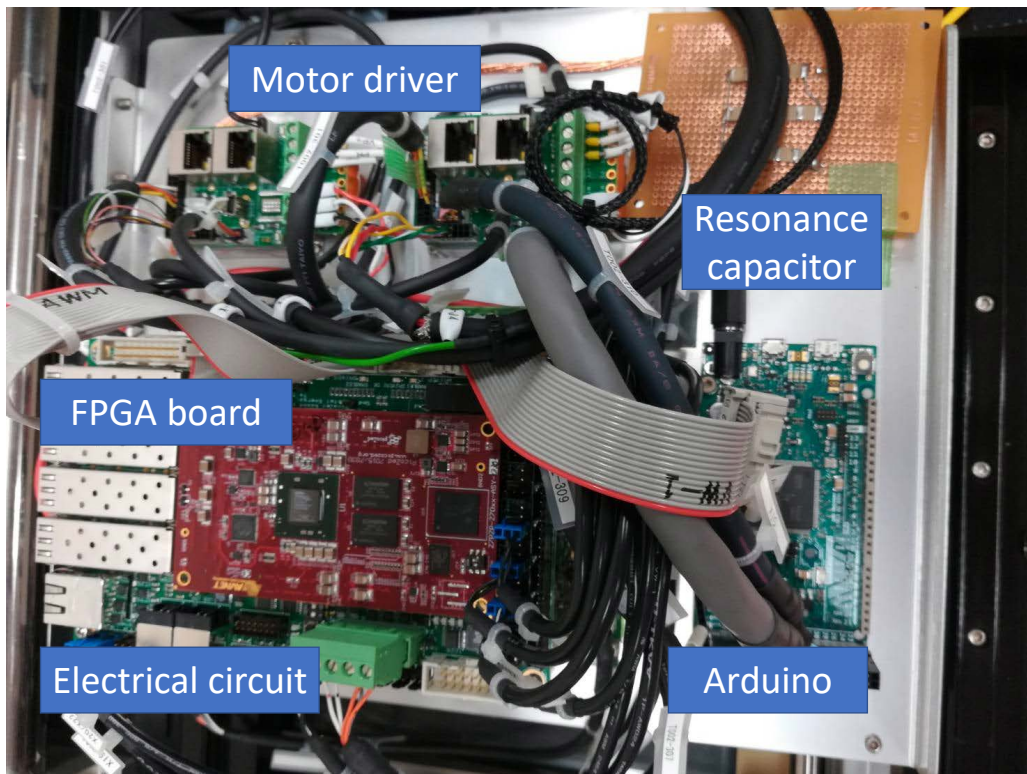


(b) Detail view around fine stage.

Fig. 43: 3D CAD model of WHPS2.



(a) Simplified electrical circuit of WHPS2.



(b) View of electrical circuit of WHPS2

Fig. 44: Electrical circuit of WHPS2.



# Chapter 7

## Coil design method for wireless power transfer considering required specifications

### 7.1 Importance of coil design for wireless power transfer

In recent years, wireless power transfer (WPT) is applied to many applications : a dynamic wireless charging system for electric vehicles (EVs), high-precision stage, robot. [110, 111, 112]. Magnetic resonance coupling of WPT has attracted attention with its long-distance and highly efficient power transmission compared with electromagnetic induction of WPT. In this method, it is necessary to equalize the resonance frequencies of the transmission and receiving sides by using a resonance capacitor.

For industrial applications, machine and circuit design specifications are often given in advance. Therefore, a coil design method that satisfy those specifications is necessary in order to apply WPT to the industrial applications. In WPT, transmission power, efficiency, direct current (DC) voltage in transmission/receiving side, etc, are used as an index for coil design, however, the coil design is performed empirically and there are few studies on theoretical design methods.

Noda, Nagashima, and Sekiya proposed the coil and power converter design method to achieve the maximum efficiency [113]. However, this method considers only the efficiency and the result is a suboptimal solution because design variables are discrete values and these are selected to maximize the efficiency. Furthermore, a solid wire is used as a wire material because they studies wireless power transmission in the MHz band. The resonance frequency of WPT used in electrical vehicle is defined at 85 kHz, and it is known that a litz wire is suitable to achieve the high efficiency because the resistance of it is smaller than that of the solid wire at the frequency.

Bosshard and Kolar proposed a coil design method considering with the efficiency, transmission power, etc [114]. In this method, the coil is designed based on the electromagnetic field analysis by the finite element method, however, this method takes long time to determine the coil parameters

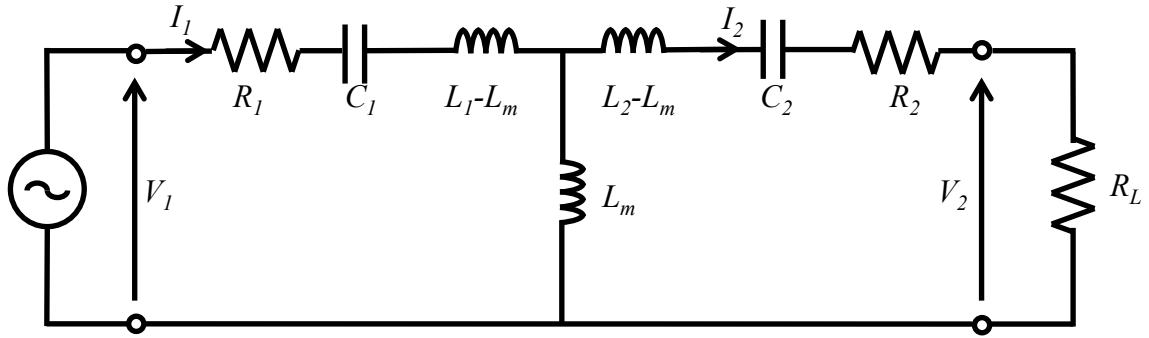


Fig. 45: Equivalent circuit of magnetic resonant coupling.

because a very large amount of electromagnetic field analysis is necessary. In addition, the result is a suboptimal solution because the coil parameters are discrete values. Furthermore, this method uses the theoretical formula to calculate alternating current (AC) resistance of the litz wire, however, The analytical solution often differs from the measured value, so the produced coil may be greatly deviated from the designed value.

A simple coil design method considering with required specifications is important to apply WPT in many applications. Therefore, this chapter proposes a coil design method considering efficiency, transmission power, and transmission/receiving side voltage. In section 7.2, we introduce power transmission characteristics in wireless power transmission system with magnetic field resonance coupling and formulate the optimization problem to solve in coil design. Next, in section 7.3, the calculation method of mutual inductance of the coil will be described. Furthermore, section 7.4 will describe how to calculate the AC resistance of the coil. Then, a comparison with two cases of a solid wire and a litz wire will be performed. Finally, we will design the coil satisfying the required specifications by solving the optimization problem based on the results of section 7.3 and 7.4.

## 7.2 Wireless power transfer using magnetic resonance coupling

### 7.2.1 Power Transmission Characteristics in Wireless Power Transmission System with Magnetic Field Resonant Coupling Method

Several circuit topology are known how to insert the resonant capacitor [115, 116]. This paper adopts a series-series (SS) system in which the resonance capacitor and the coil are connected in series because a regeneration can be easily performed from the symmetry of the circuit in this system. Fig. 45 shows an equivalent circuit of a series-series system, which is a system in which a coil and a capacitor are connected in series on both transmission and receiving sides. Here,  $R$  is a coil resistance,  $L$  is a coil inductance,  $C$  is a capacitance of the resonance capacitor,  $R_{ac}$  is an equivalent load

resistance,  $L_m$  is the mutual inductance, and the subscripts 1 and 2 represent the transmission side and the receiving side, respectively. In the magnetic resonance coupling system, the resonance frequency  $\omega_0$  is determined by the following equation using the inductance of both coils and the resonance capacitors.

$$\omega_0 = \frac{1}{\sqrt{L_1 C_1}} = \frac{1}{\sqrt{L_2 C_2}} \quad (7-1)$$

Then, from Fig. 45, the transmission power  $P_{ac}$ , the transmission efficiency  $\eta$ , and the voltage ratio for WPT are, respectively, given as follows:

$$P_{ac} = \frac{(\omega_0 L_m)^2 R_{ac}}{(R_1(R_2 + R_{ac}) + (\omega_0 L_m)^2)^2} V_1^2 \quad (7-2)$$

$$\eta = \frac{(\omega_0 L_m)^2 R_{ac}}{(R_2 + R_{ac})(R_1 R_{ac} + R_1 R_2 + (\omega_0 L_m)^2)} \quad (7-3)$$

$$A_v = \frac{\omega_0 L_m R_{ac}}{R_1 R_{ac} + R_1 R_2 + (\omega_0 L_m)^2} \quad (7-4)$$

The condition maximizing the efficiency is when the equivalent load resistance  $R_{ac}$  satisfies the following equation.

$$\frac{\partial \eta}{\partial R_{ac}} = 0 \Leftrightarrow R_{ac\eta_{max}} = \sqrt{R_2^2 + \frac{R_2(\omega_0 L_m)^2}{R_1}} \quad (7-5)$$

Then, the transmission power, efficiency, and voltage ratio are represented, respectively, by

$$P_{ac} = \frac{\sqrt{(R_1 R_2)^2 + R_1 R_2 (\omega_0 L_m)^2} (\omega_0 L_m)^2}{\left( (\omega_0 L_m)^2 + R_1 R_2 + \sqrt{(R_1 R_2)^2 + R_1 R_2 (\omega_0 L_m)^2} \right)^2} \frac{V_1^2}{R_1} \quad (7-6)$$

$$\eta = \frac{(\omega_0 L_m)^2}{\left( \sqrt{R_1 R_2} + \sqrt{R_1 R_2 + (\omega_0 L_m)^2} \right)^2} \quad (7-7)$$

$$A_v = \sqrt{\frac{R_2}{R_1}} \frac{\omega_0 L_m}{\sqrt{R_1 R_2} + \sqrt{R_1 R_2 + (\omega_0 L_m)^2}} \quad (7-8)$$

This thesis assumes that the system is operated at the maximum efficiency point, so (7-6), (7-7), and (7-8) are used for analysis. Note that the transmission power, efficiency, and voltage ratio are thus calculated from the resistance of the transmitting and receiving coils  $R_1$ ,  $R_2$ , mutual inductance  $L_m$ , and power transmission side voltage  $V_1$ .

## 7.2.2 Formulation of coil design problem

As described above, coils must be designed to support required specifications such as the transmission power, efficiency, and the receiving-side voltage. The coil design problem can be expressed as follows. As described above, coils must be designed to support required specifications such as

the transmission power, efficiency, and the receiving-side voltage. The coil design problem can be expressed as follows:

Minimize (Maximize)

$$f(R_1, R_2, L_m, V_{y1}), \quad (7-9a)$$

subject to

$$\eta_y \geq \eta_{ylim}, \quad (7-9b)$$

$$\eta_x \geq \eta_{xlim}, \quad (7-9c)$$

$$P_{acy} \geq P_{acylim}, \quad (7-9d)$$

$$P_{acx} \geq P_{acxlim}, \quad (7-9e)$$

$$V_{y2lowlim} \leq V_{DCy} \leq V_{y2uplim}, \quad (7-9f)$$

$$V_{x2lowlim} \leq V_{DCx} \leq V_{x2uplim}. \quad (7-9g)$$

Here, (7-9a) and (7-9b) are efficiency constraints, (7-9c) and (7-9d) are transmission power constraints, and (7-9f) and (7-9g) are receiving-side voltage constraints. Also,  $P_{lim}$ ,  $\eta_{lim}$  are, respectively, the required transmission power and efficiency, and  $V_{lowlim}$ ,  $V_{uplim}$  are, respectively, the upper and lower limits of the receiving-side voltage.

From (7-6), (7-7), (7-8), the transmission power, efficiency, and receiving-side voltage are functions of  $R_1$ ,  $R_2$ ,  $L_m$ , and  $V_1$ , so the above problem is an optimization problem with variables of  $R_1$ ,  $R_2$ ,  $L_m$ , and  $V_{y1}$ . However,  $R_1$ ,  $R_2$ ,  $L_m$  are unfortunately not independent of each other because they are determined by the shape of the coils and the distance between the transmission and receiving coils. These relationships are explained in later sections.

From (7-6), (7-7), (7-8), the transmission power, efficiency, and receiving-side voltage are functions of  $R_1$ ,  $R_2$ ,  $L_m$ , and  $V_1$ , so the above problem is an optimization problem with variables of  $R_1$ ,  $R_2$ ,  $L_m$ , and  $V_{y1}$ . However,  $R_1$ ,  $R_2$ ,  $L_m$  are unfortunately not independent of each other because they are determined by the shape of the coils and the distance between the transmission and receiving coils.

## 7.3 Modeling of mutual inductance

### 7.3.1 Mutual inductance between opposing rectangular coils

The rectangular coils are arranged to face each other as shown in Fig. 46, and current flows in coil T, which represents the i-th coil from the inside of the transmission coil Coil R represents the j-th coil from the inside of the receiving coil. The magnetic flux passing through the coil R caused by the

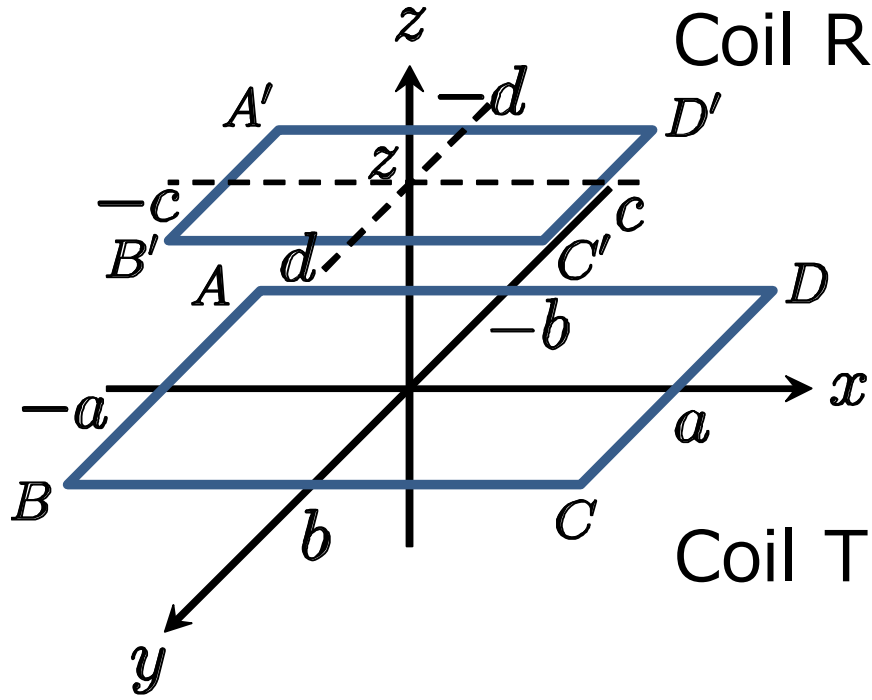


Fig. 46: Rectangular coil.

current flowing in a side  $CD$  is expressed by the following equation.

$$\Phi_{CD} = \frac{\mu_0}{2\pi} \left[ R_{CA'} - (a+c)\operatorname{arctanh}\frac{a+c}{R_{CA'}} - R_{CD'} + (a-c)\operatorname{arctanh}\frac{a-c}{R_{CD'}} \right. \\ \left. - R_{CB'} + (a+c)\operatorname{arctanh}\frac{a+c}{R_{CB'}} + R_{CC'} - (a-c)\operatorname{arctanh}\frac{a-c}{R_{CC'}} \right] \quad (7-10)$$

where  $R_{AA'}$  represents the distance between points  $A$  and  $A'$ . The mutual inductance of the coil T and coil R is

$$M_{ij} = \Phi_{AB} + \Phi_{BC} + \Phi_{CD} + \Phi_{DA}. \quad (7-11)$$

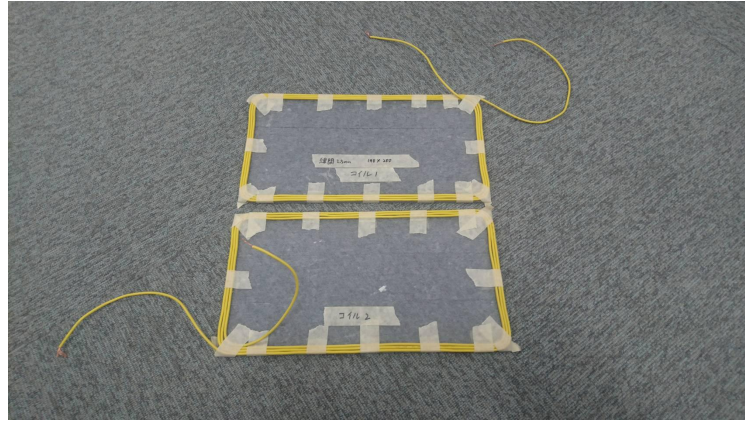
The total mutual inductance is taken as the sum of (7-11), as follows:

$$M = \sum_{i=1}^{N^T} \sum_{j=1}^{N^R} M_{ij} \quad (7-12)$$

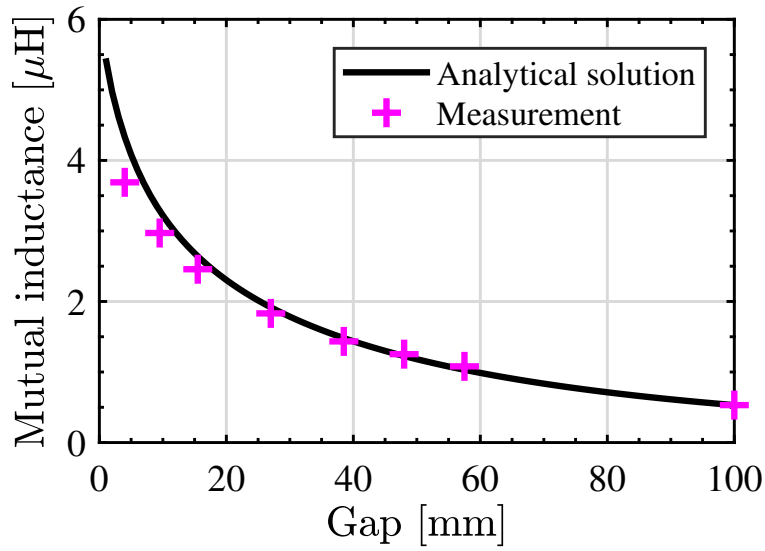
The mutual inductance of the coil whose number of turns is three, and the size is  $148 \text{ mm} \times 280 \text{ mm}$  shown in Fig. 47(a) is measured. The experimental result is shown in Fig. 47(b). From this result, the analytical solution and measured value are matched well.

### 7.3.2 The method of image and change of self inductance by mirror image

Fig. 48(a) shows a half space of permeability  $\mu_1, \mu_2$  in contact with the plane with the current  $I_1$  parallel to the interface flowing through the magnetics  $\mu_1$ . Then, the magnetic field in the magnetics  $\mu_1$



(a) KIV coils



(b) Mutual inductance

Fig. 47: Experimental results.

is equal to the magnetic field formed by the original current  $I_1$  and the image current  $I_2 = -\frac{\mu_2 - \mu_1}{\mu_2 + \mu_1} I_1$ . A schematic diagram is shown in Fig. 48(b).

Consider the round-trip current parallel to the complete conductor. Then the combined self inductance is

$$L = L_s + L'_s - 2M, \quad (7-13)$$

where  $L_s$  is the self-inductance of original coil,  $L'_s$  is the self-inductance of mirror coil, and  $M$  is the mutual inductance with the mirror current.

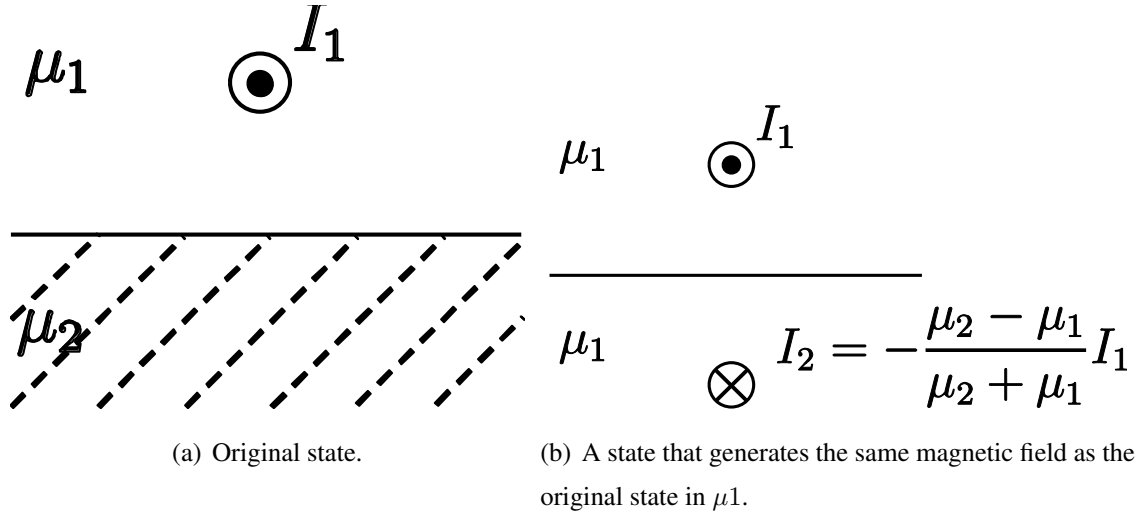


Fig. 48: Image method.

### 7.3.3 Assumption of virtual mirror plane

The increment of self-inductance is verified by the experiment under the condition shown in Fig. 49(a). By transforming (7-13), the mutual inductance between the original and image coils is expressed by the following equation.

$$M(d) = \frac{L_s + L'_s - L}{2} \quad (7-14)$$

$L_s$  is the self-inductance without the ferrite, and  $L$  is the self-inductance with the ferrite, then the right-hand side is known. The mutual inductance between the original and image coils is a function of the distance  $d$  (Distance from Coil to Image : DCI) between the coil and the mirror image plane from (7-10). The thickness of the acrylic plate is 2 mm, however, the increment of self-inductance does not match when substituting  $d = 2$  mm to (7-14).

Therefore, we assume that DCI is treated as a tuning parameter like Fig. 49(b). In the field of overhead transmission lines, a virtual mirror image plane to the earth is often used to considering the electric field because the earth is not an ideal conductor [117]. The influence of ferrite may be able to consider in the same way. When  $d = 27$  mm, the increment of self-inductance matched the equation. Thus, we consider the influence of ferrite by using  $d = 27$  mm in our calculations.

### 7.3.4 Mutual inductance when the ferrite exists above and below

We consider a rectangular loop sandwiched between two semi-infinite blocks of high-permeability material. The distances from the coil to the upper and lower ferrite are  $d_{\text{upper}}$ ,  $d_{\text{lower}}$ , respectively. Then the position of the  $i$ -th order current for the upper and lower ferrite is given in the following set

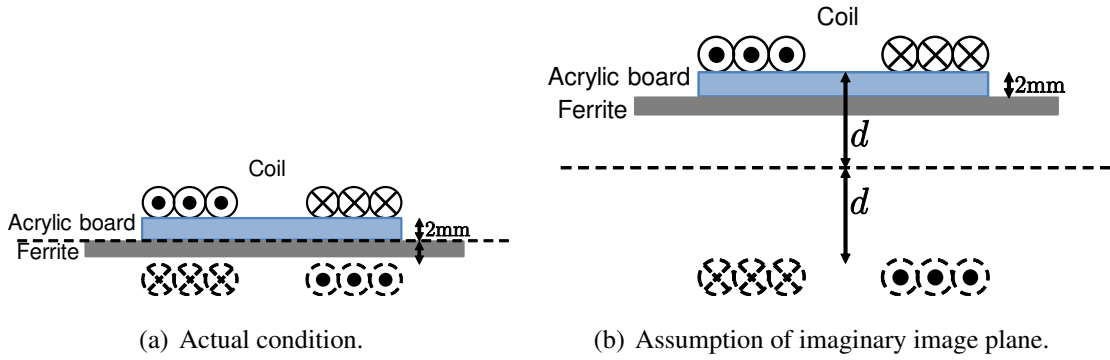


Fig. 49: Imaginary image plane.

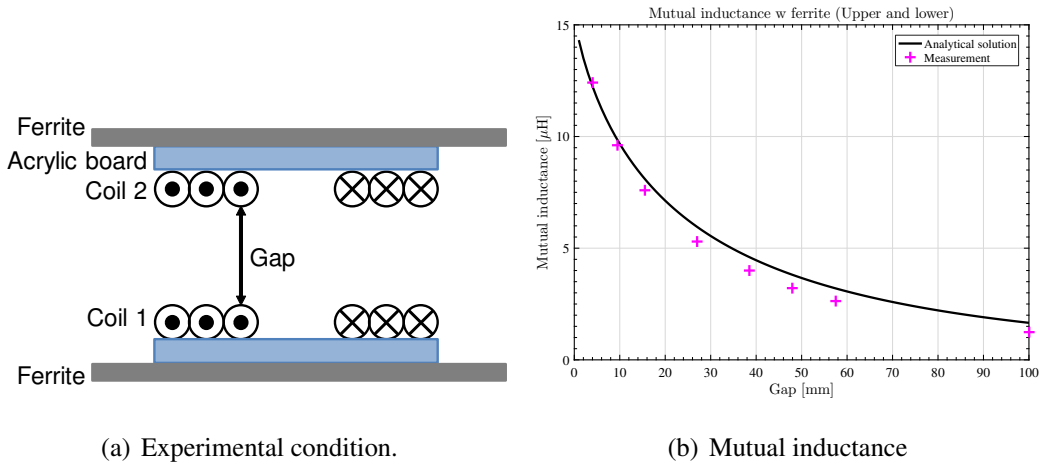


Fig. 50: Experimental result of the mutual inductance. Both coils have the ferrites.

of equations[118].

$$z_{\text{upper}} = 2 \left[ \frac{i+1}{2} \right] d_{\text{upper}} - \left[ \frac{i}{2} \right] d_{\text{lower}}, \quad (7-15)$$

$$z_{\text{lower}} = 2 \left[ \frac{i+1}{2} \right] d_{\text{lower}} - \left[ \frac{i}{2} \right] d_{\text{upper}} \quad (7-16)$$

In this analysis, up to the 100th order of image currents are used for mutual inductance calculation. Fig. 50(b) shows the experimental result when the ferrites are placed on both the transmission and receiving coils as in Fig. 50(a). From Fig. 50(b), the experimental value and analytical solution are almost in agreement.

Thus, mutual inductance considering ferrite can be calculated by the following procedure in which the mutual inductance is calculated based only on the simple self-inductance measurement.

**Step 1** Measures the self-inductance of the coil itself

**Step 2** Measure the self-inductance when ferrite is attached

**Step 3** Calculate the position of the virtual mirror plane corresponding to the increment in self-inductance by using (7-14) from the results of steps 1 and 2

**Step 4** Calculate mutual inductance using the value of step 3



Number of turns	Self inductance [ $\mu\text{H}$ ]		DCI[mm]
	w ferrite	w/o ferrite	
4	15.1	9.16	33.1
6	27.1	17.0	33.2
8	39.6	25.4	33.3
10	52.7	34.5	33.5
12	66.7	44.1	33.9

Tab. 15: Coil (150 mm  $\times$  280 mm).

Number of turns	Self inductance [ $\mu\text{H}$ ]		DCI[mm]
	w ferrite	w/o ferrite	
6	50.8	31.8	36.3
8	79.4	50.4	36.8
10	112	71.1	37.6
12	143	92.4	37.7

Tab. 16: Coil (150 mm  $\times$  580 mm).

Number of turns	Self inductance [ $\mu\text{H}$ ]		DCI[mm]
	w ferrite	w/o ferrite	
6	85.1	54.5	35.2
8	133	86.1	35.7
10	186	122	36.0
12	247	163	36.4

Tab. 17: Coil (150 mm  $\times$  1040 mm).

### 7.3.5 Consideration about distance from coil to image

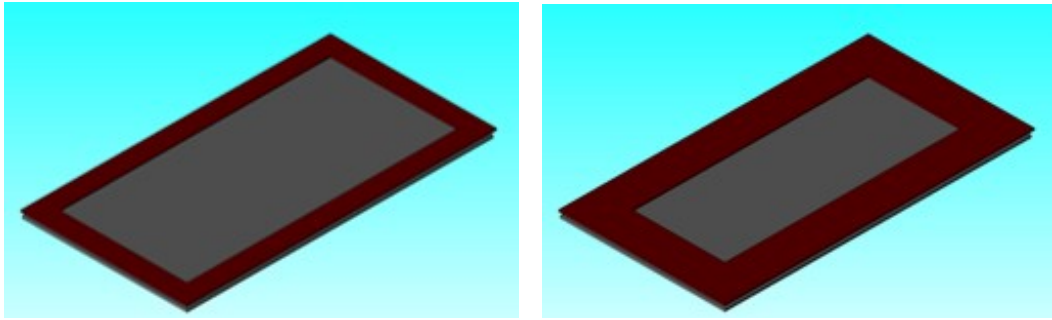
Change of DCI is measured when changing a shape of coil and number of turns of coils. Here, DCI is calculated in three coils whose size is 150 mm  $\times$  280, 580, 1040 mm, and pitch width is 2.5 mm. The calculation results from measurement values are shown in Tab. 15, 16, 17. From these result, DCI is almost same even when number of turns is changed. Therefore, it is considered that the distance calculated under certain conditions can be used in another condition because DCI is constant if the geometric arrangement of ferrite and the outer circumference of the coil do not change.

### 7.3.6 Comparison with electromagnetic field analysis

The proposed estimation method of the mutual inductance requires an experimental measurement of self inductance, however, it is better to calculate self inductance by electromagnetic field analysis.

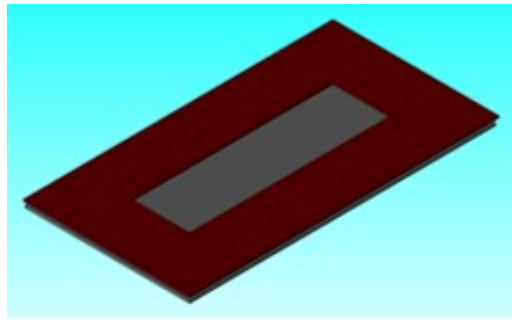
Number of turns	Experimental result		Electromagnetic field analysis
	w ferrite	w/o ferrite	w ferrite
4	8.01	11.1	10.3
8	22.0	32.1	30.5
12	35.2	53.6	50.4

Tab. 18: Comparison of self inductance [ $\mu\text{H}$ ].



(a) Analysis model (4 turns).

(b) Analysis model (8 turns).



(c) Analysis model (12 turns).

Fig. 51: Models of electromagnetic field analysis.

This section compares the experimental result and the electromagnetic field analysis result.

In this experiment, the size of coil is  $150\text{ mm} \times 280\text{ mm}$ , pitch width is 4 mm, gap between coil and ferrite is 4 mm, and material of ferrite is PE90. The electromagnetic field analysis is performed by using JMAG, and models of coil are shown in Fig. 51. The analysis results and experimental results are shown in Tab. 18. From Tab. 18, the error between the electromagnetic field analysis and measured values are about 5%. This thesis claims that only one electromagnetic field analysis (or experiment) is required to estimate the mutual inductance of the coil because the distance from coil to image is not so changed even if the number of turns, pitch width, and the gap are changes when the relationship of the outer of coil and ferrite does not change. By functionalizing the mutual inductance, the coil can be designed by optimization. The functionalization saves the time for designing coil comparing with using electromagnetic field analysis even when discrete design values are given.

## 7.4 Modeling of resistance

The resistance is classified into the direct current resistance, the influence of the skin effect caused by the flow of AC, and the influence of the proximity effect by the internal/external magnetic field. Many windings are composed of round conductors for lower price, but they have large loss due to a skin effect. On the other hand, a foil wire or litz wire is usually used to reduce a loss in the high frequency, however, the loss may be further increased by using these wires depending on the frequency band. The winding configuration is one degree of freedom to tune the winding loss, and there are many researches about proper winding configuration. This section describes skin effect and proximity effect, and introduce resistance models of the solid and litz wires.

### 7.4.1 Factor of AC resistance

#### Skin effect

The magnetic field due to the current flowing inside the conductor is expressed by the following equation according to Ampere's law.

$$\oint_C \mathbf{H} dl = \int \int_S \mathbf{J} dS. \quad (7-17)$$

Here,  $\mathbf{H}$  is the strength of the magnetic field, and  $\mathbf{J}$  is the current density. The magnetic field induces an electric field inside the conductor when the alternative current flows in the conductor. Most of the current flows through the outer layer of the conductor because the current generated by the induced electric field and original current are canceled. The current density decreases from the conductor surface toward the center, and the distance until the current density becomes  $\frac{1}{e}$  of the maximum current density is called the skin depth  $\delta$ . The skin depth is approximated as follows:

$$\delta = \frac{1}{\sqrt{\pi \mu_0 \sigma f}}, \quad (7-18)$$

when relative permeability is  $\mu_r \simeq 1$ . Here,  $\mu_0$  is the permeability of the vacuum,  $\sigma$  is the conductivity of the conductor,  $f$  is the frequency of the current. For simplicity, it is often assumed that a current with a constant power density flows from the conductor surface to the skin depth.

The loss per unit length due to the skin effect including the DC resistance can be represented by the following equation.

$$P_S = F_{R/S}(f) \cdot R_{DC} \cdot \hat{I}^2. \quad (7-19)$$

Here,  $R_{\text{DC}}$  is the DC resistance,  $\hat{I}$  is the peak current,  $F_{\text{R/S}} = R_{AC}/R_{DC}$  is the increase of resistance due to the skin effect.  $F_{R/S}$  depends on a cross-section of the conductor. Generally speaking, the loss of the solid wire due to the skin effect is larger than that of the litz wire because the litz wire reduces the influence of the skin effect by twisting many strands.

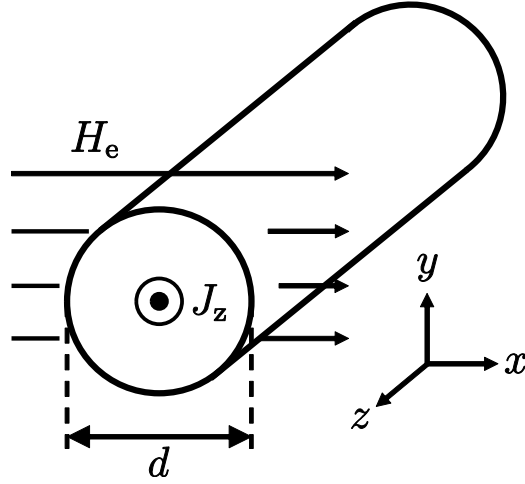


Fig. 52: Cross section of a round conductor that is influenced by an external magnetic field in  $x$ -direction. The conductor is infinitely long in  $z$ -direction.

### Proximity effect

The proximity effect is a loss caused by the change in the current distribution of the conductor by penetrating the magnetic field to the conductor. The loss due to the proximity effect is represented as follows:

$$P_P = G_{R/S}(f) \cdot R_{DC} \cdot (\hat{H}_e^2 + \hat{H}_i^2) \quad (7-20)$$

Here,  $\hat{H}_e$  is the peak value of the external magnetic field,  $\hat{H}_i$  is the peak value of the internal magnetic field,  $G_{R/S}$  represents the increase of resistance due to the proximity effect. Generally speaking, the loss of the litz wire due to the proximity effect is larger than that of the solid wire because  $\hat{H}_i$  which is the magnetic field between the strands of the conductor is zero in the solid wire, however, an internal magnetic field depending on the number of strands and the twisting method occurs in the litz wire.

### 7.4.2 AC resistance of solid wire [3]

It is known that the solid wire is less expensive and has a large loss due to the skin effect. It is necessary to select the optimum conductor diameter because the loss of the skin effect decreases as the conductor diameter increases, however, the loss of the proximity effect increases as increasing diameter.

A crosssection of the solid wire is shown in Fig. 52. Here,  $d$  is a diameter of conductor, and  $l$  is a length of wire. It can be assumed that the solid wire has an infinite length with respect to the  $z$  direction when  $d \ll l$ .

First, the skin effect of the solid wire is described. The skin effect per unit length is expressed as

follows:

$$P_S = F_R(f) \cdot R_{DC} \cdot \frac{\hat{I}^2}{2} \quad (7-21)$$

with

$$\begin{aligned} \delta &= \frac{1}{\sqrt{\pi\mu_0\sigma f}}, \\ \xi &= \frac{d}{\sqrt{2}\delta}, \\ R_{DC} &= \frac{4}{\sigma\pi d^2}, \\ \text{and} \\ F_R &= \frac{\xi}{2\sqrt{2}} \frac{1}{\text{ber}_1(\xi)^2 + \text{bei}_1(\xi)^2} \cdot \\ &\quad (-\text{ber}_0(\xi)\text{ber}_1(\xi) + \text{ber}_0(\xi)\text{bei}_1(\xi) \\ &\quad -\text{bei}_0(\xi)\text{ber}_1(\xi) - \text{bei}_0(\xi)\text{bei}_1(\xi)) \end{aligned} \quad (7-22)$$

Here,  $\text{ber}_n(x)$ ,  $\text{bei}_n(x)$  are Kelvin functions, and they represent the real part and the imaginary part of the first kind of  $n$  order Bessel function  $J_n(xe^{\frac{3\pi j}{4}})$ , respectively.

Next, the proximity effect is described. The proximity effect per unit length is given by the following equation when the external magnetic field is  $H_{\text{mathrme}}$ .

$$P_P = G_R(f) \cdot R_{DC} \cdot \hat{H}_e^2 \quad (7-23)$$

with

$$\begin{aligned} \delta &= \frac{1}{\sqrt{\pi\mu_0\sigma f}}, \\ \xi &= \frac{d}{\sqrt{2}\delta}, \\ R_{DC} &= \frac{4}{\sigma\pi d^2}, \\ \text{and} \\ G_R &= -\frac{\xi\pi^2 d^2}{2\sqrt{2}} \frac{1}{\text{ber}_0(\xi)^2 + \text{bei}_0(\xi)^2} \cdot \\ &\quad (\text{ber}_2(\xi)\text{ber}_1(\xi) + \text{ber}_2(\xi)\text{bei}_1(\xi) \\ &\quad -\text{bei}_2(\xi)\text{ber}_1(\xi) + \text{bei}_2(\xi)\text{bei}_1(\xi)) \end{aligned} \quad (7-24)$$

### 7.4.3 AC resistance of litz wire [3]

The cross section of litz wire is shown in Fig. 53.  $d_a$  is a total diameter, and  $d_i$  is a diameter of one strand.  $H_e$  is an external magnetic field, and  $H_i$  is an internal magnetic field between strands.  $n$  is a number of strands.

Ideally, the strands are twisted such that each strand equally occupies each position in the bundle. This greatly reduces the effect of bundle level, so it is ignored in the following equation. However, the influence of bundle level may affect winding loss if the litz wire is not ideally twisted.

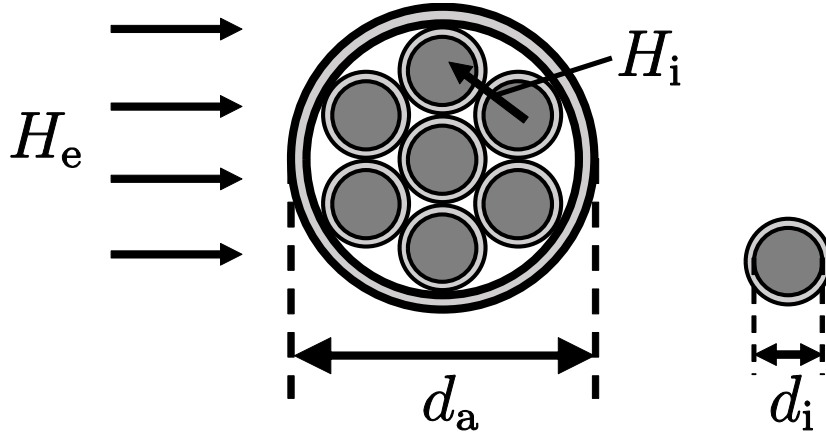


Fig. 53: Cross-sectional area of litz-wire winding.

The skin effect of litz wire is described. The loss due to the skin effect of the litz wire with the number of strands  $n$  is given by the following equation.

$$P_{S,L} = n \cdot F_R(f) \cdot R_{DC} \cdot \frac{\hat{I}^2}{2n^2}, \quad (7-25)$$

$$R_{DC} = \frac{4}{\sigma \pi d_i^2} \quad (7-26)$$

Here,  $F_R$  is a value which substitutes  $d = d_i$  to (7-22).

Next, the proximity effect of litz wire is described. The proximity effect on the litz wire can be regarded as the sum of the external magnetic field  $H_e$  and the internal magnetic field  $H_i$  between strands. The loss due to the proximity effect of the litz wire with the number of strands  $n$  is given as follows:

$$\begin{aligned} P_{P,L} &= P_{P,L,e} + P_{P,L,i} \\ &= n \cdot G_R(f) \cdot R_{DC} \cdot \left( \hat{H}_e^2 + \frac{\hat{I}^2}{4\pi^2 d_a^2} \right), \end{aligned} \quad (7-27)$$

where,  $G_R$  is a value which substitutes  $d = d_i$  to (7-24). The internal magnetic field  $H_i^2 = \frac{\hat{I}^2}{4\pi^2 d_a^2}$  is calculated on the assumption of a uniform current flow in the conductor.

#### 7.4.4 An increase of resistance when using ferrite

It is known that the resistance of coil increase when using the ferrite. In general, total loss of the coil is sum of capper loss of the coil and iron loss of the ferrite given in

$$\begin{aligned} P &= P_h + P_e = k_h f B^2 + k_e f^2 B^2, \\ &= (k_h f + k_e f) B^2, \end{aligned} \quad (7-28)$$

$$P_c = I^2 R. \quad (7-29)$$

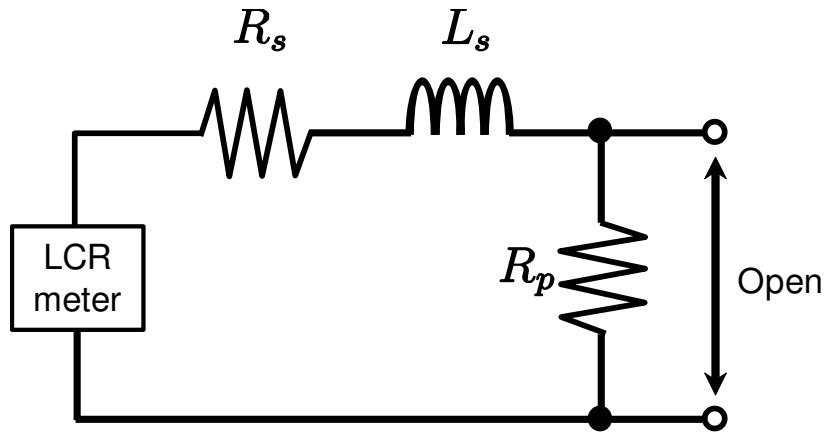


Fig. 54: Equivalent circuit of the coil with ferrite.

Here,  $P$  is total loss,  $P_h$ ,  $P_e$ ,  $P_c$  are loss of hysteresis, eddy current, and copper.  $B$  is magnetic flux density, and  $k_h$ ,  $k_e$  are coefficients of the loss of hysteresis and eddy current. The effect of the ferrite can be measured by LCR meter because the an equivalent circuit of the inductor with ferrite is shown in Fig. 54. [119] considers only the copper loss because the iron loss is enough smaller than the copper loss, however, consideration of the iron loss is important for designing the coil more strictly.

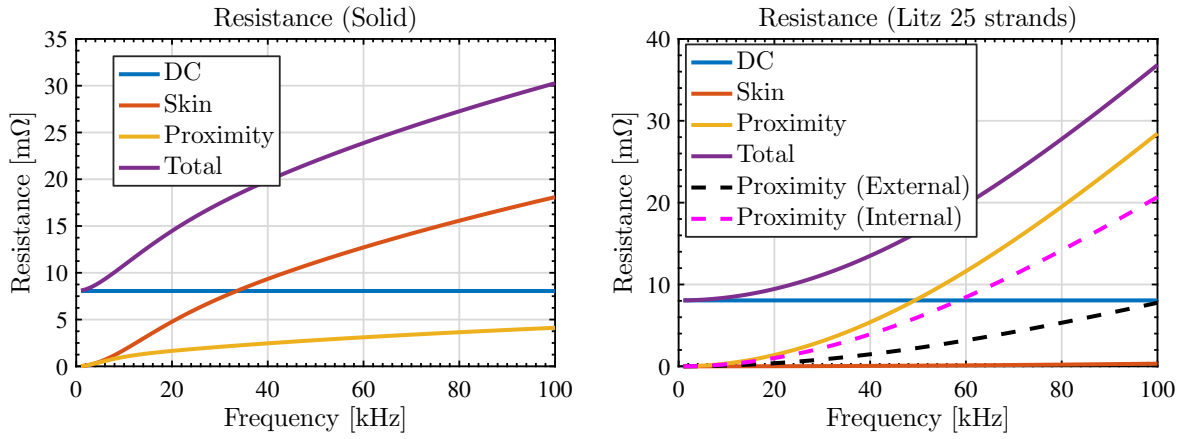
## 7.4.5 Verification of solid and litz wire by simulation and experiment

### Verification by simulation

Simulations are conducted under the following four conditions. The number of strands of the litz wire and the diameter of the strand are determined so that the total cross-section of litz wire is same as the cross-section of the solid wire. In this simulation, the coil size is  $150 \times 250$  mm, pitch width is 5 mm, and number of turns of coil is three.

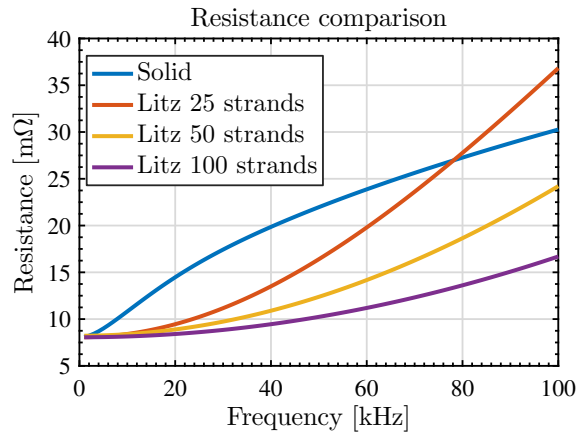
- Solid wire : Diameter:2.5 mm
- Litz wire : Number of strands:25, Diameter of each strands:0.5 mm
- Litz wire : Number of strands:50, Diameter of each strands:0.35 mm
- Litz wire : Number of strands:100, Diameter of each strands:0.25 mm

The simulation result is shown in Fig. 55. Fig. 55(a), 55(b) represents the AC resistance of the solid wire and litz wire (25 strands), respectively. From these results, AC resistance of the solid wire is increased mainly due to the skin effect, however, that of the litz wire is increased mainly due to the proximity effect. It is also understood that the influence by the internal magnetic field is larger than the influence by the external magnetic field. From Fig. 55(c), the AC resistance becomes smaller as



(a) Solid wire.

(b) Litz wire (25 strands).



(c) Resistance comparison.

Fig. 55: Simulation result

the number of strands of litz wire is larger In addition, litz wire is better at the low frequency and the solid wire is better in the high frequency.

### Verification by experiment

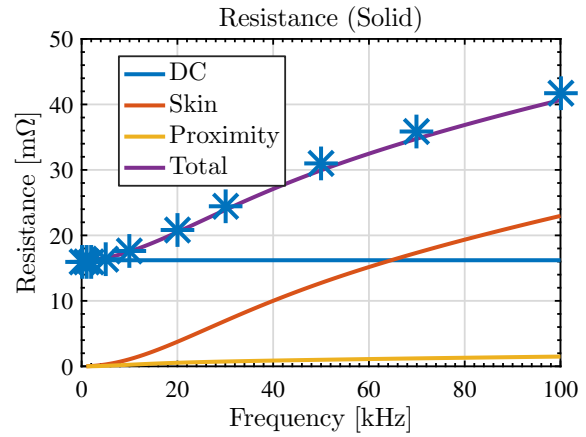
The resistance of the solid wire is verified by experiment. We design a coil which is made by the solid wire whose diameter is 2 mm, and whose size, pitch width, and number of turns is  $150 \times 250$  mm, 5 mm, and three, respectively. Experiment results and theoretical values are shown in Fig. 56(b). The measured value and the theoretical value almost same.

Next, the resistance of the litz wire is verified by experiment. The AC resistance of litz wire whose number of strand is  $0.1 \text{ mm} \times 160$ , total diameter is 1.5 mm, and length is 1 m. Experiment results and theoretical values are shown in Fig. 57. It can be seen that the theoretical value of the litz wire is much smaller than the measured value. One of the reason of the difference between the analytical solution and the measured value is an unbalance current flow in the strands which is pointed out by the litz wire analysis using earth simulator [120, 121], despite calculating the internal magnetic field on the assumption that a uniform current flows in the conductor in analytical model of litz wire. Therefore,





(a) Rectangular coil (Solid wire)



(b) Resistance of the rectangular coil (Solid wire)

Fig. 56: Measurement result of resistance of the solid wire.

the analytical solution is not enough to estimate the AC resistance of the litz wire, and it is necessary to consider the structure of the litz wire.

#### 7.4.6 Numerical calculation method of AC resistance of Litz wire

This section estimates the influence of the internal magnetic field on the litz wire by using a numerical calculation method of the AC resistance considering the structure of the litz wire proposed by Zhang [4, 5].

##### Outline of numerical calculation method [4, 5]

[4, 5] proposed a AC resistance method of litz wire by improving Partial element equivalent circuit (PEEC) method. The magnetic field is calculated by solving the integral Maxwell equations in an electromagnetic field analysis, however, PEEC method divide an object into meshes and analyze the integral equation by regarding as Kirchhoff's voltage law for each mesh as shown in Fig. 58. Self-inductance of each element and mutual inductance between elements can be expressed by using a Green function by considering the object as a multilayer. The Green function is effective only for a single  $z$  in in multilayered objects, thus they use the Toeplitz and Hankel matrix to correlate each layer. Finally, the resistance at each frequency is obtained by performing frequency sweep.

These papers make a model of litz wire and mention that the calculation result and the experimental result are matched well. The calculation method proposed in [4, 5] seems to be more reliable than the conventional model because the theoretical value is far from the measured value as shown in Fig. 57.

##### Comparison between experimental value and numerical calculation result

This experiment uses the litz wire whose number of strand is  $0.1 \text{ mm} \times 160$ , total diameter is 1.5 mm, and length is 1 m. Comparison results with the measurement value of the litz wire and the

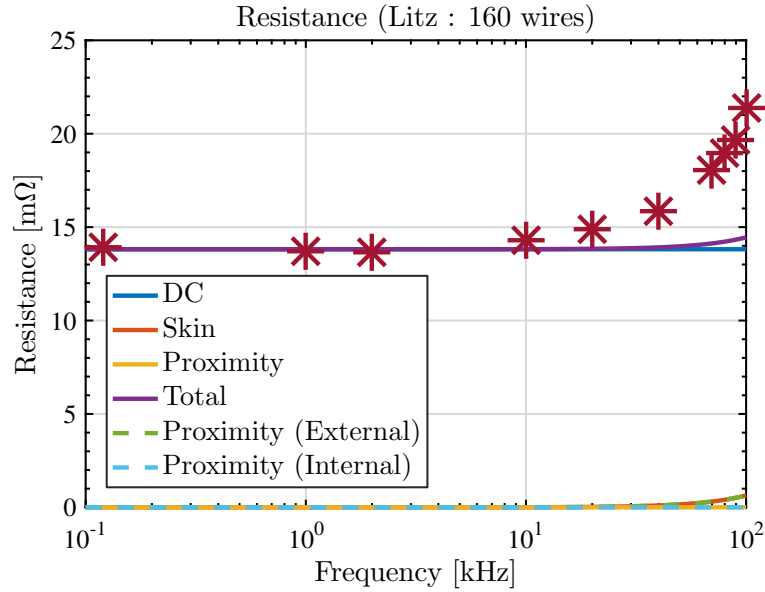


Fig. 57: Measurement result of resistance of the litz wire.

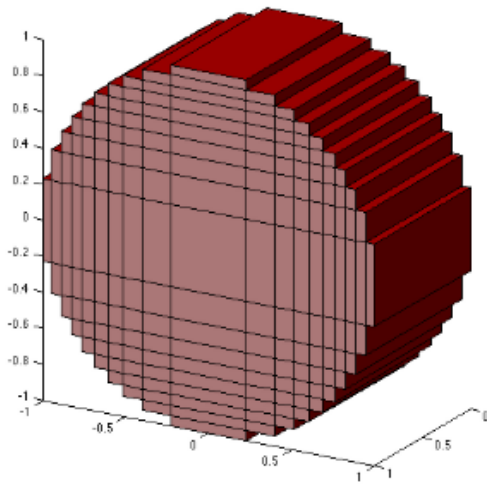
numerical calculation result proposed in [4, 5] is shown in Fig. 59(b). In this calculation, a litz wire model whose length is 1.0cm shown in Fig. 59(a) is used, and the calculation result is multiplied by 100 according to experimental conditions. The numerical calculation result and the experimental result is matched well.

In this experiment result and numerical calculation result, the effect of the skin effect and the proximity effect by the internal magnetic field is taken into consideration. In the case of the litz wire, the loss due to the skin effect is very small, so the increase in AC resistance is mainly the effect of the proximity effect by the internal magnetic field. The framework combining the effect of the internal magnetic field which is obtained by the simple numerical calculation and the external magnetic field which is calculated theoretically is useful from the point of view shortening the design time because making a model of the whole coil needs long time. From the above, it is possible to model AC resistance in the litz wire.

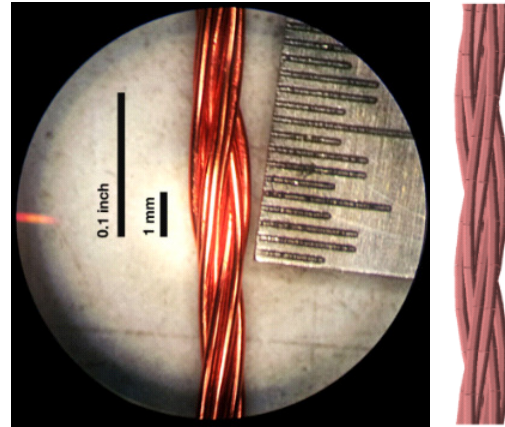
In this experiment result and numerical calculation result, the effect of the skin effect and the proximity effect by the internal magnetic field is considered. In the case of the litz wire, the loss due to the skin effect is very small, so the increase in AC resistance is mainly caused by the proximity effect by the internal magnetic field. The influence of the proximity effect by the internal magnetic field can be estimated by using the numerical calculation.

### Validation of resistance of rectangular coil using Litz wire

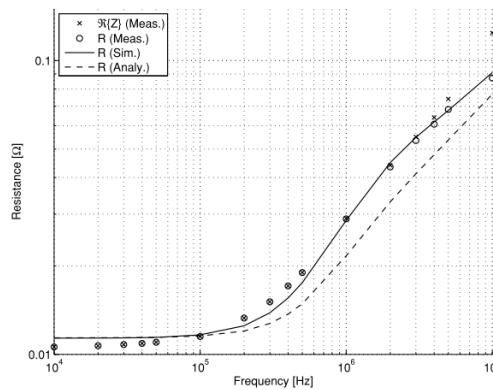
Next, it is verified whether the resistance of the rectangular coil can be estimated from the above result. The internal magnetic field which is difficult to model is calculated by using numerical simulation. The increment of the AC resistance due to the external magnetic field depends only on the



(a) The filament discretization in the Partial Element Equivalent Circuit method



(b) Modeling of litz wire



(c) Modeling of litz wire

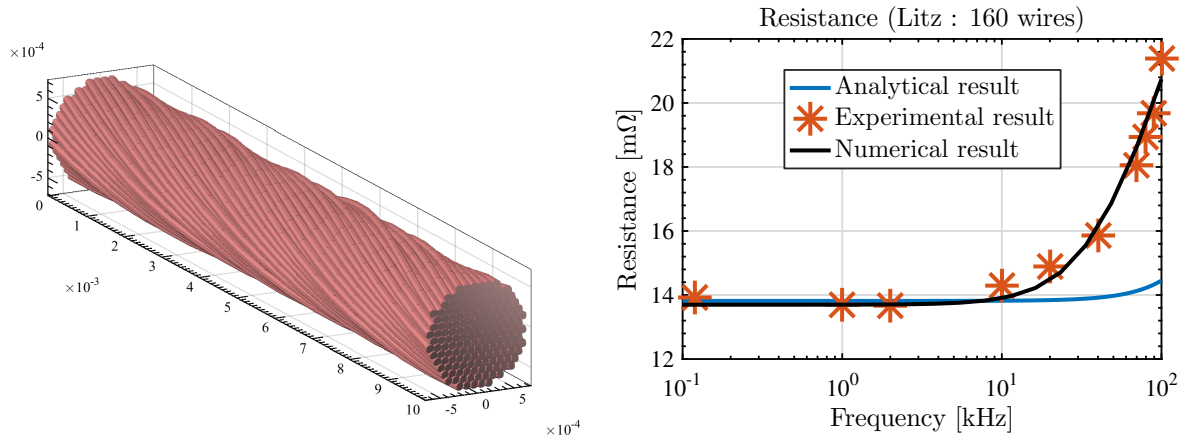
Fig. 58: Modeling and resistance calculation of litz wire in [4, 5].

shape of the coil. We design a coil whose number of turns is three, pitch width is 5 mm, and the size is 148 mm  $\times$  150 mm by using litz wire whose number of strand is 0.1 mm  $\times$  160 and total diameter is 1.5 mm. The analytical solution and the experimental result are shown in Fig. 59(c). From Fig. 59(c), the analytical solution and the experimental result are matched well. Therefore, it is shown functionalization of the AC resistance of litz wire is possible. From above result, the mutual inductance and AC resistance are modeled, thus the coil design considering specification becomes possible.

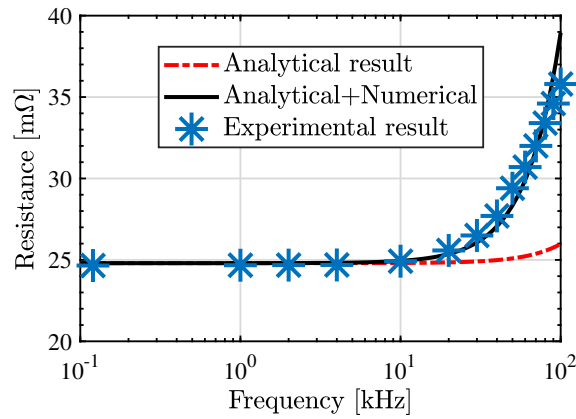
## 7.5 Coil design satisfying required specifications

The coils are designed considering the requirement specifications calculated mutual inductance and resistance, including:

- Optimized efficiency of each axis: more than 90 %
- Y axis load power: 102 W



(a) Model of the litz wire for the numerical calculation. (b) Comparison of the measural and numerical result.



(c) Resistance of the rectangular coil made by litz wire.

Fig. 59: Resistance of the litz wire.

- X axis load power: 77 W
- Y axis transmission side voltage: 60 – 120 V
- Y axis receiving side voltage: 24 – 60 V
- X axis receiving side voltage: 24 – 36 V

There are usually 8 variables for the coil design: the size of the coils (width and height, 4 variables), the number of turns of each coil (2 variables), the pitch of each coil (2 variables), the distance between both coils, and the source voltage. In this paper, the frame shape is given in advance and the litz wire has a twist of  $7 \times 43 = 301$  strands. Therefore, our design variables are the number of turns (1 to 10 turns), the gap of coils (5 to 50 mm), and the source voltage (60 to 120V).

Tab. 19, 20 show the measured values in Fig. 60 and the designed values obtained by optimization. The measured values of the resistance and mutual inductance are close to the designed values, and the resulting coils satisfy all constraints.



Fig. 60: Designed coil.

## 7.6 Conclusion of coil design considering required specifications

In this chapter, the coil design method considering required specifications such as transmission power, efficiency, and secondary side voltage is proposed in order to further disseminate wireless power transmission technology. First, we formulated an optimization problem to be solved for coil design, and modeled the mutual inductance and AC resistance of the coil using litz wire. Then, the coil design satisfying the required specification was realized by performing optimization calculation based on these modeling.

Future tasks include selections of evaluation function in optimization problem and analysis of its convexity.

Tab. 19: Coil parameters (Y axis).

	Designed	Measured	Constraint
Width(1st) [mm]	600	–	–
Height(1st) [mm]	150	–	–
Number of turns(1st)	10	10	–
Resistance(1st) [ $\Omega$ ]	0.17	0.192	–
Self inductance(2nd) [ $\mu H$ ]	–	94	–
Width(2nd) [mm]	280	–	–
Height(2nd) [mm]	150	–	–
Number of turns(2nd)	10	10	–
Resistance(2nd) [ $\Omega$ ]	0.09	0.1	–
Self inductance(2nd) [ $\mu H$ ]	–	55	–
Gap [mm]	10	10	–
Self inductance [ $\mu H$ ]	39	35	–
Voltage(1st) [V]	90	90	60–120
Voltage(2nd) [V]	58.5	58.3	24–60
Voltage ratio	0.72	0.72	–
Efficiency [%]	98.8	98.5	90–
Transmission power [W]	224	251	214–251

Tab. 20: Coil parameters (X axis).

	Designed	Measured	Constraint
Width(1st) [mm]	1040	–	–
Height(1st) [mm]	150	–	–
Number of turns(1st)	8	8	–
Resistance(1st) [ $\Omega$ ]	0.227	0.255	–
Self inductance(2nd) [ $\mu H$ ]	–	111	–
Width(2nd) [mm]	280	–	–
Height(2nd) [mm]	150	–	–
Number of turns(2nd)	10	10	–
Resistance(2nd) [ $\Omega$ ]	0.09	0.09	–
Self inductance(2nd) [ $\mu H$ ]	–	52	–
Gap [mm]	10	10	–
Self inductance [ $\mu H$ ]	34	28	–
Voltage(1st) [V]	58.3	58.3	24–60
Voltage(2nd) [V]	32.9	30.7	24–36
Voltage ratio	0.63	0.59	–
Efficiency [%]	98.5	98.0	90–
Transmission power [W]	93	107	93–108

# Chapter 8

## Drastic solution of cable disturbance by WHPS1

This chapter shows that cable disturbance can be suppressed by WHPS1. The control performance is discussed after introducing load voltage stabilization control and coil design of WHPS1.

### 8.1 Load voltage stabilization control on the receiving side

It is known that a system of the DC link voltage is unstable when the load is constant power load like a motor [122]. Thus, the stabilization control of the DC link voltage is required. It is better that the stabilization control is implemented only in the receiving side to avoid a performance degradation due to the communication delay. Several methods are proposed to keep the DC link voltage constant by using only the receiving side information: a) two mode method using HAR as a AC/DC converter in the receiving side [122], b) a synchronous pulse width modulation (PWM) rectification method using synchronous rectification [123]. This paper uses the former method to control the DC link voltage.

The HAR circuit is a AC/DC converter circuit whose upper arms are diodes and lower arms are switching devices. This circuit operates in two modes according to the state of the lower arm shown in Fig. 61(a), Fig. 61(b). In the rectification mode shown in Fig. 61(a), the electric power is transmitted from the transmission side to the load. On the other hand, in the short mode shown in Fig. 61(b), the electric power is not transmitted from the transmission side because the receiving side is shorted. The transmission power is controlled to switch these two modes properly.

The DC link voltage is controlled using a hysteresis comparator on the receiving side [122]. The upper threshold voltage  $V_{high}$  and the lower threshold voltage  $V_{low}$  of the hysteresis comparator are

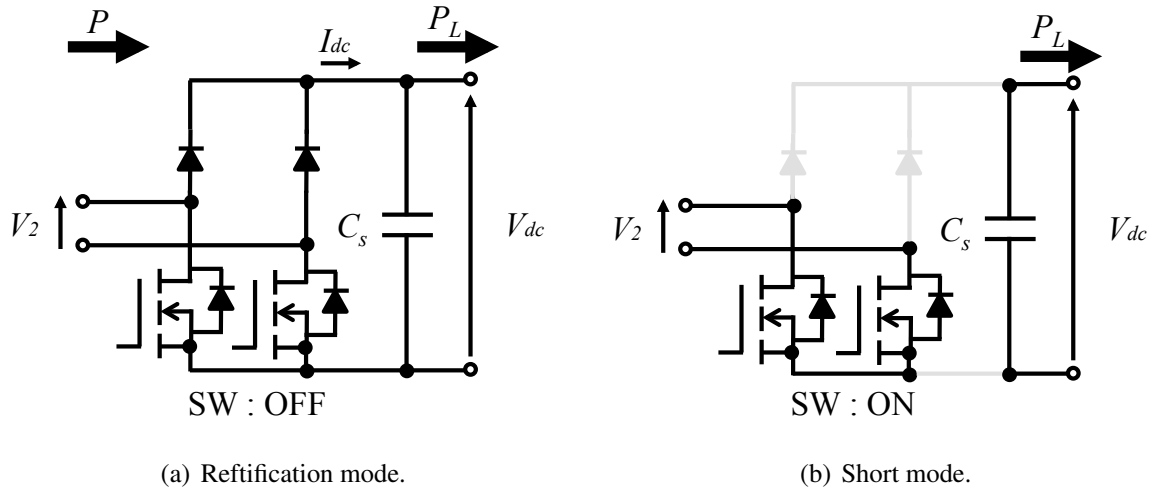


Fig. 61: Operation state of 2-mode method.

defined as follows:

$$V_{\text{high}} = V_{\text{dc}}^* + \Delta V_{\text{high}} \quad (8-1)$$

$$V_{\text{low}} = V_{\text{dc}}^* - \Delta V_{\text{low}} \quad (8-2)$$

Here,  $V_{\text{dc}}^*$  is a reference of the load voltage, and  $\Delta V_{\text{high}}$ ,  $\Delta V_{\text{low}}$  are upper and lower hysteresis width of the voltage. The HAR circuit is driven as the rectification mode when  $V_{\text{dc}}$  becomes smaller than  $V_{\text{low}}$ . Then the electrical power is supplied to the load, and the DC link voltage  $V_{\text{dc}}$  increases if the transmission power is larger than the power consumption of the load. The mode of the HAR circuit is switched to the short mode when  $V_{\text{dc}}$  becomes larger than  $V_{\text{high}}$ . Then the DC link voltage  $V_{\text{dc}}$  decrease because the load power is supplied from the smoothing capacitor. The DC link voltage is kept within the hysteresis width by switching operation modes properly. The DC link voltage waveform using 2-mode method is shown in Fig. 62. The rate of increase and decrease of the voltage is determined by the input and output power and the capacity of the smoothing capacitor. Therefore,  $T_{\text{short}}$  and  $T_{\text{rect}}$  can be adjusted considering with the switching response property of the switching device by making the capacity of the smoothing capacitor sufficiently large.

## 8.2 Verification of cable disturbance rejection by experiment

### 8.2.1 Coil design for WHPS1

In this experiment, spiral rectangular coils are designed for WPT. Parameters of the coils are shown in Tab. 21. The mutual inductance between the transmission and receiving coils is decided considering the efficiency and the transmission power. An equivalent circuit of wireless power transfer using magnetic field resonance coupling is represented in Fig. 63. From the equivalent circuit, the



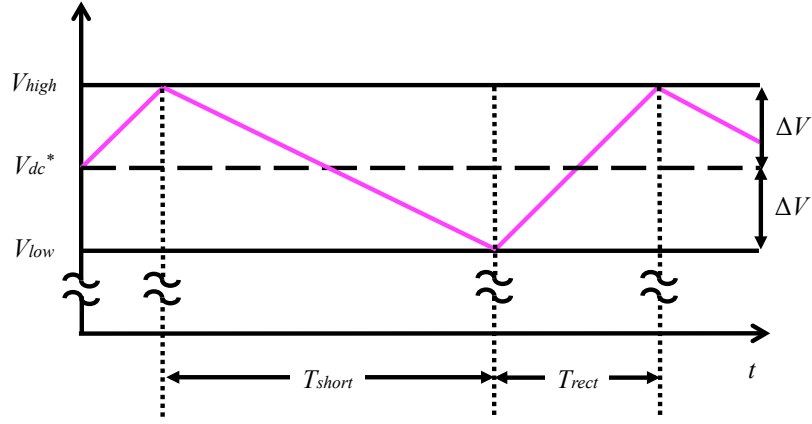


Fig. 62: Waveform of the DC link voltage.

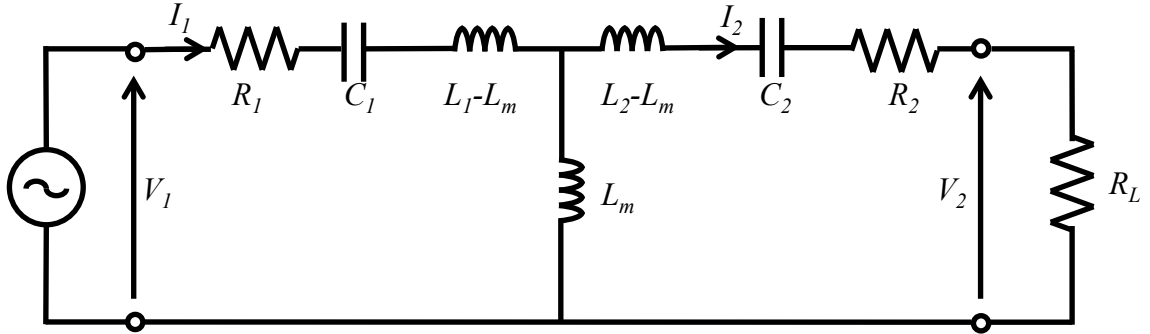


Fig. 63: Equivalent circuit of WPT using magnetic field resonance coupling.

transmission power  $P_R$  and the efficiency  $\eta$  are defined as follows:

$$P_R = \frac{(\omega_0 L_m)^2 R_L}{R_1 R_2 + R_1 R_L + (\omega_0 L_m)^2} V_1^2, \quad (8-3)$$

$$\eta = \frac{(\omega_0 L_m)^2 R_L}{(R_2 + R_L) \{R_1 R_2 + R_1 R_L + (\omega_0 L_m)^2\}}. \quad (8-4)$$

Here,  $R_L$  is an equivalent load resistance, and  $\omega_0 = 85$  kHz in this experiment. The equivalent load resistance  $R_L$  is represented in (8-5).

$$R_L = \frac{V_{2dc}^2}{P_L} \quad (8-5)$$

Here,  $V_{2dc}$  is the DC link voltage of the receiving side, and  $P_L$  is the power consumption in the receiving side. In this paper,  $P_L$  is a maximum power consumption of the motor which is calculated from a trajectory of the stage. The relationship between the efficiency and the equivalent load resistance is shown in Fig. 64. The mutual inductance  $L_m$  needs to be more than  $30 \mu\text{H}$  to achieve that the efficiency is more than 90%.

The position relation between the transmitting and receiving coils is shown in Fig. 65(a). Measurement result of the mutual inductance when changing the relative position and gap of each coil

Tab. 21: Coil parameter.

	Unit	Transmitting coil	Receiving coil
Outer size	mm	1040 × 150	178 × 115
Inner size	mm	925 × 37	75 × 15
Number of turns		22	17.5
Resistance	$\Omega$	2.52	0.22
Self inductance	$\mu\text{H}$	413	35.0

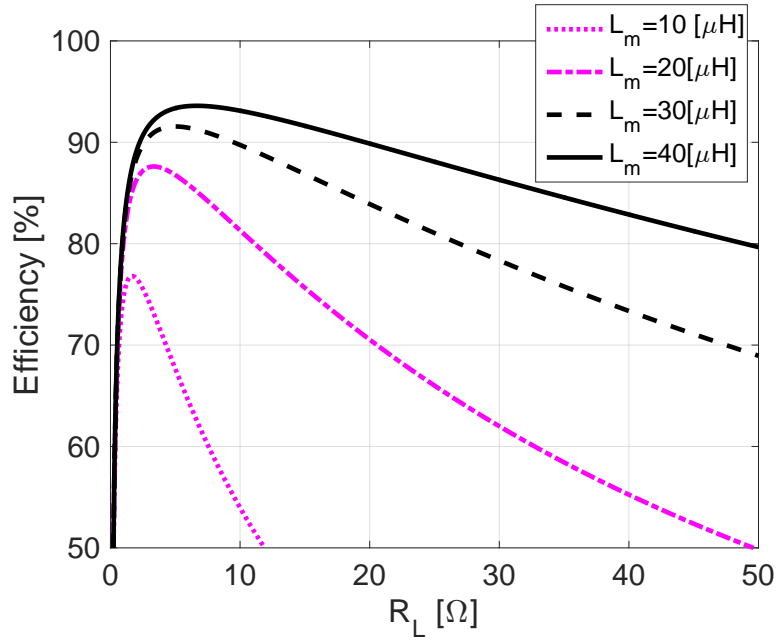


Fig. 64: The relationship between the efficiency and the equivalent load resistance.

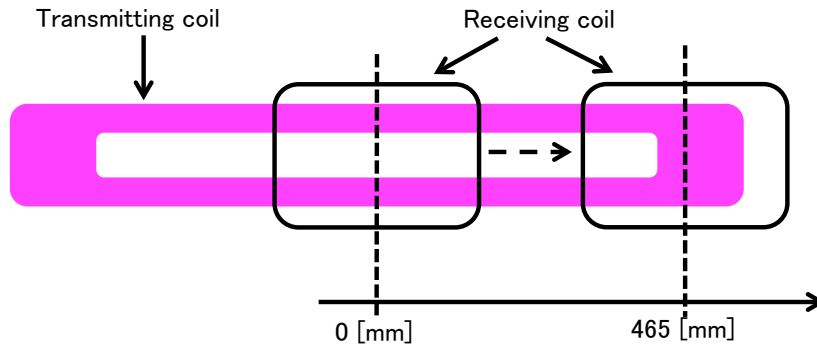
is shown in Fig. 65(b). From this measurement, the gap between both coils is set to 5 mm, then the mutual inductance is about 30  $\mu\text{H}$  at all positions.

### 8.2.2 Experiment of trajectory tracking by WHPS1

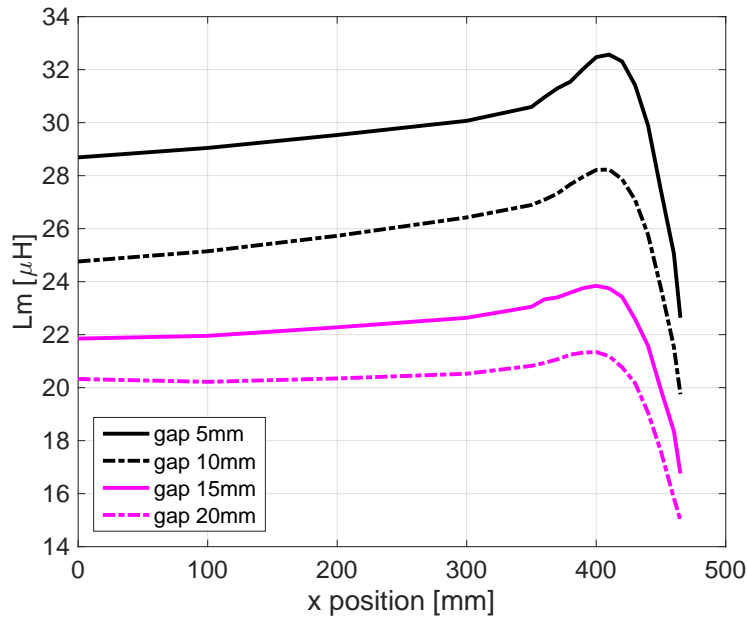
This section indicates that cable disturbance exists by comparing the case of wired and that of wireless. Experimental results demonstrate the effectiveness of W-HPS.

#### Experimental conditions

Fig. 68(g) shows the target position and velocity trajectories of the stage. The target position trajectory whose movement distance is 300 mm is based on a trapezoidal velocity trajectory whose maximum velocity is 200 mm/s. The trajectories during 0.0 s to 0.5 s are in the acceleration region. The trajectories during 0.5 s to 1.5 s are in the constant velocity region. The trajectories during 1.5 s



(a) Relative position between transmitting coil and receiving coil.



(b) Measurement result.

Fig. 65: Position dependency of the mutual inductance.

to 2.0 s are in the deceleration region. Bode diagrams of the plant of the stage and the closed loop system are shown in Fig. 66. A Proportional-Integral (PI) current controller, a PI velocity controller, and P position controller are designed for W-HPS, so that the closed-loop bandwidth of the current, velocity, and position loop can be 2500 Hz, 100 Hz, and 30 Hz, respectively. The DC link voltage is controlled to be 36 V by using 2-mode methods.

## Experimental results

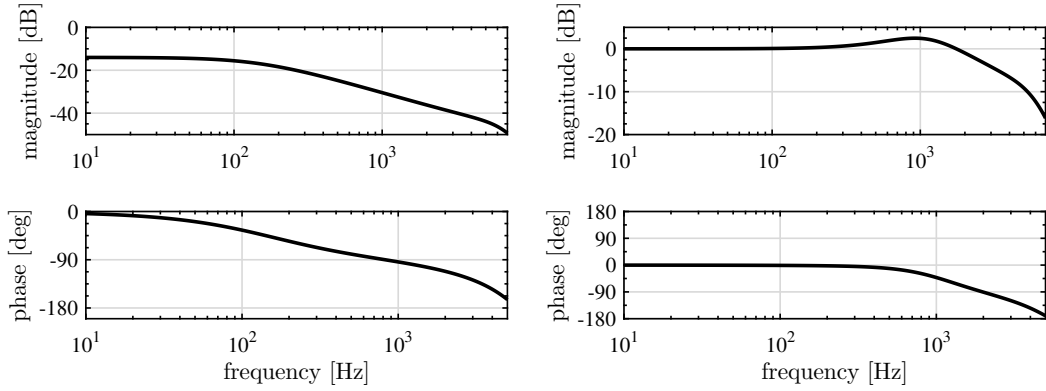
Fig. 68 shows the experimental results. Fig. 67(f) shows the DC link voltage in the case of WPT. The DC link voltage is stabilized around 36.5 V by 2-mode method and it slightly rises due to regeneration during the deceleration region. Fig. 67(d) and Fig. 67(e) show q-axis current in the case of wired and wireless, respectively. The current can be reduced in the case of WPT. Fig. 67(b) is the position error in time domain and Fig. 67(c) is a result of fast fourier transform (FFT) of it. From Fig.

67(b), the tracking error of the stage is less than  $50 \mu\text{m}$  in every region, so the W-HPS can track the target trajectory. In addition, Fig. 67(b) and Fig. 67(c) show that tracking performance is improved in the case of wireless, and especially, the error around 92 Hz is greatly reduced. In this experiment, it is expected that a main frequency of the cable disturbance is 92 Hz.

From these results, it showed that the cable disturbance actually exists and that the cable disturbance can be greatly reduced in W-HPS.

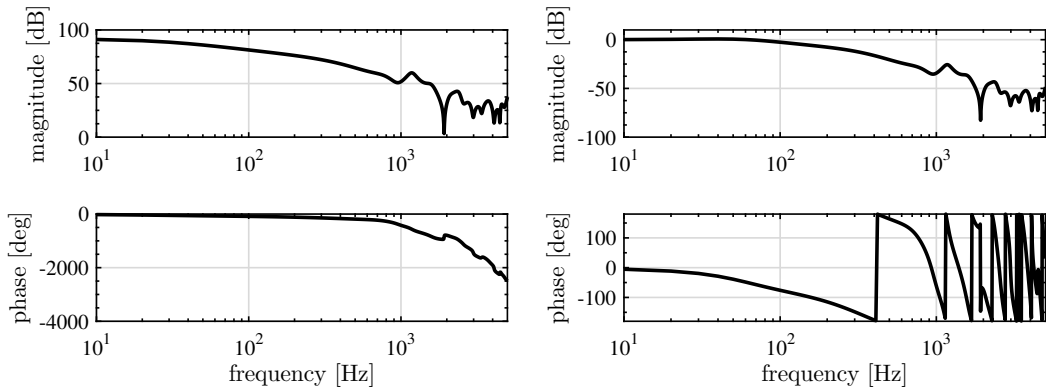
### **8.3 Conclusion of WHPS1**

This chapter proposed a novel moving coil wireless linear motor using the resonant magnetic coupling which relax the trade-off between the moving coil linear motor and the moving magnet linear motor. Experimental results show that the concept of MC-WLM is feasible, the cable disturbance exists when wired, and it can be reduced radically by using MC-WLM.



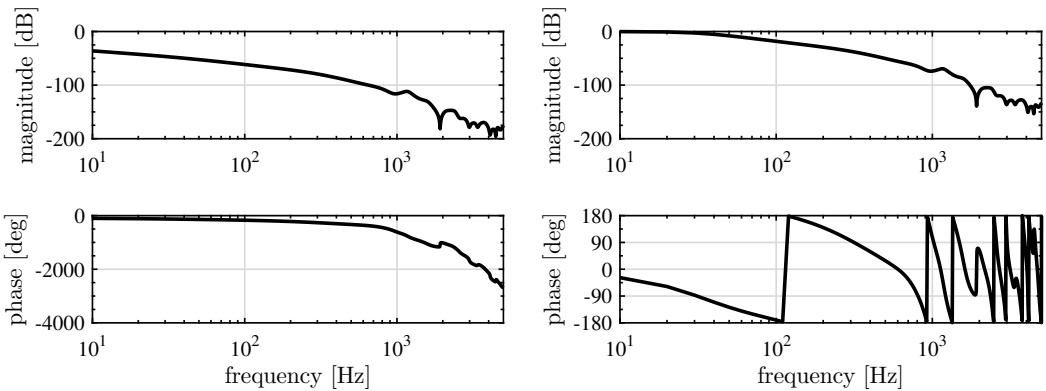
(a) Plant (from voltage to current).

(b) Closed loop system of the current loop.



(c) Plant (from force to velocity).

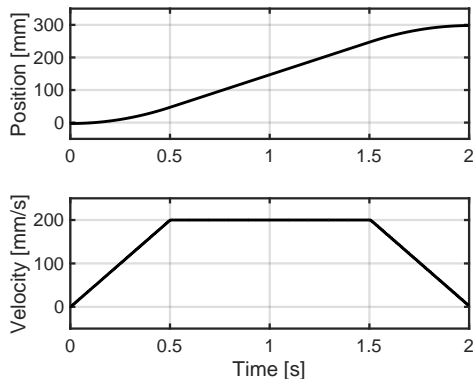
(d) Closed loop system of the velocity loop.



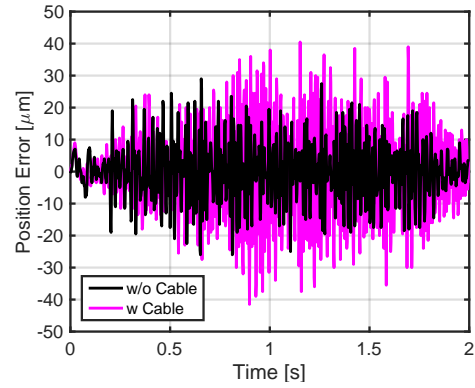
(e) Plant (from force to position).

(f) Closed loop system of the position loop.

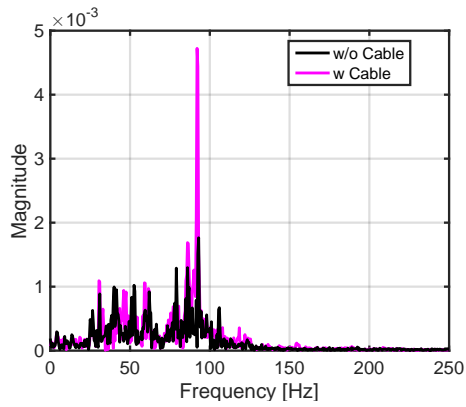
Fig. 66: Frequency response of the system.



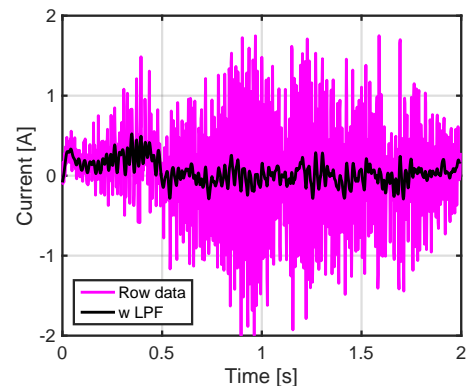
(a) Target trajectory.



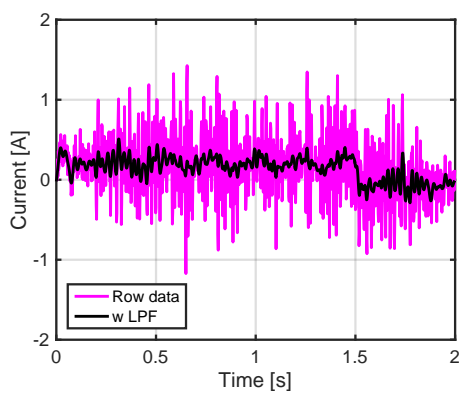
(b) Position error.



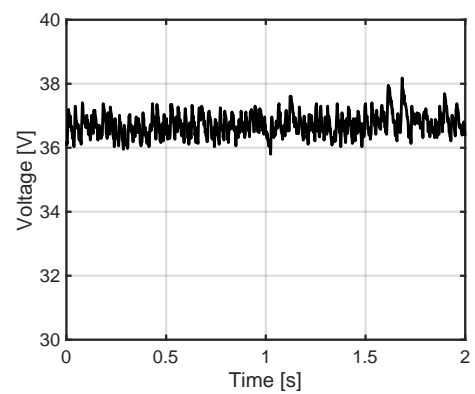
(c) Position error FFT.



(d) q-axis current of wired case.



(e) q-axis current of wireless case.



(f) DC link voltage.

Fig. 67: Experimental results.

# Chapter 9

## Control for multi-axis high-precision stage using wireless power transfer

### 9.1 Experimental verification of disturbance caused by cable tension in WHPS2

First, this chapter analyzes the cable disturbance of Y-axis coarse stage. Fig. 68(g) shows the target position and velocity trajectories of the stage. The target position trajectory whose movement distance is 160 mm is based on a trapezoidal velocity trajectory with maximum velocity 160 mm/s. The trajectories from 0.0 s to 0.5 s are in the acceleration region. The trajectories from 0.5 s to 1.0 s are in the constant velocity region. The trajectories from 1.0 s to 1.5 s are in the deceleration region. A proportional-integral (PI) current controller, PI velocity controller, and P position controller are designed for WHPS2 so that the closed-loop bandwidth of the current, velocity, and position can be 2500 Hz, 100 Hz, 15 Hz, respectively. The DC link voltage is controlled to be 30 V by using 2-mode methods on the Y-axis.

Experimental results in the constant velocity region are shown in Fig. 68. Experiments are conducted three times to verify the reproducibility, and these are shown in black solid line, red solid line, and blue dotted line. From Fig. 68(a), 69(b), tracking error is obviously improved by using WPT technology. Fig. 68(e), 68(f) show the disturbance estimated by a disturbance observer by using the plant model of WHPS2 shown in Fig. 9. The disturbance is mainly caused by the tension of cable because the friction disturbance is included in the plant model. From these figures, the amplitude of disturbance is reduced by multi-axis WHPS.

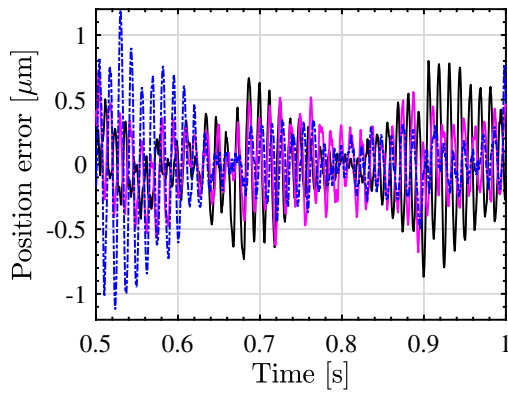
Fig. 70 shows a frequency analysis of the estimated disturbance. From Fig. 69(a), the disturbance caused by the cable tension happens in the low frequency region (less than 10 Hz) without reproducibly and at 70 Hz. On the other hand, the disturbance caused by the cable tension is significantly

reduced by multi-axis WHPS shown in Fig. 69(b) and Fig. 69(c).

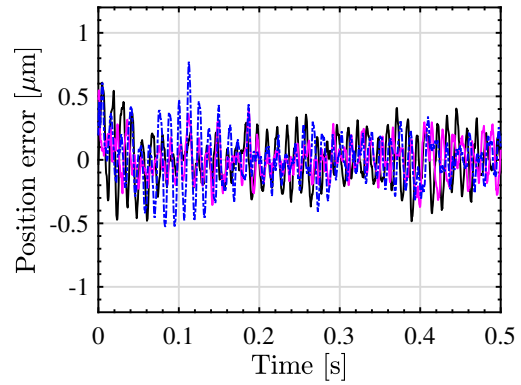
From Fig. 69(b) and Fig. 69(c), the estimated disturbance has large peak at a relatively high frequency. This experiment uses the cable carrier which connects many links shown in Fig. 70(a), thus vibration may occur when the link grounds. Fig. 70(b) shows a frequency analysis result when the different speed. From Fig. 70(b), the frequency of estimated disturbance is shifted as the speed of the stage increases. For this reason, it is believed that the grounding of the links causes the disturbance at the relatively high frequency.

From the above analysis, the experimental results show WHPS drastically solve the disturbance caused by the tension of cables.

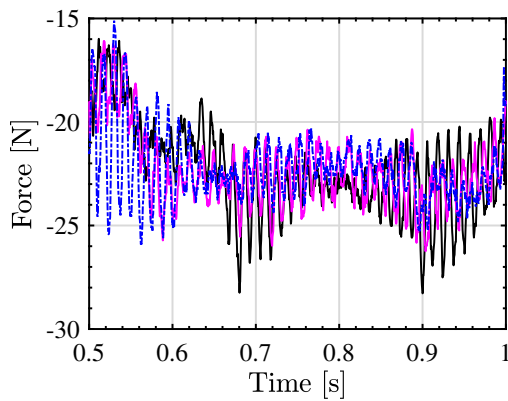




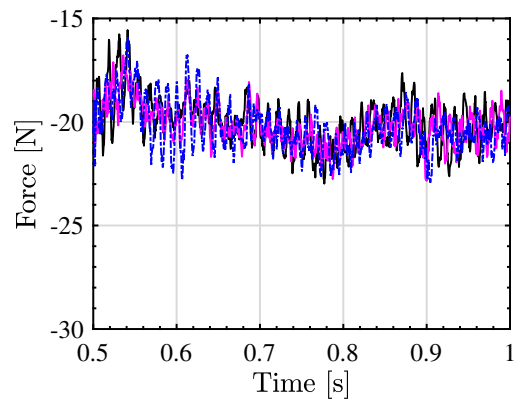
(a) Tracking error (with cable).



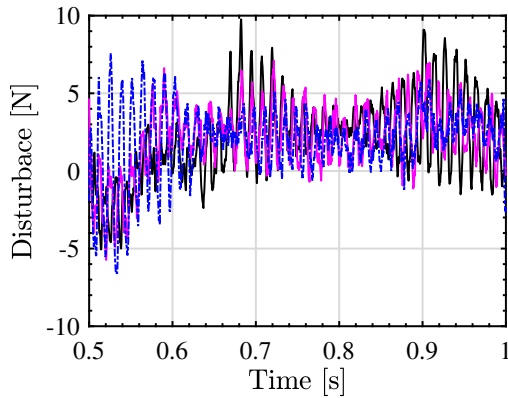
(b) Tracking error (w/o cable).



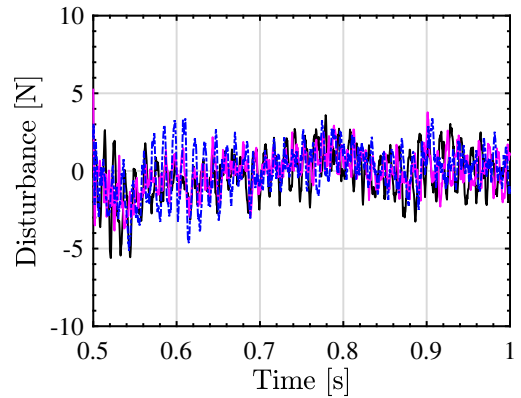
(c) Thrust (with cable).



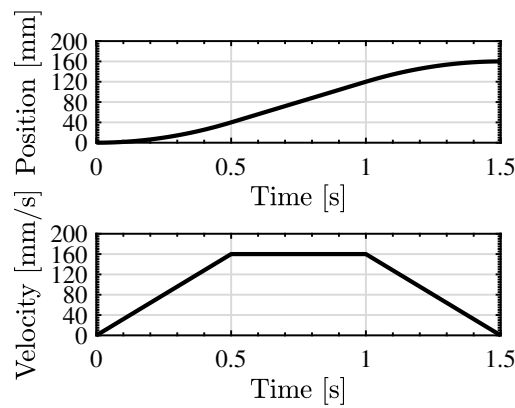
(d) Thrust (w/o cable).



(e) Estimated disturbance (with cable).

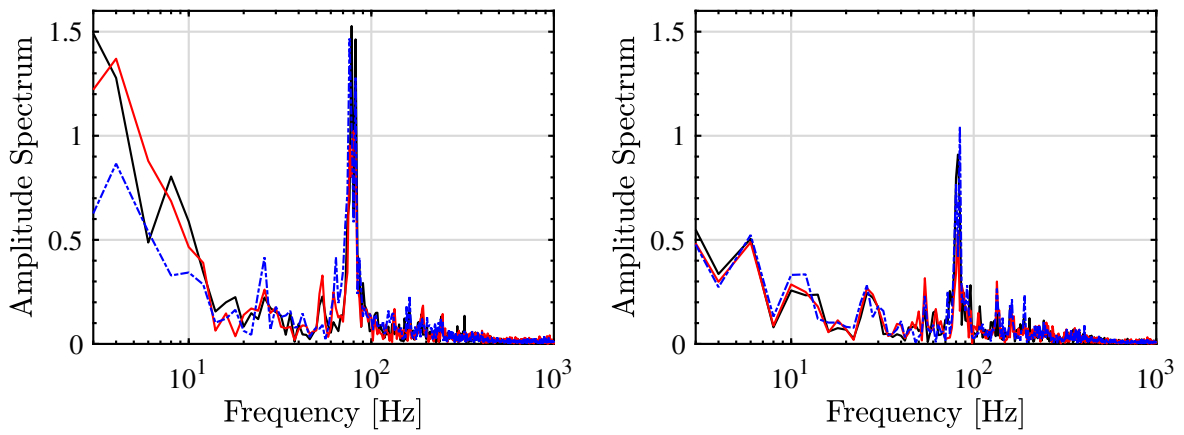


(f) Estimated disturbance (w/o cable).



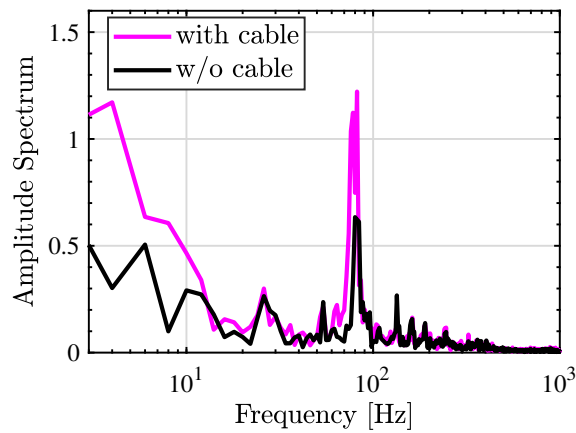
(g) Target trajectory.

Fig. 68: Experimental results.



(a) Frequency analysis result (with cable).

(b) Frequency analysis result (w/o cable).

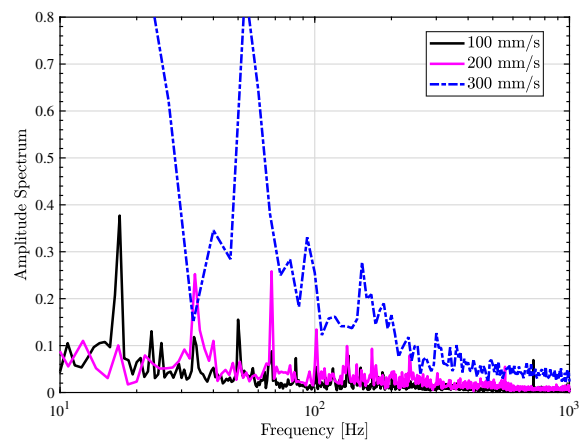


(c) Comparison with average of frequency analysis result of estimated disturbance.

Fig. 69: Frequency analysis of estimated disturbance.



(a) Cable carrier used in the experiment.



(b) Frequency analysis in the case of different velocity.

Fig. 70: Comparison with frequency analysis results in different speed.

## 9.2 Transmitting power feedforward control using target trajectory in WHPS2

### 9.2.1 Power consumption of the primary side when using 2-mode method

In the precision positioning stage, it is important to increase the power transmission efficiency of WPT to avoid an increase in temperature. Therefore, this section derives the target trajectory of required power from the target trajectory of the stage to achieving higher efficiency.

The RMS values of current of the primary side in the short mode  $I_{1s}$  and the rectification mode  $I_{1r}$  are

$$I_{1s} \simeq \frac{R_2 V_{DC}}{R_1 R_2 + (\omega_0 L_m)^2}, \quad (9-1)$$

$$I_{1r} \simeq \frac{R_2 V_{DC} + \frac{2\sqrt{2}}{\pi} \omega_0 L_m V_L}{R_1 R_2 + (\omega_0 L_m)^2}. \quad (9-2)$$

From these equations, the power supplied by the primary inverter are given as

$$P_{1s} \simeq \frac{R_2 V_{DC}^2}{R_1 R_2 + (\omega_0 L_m)^2}, \quad (9-3)$$

$$P_{1r} \simeq \frac{R_2 V_{DC} + \frac{2\sqrt{2}}{\pi} \omega_0 L_m V_L}{R_1 R_2 + (\omega_0 L_m)^2} V_{DC}. \quad (9-4)$$

The RMS value of the input voltage is calculated by the fourier series of the DC input voltage.

$$V_{DC} = \frac{2\sqrt{2}}{\pi} V_1 \quad (9-5)$$

The ratio of short and rectification modes is defines as follows to calculate the overall input power.

$$m_p = \frac{t_s}{t_s + t_r} \quad (9-6)$$

$$= \frac{\ln\left(\frac{V_{low}}{V_{up}}\right)}{\ln\left(\frac{V_{low}}{V_{up}}\right) + \ln\left(\frac{V_{up} + R_L I_a}{V_{low} + R_L I_a}\right)} \quad (9-7)$$

Here,  $V_{up}$  and  $V_{low}$  are the upper and lower limit of hysteresis comparator.  $I_a$  which is the output current of the secondary converter is given as

$$I_a = \frac{2\sqrt{2} \omega_0 L_m V_{DC} - \frac{2\sqrt{2}}{\pi} R_1 V_L}{R_1 R_2 + (\omega_0 L_m)^2}. \quad (9-8)$$

The overall input power is derived by

$$P_1 = m_p P_{1s} + (1 - m_p) P_{1r} \quad (9-9)$$

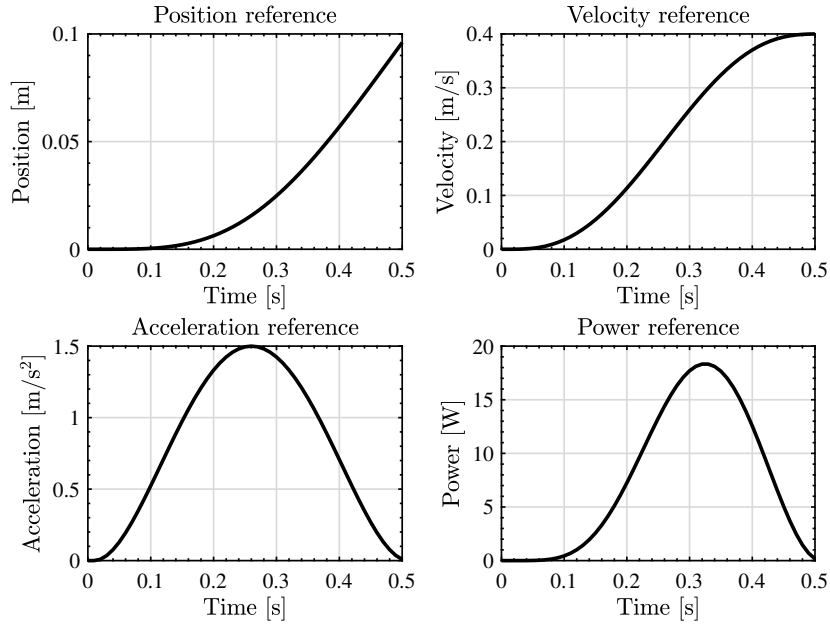


Fig. 71: Target position, velocity, acceleration, and load power trajectories.

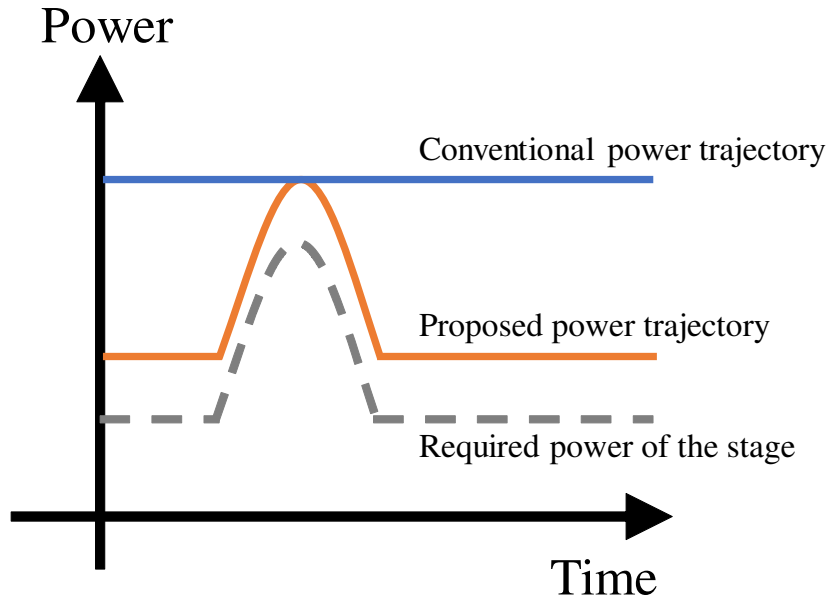


Fig. 72: Conceptual diagram of reference signal of transmission power.

### 9.2.2 Input voltage control based on load power trajectory

This section assumes the DC link voltage on the secondary side is constant. Then, the relationship between the input voltage and the load power is given in

$$V_1 = \frac{R_1}{\omega_0 L_m} \left\{ V_2 + \frac{(1 + \frac{L_m^2 \omega_0^2}{R_1 R_2}) R_2 P_L}{V_2} \right\} \quad (9-10)$$

Conceptual diagram of power reference signal is shown in Fig. 72. The required load power trajectory

Tab. 22: Trade-off of the transmission efficiency and loss.

	Proposed	Conventional
$V_1$	Time-variant	Constant
$V_L$	2-mode	2-mode
Short mode loss	Large	Small
WPT efficiency	High	Low

Tab. 23: Experimental result.

Method	Overall input power [W]
Conventional (40 V)	46.8
Conventional (24 V)	40.4
Proposed	39.0

is given in advance. The input voltage trajectory of the proposed method is determined by (9-10), and that of the conventional method is constant value which matches maximum value of the proposed method. The proposed method can reduce the loss in the short mode by modifying voltage reference, however, the WPT efficiency of the proposed method becomes worse than that of the conventional method. Comparison of each method is summarized in Tab. 22.

### 9.2.3 Experimental verification of input voltage control based on load power trajectory

The experimental setup is shown in Fig. 73. This experiment only uses the Y-axis of WHPS2 for simplicity. Signals of the time-variant input voltage is generated by Arduino, and the signals are amplified by voltage amplifier. Input voltage and current are measured by calculating transmission power.

The experimental results are shown in Fig. 74. The velocity trajectory of the stage shown in Fig. 74(a) consists of acceleration, constant velocity, and deceleration region. From Fig. 74(b), the input voltage signal is modified based on the target power trajectory. Then, the time of short mode becomes small shown in Fig. 74(d). From Fig. 74(c), the overall input power is calculated and summarized in Tab. 23. The overall transmission power of the proposed method is smaller than that of the conventional method. It is shown that the voltage signal modification can improve the total efficiency of whole system.

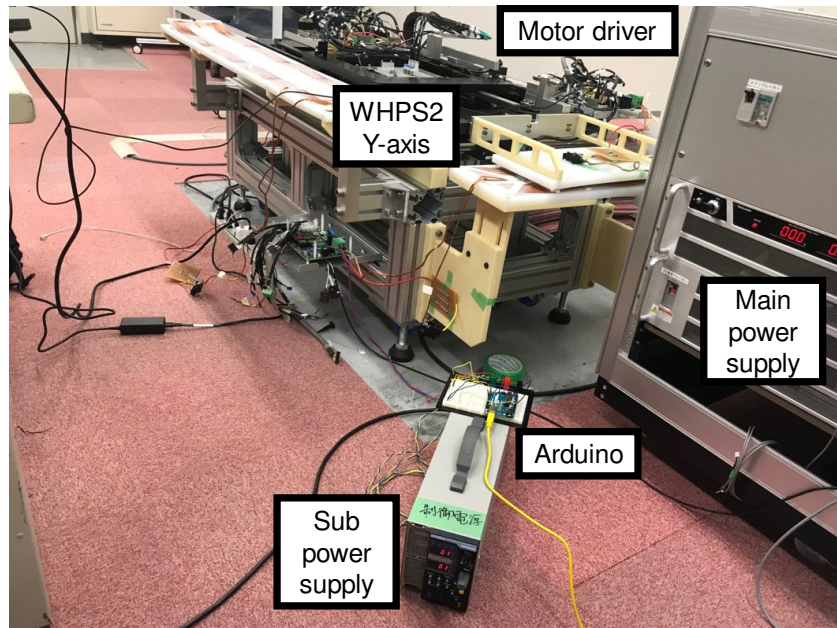
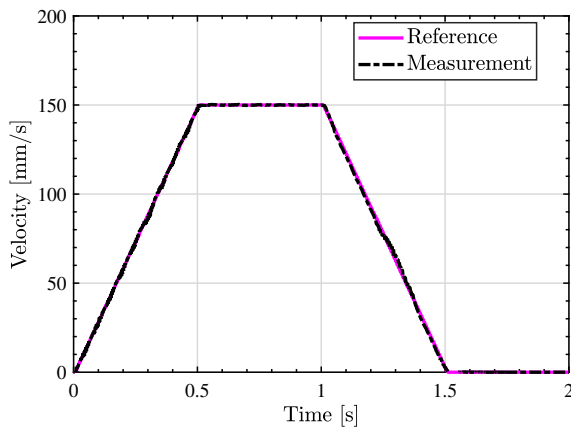


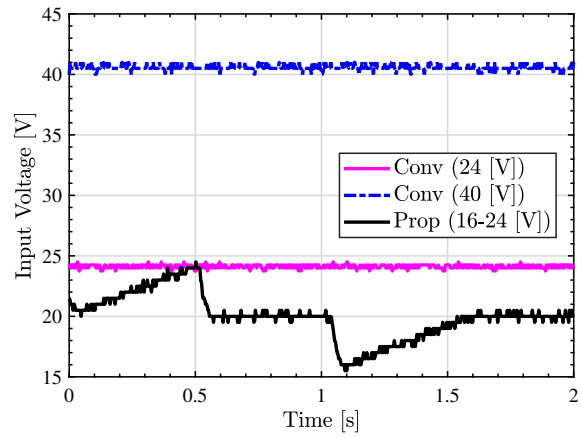
Fig. 73: Experimental setup of primary voltage modification

### 9.3 Conclusion of control system design for WHPS2

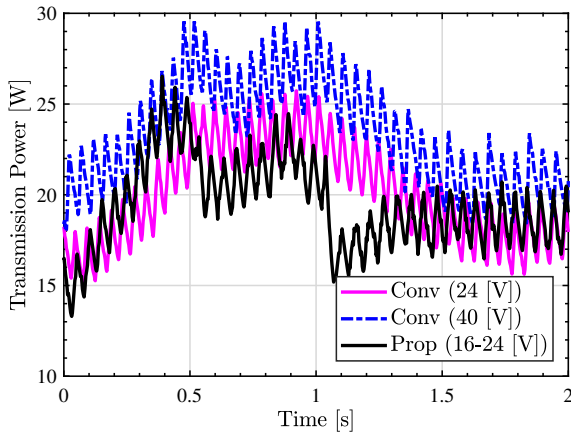
In this study, a novel multi-axis high precision stage using WPT technology was proposed. The paper focused on a coil design method considering the required specifications for WHPS2. The designed coil satisfied all requirements and the experimental result demonstrates the effectiveness of WHPS2. Future research could consider the performance associated with optimal voltage control on the receiving side and the regeneration to the transmission side.



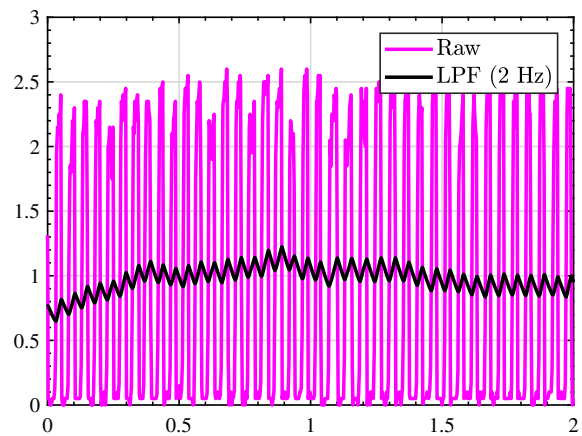
(a) Velocity trajectory of WHPS2.



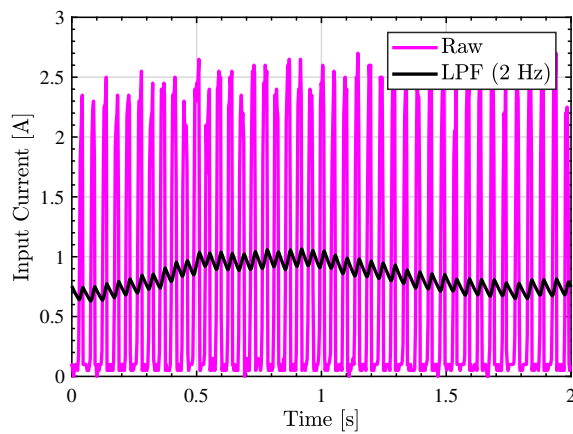
(b) Voltage trajectory of each method.



(c) Transmission power.



(d) Primary current (Proposed).



(e) Primary current (Conventional).

Fig. 74: Experimental result of the primary voltage modification.

# Chapter 10

## Conclusion

Semiconductor and liquid crystal manufacturing equipment is a equipment to produce semiconductors and liquid crystal displays, and to increase the size, speed, and accuracy of the equipment is required to produce high performance and low price products. There are several causes which degrade the position accuracy of the high-precision stage. This thesis focused on the mechanical resonance and the cable disturbance, and solved these problems by proposing high-precision stages with novel mechanical structure.

In chapter 1, the background of the high-precision control was introduced and the error factors in the high-precision stage are classified. This thesis is roughly divided into two parts, which are described about the mechanical resonance in chapter 2–5, and the cable disturbance in chapter 6–9.

Chapter 2 introduces a novel high-precision stage called a catapult stage which has a new mechanical structure with the coarse and fine motion coupling and separation mechanism to improve the mechanical resonance. The conventional high-precision stage aims to reduce the weight of fine part by using dual-actuator structure, however, an actuator for driving the fine part becomes large because the fine and coarse parts should have same acceleration to avoid contact with each other. Therefore, it is difficult to increase the FB bandwidth of the fine part in conventional high-precision stage because the fine part need to have a large motor to accelerate itself, and it is expected that the limit of the throughput is close. Our laboratory designed the catapult stage which allows contact between the coarse and fine stages to solve this problem. The thrust of the fine stage becomes small because the fine stage does not need to accelerate and decelerate itself. As a result, the control performance of the fine stage is improved by reducing the weight of the actuator in the fine stage.

Next, chapter 3 proposed a basis control system design for the catapult stage which considers the characteristics of the catapult stage. However, the basic control system cannot avoid a tracking error at the beginning of the constant velocity region because the control system drives the fine stage after entering the constant velocity region. Therefore, chapter 4 proposes a feedforward control considering with constraints in the acceleration region. This chapter derives the mode switching condition using



final state control with constraints and generates the trajectory at the end of acceleration region. Then, the tracking error at the beginning of the constant velocity region becomes zero considering with thrust limitations.

In addition, in chapter 5, a feedback control method considering with constraints in the constant velocity region to improve a disturbance suppression performance was proposed. In general, a two-degrees-of-freedom control that combines feedforward and feedback control is widely used in a trajectory tracking control for a high-precision stage. The FF control is mainly used to improve the tracking performance, and the FB controller is usually designed to optimize its performance related to suppression of disturbance that is analyzed and expected in advance. In this case, the controller achieves good suppression of expected disturbances. However, performance related to the suppression of sudden and unexpected disturbances may degrade because of actuator saturation. Therefore, the FB controller should be able to manage not only expected disturbances but also sudden disturbances. Chapter 5 proposed a suppression control method for sudden disturbances based on model predictive control and RG. The proposed method makes it possible to improve the disturbance suppression performance within the constraints by modifying the reference signals properly. A basic control methods described in chapters 3, 4 and 5 establish for the practical catapult stage.

Chapter 6 introduced previous studies about the cable disturbance which is an another cause of tracking error in the high-precision stage. To reduce the cable disturbance, contactless actuators (e.g. linear motors and voice coil motors) and contactless gravity compensation (e.g. air bearings and magnetic levitation) are commonly used to avoid floor vibrations and friction of the high-precision stages. However, in reality, power cables, sensor cables, and cooling pipes are all connected. The power cable issue can be addressed by the moving magnet design, but the moving component becomes heavier, which is problematic because its control bandwidth is limited by the resonance frequency inversely proportional to the mass. In order to solve this problem, chapter 6 proposed novel high-precision stages using wireless power transfer (WPT) with magnetic resonance coupling. One is a single-axis wireless high-precision stage driven by WPT (Wireless High Precision Stage 1 : WHPS1), and the other is a multi-axis wireless high-precision stage (WHPS2). WHPS1 was designed to verify the required technology and conditions for applying WPT to the high-precision stage. WHPS2 has the feature of performing WPT over two stages, and system design considering its characteristics is important. In addition, coil design considering required specifications is necessary because the required specifications such as power and efficiency are given in advance from the target trajectory and the rating of the motor driver.

Therefore, chapter 7 proposed a coil design method considering the required specification for 85 kHz WPT system. In many studies on WPT, the coil design is performed empirically, and there are few studies on theoretical coil design method. Chapter 7 described a coil design method considering various required specifications such as efficiency, transmission power, and transmitting and receiving side voltage. For that purpose, chapter 7 first formulated the optimization problem to be solved for

coil design, and describe the calculation method of mutual inductance and AC resistance of the coil. Finally, the coil satisfying the desired condition can be designed by solving the optimization problem.

In chapter 8,9, the effect of the cable disturbance is discussed by driving WHPS1 and WHPS2. In this system, S-S circuit topology is used, however in general, the system becomes unstable if the constant power load is connected to the S-S circuit topology. Thus, the DC link voltage is stabilized by performing 2-mode method using the hysteresis comparator on the power receiving side in WHPS1 and WHPS2. It is shown that the tracking performance is greatly improved by using WHP in the high-precision stage by analyzing the tracking error in the case of using or not using the cable carrier.

Finally, chapter 9 describes the control method of WHPS2. WHPS2 has the characteristics of performing multi-stage WHP, and control system design considering its characteristics is important. Therefore, chapter 9 derives the optimal power trajectory from the target position trajectory to achieve higher power transmission efficiency. The concept of multi-axis high-precision stage using WHP can be realized by using WHPS2, and WHPS2 drastically solves the cable disturbance which has been considered difficult to solve.

From the above, this thesis solved two major causes of tracking error which are mechanical resonance and the cable disturbance by proposing high-precision stages with novel mechanical structure. Studies of chapters 2–5 made it possible to drive the catapult stage on the actual target trajectory, and the fundamental methods for the practical catapult stage were established. In addition, the control method proposed in chapters 3–5 can be widely applied to another control systems with constraints. A series of studies proposed a control system design that considers constraints both feedforward control and feedback control, and a new framework of the control system with constraints was established. The method proposed in this thesis can be applied to real industrial machines because not only theoretical proposal and verification by simulation but also experimental verifications were performed. The control method proposed in this thesis will improve the performance of the industrial machines because conservativeness of mechanical design can be reduced by explicitly considering constraints.

The studies of chapters 6–9 codified the system design methods for WHPS by examined various technologies of WPT. The multi-axis high-precision stage using WPT can be realized, and its effectiveness is shown by experiment. In addition, the coil design method for WPT proposed in this thesis is also applicable to general systems having required specifications. WPT technology will be further expanded because the proposed coil design method reduces labor of coil design.

I hope that the ultimate high-precision stage which eliminates all causes of tracking error will be completed by integrating these two novel high-precision stages.

## **Acknowledgement**

This work was partly supported by JSPS KAKENHI Grant Number 18H03768.

# Chapter 11

## Appendix

### 11.1 Derivations of coefficient in (4-11)

Coefficients of a discrete-time state-space equation  $\mathbf{A}$ ,  $\mathbf{B}$  and  $\mathbf{C}$  are given by (11-1) because the plant model  $P(s)$  is defined in (5-8).

$$\mathbf{A} = \begin{bmatrix} 1 & \tau \\ 0 & 1 \end{bmatrix}, \quad \mathbf{B} = \begin{bmatrix} \frac{\tau^2}{2M} & \frac{\tau}{M} \end{bmatrix}^T, \quad \mathbf{C} = \begin{bmatrix} 1 & 0 \end{bmatrix} \quad (11-1)$$

Here,  $\tau$  is the control period. First of all, let us consider  $\mathbf{Q}^{-1}\boldsymbol{\Sigma}^T(\boldsymbol{\Sigma}\mathbf{Q}^{-1}\boldsymbol{\Sigma}^T)^{-1}$ .  $\mathbf{Q}$  is a unit matrix to minimize the energy consumption.  $\mathbf{A}^n$ ,  $\mathbf{A}^{n-1}\mathbf{B}$  need to be calculated because  $\boldsymbol{\Sigma}$  is given in (4-10).  $a_{ij}$  and  $b_j$  are expressed in (11-2) by  $\mathbf{A}^n$  and  $\mathbf{A}^n\mathbf{B}$ .

$$\mathbf{A}^n = \begin{bmatrix} 1 & n\tau \\ 0 & 1 \end{bmatrix}, \quad \mathbf{A}^n\mathbf{B} = \begin{bmatrix} 1 & n\tau \\ 0 & 1 \end{bmatrix} \begin{bmatrix} \frac{\tau^2}{2M} \\ \frac{\tau}{M} \end{bmatrix} = \begin{bmatrix} \frac{\tau^2}{M} \left\{ \frac{1}{2} + n \right\} \\ \frac{\tau}{M} \end{bmatrix}, \quad \begin{bmatrix} a_{11} & a_{12} \\ a_{21} & a_{22} \end{bmatrix} = \mathbf{A}^k|_{k=N}, \quad \begin{bmatrix} b_1 \\ b_2 \end{bmatrix} = \mathbf{A}^k\mathbf{B}|_{k=N} \quad (11-2)$$

Thus,  $\boldsymbol{\Sigma}_{\text{tr}}$  is given by (11-3)

$$\boldsymbol{\Sigma}_{\text{tr}} = \begin{bmatrix} \mathbf{A}^{N-2}\mathbf{B} & \cdots & \mathbf{B} \end{bmatrix} = \begin{bmatrix} \frac{\tau^2}{M} \left\{ \frac{1}{2} + (N-2) \right\} & \cdots & \frac{\tau^2}{M} \left\{ \frac{1}{2} + (N-N) \right\} \\ \frac{\tau}{M} & \cdots & \frac{\tau}{M} \end{bmatrix} \quad (11-3)$$

Therefore,  $\boldsymbol{\Sigma}_{\text{tr}}\boldsymbol{\Sigma}_{\text{tr}}^T$  is provided in (11-4).

$$\boldsymbol{\Sigma}_{\text{tr}}\boldsymbol{\Sigma}_{\text{tr}}^T = \begin{bmatrix} \frac{\tau^2}{M} \left\{ \frac{1}{2} + (N-2) \right\} & \cdots & \frac{\tau^2}{M} \left\{ \frac{1}{2} + (N-N) \right\} \\ \frac{\tau}{M} & \cdots & \frac{\tau}{M} \end{bmatrix} \begin{bmatrix} \frac{\tau^2}{M} \left\{ \frac{1}{2} + (N-2) \right\} \\ \vdots \\ \frac{\tau^2}{M} \left\{ \frac{1}{2} + (N-N) \right\} \\ \frac{\tau}{M} \end{bmatrix} = \begin{bmatrix} \frac{\tau^4}{M^2} \sum_{k=0}^{N-2} \left( k + \frac{1}{2} \right)^2 & \frac{\tau^3}{M^2} \sum_{k=0}^{N-2} \left( k + \frac{1}{2} \right) \\ \frac{\tau^3}{M^2} \sum_{k=0}^{N-2} \left( k + \frac{1}{2} \right) & \frac{\tau^2}{M^2} (N-1) \end{bmatrix} \quad (11-4)$$

Next, a determinant  $|\boldsymbol{\Sigma}_{\text{tr}}\boldsymbol{\Sigma}_{\text{tr}}^T|$  and a cofactor matrix  $\text{adj}(\boldsymbol{\Sigma}_{\text{tr}}\boldsymbol{\Sigma}_{\text{tr}}^T)$  should be calculated in order to obtain the inverse matrix  $(\boldsymbol{\Sigma}_{\text{tr}}\boldsymbol{\Sigma}_{\text{tr}}^T)^{-1}$ . The determinant  $|\boldsymbol{\Sigma}_{\text{tr}}\boldsymbol{\Sigma}_{\text{tr}}^T|$  and the cofactor matrix  $\text{adj}(\boldsymbol{\Sigma}_{\text{tr}}\boldsymbol{\Sigma}_{\text{tr}}^T)$  are shown in (11-5), respectively.

$$|\boldsymbol{\Sigma}_{\text{tr}}\boldsymbol{\Sigma}_{\text{tr}}^T| = \frac{\tau^6}{M^4} \left[ \sum_{k=0}^{N-2} \left( k + \frac{1}{2} \right)^2 (N+1) - \left\{ \sum_{k=0}^{N-2} \left( k + \frac{1}{2} \right) \right\}^2 \right], \quad \text{adj}(\boldsymbol{\Sigma}_{\text{tr}}\boldsymbol{\Sigma}_{\text{tr}}^T) = \begin{bmatrix} \frac{\tau^2}{M^2} (N-1) & -\frac{\tau^3}{M^2} \sum_{k=0}^{N-2} \left( k + \frac{1}{2} \right) \\ -\frac{\tau^3}{M^2} \sum_{k=0}^{N-2} \left( k + \frac{1}{2} \right) & \frac{\tau^4}{M^2} \sum_{k=0}^{N-2} \left( k + \frac{1}{2} \right)^2 \end{bmatrix} \quad (11-5)$$

Finally,  $\Sigma_{\text{tr}}^T (\Sigma_{\text{tr}} \Sigma_{\text{tr}}^T)^{-1}$  is derived in (11-6).

$$\Sigma_{\text{tr}}^T (\Sigma_{\text{tr}} \Sigma_{\text{tr}}^T)^{-1} = \begin{bmatrix} \frac{\tau^2}{M} \{\frac{1}{2} + (N-2)\} & \frac{\tau}{M} \\ \vdots & \vdots \\ \frac{\tau^2}{M} \{\frac{1}{2} + (N-N)\} & \frac{\tau}{M} \end{bmatrix} \cdot \begin{bmatrix} \frac{\tau^2}{M^2} (N-1) & -\frac{\tau^3}{M^2} \sum_{k=0}^{N-2} (k+\frac{1}{2}) \\ -\frac{\tau^3}{M^2} \sum_{k=0}^{N-2} (k+\frac{1}{2}) & \frac{\tau^4}{M} \sum_{k=0}^{N-2} (k+\frac{1}{2})^2 \end{bmatrix} \cdot \frac{M^4}{\tau^6} \frac{1}{\left[ \sum_{k=0}^{N-2} (k+\frac{1}{2})^2 (N+1) - \left\{ \sum_{k=0}^{N-2} (k+\frac{1}{2}) \right\}^2 \right]} \quad (11-6)$$

Besides, the sum of the 1th, 2nd, 3rd and 4th power of a natural number is expressed by (11-7), respectively.

$$\sum_{k=1}^n k = \frac{1}{2}n(n+1), \quad \sum_{k=1}^n k^2 = \frac{1}{6}n(n+1)(2n+1), \quad \sum_{k=1}^n k^3 = \frac{1}{4}n^2(n+1)^2, \quad \sum_{k=1}^n k^4 = \frac{1}{30}n(n+1)(2n+1)(3n^2+3n-1) \quad (11-7)$$

By substituting (11-7) into (11-6), (11-8) is obtained.

$$q_{i1} = \frac{6M}{\tau^2(N-2)(N-1)} (N-2i+2) \quad (11-8)$$

$$q_{i2} = \frac{M}{\tau(N-2)(N-1)N} \{-2N^2 + (-5+6i)N + (6-6i)\}$$

## 11.2 Derivations of coefficient in (4-16)

Coefficients of a state-space equation of an augment system  $\mathbf{A}_{\text{aug}}$ ,  $\mathbf{B}_{\text{aug}}$  and  $\mathbf{C}_{\text{aug}}$  are given by (11-9).

$$\mathbf{A}_{\text{aug}} = \begin{bmatrix} 1 & \tau & \frac{\tau^2}{2M} \\ 0 & 1 & \frac{\tau}{M} \\ 0 & 0 & 1 \end{bmatrix}, \quad \mathbf{B}_{\text{aug}} = \begin{bmatrix} 0 & 0 & 1 \end{bmatrix}^T, \quad \mathbf{C}_{\text{aug}} = \begin{bmatrix} 1 & 0 & 0 \end{bmatrix} \quad (11-9)$$

First of all, let us consider  $\mathbf{Q}^{-1} \Sigma_{\text{aug}}^T (\Sigma_{\text{aug}} \mathbf{Q}^{-1} \Sigma_{\text{aug}}^T)^{-1}$  in (4-14).  $\mathbf{Q}$  is a unit matrix to minimize the jerk.  $\mathbf{A}_{\text{aug}}^n$  and  $\mathbf{A}_{\text{aug}}^n \mathbf{B}_{\text{aug}}$  need to be calculated because  $\Sigma_{\text{aug}}$  is given in (4-3).  $a_{ij}$  is expressed in (11-10) by  $\mathbf{A}_{\text{aug}}^n$  and  $\mathbf{A}_{\text{aug}}^n \mathbf{B}_{\text{aug}}$ .

$$\mathbf{A}_{\text{aug}}^n = \begin{bmatrix} 1 & n\tau & \frac{n^2\tau^2}{2M} \\ 0 & 1 & \frac{n\tau}{M} \\ 0 & 0 & 1 \end{bmatrix}, \quad \mathbf{A}_{\text{aug}}^n \mathbf{B}_{\text{aug}} = \begin{bmatrix} 1 & n\tau & \frac{n^2\tau^2}{2M} \\ 0 & 1 & \frac{n\tau}{M} \\ 0 & 0 & 1 \end{bmatrix} \begin{bmatrix} 0 \\ 0 \\ 1 \end{bmatrix} = \begin{bmatrix} \frac{n^2\tau^2}{2M} \\ \frac{n\tau}{M} \\ 1 \end{bmatrix}, \quad \begin{bmatrix} a_{11} & a_{12} & a_{13} \\ a_{21} & a_{22} & a_{23} \\ a_{31} & a_{32} & a_{33} \end{bmatrix} = \mathbf{A}_{\text{aug}}^k|_{k=N} \quad (11-10)$$

Thus,  $\Sigma_{\text{aug}}$  is given by (11-11)

$$\Sigma_{\text{aug}} = \begin{bmatrix} \mathbf{A}_{\text{aug}}^{N-1} \mathbf{B}_{\text{aug}} & \mathbf{A}_{\text{aug}}^{N-2} \mathbf{B}_{\text{aug}} & \cdots & \mathbf{B}_{\text{aug}} \end{bmatrix} = \begin{bmatrix} \frac{(N-1)^2\tau^2}{2M} & \frac{(N-2)^2\tau^2}{2M} & \cdots & 0 \\ \frac{(N-1)\tau}{M} & \frac{(N-2)\tau}{M} & \cdots & 0 \\ 1 & 1 & \cdots & 1 \end{bmatrix} \quad (11-11)$$

Therefore,  $\Sigma_{\text{aug}} \Sigma_{\text{aug}}^T$  is provided in (11-12).

$$\Sigma_{\text{aug}} \Sigma_{\text{aug}}^T = \begin{bmatrix} \frac{(N-1)^2\tau^2}{2M} & \frac{(N-2)^2\tau^2}{2M} & \cdots & 0 \\ \frac{(N-1)\tau}{M} & \frac{(N-2)\tau}{M} & \cdots & 0 \\ 1 & 1 & \cdots & 1 \end{bmatrix} \begin{bmatrix} \frac{(N-1)^2\tau^2}{2M} & \frac{(N-1)\tau}{M} & 1 \\ \frac{(N-2)^2\tau^2}{2M} & \frac{(N-2)\tau}{M} & 1 \\ \vdots & \vdots & \vdots \\ 0 & 0 & 1 \end{bmatrix} = \begin{bmatrix} \frac{\tau^4}{4M^2} \sum_{k=0}^{N-1} k^4 & \frac{\tau^3}{2M^2} \sum_{k=0}^{N-1} k^3 & \frac{\tau^2}{2M} \sum_{k=0}^{N-1} k^2 \\ \frac{\tau^3}{2M^2} \sum_{k=0}^{N-1} k^3 & \frac{\tau^2}{M^2} \sum_{k=0}^{N-1} k^2 & \frac{\tau}{M} \sum_{k=0}^{N-1} k \\ \frac{\tau^2}{2M} \sum_{k=0}^{N-1} k^2 & \frac{\tau}{M} \sum_{k=0}^{N-1} k & N \end{bmatrix} \quad (11-12)$$

Next, a determinant  $|\Sigma_{\text{aug}}\Sigma_{\text{aug}}^T|$  and a cofactor matrix  $\text{adj}(\Sigma_{\text{aug}}\Sigma_{\text{aug}}^T)$  should be calculated in order to obtain the inverse matrix  $(\Sigma_{\text{aug}}\Sigma_{\text{aug}}^T)^{-1}$ . The determinant  $|\Sigma_{\text{aug}}\Sigma_{\text{aug}}^T|$  and the cofactor matrix  $\text{adj}(\Sigma_{\text{aug}}\Sigma_{\text{aug}}^T)$  are shown in (11-13), (11-14), respectively.

$$|\Sigma_{\text{aug}}\Sigma_{\text{aug}}^T| = \frac{\tau^6}{4M^4} \left\{ \sum_{k=0}^{N-1} k^2 \sum_{k=0}^{N-1} k^4 \cdot N + 2 \sum_{k=0}^{N-1} k \sum_{k=0}^{N-1} k^2 \sum_{k=0}^{N-1} k^3 - \left( \sum_{k=0}^{N-1} k^2 \right)^3 - \left( \sum_{k=0}^{N-1} k \right)^2 \sum_{k=0}^{N-1} k^4 - \left( \sum_{k=0}^{N-1} k^3 \right)^2 \cdot N \right\} \quad (11-13)$$

$$\text{adj}(\Sigma_{\text{aug}}\Sigma_{\text{aug}}^T) = \begin{bmatrix} \frac{\tau^2}{M^2} \left( \sum_{k=0}^{N-1} k^2 \cdot N - \left( \sum_{k=0}^{N-1} k \right)^2 \right) & -\frac{\tau^3}{2M^2} \left( \sum_{k=0}^{N-1} k^3 \cdot N - \sum_{k=0}^{N-1} k \sum_{k=0}^{N-1} k^2 \right) & \frac{\tau^3}{M^4} \left( \sum_{k=0}^{N-1} k \sum_{k=0}^{N-1} k^3 - \left( \sum_{k=0}^{N-1} k^2 \right)^2 \right) \\ -\frac{\tau^3}{2M^2} \left( \sum_{k=0}^{N-1} k^3 \cdot N - \sum_{k=0}^{N-1} k \sum_{k=0}^{N-1} k^2 \right) & \frac{\tau^4}{4M^2} \left( \sum_{k=0}^{N-1} k^4 \cdot N - \left( \sum_{k=0}^{N-1} k^2 \right)^2 \right) & -\frac{\tau^5}{4M^2} \left( \sum_{k=0}^{N-1} k \sum_{k=0}^{N-1} k^4 - \sum_{k=0}^{N-1} k^2 \sum_{k=0}^{N-1} k^3 \right) \\ \frac{\tau^2}{M^2} \left( \sum_{k=0}^{N-1} k \sum_{k=0}^{N-1} k^3 - \left( \sum_{k=0}^{N-1} k^2 \right)^2 \right) & -\frac{\tau^5}{4M^3} \left( \sum_{k=0}^{N-1} k \sum_{k=0}^{N-1} k^4 - \sum_{k=0}^{N-1} k^2 \sum_{k=0}^{N-1} k^3 \right) & \frac{\tau^6}{4M^4} \left( \sum_{k=0}^{N-1} k^2 \sum_{k=0}^{N-1} k^4 - \left( \sum_{k=0}^{N-1} k^3 \right)^2 \right) \end{bmatrix} \quad (11-14)$$

Finally,  $\Sigma_{\text{aug}}^T (\Sigma_{\text{aug}}\Sigma_{\text{aug}}^T)^{-1}$  is derived in (11-15).

$$\Sigma_{\text{aug}}^T (\Sigma_{\text{aug}}\Sigma_{\text{aug}}^T)^{-1} = \begin{bmatrix} \frac{(N-1)^2 \tau^2}{2M} & \frac{(N-1)\tau}{M} & 1 \\ \frac{(N-2)^2 \tau^2}{2M} & \frac{(N-2)\tau}{M} & 1 \\ \vdots & \vdots & \vdots \\ 0 & 0 & 1 \end{bmatrix} \cdot \frac{4M^4}{\tau^6} \cdot \frac{1}{\left\{ \sum_{k=0}^{N-1} k^2 \sum_{k=0}^{N-1} k^4 \cdot N + 2 \sum_{k=0}^{N-1} k \sum_{k=0}^{N-1} k^2 \sum_{k=0}^{N-1} k^3 - \left( \sum_{k=0}^{N-1} k^2 \right)^3 - \left( \sum_{k=0}^{N-1} k \right)^2 \sum_{k=0}^{N-1} k^4 - \left( \sum_{k=0}^{N-1} k^3 \right)^2 \cdot N \right\}} \cdot \begin{bmatrix} \frac{\tau^2}{M^2} \left( \sum_{k=0}^{N-1} k^2 \cdot N - \left( \sum_{k=0}^{N-1} k \right)^2 \right) & -\frac{\tau^3}{2M^2} \left( \sum_{k=0}^{N-1} k^3 \cdot N - \sum_{k=0}^{N-1} k \sum_{k=0}^{N-1} k^2 \right) & \frac{\tau^3}{M^4} \left( \sum_{k=0}^{N-1} k \sum_{k=0}^{N-1} k^3 - \left( \sum_{k=0}^{N-1} k^2 \right)^2 \right) \\ -\frac{\tau^3}{2M^2} \left( \sum_{k=0}^{N-1} k^3 \cdot N - \sum_{k=0}^{N-1} k \sum_{k=0}^{N-1} k^2 \right) & \frac{\tau^4}{4M^2} \left( \sum_{k=0}^{N-1} k^4 \cdot N - \left( \sum_{k=0}^{N-1} k^2 \right)^2 \right) & -\frac{\tau^5}{4M^2} \left( \sum_{k=0}^{N-1} k \sum_{k=0}^{N-1} k^4 - \sum_{k=0}^{N-1} k^2 \sum_{k=0}^{N-1} k^3 \right) \\ \frac{\tau^2}{M^2} \left( \sum_{k=0}^{N-1} k \sum_{k=0}^{N-1} k^3 - \left( \sum_{k=0}^{N-1} k^2 \right)^2 \right) & -\frac{\tau^5}{4M^3} \left( \sum_{k=0}^{N-1} k \sum_{k=0}^{N-1} k^4 - \sum_{k=0}^{N-1} k^2 \sum_{k=0}^{N-1} k^3 \right) & \frac{\tau^6}{4M^4} \left( \sum_{k=0}^{N-1} k^2 \sum_{k=0}^{N-1} k^4 - \left( \sum_{k=0}^{N-1} k^3 \right)^2 \right) \end{bmatrix} \quad (11-15)$$

By substituting (11-7) into (11-15), (11-16) is obtained.

$$\begin{aligned} q_{11} &= \frac{M}{\tau^2(N-2)(N-1)N(N+1)(N+2)} \{360(N-i)^2 + 360(N-1)(N-i) - 60(N-2)(N-1)\} \\ q_{12} &= \frac{-M}{\tau(N-2)(N-1)N(N+1)(N+2)} \{180(N-1)(N-i)^2 - 12(2N-1)(8N-11)(N-i) + 18(N-2)(N-1)(2N-1)\} \\ q_{13} &= \frac{1}{N(N+1)(N+2)} \{30(N-i)^2 - 18(2N-1)(N-i) + 3(3N^2 - 3N + 2)\} \end{aligned} \quad (11-16)$$

# Thanks

まず初めに本研究を進めるにあたり、研究相談会及び研究発表会の場において熱意ある指導と適切な助言をしてくださった藤本博志准教授、研究発表会の場において丁寧な指導をしてくださった堀洋一教授に心から感謝いたします。先生方の厳しくも暖かい指導があったからこそ、最後まで研究を続けることができました。ご迷惑することも多かったのですが、そのたびにフォローしていただき先生方の大きさを感じました。先生方の指導を胸にこれからも頑張っていきたいと思います。本当にありがとうございました。

また、実験装置改造や研究全般にご尽力いただいた佐伯和明様、実験機の設計をしていただいた原篤史様、実験機の立ち上げや実験方法、制御理論について適切な助言をしてくださった坂田晃一様、電気回路の設計及び解析を行なってくださった陳照祥様、鈴木一弘様、横山和弘様をはじめとする株式会社ニコンの方々には感謝の念が尽きません。カタパルトステージも WHPS2 もニコンの皆様のご協力がなければ完成しませんでした。非常に素直でいい子な2つの実験機を与えてくださったこと、大変幸せに思っています。

さらに、大西亘さんには共同研究先が同じということもあり数多くのご助言をいただき、また熱心に研究内容に関する議論をしていただきました。大西さんは研究面でも生活面でも尊敬できる部分が多く、今後の人生の模範としていきたいと思っております。深く感謝申し上げます。また同期の山田翔太君には本当にお世話になりました。山田君とは高校の頃から含めると（高校の頃はあまり認識していなかったが）、合計11年間も同じような道りを歩んできました。特に同じ研究室に入ってからの6年間では自分のスケジュール管理の甘さも相まって、非常に多くの部分を助けていただきました。山田君がいなかったらおそらく私は博士審査にのぞめなかったと思います。これからも長い付き合いになると思いますが、今後ともよろしく願います。後輩は非常にたくさんいるので感謝の念と伝えきことは難しいのですが、延命朋希君、李堯希君、長谷川顯之君には特にお世話になりました。延命君とは一緒にイタリアの観光にも行きましたね。詐欺に遭いかけるなど色々トラブルもありましたが今ではいい思い出です。また研究が辛くなったときに一緒に卓球や筋トレとしたことはとても良い気分転換になりました。研究が停滞しても卓球や筋肉の面で進捗が感じられたことは自分の支えになり、非常にありがたかったです。研究室の皆様の支えがあったからこそ楽しい研究生生活を送ることができました。感謝しております。

居村岳広先生や畑勝裕君、ロビソンさん、ジュゼッペ先生を初めとするワイヤレスチームの皆様には無線電力伝送に関する多くの助言と頂きました。博士以前は制御に関する研究に従事

していたこともあり無線電力伝送に関しては不明瞭な部分も多かったのですが、居村先生や畑君の助言により無線電力伝送に関する理解を深めることができ、研究につなげることができました。誠にありがとうございます。そして清水修先生にはコイルの設計に関して大変多くの議論をさせていただきました。清水先生のおかげで自分の研究の立ち位置を見直すことができました。ありがとうございます。私の実験機の引き継ぎをしてくれた堅田龍之介君とは一緒に実験やシミュレーションを行なったりと大変お世話になりました。WHPS2はとてもいい子なので大切に扱ってあげてください。体調には気をつけてあまり無理することなく研究に励んでください。

最後に、学ぶ機会を与えてくれた母の支援に心から感謝いたします。生活が苦しい中、非常に長い年月にわたって私を支え続けてくれて本当にありがとうございました。これからは自分が母を助けていく番と思っています。いつまでも元気でいてください。これからもよろしくお願いいたします。

# Reference

- [1] T. Totani and N. Hidekazu, “Final-state control using compensation input,” *Transactions of the Society of Instrument and Control Engineers*, vol. 30, no. C, pp. 253–260, 1994.
- [2] M. Hirata and M. Tomizuka, “Short Track Seeking of Hard Disk Drives Under Multirate Control-Computationally Efficient Approach Based on Initial Value Compensation,” *IEEE/ASME Transactions on Mechatronics*, vol. 10, pp. 535–545, oct 2005.
- [3] J. Mühlethaler, “Modeling and Multi-Objective Optimization of Inductive Power Components,” no. 20217, p. 223, 2012.
- [4] R. Y. Zhang, J. K. White, and J. G. Kassakian, “Fast Simulation of Complicated 3-D Structures Above Lossy Magnetic Media,” *IEEE transactions on Magnetics*, vol. 50, no. 10, pp. 1–17, 2014.
- [5] R. Y. Zhang, J. K. White, J. G. Kassakian, and C. R. Sullivan, “Realistic Litz Wire Characterization using Fast Numerical Simulations,” in *Applied Power Electronics Conference and Exposition*, pp. 738–745, 2014.
- [6] H. Butler, “Position Control in Lithographic Equipment,” *IEEE Control Systems*, vol. 31, pp. 28–47, oct 2011.
- [7] M. F. Heertjes, “Variable Gains in Motion Control of Wafer Scanners,” in *IEEJ International Workshop on Sensing, Actuation, and Motion Control*, 2015.
- [8] T. Oomen, “Advanced Motion Control for Precision Mechatronics: Control, Identification, and Learning of Complex Systems,” *IEEJ Journal of Industry Applications*, vol. 7, no. 2, pp. 127–140, 2018.
- [9] K. Saiki, A. Hara, K. Sakata, and H. Fujimoto, “A Study on High-Speed and High-Precision Tracking Control of Large-Scale Stage Using Perfect Tracking Control Method Based on Multirate Feedforward Control,” *IEEE Transactions on Industrial Electronics*, vol. 57, no. 4, pp. 1393–1400, 2010.



- [10] Y. Yagisawa, M. Hirata, M. Suzuki, and S. Maruyama, “C111 Control System Design of FPD Exposure Apparatus by Taking Account of Coupling between Axes,” *The Proceedings of the Symposium on the Motion and Vibration Control*, vol. 2015.14, pp. 178–181, 2015.
- [11] 佐伯和明, “制御屋と呼ばれたい.pdf,” システム制御情報学会誌, vol. 52, no. 12, pp. 463—466, 2008.
- [12] Nikon Corporation, “FPD manufacturing system.”
- [13] 総務省, “第3節 IoT化する情報通信産業,” tech. rep., 2017.
- [14] 総務省, “4K・8Kロードマップに関するフォローアップ会合 第二次中間報告,” tech. rep., 2015.
- [15] S. Ozawa, “The Current Lithography Technologies of the LCD Exposure System,” *IEICE Trans. C*, vol. J84-C, no. 12, pp. 1227–1231, 2001.
- [16] Nikon, “FPD 露光装置 FX-101S リーフレット,” tech. rep., 2014.
- [17] S. Ozawa, “The Current Lithography Technologies of the LCD Exposure System,” *IEICE Trans. C*, vol. 1227-1231, no. 84, p. 12, 2001.
- [18] S. Okazaki, “リソグラフィー技術:露光装置の原理とレジストプロセス技術,” 応用物理, vol. 69, no. 2, pp. 196–200, 2000.
- [19] N. Mizusawa, “X線等倍露光装置,” *The Reference Collection of Annual Meeting*, vol. 2000.5, pp. 299–300, 2000.
- [20] K. Yoshida, “New Technical Trend of Large-Size Photomask for FPD,” *Journal of printing science and technology*, vol. 47, no. 6, pp. 377–386, 2010.
- [21] M. A. van de Kerkhof, A. W. E. Minnaert, M. Pieters, H. Meiling, J. Smits, R. Peeters, R. van Es, G. Fisser, J. W. de Klerk, R. Moors, E. Verhoeven, and L. Levasier, “EUV for HVM: towards an industrialized scanner for HVM NXE3400B performance update,” *Extreme Ultraviolet (EUV) Lithography IX*, no. March 2018, p. 13, 2018.
- [22] S. Wakui, “半導体露光装置における精密位置決め技術開発の実相,” 機械設計, vol. 50, no. 8, pp. 18–23, 2006.
- [23] Y. K. Yoshiyuki TOMITA, Eiji KOJIMA, Shunichi KAWACHI and S. OOTSUKA, “Development and Applications of Sumitomo Precision Stage Technologies for FPD Process,” *Journal of the Japan Society for Precision Engineering*, vol. 78, no. 2, pp. 117–121, 2011.

- [24] S. WAKUI, “Roles of an Active Anti-Vibration Apparatus in Precision Positioning,” *Journal of the Japan Society for Precision Engineering*, vol. 73, no. 4, pp. 405–409, 2007.
- [25] S. Wakui, “回想の半導体露光装置用ウエハステージモデル化の満たされない想い—,” *精密工学会誌*, vol. 77, no. 5, pp. 447–452, 2011.
- [26] M. Li, Y. Zhu, K. Yang, C. Hu, and H. Mu, “An Integrated Model-Data-Based Zero-Phase Error Tracking Feedforward Control Strategy with Application to an Ultraprecision Wafer Stage,” *IEEE Transactions on Industrial Electronics*, vol. 64, no. 5, pp. 4139–4149, 2017.
- [27] C. E. . Okwudire and D. D. . Yoon, “Magnet assisted stage for vibration and heat reduction in wafer scanning,” 2018.
- [28] M. Tomizuka, “Zero Phase Error Tracking Algorithm for Digital Control,” *Journal of Dynamic Systems, Measurement, and Control*, vol. 109, no. 1, p. 65, 1987.
- [29] H. Fujimoto, Y. Hori, and A. Kawamura, “Perfect tracking control based on multirate feedforward control with generalized sampling periods,” *IEEE Transactions on Industrial Electronics*, vol. 48, pp. 636–644, jun 2001.
- [30] J. Lunenburg, O. Bosgra, and T. Oomen, “Inversion-Based Feedforward Design for Beyond Rigid Body Systems : A Literature Survey,” *DCT Report 2009.105, Eindhoven University of Technology, Eindhoven, The Netherlands*, no. November, 2009.
- [31] M. J. C. Ronde, M. G. E. Schneiders, E. J. G. J. Kikken, M. J. G. Van De Molengraft, and M. Steinbuch, “Model-based spatial feedforward for over-actuated motion systems,” *Mechatronics*, vol. 24, no. 4, pp. 307–317, 2014.
- [32] K. Åström, “Theory and applications of adaptive control—A survey,” *Automatica*, vol. 19, pp. 471–486, sep 1983.
- [33] K. J. Hunt, D. Sbarbaro, R. Zbikowski, and P. J. Gawthrop, “Neural networks for control systems—A survey,” *Automatica*, vol. 28, no. 6, pp. 1083–1112, 1992.
- [34] G. Pipeleers and K. L. Moore, “Unified analysis of iterative learning and repetitive controllers in trial domain,” *IEEE Transactions on Automatic Control*, vol. 59, no. 4, pp. 953–965, 2014.
- [35] D. Bristow, M. Tharayil, and A. Alleyne, “A survey of iterative learning control,” *Control Systems, IEEE*, vol. 26, no. 3, pp. 96–114, 2006.
- [36] M. Baggen, M. Heertjes, and R. Kamidi, “Data-based feed-forward control in MIMO motion systems,” in *American Control Conference*, pp. 3011–3016, 2008.

- [37] M. Heertjes, D. Hennekens, and M. Steinbuch, “MIMO feed-forward design in wafer scanners using a gradient approximation-based algorithm,” *Control Engineering Practice*, vol. 18, no. 5, pp. 495–506, 2010.
- [38] M. Heertjes and D. Bruijnen, “MIMO FIR feedforward design for zero error tracking control,” *Proceedings of the American Control Conference*, pp. 2166–2171, 2014.
- [39] F. Song, Y. Liu, J. Xu, X. Yang, and Q. Zhu, “Data-Driven Iterative Feedforward Tuning for a Wafer Stage: A High-Order Approach Based on Instrumental Variables,” *IEEE Transactions on Industrial Electronics*, vol. 66, no. 4, pp. 3106–3116, 2018.
- [40] S. Arimoto, S. Kawamura, and F. Miyazaki, “Iterative learning control for robot systems,” in *Proceedings of IECON*, 1984.
- [41] F. Boeren, A. Bareja, T. Kok, and T. Oomen, “Frequency-Domain ILC Approach for Repeating and Varying Tasks: With Application to Semiconductor Bonding Equipment,” *IEEE/ASME Transactions on Mechatronics*, vol. 4435, no. c, pp. 1–1, 2016.
- [42] T. D. Son, G. Pipeleers, and J. Swevers, “Robust Monotonic Convergent Iterative Learning Control,” *IEEE Transactions on Automatic Control*, vol. 61, pp. 1063–1068, apr 2016.
- [43] J. Zhou, H. Yue, J. Zhang, and H. Wang, “Iterative learning double closed-loop structure for modeling and controller design of output stochastic distribution control systems,” *IEEE Transactions on Control Systems Technology*, vol. 22, no. 6, pp. 2261–2276, 2014.
- [44] N. Liu and A. Alleyne, “Iterative Learning Identification for Linear Time-Varying Systems,” *IEEE Transactions on Control Systems Technology*, vol. 24, pp. 310–317, jan 2016.
- [45] Z. Cao, R. Zhang, Y. Yang, J. Lu, and F. Gao, “Discrete-Time Robust Iterative Learning Kalman Filtering for Repetitive Processes,” *IEEE Transactions on Automatic Control*, vol. 61, no. 1, pp. 270–275, 2016.
- [46] T. Oomen and C. R. Rojas, “Sparse iterative learning control with application to a wafer stage: Achieving performance, resource efficiency, and task flexibility,” *Mechatronics*, vol. 47, pp. 134–147, nov 2017.
- [47] M. van de Wal, G. van Baars, F. Sperling, and O. Bosgra, “Multivariable feedback control design for high-precision wafer stage motion,” *Control Engineering Practice*, vol. 10, pp. 739–755, jul 2002.
- [48] M. F. Heertjes, B. Van der Velden, and T. Oomen, “Constrained Iterative Feedback Tuning for Robust Control of a Wafer Stage System,” *IEEE Transactions on Control Systems Technology*, vol. 24, pp. 56–66, jan 2016.

- [49] R. van Herpen, T. Oomen, E. Kikken, M. van de Wal, W. Aangenent, and M. Steinbuch, “Exploiting additional actuators and sensors for nano-positioning robust motion control,” *Mechanics*, vol. 24, pp. 619–631, sep 2014.
- [50] K. Sakata, H. Asaumi, K. Hirachi, K. Saiki, and H. Fujimoto, “Self Resonance Cancellation Techniques for a Two-Mass System and Its Application to a Large-Scale Stage,” *IEEJ Journal of Industry Applications*, vol. 3, no. 6, pp. 455–462, 2014.
- [51] K. Sakata, H. Fujimoto, T. Ohtomo, and K. Saiki, “Auto Focus and Leveling Control of Large-Scale High-Precision Scan-Stage Using Driving Force and Surface Shape of the Stage,” *IEEJ Transactions on Industry Applications*, vol. 129, no. 6, pp. 564–570, 2009.
- [52] D. MIURA, R. KAWAI, Y. BU, T. MIZUNO, T. MARUYAMA, and T. TERASHIMA, “Investigation of Linear DC Motor Focused on Displacement Sensor Position not Affected by Pitching of Mover,” *Journal of the Japan Society of Applied Electromagnetics and Mechanics*, vol. 26, no. 1, pp. 133–138, 2018.
- [53] Pai-Hsueh Yang, B. Alamo, and G. Andeen, “Control design for a 6 DOF e-beam lithography stage,” in *Proceedings of the 2001 American Control Conference.*, vol. 3, pp. 2255–2260, IEEE, 2001.
- [54] K. Sakata, H. Fujimoto, A. Hara, T. Ohtomo, and K. Saiki, “Design fabrication and control of 4-DOF high-precision stage,” in *2010 11th IEEE International Workshop on Advanced Motion Control (AMC)*, pp. 366–370, IEEE, mar 2010.
- [55] W. Ohnishi, H. Fujimoto, Y. Hori, K. Sakata, K. Suzuki, and K. Saiki, “Attitude Control Method for High-Precision Stage by Compensating for Nonlinearity and Coupling Arising from Euler’s Equation and Coordinate Rotation,” *IEEJ Transactions on Industry Applications*, vol. 134, no. 3, pp. 293–300, 2014.
- [56] W. Ohnishi, H. Fujimoto, K. Sakata, K. Suzuki, and K. Saiki, “Decoupling Control Method for High-Precision Stages using Multiple Actuators considering the Misalignment among the Actuation Point, Center of Gravity, and Center of Rotation,” *IEEJ Journal of Industry Applications*, vol. 5, no. 2, pp. 141–147, 2016.
- [57] W. Ohnishi, H. Fujimoto, K. Sakata, K. Suzuki, and K. Saiki, “Integrated design of mechanism and control for high-precision stages by the interaction index in the Direct Nyquist Array method,” in *2015 American Control Conference (ACC)*, pp. 2825–2830, IEEE, jul 2015.
- [58] W. Ohnishi, H. Fujimoto, K. Sakata, K. Suzuki, and K. Saiki, “Decoupling Control Method for High-Precision Stages using Multiple Actuators considering the Misalignment among the

- Actuation Point, Center of Gravity, and Center of Rotation,” *IEEJ Journal of Industry Applications*, vol. 5, no. 2, pp. 141–147, 2016.
- [59] H. Chen, M. Zhang, H. Mu, Y. Zhu, C. Hu, and T. Cai, “Conceptual Design and Trajectory Planning of a Precision Repetitive-Scanning Stage With Separated Drive Unit for Energy Saving,” *IEEE/ASME Transactions on Mechatronics*, vol. 21, pp. 2142–2153, aug 2016.
- [60] R. Voorhoeve, R. D. Rozario, and T. Oomen, “Identification for Motion Control : Incorporating Constraints and Numerical Considerations,” in *American Control Conference*, pp. 6209–6214, 2016.
- [61] K. Sakata, H. Fujimoto, A. Hara, and K. Saiki, “Design fabrication of high-precision stage and ultrahigh-speed nanoscale positioning,” in *American Control Conference*, pp. 2254–2259, 2009.
- [62] W. Ohnishi, H. Fujimoto, K. Sakata, K. Suzuki, and K. Saiki, “Design and Control of 6-DOF High-Precision Scan Stage with Gravity Canceller,” in *American Control Conference*, pp. 997–1002, 2014.
- [63] M. Binnard, “Planar motor with linear coil arrays,” *United States Patent*, no. US6452292, 2002.
- [64] J. M. M. Rovers, J. W. Jansen, J. C. Compter, and E. a. Lomonova, “Analysis method of the dynamic force and torque distribution in the magnet array of a commutated magnetically levitated planar actuator,” *IEEE Transactions on Industrial Electronics*, vol. 59, no. 5, pp. 2157–2166, 2012.
- [65] Y. M. Choi and D. G. Gweon, “A High-Precision Dual-Servo Stage Using Halbach Linear Active Magnetic Bearings,” *IEEE/ASME Transactions on Mechatronics*, vol. 16, pp. 925–931, oct 2011.
- [66] W. Kim, T. Hu, and N. Bhat, “Design and control of a 6-DOF high-precision integrated positioner,” in *American Control Conference*, vol. 3, pp. 2493–2498, 2004.
- [67] H. Stearns, S. Mishra, and M. Tomizuka, “Iterative tuning of feedforward controller with force ripple compensation for wafer stage,” in *International Workshop on Advanced Motion Control, AMC*, vol. 1, pp. 234–239, 2008.
- [68] T. Oomen, R. van Herpen, S. Quist, M. van de Wal, O. Bosgra, and M. Steinbuch, “Connecting System Identification and Robust Control for Next-Generation Motion Control of a Wafer Stage,” *IEEE Transactions on Control Systems Technology*, vol. 22, pp. 102–118, jan 2014.
- [69] A. Okuyama, “Fast-Seeking Control for Two-Stage Actuator System in Optical Disc Drives,” *IEEJ Transactions on Industry Applications*, vol. 129, no. 4, pp. 368–374, 2009.

- [70] J.-d. Yang and X.-d. Pei, "Seek time and trajectories of time optimal control for a dual stage optical disk drive actuator," *IEEE Transactions on Magnetics*, vol. 32, no. 5, pp. 3857–3859, 1996.
- [71] T. Atsumi, S. Nakamura, M. Odai, I. Naniwa, and S. Nosaki, "Experimental Evaluation of Triple-Stage-Actuator System with Thermal Actuator for Hard Disk Drives," *Journal of Advanced Mechanical Design, Systems, and Manufacturing*, vol. 7, no. 4, pp. 722–735, 2013.
- [72] K. Mori, T. Munemoto, H. Otsuki, Y. Yamaguchi, and K. Akagi, "A dual-stage magnetic disk drive actuator using a piezoelectric device for a high track density," *IEEE Transactions on Magnetics*, vol. 27, no. 6, pp. 5298–5300, 1991.
- [73] C.-W. Lee and S.-W. Kim, "An ultraprecision stage for alignment of wafers in advanced microlithography," *Precision Engineering*, vol. 21, pp. 113–122, sep 1997.
- [74] K. Tokuyama, H. Fujimoto, D. Yumiza, and K. Saiki, "Proposal of reducing impact force control system for scan stage with decouplable structure of coarse and fine parts," in *2013 IEEE International Conference on Mechatronics (ICM)*, pp. 810–815, IEEE, feb 2013.
- [75] K. Ohishi and T. Mashimo, "Design Method of Digital Robust Speed Servo System Considering Output Saturation," *IEEJ Transactions on Industry Applications*, vol. 119, no. 1, pp. 88–96, 1999.
- [76] R. Furusawa, K. Ohishi, K. Kageyama, M. Takatsu, and S. Urushihara, "Fine force control based on reaction force observer for electric injection molding machine," in *2011 IEEE International Symposium on Industrial Electronics*, pp. 2165–2170, IEEE, jun 2011.
- [77] T. Yamaguchi, K. Shishida, S. Tohyama, and H. Hirai, "Mode switching control design with initial value compensation and its application to head positioning control on magnetic disk drives," *IEEE Transactions on Industrial Electronics*, vol. 43, no. 1, pp. 65–73, 1996.
- [78] T. Yamaguchi, Y. Soyama, H. Hosokawa, K. Tsuneta, and H. Hirai, "Improvement of settling response of disk drive head positioning servo using mode switching control with initial value compensation," *IEEE Transactions on Magnetics*, vol. 32, pp. 1767–1772, may 1996.
- [79] T. Yamaguchi, H. Numasato, and H. Hirai, "A mode-switching control for motion control and its application to disk drives: design of optimal mode-switching conditions," *IEEE/ASME Transactions on Mechatronics*, vol. 3, no. 3, pp. 202–209, 1998.
- [80] M. Hirata and F. Ueno, "Final-State Control Using Polynomial and Time-Series Data," *IEEE Transactions on Magnetics*, vol. 47, pp. 1944–1950, jul 2011.

- [81] M. Hirata and F. Ueno, “Polynomial-input-type final-state control taking account of input saturation,” *Preprints of the 18th IFAC World Congress*, pp. 4061—4066, 2011.
- [82] T. Yoshiura and S. Hara, “Proposal of updating final-state control and its application to a connection control problem,” *2014 IEEE 13th International Workshop on Advanced Motion Control (AMC)*, pp. 681–686, mar 2014.
- [83] S. Boyd and L. Vandenberghe, *Convex Optimization*, vol. 0. 2004.
- [84] T. Tanaka and M. Hirata, “Determination of the end of track seeking of hard disk drives using a maximal output admissible set,” in *IEEJ MEC-13-163*, pp. 25–30, 2013.
- [85] MathWorks, “Linear Programming Algorithms.”
- [86] R. Van Herpen, T. Oomen, E. Kikken, M. Van De Wal, W. Aangenent, and M. Steinbuch, “Exploiting additional actuators and sensors for nano-positioning robust motion control,” *Mechanics*, vol. 24, no. 6, pp. 619–631, 2014.
- [87] Y. Yazaki, H. Fujimoto, Y. Hori, K. Sakata, A. Hara, and K. Saiki, “Method to Shorten Settling Time Using Final State Control for High-Precision Stage with Decouplable Structure of Fine and Coarse Parts,” *IEEJ Transactions on Industry Applications*, vol. 135, no. 3, pp. 227–236, 2015.
- [88] Y. Yazaki, H. Fujimoto, K. Sakata, A. Hara, and K. Saiki, “Application of mode switching control using initial state variables in constraint final-state control to high-precision dual stage,” in *2015 American Control Conference (ACC)*, pp. 4155–4161, IEEE, jul 2015.
- [89] E. Gilbert, I. Kolmanovsky, and K. T. Tan, “Nonlinear control of discrete-time linear systems with state and control constraints: a reference governor with global convergence properties,” *Proceedings of 1994 33rd IEEE Conference on Decision and Control*, vol. 1, pp. 144–149, 1994.
- [90] Y. Ohta and I. Masubuchi, “On the implementation of reference governor,” in *Proc. 40th Annual Conference of IEEE Industrial Electronics Society (IECON 2014)*, pp. 215–220, 2014.
- [91] A. Bemporad, A. Casavola, and E. Mosca, “Nonlinear control of constrained linear systems via predictive reference management,” *IEEE Transactions on Automatic Control*, vol. 42, no. 3, pp. 340–349, 1997.
- [92] A. Casavola, E. Mosca, and M. Papini, “Control Under Constraints: An Application of the Command Governor Approach to an Inverted Pendulum,” *IEEE Transactions on Control Systems Technology*, vol. 12, no. 1, pp. 193–204, 2004.

- [93] E. G. Gilbert and C. J. Ong, “Constrained linear systems with hard constraints and disturbances: An extended command governor with large domain of attraction,” *Automatica*, vol. 47, no. 2, pp. 334–340, 2011.
- [94] M. J. Dillsaver, U. V. Kalabic, I. V. Kolmanovsky, and C. E. S. Cesnik, “Constrained control of very flexible aircraft using reference and extended command governors,” in *2013 American Control Conference*, pp. 1608–1613, IEEE, jun 2013.
- [95] S. Aghaei, F. Sheikholeslam, M. Farina, and R. Scattolini, “An MPC-based reference governor approach for offset-free control of constrained linear systems,” *International Journal of Control*, vol. 86, no. 9, pp. 1534–1539, 2013.
- [96] T. Hatanaka and K. Takaba, “Design of Reference Governor for Constrained Systems Subject to Disturbance,” *Transactions of the Society of Instrument and Control Engineers*, vol. 40, no. 8, pp. 806–814, 2004.
- [97] I. Kolmanovsky, E. Gilbert, and H. Tseng, “Constrained control of vehicle steering,” *2009 IEEE Control Applications, (CCA) & Intelligent Control, (ISIC)*, no. 2, pp. 576–581, 2009.
- [98] A. Vahidi, I. Kolmanovsky, and A. Stefanopoulou, “Constraint handling in a fuel cell system: A fast reference governor approach,” *IEEE Transactions on Control Systems Technology*, vol. 15, no. 1, pp. 86–98, 2007.
- [99] C. Petersen, M. Baldwin, and I. Kolmanovsky, “Model Predictive Control Guidance with Extended Command Governor Inner-Loop Flight Control for Hypersonic Vehicles,” *AIAA Guidance, Navigation, and Control (GNC) Conference*, pp. 1–20, 2013.
- [100] C. Petersen, a. Jaunzemis, M. Baldwin, M. J. Holzinger, and I. Kolmanovsky, “Model Predictive Control and Extended Command Governor for Improving Robustness of Relative Motion Guidance and Control,” *AAS/AIAA Space Flight Mechanics Meeting*, pp. 1–18, 2014.
- [101] C. Vermillion, “Reference governor design for computationally efficient attitude and tether tension constraint enforcement on a lighter-than-air wind energy system,” in *Control Conference (ECC), 2013 European*, pp. 1004–1010, 2013.
- [102] S. OH-HARA, K. HIRATA, and H. MINEMURA, “Experimental Evaluations of Reference Governors Control Schemes for a RC Helicopter,” *Transactions of the Japan Society of Mechanical Engineers Series C*, vol. 71, no. 707, pp. 2305–2312, 2005.
- [103] K. KOGISO and K. HIRATA, “A Reference Governor in a Piecewise State Affine Function: Its Implementation and Experimental Validation,” *Transactions of the Society of Instrument and Control Engineers*, vol. 40, no. 2, pp. 247–256, 2004.



- [104] H. Guo, Y. Ohta, and I. Masubuchi, “入力の連続性を考慮したゲインスケジュールドリファレンスガバナを用いたハードディスクのロングシーク制御,” vol. 49, no. 9, pp. 832–839, 2013.
- [105] H. Guo, Y. Ohta, and I. Masubuchi, “拘束システムに対するリファレンスガバナの実装,” *Transactions of the Institute of Systems, Control and Information Engineers*, vol. 27, no. 4, pp. 187–192, 2014.
- [106] G. Goodwin, S. Graebe, and M. Salgado, *Control System Design*. Prentice-Hall, 2001.
- [107] E. G. Gilbert and K. T. Tan, “Linear systems with state and control constraints: The theory and application of maximal output admissible sets,” *IEEE Transactions on Automatic Control*, vol. 36, no. 9, pp. 1008–1020, 1991.
- [108] K. Hirata and K. Kogiso, “An Off-Line Reference Management Technique for Constraint Fulfillment,” *Transactions of the Institute of Systems, Control and Information Engineers*, vol. 14, no. 11, pp. 554–559, 2001.
- [109] Y. Yazaki, T. Nishimura, W. Ohnishi, T. Imura, and H. Fujimoto, “Moving coil type wireless linear motor based on magnetic resonance coupling,” in *IECON 2017 - 43rd Annual Conference of the IEEE Industrial Electronics Society*, pp. 7288–7293, IEEE, oct 2017.
- [110] T. Tohi, Y. Kaneko, and S. Abe, “Maximum Efficiency of Contactless Power Transfer Systems using  $k$  and  $Q$ ,” *IEEJ Transactions on Industry Applications*, vol. 132, no. 1, pp. 123–124, 2012.
- [111] T. Imura, T. Yasuda, K. Oshima, T. Nayuki, M. Sato, and A. Oshima, “Wireless power transfer for electric vehicle at the kilohertz band,” *IEEJ Transactions on Electrical and Electronic Engineering*, vol. 11, pp. S91–S99, 2016.
- [112] M. Sugino, H. Kondo, and S. Takeda, “Linear Motion Type Transfer Robot using the wireless power transfer system (In Japanese),” in *Proceedings of the Institute of Electronics, Information and Communication Engineers*, pp. 38–39, 2016.
- [113] T. Noda, T. Nagashima, and H. Sekiya, “A Comprehensive Design Method of Inductively Coupled Wireless Power Transfer System for Maximizing Overall Efficiency,” pp. 2–7.
- [114] R. Bosshard and J. W. Kolar, “Multi-Objective Optimization of 50 kW/85 kHz IPT System for Public Transport,” *IEEE Journal of Emerging and Selected Topics in Power Electronics*, vol. 4, no. 4, pp. 1370–1382, 2016.

- [115] T. Imura and Y. Hori, “Maximizing air gap and efficiency of magnetic resonant coupling for wireless power transfer using equivalent circuit and Neumann formula,” *IEEE Transactions on Industrial Electronics*, vol. 58, no. 10, pp. 4746–4752, 2011.
- [116] X. Huang, Q. Ji, L. Tan, W. Wang, J. Zhao, and Y. Zhou, “Study on series-parallel model of wireless power transfer via magnetic resonance coupling,” *Diangong Jishu Xuebao/Transactions of China Electrotechnical Society*, vol. 28, no. 3, pp. 171 – 176+187, 2013.
- [117] N. Misac, N., *ELECTROMAGNETIC METHODS IN APPIED GEOPHYSICS-THEORY*. 1988.
- [118] A. Juhas, N. Pekari, and H. Toepfer, “Magnetic Field of Rectangular Current Loop with Sides Parallel and Perpendicular to the Surface of High-permeability Material,” vol. 11, no. 4, pp. 701–717, 2014.
- [119] Y. Kamiya, K. Nakaura, T. Nakamura, Y. Daisho, S. Takahashi, K. Yamamoto, T. Sato, H. Matsuki, and K. Natusawa, “Development and Performance Evaluation of a Non-contact Rapid Charging Type Inductive Power Supply (IPS) System for Electric Vehicles (First Report) : Design Optimization of Track & Pick up Part of IPS and Performance Evaluation of the System,” *Transactions of Society of Automotive Engineers of Japan*, vol. 38, no. 6, pp. 175–180, 2007.
- [120] K. Ito, “A Basic Magnetic Analysis of Litz Wire by the Finite Element Method,” Tech. Rep. 23, 2014.
- [121] K. Ito, K. Ida, Y. Kawase, T. Yamaguchi, R. Kawai, D. Kato, Y. Hukui, and N. Nishikawa, “大規模数値解析によるコイル損失低減技術の開発.pdf,” tech. rep., 2015.
- [122] D. Gunji, T. Imura, and H. Fujimoto, “Stability Analysis of Constant Power Load and Load Voltage Control Method for Wireless In-Wheel Motor,” pp. 1944–1949, 2015.
- [123] M. Sato, G. Yamamoto, D. Gunji, T. Imura, and H. Fujimoto, “Development of Wireless In-Wheel Motor Using,” *IEEE Transactions on Power Electronics*, vol. 31, no. 7, pp. 5270–5278, 2016.

# Present

## Journal

- [1] 著者 矢崎雄馬, 藤本博志, 堀洋一, 坂田晃一, 原篤史, 佐伯和明  
題名 粗微動間連結分離機構を有する精密位置決めステージの  
終端状態制御法を用いた整定時間短縮法  
学会誌名 電気学会論文誌 D, vol.135, pp. 227–236, 2015
- [2] 著者 Yazaki. Y., Fujimoto. H., Sakata. K., Hara. A., Saiki. K.  
題名 Development and control for High-Precision Stage  
with Decouplable Structure of Fine and Coarse Parts  
学会誌名 電気学会論文誌 D (submitted)
- [3] 著者 Yazaki. Y., Fujimoto. H.  
題名 Development and control for High-Precision Stage  
with Decouplable Structure of Fine and Coarse Parts  
学会誌名 電気学会論文誌 D (submitted)

## Tutorial paper on scholarly journal

- [4] 著者 藤本博志, 矢崎雄馬  
題名 粗微動間連結分離機構を有する新たな精密位置決めステージの制御法  
雑誌名 電気学会技術報告書「ナノスケールサーボのための革新的な制御技術」,  
vol. 1347, pp. 44–49, 2015

## Peer-reviewed international conference papers

- [5] 著者 Yazaki. Y., Fujimoto. H., Sakata. K., Hara. A., Saiki. K.  
題名 Settling Time Shortening Method Using Final State Control for High-precision Stage with Decouplable Structure of Fine and Coarse Parts  
会議名 40th Annual Conference of the IEEE Industrial Electronics Society  
場所 Dallas, TX  
発表日 29th, October, 2014  
開催期間 29th, October – 1st, November, 2014
- [6] 著者 Yazaki. Y., Fujimoto. H.  
題名 Generation Method of Admissible Sets for Mode Switching Control Using Final-State Control with Thrust Limitation  
会議名 IEEE/IES International Conference on Mechatronics, ICM2015  
場所 Nagoya, Japan  
発表日 7th, March, 2015  
開催期間 6th–8th, March, 2015
- [7] 著者 Yazaki. Y., Fujimoto. H., Sakata. K., Hara. A., Saiki. K.  
題名 Application of Mode Switching Control Using Initial State Variables in Constraint Final-State Control to High-Precision Dual Stage  
会議名 2015 American Control Conference  
場所 Boston, USA  
発表日 3rd, July, 2015  
開催期間 1st–3rd, July, 2015
- [8] 著者 Yazaki. Y., Fujimoto. H.  
題名 Sudden Disturbance Suppression Control Considering with Constraint by Reference Governor for High Precision Stage  
会議名 2016 American Control Conference  
場所 Chicago, USA  
発表日 July, 2015  
開催期間 6th–8th, July, 2015

- [9] 著 者 Yazaki. Y., Fujimoto. H., Sakata. K., Hara. A., Saiki. K.  
 題 名 Reduction of Impact Force by Model Prediction and  
 Final-State Control for a High Precision Catapult Stage  
 会 議 名 42nd Annual Conference of the IEEE Industrial Electronics Society  
 場 所 Firenze, Itaria USA  
 発 表 日 October, 2016  
 開催期間 23rd–27th, Octover, 2016
- [10] 著 者 Yazaki. Y., Takurou Nishimura, Wataru Ohnishi, Takehiro Imura, Hiroshi Fujimoto  
 題 名 Moving Coil Type Wireless Linear Motor based on Magnetic Resonance Coupling  
 会 議 名 43rd Annual Conference of the IEEE Industrial Electronics Society  
 場 所 Beijing, China  
 発 表 日 Octover, 2017  
 開催期間 29th Oct–1st Nov, 2017
- [11] 著 者 Yazaki. Y., Fujimoto. H.  
 題 名 Vibration Suppression Control for Two-Inertia System using Reference Governor  
 会 議 名 The 15th Inernational Workshop on Adadvanced Motion Control  
 場 所 Tokyo, Japan  
 発 表 日 March, 2018  
 開催期間 9th–11th, March, 2018
- [12] 著 者 Yazaki. Y., Ohnishi. W, Imura. T, Fujimoto.  
 H, Sakata. K, Hara. A, Chen. Z, Yokoyama. K, Suzuki. K  
 題 名 Development of Multi-axis High-Precision Stage  
 using Multistep Wireless Power Transfer  
 会 議 名 44th Annual Conference of the IEEE Industrial Electronics Society  
 場 所 Washington D.C., USA  
 発 表 日 October, 2018  
 開催期間 21st–23rd, Octrver, 2018

- [13] 著 者 Yazaki. Y, Ohnishi. W, Imura. T, Fujimoto.  
H, Sakata. K, Hara. A, Chen. Z, Yokoyama. K, Suzuki. K  
題 名 Evaluation of Disturbance Caused by Cable Tension in  
Multi-axis High-Precision Stage using Wireless Power Transfer  
会 議 名 The IEEJ International Workshop on SAMCON 2019  
場 所 Chiba university, Japan  
発 表 日 March, 2019  
開催期間 4th–6th, March, 2019

## Domestic conference papers

- [14] 著 者 矢崎雄馬, 藤本博志, 堀洋一, 坂田晃一, 原篤史, 佐伯和明  
題 名 粗微動間連結分離機構を有する精密位置決めステージの整定時間短縮制御法の提案  
会 議 名 平成 26 年産業計測制御/メカトロニクス制御合同研究会  
IIC-14-66, MEC-14-54, pp. 61-66, 2014  
場 所 芝浦工業大学, 東京  
発 表 日 2014 年 3 月 10 日  
開催期間 2014 年 3 月 10-11 日
- [15] 著 者 矢崎雄馬, 藤本博志  
題 名 推力制約を持つ終端状態制御における初期状態変数を用いた制御切り替え条件  
会 議 名 平成 26 年メカトロニクス制御研究会  
「ナノスケールサーボのための制御技術」, MEC-14-153, pp. 33-38, 2014  
場 所 電気学会会議室, 東京  
発 表 日 2014 年 9 月 1 日  
開催期間 2014 年 9 月 1 日
- [16] 著 者 矢崎雄馬, 藤本博志, 坂田晃一, 原篤史, 佐伯和明  
題 名 制約付き終端状態制御における初期状態変数を用いたモード切り替え制御  
及び超精密 2 段ステージへの適用  
会 議 名 平成 26 年メカトロニクス制御研究会  
「モーションコントロール」, MEC-14-167, pp. 45-50, 2014  
場 所 横浜国立大学, 神奈川  
発 表 日 2014 年 10 月 11 日  
開催期間 2014 年 10 月 11 日

- [17] 著 者 矢崎雄馬, 藤本博志  
 題 名 リファレンスガバナを用いた精密位置決め制御  
 ～制約を考慮した突発外乱抑圧制御～  
 会 議 名 平成 27 年メカトロニクス制御研究会  
 「精密サーボシステムと制御技術」, MEC-15-14, pp. 7-12, 2014  
 場 所 電気学会会議室, 東京  
 発 表 日 2015 年 9 月 10 日  
 開催期間 2015 年 9 月 10 日
- [18] 著 者 西村拓朗, 矢崎雄馬, 大西亘, 佐藤基, 居村岳広, 藤本博志, 堀洋一  
 題 名 磁界共振結合を用いた Moving Coil 型ワイヤレスリニアモータの基礎検討  
 会 議 名 平成 28 年メカトロニクス制御研究会  
 「精密サーボシステムと制御技術」, pp. 33-38, 2016  
 場 所 電気学会会議室, 東京  
 発 表 日 2016 年 9 月 29 日  
 開催期間 2016 年 9 月 29 日

## Peer-reviewed international conference papers (Co-author)

- [19] 著 者 Riccardo. A., Roberto. O., Yazaki. Y.,  
 Ohnishi. W, Fujimoto. H., Stefano. B., Emanuele. S.  
 題 名 Feasible trajectory generation for a dual stage positioning system  
 using a simplified model predictive control approach  
 会 議 名 IEEE/IES International Conference on Mechatronics, ICM2015  
 場 所 Nagoya, Japan  
 発 表 日 7th, March, 2015  
 開催期間 6th-8th, March, 2015

## Patent

- [20] 整理番号 14-0350-001JP01  
 開発名称 制御装置  
 出 願 日 2014 年 8 月 29 日

## Award

- [21] 受賞者 矢崎雄馬  
題名 粗微動間連結分離機構を有する精密位置決めステージの整定時間短縮制御法の提案  
受賞名 メカトロニクス制御時術委員会優秀論文発表賞  
受賞日 2015年1月7日
- [22] 受賞者 矢崎雄馬  
題名 粗微動間連結分離機構を有する精密位置決めステージの整定時間短縮制御法の提案  
受賞名 電気学会産業応用部門 部門優秀論文発表賞  
受賞日 2015年3月31日